Using new methods to understand how fault properties influence earthquake properties

Joshua Richard Williams

Submitted in accordance with the requirements for the degree of
Doctor of Philosophy

The University of Leeds
School of Earth and Environment

August 2019

The candidate confirms that the work submitted is his own, except where work which has formed part of jointly authored publications has been included. The contribution of the candidate and the other authors to this work has been explicitly indicated below. The candidate confirms that appropriate credit has been given within the thesis where reference has been made to the work of others.

The work in Chapter 2 of the thesis has appeared in publication as follows:
Williams, J.R., Hawthorne, J.C., Rost, S. and Wright, T.J., 2019. Stress Drops on the Blanco Oceanic Transform Fault from Interstation Phase Coherence. Bulletin of the Seismological Society of America, 109(3), pp.929-943.doi:10.1785/0120180319.

The phase coherence method used in this chapter originated from Jessica Hawthorne. I expand on the method here, and test the method on data for the Blanco fault and identify several limitations of the method. I performed all data processing and analysis, and used synthetics provided by Jessica Hawthorne to examine the effect of azimuthal variation of stations on the results of the phase coherence method. I wrote the manuscript for this chapter, which was improved by suggestions and comments from the co-authors.

The work in Chapter 3 of the thesis uses the phase coherence method originated from Jessica Hawthorne. I develop the method and use it on P waves and S waves of aftershocks of the El Mayor-Cucapah earthquake. I performed all data processing and analysis, and used a synthetic code provided by Jessica Hawthorne to examine the effect of azimuthal variation of stations on the results of the phase coherence method. I wrote this chapter, and it was improved by suggestions and comments from Jessica Hawthorne and Sebastian Rost.

The work in Chapter 4 of the thesis has appeared in a paper which has been submitted for publication as follows:
Williams, J.R.., Hawthorne, J.C. and Lengliné, O., in review. The long recurrence intervals of small repeating earthquakes may be due to the slow slip rates of small fault strands.

The hypothesis of fault strand-dependent slip rates explaining the unusual recurrence interval-moment scaling of repeating earthquakes originated from Jessica Hawthorne and was built upon by me. I tested this hypothesis by analysing the NCSN earthquake catalog which is available online, and the catalog from *Lengliné and Marsan* (2009) as provided by email from Olivier Lengliné. I performed all data analysis and wrote the manuscript, which was improved by suggestions from the co-authors.

Acknowledgements

First of all, the work in this PhD was supported by the Leeds-York Doctoral Training Programme of the National Environment Research Council. The council uses money from the taxpayer as my family like to remind me, so cheers for that!

The last 4 years have been a series of ups and downs with fantastic highs and awful lows. I would not have made it through this process without the help of the fantastic people that I mention here. I'd like to thank my family: Dad, Mum, James and Katy, for being there for me and willing to talk me through any problem I encountered. You also provided me with a place to live for the last month for which I and my bank account are eternally grateful. Being at home was made much better by the recent addition of Toby, whom I'm sure cares very little about this thesis. I'd also like to thank my partner-in-crime Katrina for making me happy, for making me laugh, and for making my life better. I quite literally could not have done this without you, and I look forward to our future where we finally live on the same continent. Katrina's family, the Piekarski clan, took me into their home and gave me a second family to cherish. Colleen, John, Leslie, Jonny, and Chris (and Charlie), thank you for taking me in and making me feel like part of the family. Thank you also to my extended family and the Piekarskis and Harringtons for giving me things to look forward to when I needed them most.

This thesis could not possibly exist without the support of my supervisory team and their push for me to make it through. Thank you to Jess Hawthorne who was there with me every step of the way and guided me throughout my PhD, pushing me to improve my work to the highest level. Thank you also to Sebastian Rost and Tim Wright for providing guidance and support, and for always being willing to talk. My PhD was also made exponentially better by the people I had around me. Thank you to Charles Kingsley Dunham, Matt Rowlinson, Maurits Metman, Claire Harnett, George Taylor and many others for helping me enjoy myself when I was down. Thank you also to Paddy Sugden, Beth Woodhams, and Chetan Deva who played endless board games and card games, and for goodness sake Chetan, you can't chow from the right. Outside of Leeds, I was surrounded by many fabulous people including James Singleton, Lizzie Clark, Hannah Colson, Simon Thorpe, Fred Jackson, Trevor Nicholas, Simon Taylor and many others. Special shoutout goes to the group of friends which I've always had

and are always willing to provide a distraction: Mathew Price, Will Jones, Jack Parton, Thomas Bamford and Chris Cullen. All of you were there for me, and I cannot express my gratitude enough. Finally, I'd like to thank the office of 8.152 for getting me through the day-to-day, the football group for putting up with my dreadful footballing abilities, and Richard Rigby, the IT genius who saved my work countless times. Thank you.

Abstract

In this thesis, I investigate the interaction of aseismic slip with earthquake stress drops and the interaction of fault properties with properties of repeating earthquakes. I use and develop a new inter-station phase coherence-based approach to estimate the rupture extents and stress drops of earthquakes. This new method is sensitive to different properties than spectral corner frequency approaches, and may be useful for examining properties such as rupture velocity. I use the phase coherence method to examine how stress drops vary with aseismic slip.

The seismic coupling, and thus aseismic slip, varies along the Blanco fault. I find that the stress drops of earthquakes in areas with more aseismic slip are lower than earthquakes in areas with less aseismic slip, which may be caused by a shortened seismic cycle on the hotter, more aseismic section of the fault. I also examine stress drops of aftershocks of the 2010 M_W 7.2 El Mayor-Cucapah earthquake to test whether changes in post-seismic slip rate cause changes in stress drops of aftershocks. The result of this comparison is unclear, but I find that the phase coherence method can be applied to the P wave and S wave which is useful for noisy datasets.

Finally, I examine repeating earthquakes in Parkfield, California to test whether the observed recurrence interval-moment scaling $M_0^{\frac{1}{6}}$ is due to spatially variable slip rates on a fault. In this hypothesis, repeating earthquakes occur on smaller faults with lower slip rates and recurrence interval-moment scaling reflects the scaling of slip rate with fault length. I find that the recurrence interval-moment scaling of repeating earthquakes varies with the distance between sequences, which suggests that repeating earthquakes occur on smaller, lower slip rate faults. This result suggests that repeating earthquake properties may reflect fault properties rather than the amount of aseismic slip.

Contents

List of Figures

List of Tables

Nomenclature

List of acronyms

AICD	Akaike Information Criterion Derivative
ASL	Albuquerque Seismological Laboratory
ASTF	Apparent Source Time Function
AZ	Arizona state, United States
BDSN	Berkeley Digital Seismic Network
BLD	Blanco Depression (includes West and East Blanco Depressions)
BLR	Blanco Ridge
CA	California state, United States
CAS	Cascadia Depression
CNDC	Canadian National Data Center
COLZA	Central Oregon Locked Zone Array
COV	Coefficient Of Variation
E	East
EBD	East Blanco Depression
eGf	empirical Green's function
EMC	El Mayor-Cucapah
GDP	Gorda Depression
GPS	Global Positioning System
GRI	Gorda Ridge
ID	Idaho state, United States

InSAR	Interferometric Synthetic Aperture Radar
IRIS	Incorporated Research Institutions for Seismology
JDF	Juan de Fuca Ridge
JdF	Juan de Fuca
lc	Loop closure
LIGO	Laser Interferometer Gravitational-wave experiment
MT	Montana state, United States
N	North
NCEDC	Northern California Earthquake Data Center
NCSN	Northern California Seismic Network
NEIC	National Earthquake Information Center
NERC	National Environment Research Council
NSF	National Science Foundation
NV	Nevada state, United States
NW	North West
OBS	Ocean Bottom Seismometers
OBSIP	Ocean Bottom Seismograph Instrument Pool
OSU	Oregon State University
P arrival	Arrival of the primary/pressure wave
P wave	Primary/pressure/compressional wave
PAZ	Puerta Accommodation Zone
PIAZ	Paso Inferior Accommodation Zone
PNNL	Pacific Northwest National Laboratory
PP	Parks Plateau
pP,sP,sS,pS	Depth phase acronyms
RESNOM	Red Sísmica del Noroeste de México

S	South
S arrival	Arrival of the secondary/shear
S wave	Secondary/shear wave
SAFOD	San Andreas Fault Observatory at Depth
SAGE	Seismological facilities for the Advancement of Geoscience and Earthscope
SCEDC	Southern California Earthquake Data Center
SE	South East
SNR	Signal-to-Noise Ratio
SUR	Surveyor Depression
U.S.	United States of America
USGS	United States Geological Survey
UT	Utah state, United States
W	West
WA	Washington state, United States
WBD	West Blanco Depression
X-D	X dimensional e.g. 1-D - one dimensional

List of symbols

β	Shear wave velocity	[km/s]
Δt_{ij}	Difference in time between main arrival and depth phase arrival	[s]
ΔV_S	Change in shear wave velocity	[%]
$\Delta\sigma$	Stress drop	[MPa]
γ	Scaling exponent of recurrence interval-moment relation of earthquakes	[-]
$\hat{x}_j$	Cross spectra at station j	[-]
λ	Wavelength	[m]
μ	Shear modulus	[GPa]

Ω_0	Maximum amplitude of earthquake amplitude spectra	[-]
ρ	Density	[kg/m^3]
σ_1	Maximum principal stress	[MPa]
σ_2	Intermediate principal stress	[MPa]
σ_3	Minimum principal stress	[MPa]
$\mathrm{m_b}$	Body-wave magnitude	[-]
$\mathrm{M_W}$	Moment magnitude	[-]
$\tilde{\delta}$	Averaged slip over the fault	[m]
A	Rupture area	[km^2]
a	Radius of repeating asperity	[m]
C_p	Phase Coherence	[-]
D	Rupture diameter	[m]
$d(f)$	Earthquake displacement spectra	[-]
f	Frequency	[Hz]
f_c	Corner frequency	[Hz]
f_f	Falloff frequency	[Hz]
F_{scal}	Scaling factor on falloff frequency to account for the azimuthal spread of stations	[-]
g_{ij}	Path term/Green's function of earthquake i at station j	[-]
i, j, l	Subscript, denote individual earthquakes or stations	[-]
K	Bulk Modulus	[Pa]
k	Constant	[-]
L	Characteristic dimension of earthquake	[km]
M	Earthquake magnitude (generic)	[-]
M_0	Seismic moment	[Nm]
$M_{0,ratio}$	Moment ratio	[-]
N	Number of stations	[-]

n	High frequency falloff rate of earthquake spectra	[-]
r	Radius of an earthquake	[m]
r_∞	Characteristic nucleation dimension	[m]
Re	Taking the real component of a number	[-]
s_{ij}	Source term of earthquake i at station j	[-]
t	Time	[s]
t_r	Recurrence interval	[s]
t_{ij}	Arrival time of earthquake i at station j	[s]
$t_{loop,j}$	Loop closure of travel times at station j	[s]
V_L	Loading velocity	[mm/yr]
V_P	Velocity of primary/pressure wave	[km/s]
V_S	Velocity of secondary/shear wave	[km/s]
V_W	Velocity of propagation wave	[km/s]
x	Distance from boundary of larger locked asperity	[m]
Y	Real number that accounts for reflection coefficient and amplitude of depth phase	[-]

Chapter 1

Introduction

"In the beginning the Universe was created. This has made a lot of people very angry and been widely regarded as a bad move."

Douglas Adams, The Hitchhiker's Guide to the Galaxy

Over the last 50 years, understanding of earthquakes has increased at a rapid rate; from the confirmation of plate tectonics in the 1960s (e.g., *Isacks et al.*, 1968), to modern state of the art research which uses numerical modelling to investigate rate and state friction and other properties of earthquakes (e.g., *Marone*, 1998, *Yabe and Ide*, 2018, *Cattania and Segall*, 2019). Nonetheless, there are areas of earthquake physics that are not fully understood which are crucial for estimating seismic hazard.

This thesis focuses on the properties of small $M < 6$ earthquakes. Small earthquakes cause small amounts of ground motion and thus are usually less dangerous than larger earthquakes. However, the properties of small earthquakes appear to follow the same physical processes as the properties of large earthquakes, otherwise known as self-similarity (e.g., *Omori*, 1894, *Gutenberg and Richter*, 1944, *Utsu*, 1961, *Aki*, 1967). For example, the number of earthquakes on a fault decreases log-linearly with increasing magnitude for all earthquake magnitudes (*Gutenberg and Richter*, 1944). The self-similar behaviour of small earthquakes suggests that observations of their properties may be used to infer the properties of large earthquakes (e.g., *Brodsky*, 2019). Smaller earthquakes significantly outnumber larger earthquakes (*Gutenberg and Richter*, 1944), so one can examine the physics and properties of earthquakes in greater detail and with more robust statistical analysis by analysing smaller earthquakes.

One earthquake property that is not fully understood is the stress drop: the change in stress on a fault due to an earthquake. Higher stress drops are associated with larger ground motions (e.g., *Bindi et al.*, 2018) and therefore may be related to the destructive power of an earthquake. Examining stress drops of earthquakes may also allow detailed modelling of the state of stress on a fault, and help us to better understand the stress conditions that trigger earthquakes. Understanding these stress conditions would significantly improve seismic hazard estimates.

Most stress drops are estimated on land-based faults due to the high quality data available (e.g., *Shearer et al.*, 2006, *Allmann and Shearer*, 2007, *Chen and Shearer*, 2013), with few studies on stress drops of offshore faults (e.g., *Moyer et al.*, 2018, *Kuna et al.*, 2019). Offshore faults, and especially oceanic transform faults, tend to feature high amounts of aseismic slip: slip that occurs on a fault without producing a seismic signal. Understanding the behaviour of stress drops on offshore faults may be crucial for understanding the interaction between earthquake properties and aseismic slip (e.g., *Moyer et al.*, 2018). Aseismic slip also occurs after large earthquakes, so examining the stress drops of aftershocks following large earthquakes may provide insight into the interaction between aseismic slip and properties of earthquakes (e.g., *Chen and Shearer*, 2013, *Abercrombie*, 2014, *Sumy et al.*, 2017, *Yamada et al.*, 2017).

Aseismic slip occurs on faults worldwide (e.g., *Behn et al.*, 2002) but often cannot be detected due to a lack of instrumentation. In these cases, authors might use repeating earthquakes to infer aseismic slip (e.g., *Igarashi et al.*, 2003, *Materna et al.*, 2018). Repeating earthquakes slip at a lower rate than the tectonic slip rate (e.g., *Nadeau and Johnson*, 1998), so this slip deficit may be related to aseismic slip. However, the interaction between repeating earthquakes and aseismic slip is still debatable (e.g., *Nadeau and Johnson*, 1998, *Beeler et al.*, 2001, *Anooshehpoor and Brune*, 2001, *Sammis and Rice*, 2001, *Chen and Lapusta*, 2009, *Cattania and Segall*, 2019).

In this thesis, I will outline the work I have done to advance the field of earthquake seismology and attempt to fill some of the gaps in knowledge identified above. I investigate the relationship between aseismic slip and fault properties with earthquake properties. In Chapter 2, I use the recently developed phase coherence method (*Hawthorne and Ampuero*, 2017, *Hawthorne et al.*, 2018, *Williams et al.*, 2019) to examine the stress drops of earthquakes on the Blanco oceanic transform fault, off the coast of Oregon, U.S., and their relation to the change in seismic coupling along the fault. My work is one of the first to employ this method and to examine its limitations. In Chapter 3, I develop the phase coherence method further by analysing the S wave and comparing the results from the S wave with the results from the P wave using the same dataset. I estimate stress drops of aftershocks of the 2010 M_W 7.2 El

Mayor-Cucapah earthquake and examine the variation of these stress drops in relation to the main shock, with magnitude and depth, and with time. In Chapter 4, I examine repeating earthquake sequences in Parkfield, California, which have an unexpected recurrence interval-moment scaling. I use a simpler approach than previous studies (e.g., *Nadeau and Johnson*, 1998, *Lengliné and Marsan*, 2009). I assess whether the unexpected scaling could be controlled by an array of fault strands that make up a larger fault zone.

Here, I provide an in-depth background to the concepts that I examine in this thesis. I begin by discussing how stress drops are usually estimated and some of their properties (Sec. 1.1). I then discuss oceanic transform faults and their properties (Sec. 1.2) and outline the detailed properties of the Blanco fault (Sec. 1.2.1 - 1.2.2) as a more in-depth background to Chapter 2. I describe some interesting properties of continental strike slip faults (Sec. 1.3) and look in detail at the 2010 El Mayor-Cucapah earthquake sequence (Sec. 1.3.1 - 1.3.2) which I examine in Chapter 3. Next, I outline our understanding of repeating earthquakes (Sec. 1.4) and examine previously suggested explanations for the scaling of recurrence intervals of repeating earthquakes with moment (Sec. 1.4.1) before testing my own hypothesis in Chapter 4. Finally, I describe the aims and objectives of this thesis (Sec. 1.5) and outline the structure of the thesis (Sec. 1.6).

1.1 Stress drops

To understand stress drops, it is useful to consider how earthquakes originate and the role of friction in rocks. For example, consider an experiment where stress is applied to a core of rock. Initially, a fault forms in the rock and partially releases some of the stress being applied (*Stein and Wysession*, 2013). If you apply further stress to the rock, the rock will eventually fail along the plane of weakness (the fault) in an earthquake, releasing stress on the fault in a stress drop. With further stress applied, the rock will remain stationary until it eventually slips along the fault again, resulting in another earthquake with another stress drop. This behaviour is often called stick-slip and is caused by the fact that it is harder to initiate movement along a fault than to maintain slip, because the static friction which prevents the initiation of slip is stronger than the dynamic friction that acts to prevent slip once it commences. In this thesis, I measure the release of stress due to an earthquake in the form of stress drops.

Note that within the last 30 years, research has shown that friction is much more complex. The most popular current theory on friction is rate and state friction, where the friction on a fault μ is determined by both the slip rate v_{slip} and the state, the history of slip of the rock θ_{slip}, following the equation $\mu_{fric} = \mu_{fric,0} + b\theta_{slip} + aln\frac{v_{slip}}{v_{0,slip}}$

where a and b characterise the material (e.g., *Marone*, 1998, *Scholz*, 2002, *Stein and Wysession*, 2013) and $v_{0,slip}$ is a reference velocity. One can describe the behaviour of rock using rate and state friction in two behaviours. If $a - b$ is negative, then the material is velocity-weakening, as in the material weakens with slip velocity. Velocity weakening material is thus susceptible to earthquakes. On the other hand, if $a - b$ is positive then the material is velocity-strengthening, and slip will happen aseismically. These two different behaviours of materials are important for the discussion of results later in my thesis.

The stress drop of an earthquake is the amount of stress released on a fault due to the earthquake. The stress drop is thus the difference between the yield stress of the fault and the final stress after the earthquake. Stress drops $\Delta\sigma$ describe the relation between the averaged slip over the fault $\tilde{\delta}$ and the characteristic dimension L of an earthquake (*Scholz*, 2002), or generally

$$\Delta\sigma = \mu\frac{\tilde{\delta}}{L}, \tag{1.1}$$

where μ is the shear modulus. A more specific definition of stress drop assumes an elliptical slip distribution (*Eshelby*, 1957) and a circular fault (*Brune*, 1970), which gives:

$$\Delta\sigma = \frac{7}{16}\frac{M_0}{r^3}. \tag{1.2}$$

Here M_0 is the seismic moment of the earthquake and r is the radius of the fault.

The stress drop obtained above is the change in the spatially averaged shear stress on a fault before and after an earthquake, otherwise known as the static stress drop (*Scholz*, 2002). If the stress drop is considered over subsections of the earthquake rupture or shorter time windows, then it is defined as a dynamic stress drop. The dynamic stress drop is difficult to obtain as it involves modelling the rupture of the earthquake (e.g., *Quin*, 1990, *Mayeda and Walter*, 1996). Most studies calculate the static stress drop of an earthquake (e.g., *Mori et al.*, 2003, *Shearer et al.*, 2006, *Allmann and Shearer*, 2007). In this thesis, I refer to the static stress drop as the stress drop.

A wide variety of stress drop values is reported in the literature. For example, *Hanks* (1977) found stress drops for Southern California in the range of 0.03 – 30 MPa and *Allmann and Shearer* (2007) found values of 0.1 – 100 MPa in Central California. In general though, stress drops are within a range of 0.01 - 1000 MPa (*Cocco et al.*, 2016) with an average value of 0.1 – 10 MPa (Figure 1.1) (*Cotton et al.*, 2013).

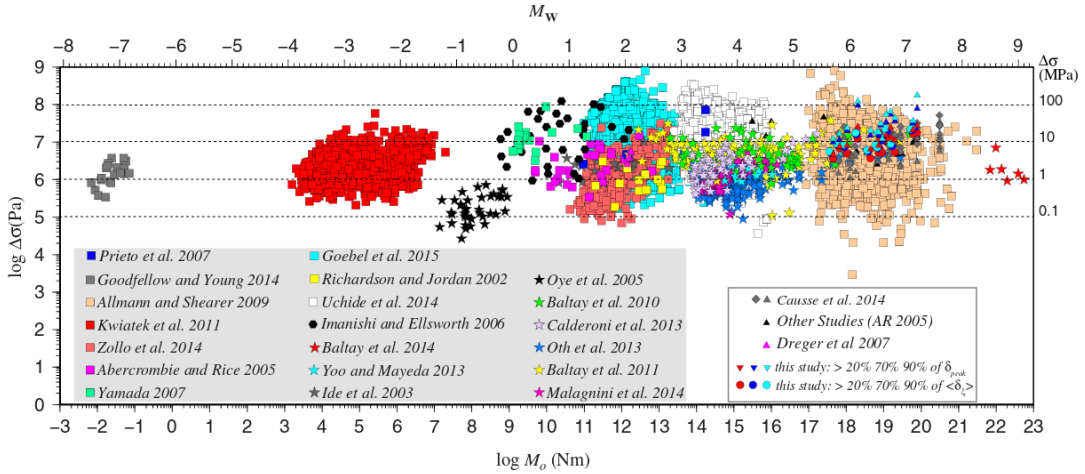

Figure 1.1: Moment scaling of stress drops from many different studies. Detailed descriptions of symbol meanings are in *Cocco et al.* (2016). Figure from *Cocco et al.* (2016).

1.1.1 Calculating stress drops: Existing methods

The values of stress drops may depend on the methods used to obtain them. Stress drops of small to intermediate magnitude earthquakes (e.g. $M_W < 7$) are normally obtained by examining the source spectrum of an earthquake. Earthquake spectra are flat at frequencies f much lower than the inverse of the earthquake duration, with a maximum amplitude Ω_0 proportional to the earthquake moment. The amplitude decays at higher frequencies due to the finite duration of the earthquake, resulting in the frequency-amplitude spectra shown in Figure 1.2. The frequency at which the amplitude begins to decrease is known as the corner frequency f_c. The earthquake spectrum $d(f)$ therefore has the form (*Brune*, 1970)

$$d(f) = \frac{\Omega_0}{1 + (f/f_c)^n}, \tag{1.3}$$

where n determines the higher frequency falloff rate and is normally assumed to be close to 2 (e.g., *Brune*, 1970, *Hanks and Kanamori*, 1979, *Andrews*, 1986, *Hough and Seeber*, 1991, *Prieto et al.*, 2004, *Shearer et al.*, 2006) but has some variation (e.g., *Anderson and Hough*, 1984, *Castro et al.*, 1990, *Purvance and Anderson*, 2003, *Allmann and Shearer*, 2007, 2009).

The corner frequency of the earthquake spectrum is related to the rupture radius of an earthquake r. Assuming a circular fault (*Brune*, 1970),

$$r = \frac{k\beta}{f_c}, \tag{1.4}$$

where β is the shear wave velocity and k is a constant, normally assumed to be 0.32

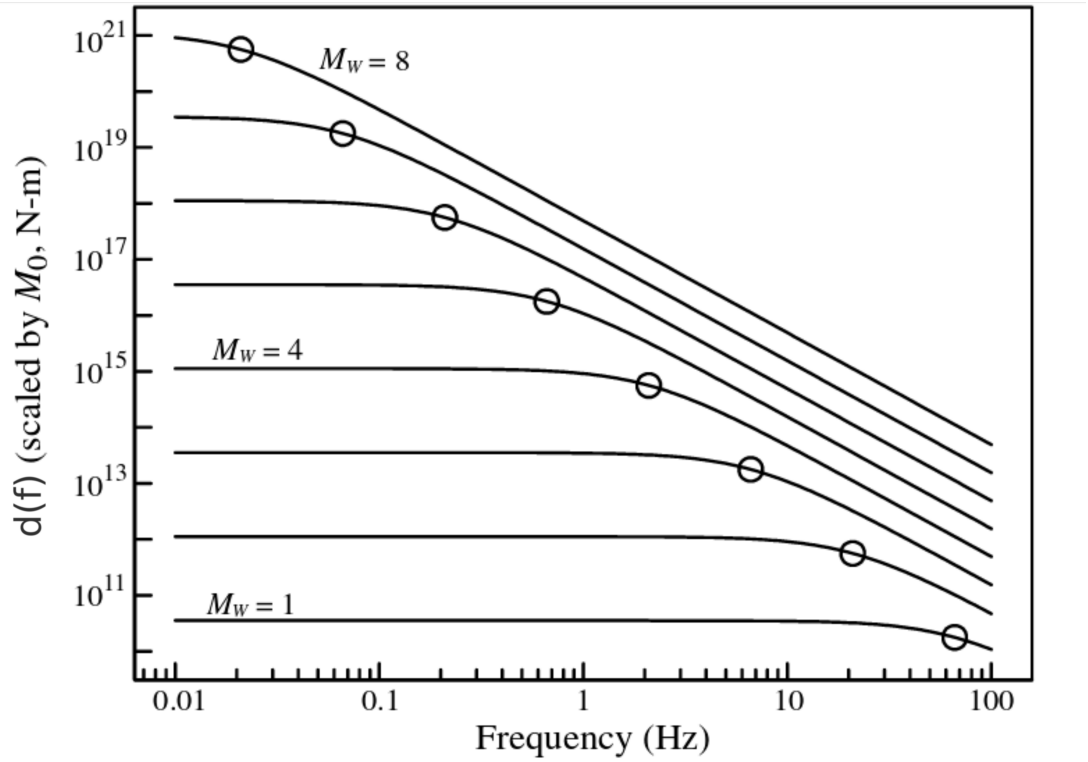

Figure 1.2: Earthquake P wave spectra using the model of *Madariaga* (1976) and assuming a constant stress drop of 3 MPa. Corner frequencies are highlighted by circles. The low frequency amplitudes of the spectra are scaled to the corresponding earthquake moments. Figure modified after *Shearer* (2009).

for P wave spectra using a rupture velocity equal to 90% of the shear wave velocity (*Madariaga*, 1976). The radius of the earthquake can be used to calculate the stress drop using Equation (1.2).

Unfortunately, the source spectrum of an earthquake is hard to isolate as earthquake seismograms and spectra are contaminated by other effects such as path effects between source and receiver. To understand how one might deal with these path effects, consider the earthquake spectrum in the log-frequency domain $d_{ij}(f)$

$$d_{ij} = s_{ij} + g_{ij} + resid_{ij}. \tag{1.5}$$

where i indexes the earthquake and j indexes the station and we have dropped frequency indexing for readability. Here s_{ij} is the source term, g_{ij} is the path term otherwise known as the Green's function, and $resid_{ij}$ is a residual term which includes the site and instrument response.

From this definition, one way to remove the path effect from the earthquake spectrum is to subtract an approximation of the path term from the earthquake spectrum.

The most common approach for obtaining an approximation of the path term is the empirical Green's function (eGf) approach (e.g., *Shearer et al.*, 2006, *Allmann and Shearer*, 2007, 2009, *Chen and Shearer*, 2013). This approach assumes that co-located earthquakes will have roughly the same Green's function (path effects) for each station. Thus subtracting the spectrum of a smaller co-located earthquake from the original earthquake will remove the path effects from the earthquake spectrum. The spectrum of the smaller earthquake is flat at low frequencies, so will not interfere with the lower corner frequency of the larger original earthquake. The eGf approach has the added benefit of removing the site response.

After removing the path effects and site response, the source dependent term of the seismic spectrum is isolated. One can obtain the corner frequency and stress drop from the isolated source dependent term. Note that the path effects and site response may change with time between earthquakes. For this reason, it may be prudent to require that small earthquakes used in the eGf approach occur within a short time frame of the main earthquake (e.g., *Allmann and Shearer*, 2007).

The eGf approach is common, but the method used to apply this approach can vary. One widely used method is the spectral decomposition method, where a global eGf is estimated and then removed from individual events to get estimates of the source spectra (e.g., *Shearer et al.*, 2006, *Allmann and Shearer*, 2007, 2009). The global eGf is a function which provides the best fit to a theoretical source model when it is subtracted from all the available event spectra. The appropriateness of a global eGf can depend on the size of the region being analysed - a single global eGf for a large region may mask the variability of stress drops within the region (*Shearer et al.*, 2019).

Other studies use many smaller earthquakes as eGfs for a target event (e.g., *Abercrombie et al.*, 2017, *Ruhl et al.*, 2017) and calculate the average spectral ratio between the target event and the smaller events. Then, they fit the spectral ratio using earthquake models with corner frequencies for the larger and smaller events. This method is typically applied to small numbers of events, whereas the global eGf spectral decomposition approach is applied to many earthquakes at once (e.g., *Shearer et al.*, 2006, *Allmann and Shearer*, 2009).

Shearer et al. (2019) compared the results of the spectral decomposition and spectral ratio fitting methods for roughly 3000 aftershocks of the 1992 M_W 7.3 Landers earthquake. They found it was difficult to constrain an optimal global eGf even with 3000 earthquakes and a small 17 x 15 km study area. For the spectral ratio fitting method, they observed that the choice of corner frequency for the smaller event can affect the estimated corner frequency of the larger event. *Shearer et al.* (2019) also

observed systematically higher corner frequencies for the spectral ratio fitting method, as well as a larger scatter. For both methods though, they concluded that the relative corner frequencies in a dataset were resolved better than the absolute corner frequencies. Thus it may be difficult to compare absolute stress drop values between studies, but comparing relative variations is still viable.

For very large earthquakes (e.g. $M_W > 7$), spectral decomposition methods are inappropriate as they rely on a point source approximation (*Ye et al.*, 2016). Instead, stress drops are often obtained by fitting datasets such as seismograms, Global Positioning Systems (GPS) data or Interferometric Synthetic Aperture Radar (InSAR) data with a synthetic earthquake rupture (e.g., *Mai and Beroza*, 2000, *Kim and Dreger*, 2008, *Causse et al.*, 2013, *Lay et al.*, 2016, *Ye et al.*, 2016). This more complex fitting approach can also be used for smaller earthquakes; *Kim et al.* (2016) calculated stress drops of M_W 2.1 repeating earthquakes in Parkfield, California. Other methods use the band limitation of the peak acceleration of an earthquake to obtain stress drops (e.g., *Hanks and Johnson*, 1976, *Hanks and McGuire*, 1981).

Here, I use a new method to obtain stress drops: the inter-station phase coherence method (e.g., *Hawthorne and Ampuero*, 2017, *Hawthorne et al.*, 2018, *Williams et al.*, 2019). This method takes advantage of the rupture directivity effect, where signals from different points in an earthquake arrive at different times depending on the distance and azimuth between the earthquake and the station. I discuss the phase coherence method in detail in Chapters 2 and 3, and use it to examine the variation in stress drops with properties along the Blanco fault and with other earthquake properties.

1.1.2 Observed properties of stress drops

Previous studies have observed a variety of relationships between earthquake dynamics and stress drops. One such relationship is that stress drops do not depend on earthquake moment (Figure 1.1) (e.g., *Abercrombie*, 1995, *Mori et al.*, 2003, *Shearer et al.*, 2006, *Allmann and Shearer*, 2007, 2009, *Chen and Shearer*, 2011, *Uchide et al.*, 2014, *Chen and McGuire*, 2016, *Cocco et al.*, 2016, *Abercrombie et al.*, 2017, *Yoshida et al.*, 2017), although some studies do observe a moment dependence for $M < 4$ earthquakes (e.g., *Kanamori et al.*, 1993, *Lin et al.*, 2012, *Oth*, 2013, *Lin et al.*, 2016, *Imanishi and Uchide*, 2017). The lack of moment dependence is consistent with the concept of earthquake self-similarity (*Aki*, 1967), where the physical properties of earthquakes maintain constant statistical relations across variations in earthquake size. Self-similarity has been observed for many earthquake properties, most famously the Gutenberg-Richter earthquake magnitude-frequency law (*Gutenberg and Richter*, 1944), and the Omori law for aftershock occurrence with time (*Omori*, 1894, *Utsu*, 1961).

One can understand the lack of moment dependence in stress drops by considering the stress drop equation (Equation (1.2)). Substituting $M_0 = \mu A\tilde{\delta}$ into Equation (1.2) where A is the rupture area gives:

$$\Delta\sigma = \frac{7}{16}\frac{\mu A\tilde{\delta}}{r^3}. \tag{1.6}$$

As the rupture area depends on r^2 assuming a circular rupture (*Brune*, 1970) and the slip of an earthquake scales linearly with the rupture extent of the earthquake (*Scholz*, 2002), stress drop does not depend on moment. This linear slip-rupture extent relation may break down for larger earthquakes because their rupture area is limited by the seismogenic width (*Scholz*, 2002).

The lack of moment dependence simplifies the comparison of earthquake stress drops with other earthquake properties such as depth and focal mechanism. Conceptually, one might expect a deeper earthquake to have a lower stress drop, as the higher temperature at depth weakens the material strength (*Brace and Kohlstedt*, 1980, *Sibson*, 1984, *Tse and Rice*, 1986). On the other hand, as the depth increases so does the normal stress, which increases the shear stress needed for an earthquake to occur. Therefore stress drop may increase with depth. However, the depth dependence of stress drops from observations is unclear; some studies find that stress drops increase with depth (e.g., *Jones and Helmberger*, 1996, *Hardebeck and Hauksson*, 1997, *Shearer et al.*, 2006, *Allmann and Shearer*, 2007, *Baltay et al.*, 2011, *Chen and Shearer*, 2013, *Oth*, 2013, *Uchide et al.*, 2014, *Goebel et al.*, 2015, *Chen and McGuire*, 2016), and others observe little to no relation between stress drops and depth (e.g., *Jin et al.*, 2000, *Kinoshita and Ohike*, 2002, *Mori et al.*, 2003, *Allmann and Shearer*, 2009, *Abercrombie et al.*, 2017, *Goebel et al.*, 2017, *Wu and Chapman*, 2017).

The depth dependence of stress drops is complicated by the rupture velocity (Equation (1.4)). Rupture velocity is normally assumed to depend on the shear wave velocity (e.g., *Madariaga*, 1976), which increases with depth. *Allmann and Shearer* (2007) found that the depth dependence in their stress drops disappears if they take a depth-varying shear wave velocity into account. However, *Uchide et al.* (2014) considered the increase in shear wave velocity with depth using a 1-D velocity model and still found an increase in stress drop with depth (Figure 1.3). Assessing the depth dependence can also be complicated by poorly resolved earthquake depths (e.g., *Williams et al.*, 2019). These problems impede the identification and understanding of depth dependence of stress drops.

Stress drops may also depend on the focal mechanism of an earthquake. One would expect the highest stress drops on reverse faults and the lowest stress drops on normal

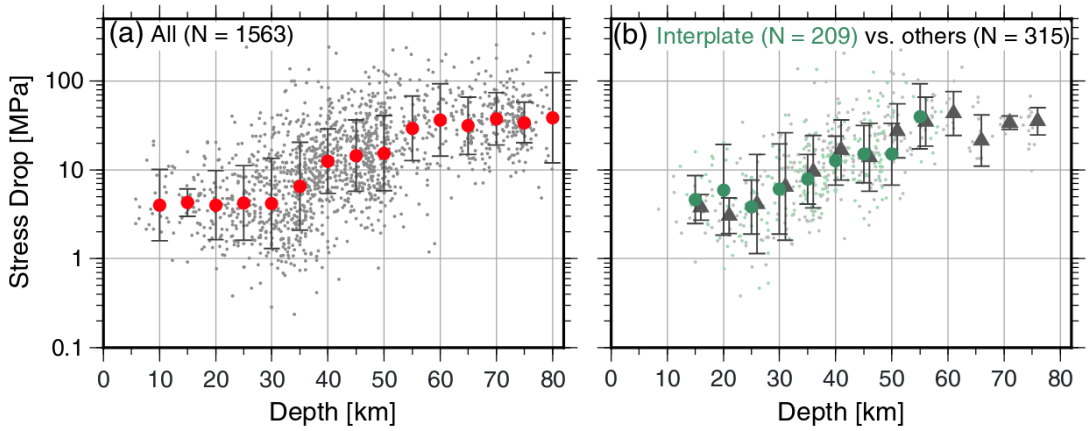

Figure 1.3: Stress versus depth for M_W 3.0 – 4.5 earthquakes that occurred before the 2011 Tohoku-oki earthquake in Japan. Symbols indicate the median stress drops in 5-km bins. (a): Median stress drops against depth for the whole catalog. (b): Median stress drops against depth for interplate and off-plate events. Events that do not have moment tensor solutions from the F-net broadband seismograph network are excluded. Figure from *Uchide et al.* (2014).

faults if stress drops behave according to Anderson's faulting theory (*Anderson*, 1951, *Sibson*, 1974, *McGarr*, 1984, *Sibson*, 1982, *Brune and Thatcher*, 2002). Anderson's faulting theory states that faults often form conjugate sets which are inclined at acute angles to the maximum principal stress σ_1, with the fault strike parallel to the direction of the intermediate principal stress σ_2 (Figure 1.4). For reverse faulting, the minimum principal stress σ_3 acts vertically, whereas for normal faulting, the maximum principal stress σ_1 acts vertically. The vertical stress or overburden can be estimated as $\rho g z$ where ρ is density, g is the acceleration due to gravity, and z is depth (*McGarr and Gay*, 1978). Therefore, σ_3 and σ_1 can be estimated for reverse and normal faults respectively, and one can use two different forms of Byerlee's law (*Sibson*, 1974, *Byerlee*, 1978, *Brace and Kohlstedt*, 1980, *McGarr et al.*, 1982) to estimate σ_1 and σ_3 for reverse and normal faults. As the shear strength is $(\sigma_1 - \sigma_3)/2$ and the difference between the principal stresses is larger for reverse faults, the shear strength is significantly higher on reverse faults compared to normal faults (*McGarr*, 1984). Assuming that the stress drop depends on the shear strength, reverse or thrust faulting earthquakes should have higher stress drops than normal faulting earthquakes.

However, the observed stress drop dependence on focal mechanism is more complicated than the simple dependence on normal stress above. Various studies have found the highest stress drops for strike slip faults (e.g., *Houston*, 2001, *Pérez-Campos et al.*, 2003, *Allmann and Shearer*, 2009), thrust faults (e.g., *Cocco and Rovelli*, 1989, *Hardebeck and Aron*, 2009, *Goebel et al.*, 2015), and normal faults (e.g., *Shearer et al.*, 2006). *Scholz et al.* (1986) even observed no variation of stress drop with focal mechanism. The lack of a systematic dependence of stress drop on focal mechanism could

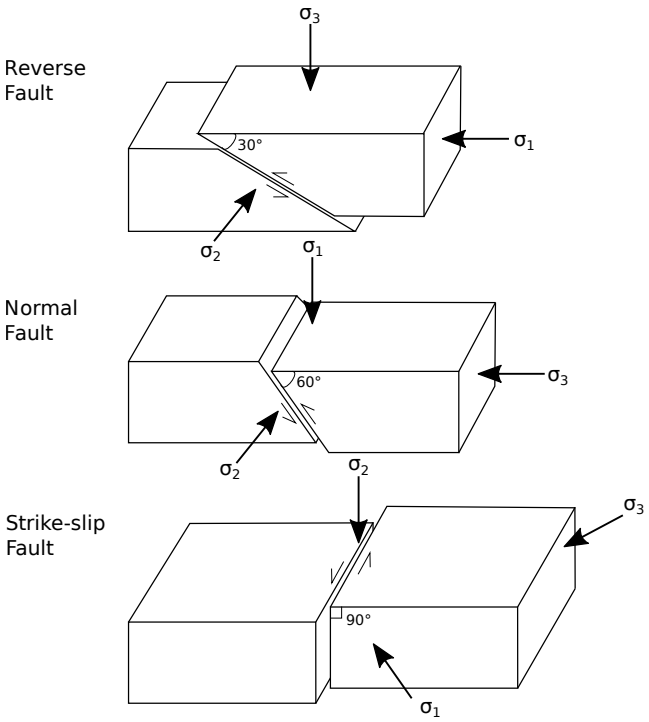

Figure 1.4: The three primary faulting types of thrust, normal, and strike slip from top to bottom. Principal stresses are labelled as σ_1, σ_2, and σ_3 where σ_1 is the maximum principal stress, σ_2 is the intermediate principal stress, and σ_3 is the minimum principal stress.

be attributed to differences in the rupture velocity or source directivity (e.g., *Allmann and Shearer*, 2009), but the difference in the dependence observed for different studies suggests that there is no definitive relation between stress drops and focal mechanism.

Another question is whether stress drops vary temporally or spatially. Spatial variation in stress drop is widely observed (e.g., *Allmann and Shearer*, 2007, 2009, *Chen and Shearer*, 2013). For example, *Allmann and Shearer* (2007) found lower stress drops in the creeping section of the Parkfield fault compared to the higher stress drops of earthquakes in the rupture area of the 2004 M_W 6 Parkfield earthquake - an important illustration of a possible interaction between aseismic slip and earthquake properties. *Jin et al.* (2000) also observed lower stress drops in the creeping region of the Atotsugawa fault zone in Japan. On a larger scale, average stress drops vary between different tectonic environments. Stress drops have been observed to be highest on the subduction interface (*Chen and McGuire*, 2016) and on oceanic transform faults (*Escudero and Doser*, 2012). The global study of stress drops by *Allmann and Shearer* (2009) also found that stress drops were highest on oceanic transform faults. The high stress drops on oceanic transform faults are particularly relevant for my work on the Blanco fault (Chapter 2).

Some authors associate variations in stress drop with a difference in fault rheology (e.g., *Uchide et al.*, 2014, *Escudero and Doser*, 2012, *Chen and McGuire*, 2016, *Staszek et al.*, 2017), with lower stress drops on lower strength sections of the fault interface (*McGarr*, 1984). This presumes that the final stress after these earthquakes is constant for the entire fault interface, with the higher stress drops on higher strength areas caused by the larger decrease from the high yield stress. This assumption highlights one of the problems of drawing conclusions from the amplitude of stress drops. Although the yield stress of an area may be consistent, the final stress after the earthquake may not always be the same. For example, consider a large asperity which undergoes both a partial rupture and a full rupture. The partial rupture may release some of the stress on the asperity, but does not have enough energy to maintain a rupture or to rupture the whole asperity, which leads to a high final stress. The full rupture ruptures the entire asperity and assuming it releases all or most of the stress, the final stress after the rupture will be much lower than in the partial rupture case. As one cannot easily differentiate between the two, it is difficult to link variations in stress drop with variations in fault rheology without considerable assumptions.

There may also be a link between the stress drop of aftershocks and the stress release of large earthquakes. For example, *Yamada et al.* (2010) examined aftershocks of the 2006 M_W 6.7 Kīholo Bay earthquake in Hawai'i and found that aftershocks which occurred on the edges of high slip areas of the main shock have higher stress drops than aftershocks in areas of low slip. Conceptually, one might expect high stress drops on the edge of high slip regions because of the large amounts of stress released by the main shock into surrounding areas. This relation between aftershocks and main shock slip is consistent with observations in other areas (e.g., *Urano et al.*, 2015, *Yamada et al.*, 2017, *Moyer et al.*, 2018), but stress drops of aftershocks may also not correlate with the slip of the main shock (e.g., *Sumy et al.*, 2017).

Aftershock stress drops have been observed to change with time. *Sumy et al.* (2017) found that aftershock stress drops increased with time, whilst others found a decrease in stress drop immediately after the main shock followed by an increase to pre-main shock levels (*Abercrombie*, 2014, *Trugman and Shearer*, 2018). The relationship between aftershock and foreshocks stress drops differs as well: *Moyer et al.* (2018) found that aftershocks had lower stress drops than foreshocks whilst *Imanishi and Uchide* (2017) found that aftershocks had higher stress drops than foreshocks. The variability of the change of stress drops with time before and after a main shock is highlighted by the work of *Chen and Shearer* (2013), who observed that stress drops can be higher or lower for aftershocks compared to foreshocks, even for main shocks which are relatively close to each other (Figure 1.5).

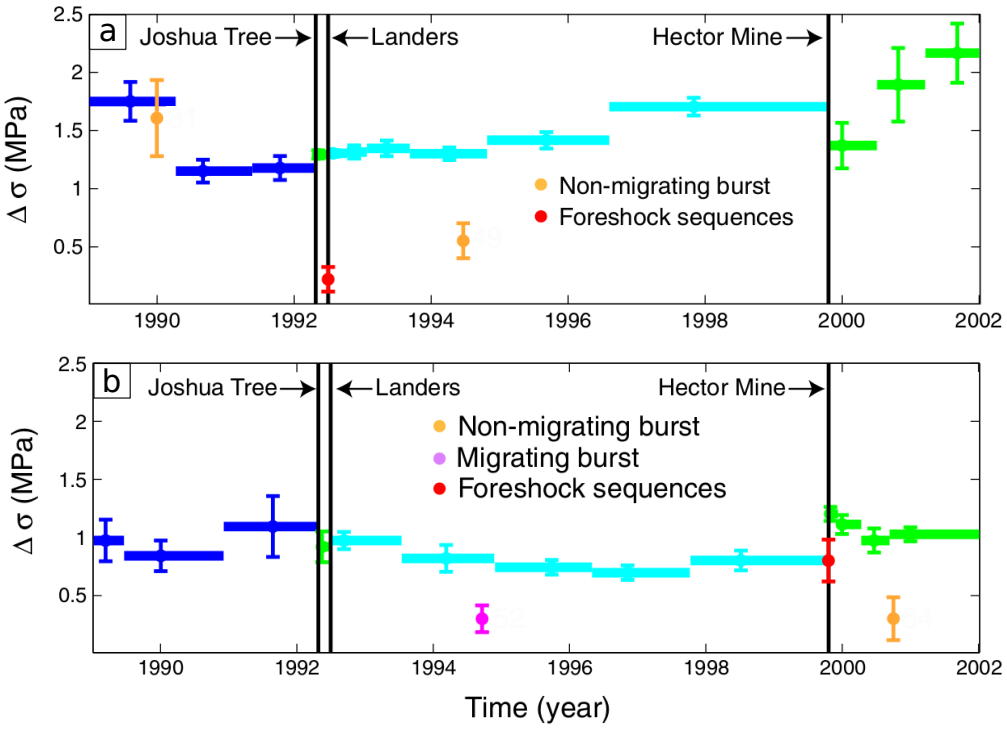

Figure 1.5: Median stress drops for different time periods for several different large events in California, plotted as thick horizontal lines with error bars indicating two standard deviations on the median. The 1992 M_W 6.1 Joshua Tree, 1992 M_W 7.3 Landers and 1999 M_W 7.1 Hector Mine earthquakes are plotted as vertical lines as annotated. (a): Stress drops for earthquakes within the Landers fault zone. (b): Stress drops for earthquakes within the Hector Mine fault zone. Figure modified after *Chen and Shearer* (2013).

Temporal change in stress drops is not limited to aftershocks and foreshocks. *Staszek et al.* (2017) and *Yoshida et al.* (2017) observe changes in stress drop with time that they associate with fluid migration or a reduction in effective stress by an increase in pore pressure. Alternatively, *Lengliné et al.* (2014) found no relation between stress drop and time associated with large scale fluid migration, and instead suggested that the variation in stress drops was linked to local fluid pressure variations, although this was still due to the injection of fluid into the reservoir. *Abercrombie* (2014) attributed the temporal variability in their estimated stress drops to increased stressing rates after the 2004 M_W 6.0 Parkfield earthquake, which reduced the healing time between earthquakes and thus reduced the strength of the fault and the stress drops. This mechanism is similar to what I suggest in my study of the Blanco fault (Chapter 2). Other studies of stress drops did not observe any change with time (e.g., *Uchide et al.*, 2014, *Wu and Chapman*, 2017). This spread of different results and suggested mechanisms for temporal variation in stress drops demonstrates the difficulty in associating temporal changes in stress drops with changes in physical properties of the subsurface.

One property of stress drops which is particularly relevant to my study of the Blanco fault is the dependence of stress drops on seismic coupling. The seismic coupling can be estimated using several different approaches. One approach is to compute the seismic flux release rate as $\sum_{i=1}^{n} \frac{M_0^i}{\mu t_r^i}$, the sum of the moment M_0^i of each earthquake divided by the multiplication of the shear modulus and the earthquakes' recurrence interval t_r^i. The seismic flux can then be divided by the tectonic flux rate $V_{plate}A_c$, where V_{plate} is the plate velocity and A_c is the seismogenic area of the plate boundary. Dividing the seismic flux release rate by the tectonic flux rate estimates the seismic coupling coefficient (e.g., *Kanamori and Stewart*, 1976, *Pacheco et al.*, 1993, *Okal and Langenhorst*, 2000, *Scholz*, 2002). Alternatively, if one can obtain geodetic measurements of the interseismic velocity in the region around the boundary, one can estimate the seismic flux accumulation rate. The geodetic coupling coefficient is the seismic flux accumulation rate divided by the tectonic flux rate, and may be a more accurate estimate of the seismic coupling as it doesn't depend on the earthquake catalog being complete (e.g., *Scholz*, 2002, *Carafa et al.*, 2017). Recent work, however, suggests that the coupling coefficients based on the seismic catalog and geodetic measurements are within 10% of each other (*Scholz and Campos*, 2012). But the tectonic flux rate still relies on an accurate estimate of the seismogenic area, and thus on accurate estimates of the area of the fault ruptured during earthquakes. Other previous estimates of the seismic coupling compare the area derived from earthquake ruptures and the area of the crust above the 600°C isotherm (*Boettcher and Jordan*, 2004), the tectonic slip rate versus the cumulative seismic slip rate (*Braunmiller and Nábělek*, 2008), or the aseismic slip rate derived from repeating earthquakes versus the seismic slip rate (*Uchida and Matsuzawa*, 2011).

In general, I use the seismic coupling to refer to the unit-less percentage of the measured quantity per study which occurs seismically, such as the slip or moment. The different approaches for estimating the seismic coupling make it difficult to compare estimates between different studies. However, most studies compare the cumulative moment rate (e.g., *Kawasaki et al.*, 2001, *Scholz and Campos*, 2012) or slip rate (e.g., *Kanamori*, 1977, *Braunmiller and Nábělek*, 2008) from earthquakes with the corresponding rate from GPS estimates of tectonic movement. The moment M_0 depends on the slip $\tilde{\delta}$ ($M_0 = \mu A \tilde{\delta}$), and therefore the moment rate depends on the slip rate. Thus it is reasonable to compare estimates made by these different methods. Other studies estimate the coupling by comparing the area of the fault ruptured in earthquakes with the total area of the fault ruptured (e.g., *Cowie et al.*, 1993). The seismic moment also depends on the rupture area A, so comparing areal estimates of coupling with results with other approaches is appropriate, but estimates of the area of the seismogenic region of the fault from earthquake locations are subject to uncertainties in those locations and the possibility of missing deep low magnitude earthquakes from the catalog, so areal estimates of the seismic coupling are likely less accurate than moment or slip based estimates.

Moyer et al. (2018) compared earthquake stress drops with the seismic coupling along faults on the East Pacific Rise, and found that stress drops on highly coupled segments were a factor of 2 larger than stress drops on less coupled segments (Figure 1.6). They suggested this variation was due to highly porous and highly damaged fault zones in areas of low seismic coupling, which result in lower stress drops. On the other hand, *Kuna et al.* (2019) examined the variation in stress drop with depth on the Blanco ridge, which is part of the Blanco fault (Sec. 1.2.1). *Kuna et al.* (2019) found that there was no significant difference in stress drops between the highly coupled crust and less coupled mantle. The difference in the results of these two studies and the general lack of studies comparing stress drops with coupling highlights that further work is needed to investigate the relation between stress drops and seismic coupling.

1.1.3 Understanding stress drops of earthquakes

As I have discussed here, the variation in the dependence of stress drops on different properties indicates that the behaviour of stress drops is not fully understood. Understanding this variation in stress is vital for creating the most realistic models of the evolution of stress in the subsurface, which can be used in seismic hazard analysis. I contribute towards our understanding of the interaction of earthquake properties with fault properties and aseismic slip by examining stress drops of earthquakes on the Blanco fault (Chapter 2), an oceanic transform fault off the coast of Oregon, United States (U.S.), and stress drops of aftershocks of the 2010 M_W 7.2 El Mayor-Cucapah

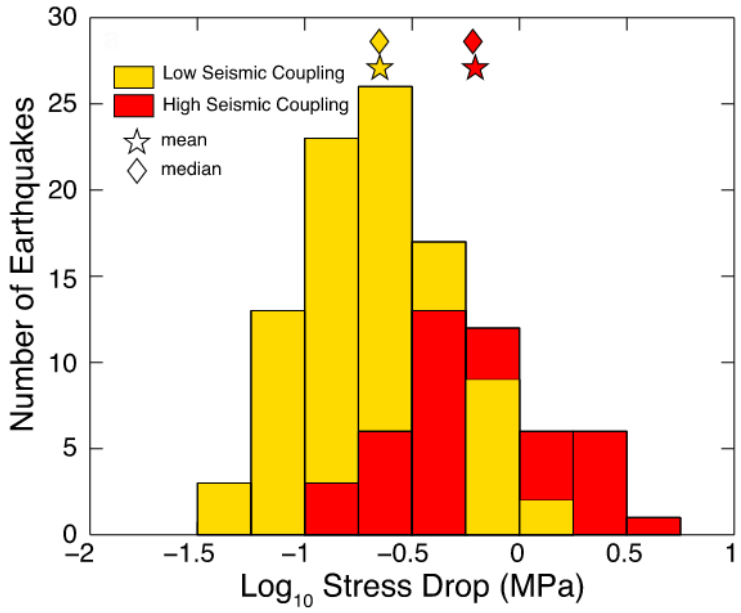

Figure 1.6: Comparison between stress drops in zones of high seismic coupling (red) and low seismic coupling (yellow) on faults in the East Pacific Rise. The mean and median values for each set are indicated by the star and diamond respectively. The mean and median stress drops of high coupling areas are approximately 0.6 MPa, and the mean/median stress drops of low coupling areas are roughly 0.2 MPa. Figure modified after *Moyer et al.* (2018).

earthquake in Mexico (Chapter 3). I examine how the stress drops vary with the seismic coupling along the Blanco fault, and look at the temporal variation of stress drops of aftershocks of the El Mayor-Cucapah earthquake, and how it might be explained by aseismic slip.

It has been suggested that Brune stress drops may not be representative of the change in stress on a fault due to an earthquake. For example, a common assumption when estimating stress drops from earthquake spectra is that the earthquake is a symmetrical circular rupture (e.g., *Abercrombie*, 1995, *Allmann and Shearer*, 2007, *Moyer et al.*, 2018). *Kaneko and Shearer* (2015) simulated an asymmetrical source model and found that changes in the source characteristics such as the source geometry or rupture speed, which are near-independent of the actual stress drop, can cause variations in the estimated stress drop by a factor of up to 8. Alternatively, *Lin and Lapusta* (2018) simulated earthquakes using rate and state friction on a velocity weakening patch surrounded by a velocity strengthening region, and found that the actual stress drops estimated directly from stress changes on the fault were consistently around 3 MPa, whilst the seismologically inferred stress drops ranged from 0.006 to 8 MPa. This difference in stress drop stems from the difference between the complex ruptures they see in their simulated earthquakes such as "ring-like" ruptures, compared to the traditional simplistic approach of a circular symmetric rupture. Perhaps then, the simplistic sym-

metric circular rupture that most assume (including in this thesis) does not accurately represent the true stress drop of earthquakes. However, without more in depth knowledge of the rupture process of each earthquake being analysed, it is a useful assumption to make.

There is also evidence from lab measurements that seismologically derived stress drops may not represent the actual change in stress on a fault. *Brace et al.* (1966) performed laboratory experiments on shear failure and found much larger stress drops of hundreds to thousands of MPa for both intact rocks and sawcut samples. Stress drops also appear to be much lower than the crustal strength with stress drops mostly below 100 MPa whereas crustal strength is estimated as 100s to 1000s of MPa (e.g., *Brace and Kohlstedt*, 1980, *Wiens and Stein*, 1983, *Stein and Wysession*, 2013). Other laboratory experiments have, on the other hand, found stress drops which are consistent with seismologically derived stress drops, in uniaxial and triaxial (e.g., *Sellers et al.*, 2003, *Passelègue et al.*, 2016) , artificial fault (e.g., *Karner and Marone*, 2000, *McLaskey et al.*, 2014), and in-situ rock fracture experiments (e.g., *Goodfellow and Young*, 2014). It is questionable though how appropriate it may be to extrapolate the results of these small scale laboratory experiments to the larger scales of earthquake ruptures.

The variations in stress that I attempt to extrapolate from stress drops in this thesis can be assumed to be deviations from the lithostatic stress model, where all three principal stresses are equal. There are also several other ways that stress can be estimated. Stress can also be measured by borehole breakouts which occur in the direction of minimum horizontal stress (e.g., *Zheng et al.*, 1989, *Werner et al.*, 1991, *Amato et al.*, 1995), but their shape and depth also indicates the magnitude of minimum and maximum horizontal in-situ stresses. Other measurements of stress come from the P and T axes of earthquake focal mechanisms, which describe the plane of maximum shear stress and the regional stress regime (*Anderson* (1951) and Figure 1.4). Changes in earthquake focal mechanisms can also indicate changes in the regional stress regime such as rotations of the maximum shear stress (e.g., *Amato et al.*, 1995, *Badawy*, 2001, *Ljunggren et al.*, 2003). There are many other ways of estimating the stress in the subsurface including stress measurements from fracking and overcoring and fault slip data from methods such as tiltmeters and deformation gauges (*Ljunggren et al.*, 2003).

These measurements of the state of stress have been used to analyse the change of stress in environments such as mines and oil wells, where the change in the state of stress can be crucial to maintaining safety or workers and monitoring the probability of large earthquakes (e.g., *Stacey and others*, 1998, *Rajmeny et al.*, 2002). One global project - the world stress map - has collated many of the stress measurements mentioned above to give a worldwide description of the state of stress and how it changes between

regions (e.g., *Zoback*, 1992a, *Heidbach et al.*, 2016). One noticeable interaction between faulting and regional stress is that faults tend to align in the optimal direction for slip (*Zoback*, 1992b, *Chang et al.*, 2010), with misaligned faults having a reduced maximum shear stress and therefore slipping less than their optimally oriented counterparts. On the other hand, if shear stress is particularly low in a region, then fault are more likely to deviate from the optimal stress alignment (*Famin et al.*, 2014).

1.2 Oceanic transform faults

In Chapter 2, I investigate the variation of stress drops with seismic coupling on the Blanco fault, an oceanic transform fault. Here I discuss some of the interesting properties of oceanic transform faults that motivated my work, before discussing the geological and thermal structure of the Blanco fault (Sec. 1.2.1).

Oceanic transform faults are strike slip faults which form steps between mid-ocean ridges or subduction zones. Oceanic transforms are widespread across the globe and can feature $M > 7$ earthquakes (Figures 1.7 and 1.13) (*Bird et al.*, 2002). However, the risk posed to people by these earthquakes is low due to the often distant location of these earthquakes from the coast and the low probability of these strike-slip earthquakes creating a tsunami. On the other hand, the large amounts of aseismic slip that these faults host (e.g., *Kanamori and Stewart*, 1976, *Okal and Stewart*, 1982, *Boettcher and Jordan*, 2004, *McGuire et al.*, 2005) could allow us to examine the relationship between earthquake properties and aseismic slip (creep).

Oceanic transform faults release more slip aseismically than in earthquakes, with a higher proportion of aseismic release than continental strike slip faults (*Behn et al.*, 2002). The large proportion of aseismic slip that occurs on oceanic transforms may be linked to serpentinisation at depth. Serpentinisation is where olivine reacts with water to form new hydrous minerals such as serpentine (*Moody*, 1976). This process changes the frictional behaviour of a rock from velocity-weakening to velocity-strengthening at low slip rates (*Reinen et al.*, 1991), enabling aseismic creep (e.g., *Scholz*, 2002, *Kuna et al.*, 2019). Serpentinisation is a useful explanation for the aseismic behaviour of oceanic transform faults (e.g., *Francis*, 1981, *Bird et al.*, 2002, *Kuna et al.*, 2019).

Oceanic transform faults feature a wide spectrum of aseismic and seismic behaviour. One such example is earthquakes with particularly low rupture velocities, which occur more commonly on oceanic transform faults than continental strike slip faults (e.g., *Kanamori and Stewart*, 1976, *Okal and Stewart*, 1982, *Pérez-Campos et al.*, 2003). *Pérez-Campos et al.* (2003) observed earthquakes with lower and normal rupture velocities on adjacent sections of the same oceanic transform, which suggests that the

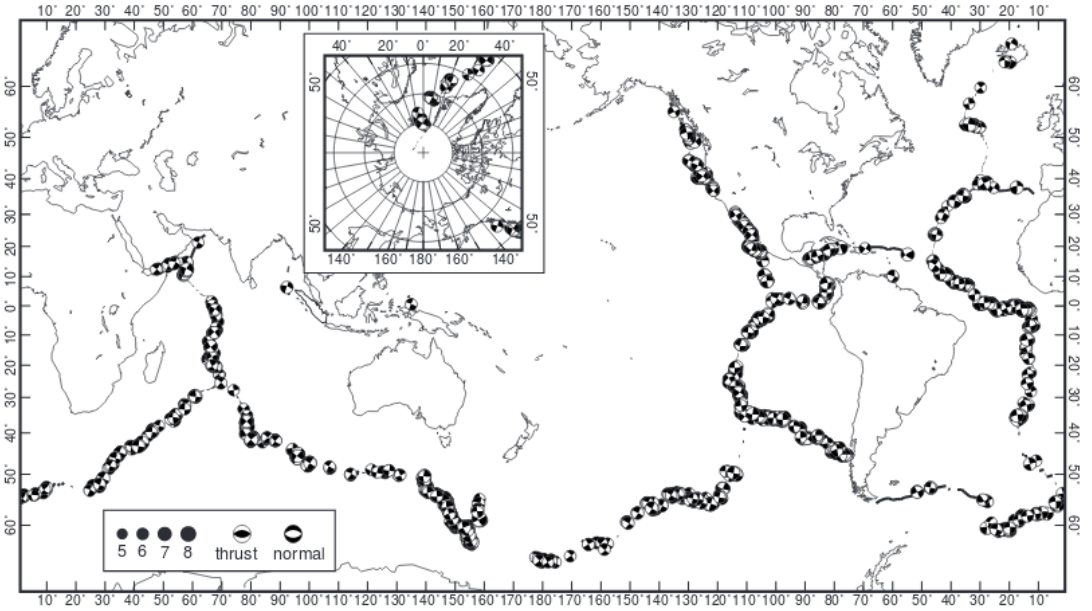

Figure 1.7: Map of $M \geq 5.0$ oceanic transform fault earthquakes and mechanisms from 1977 – 1998 from the Harvard Centroid Moment Tensor catalog. All earthquakes are located shallower than 70 km depth. Figure from *Bird et al.* (2002).

rupture velocity of an earthquake is determined by fault properties that can vary on a small scale.

At the more aseismic end of the spectrum, aseismic precursors are short-term aseismic events immediately before earthquakes which can be observed using source spectra (e.g., *Ihmlé et al.*, 1993, *Ihmlé and Jordan*, 1994, *McGuire et al.*, 1996, *McGuire and Jordan*, 2000). *Ihmlé et al.* (1993) inferred a slow precursor before the 1989 M_W 8.2 Macquarie earthquake by examining the delay in phases of low frequency (1 - 6 mHz) surface waves and normal modes relative to the origin time from high frequency waves. They observed an increase in phase delay between 1 and 6 mHz which could not be explained by conventional models of source time functions without the introduction of a slow precursor. *Ihmlé and Jordan* (1994) used a similar approach to identify possible slow precursors before 20 other events. *McGuire et al.* (1996) looked at low frequencies on the P arrival of the 1994 M_W 7.0 Romanche transform earthquake and observed a ramp in amplitude before the arrival which they attribute to a slow precursor. *McGuire and Jordan* (2000) used a similar approach to identify a possible slow precursor for the 1997 M_W 6.8 Prince Edward Island earthquake. On the other hand, it is possible that these precursors are artifically created in the source spectra by modelling uncertainties (*Abercrombie and Ekström*, 2001, 2003).

Alternatively, slow precursors might be apparent from earthquake recurrence intervals (e.g., *McGuire*, 2008, *Kuna et al.*, 2019). *McGuire* (2008) observed $M_W > 5.5$

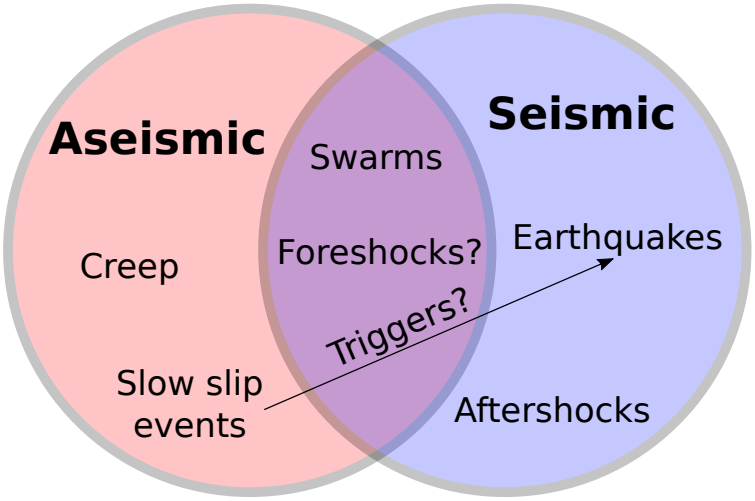

Figure 1.8: A Venn diagram of the different types of earthquakes and aseismic slip that occur on oceanic transform faults, split between completely seismic (earthquakes) and completely aseismic (creep) categories.

repeating earthquakes on East Pacific Rise transform faults, which repeated roughly every 5 years. One can infer from this that the aseismic slip is triggering large earthquakes, perhaps by increasing the stress at the nucleation point. *Kuna et al.* (2019) observed a similar pattern on the Blanco ridge with earthquakes roughly every 14 years. One possible explanation for these aseismic precursors is that they take time to achieve the high-slip rates of earthquakes due to the presence of serpentinite and its velocity-strengthening nature at low slip rates (e.g., *Reinen et al.*, 1994, *Kuna et al.*, 2019).

Aseismic and seismic slip appear to occur on the same patches of oceanic transform faults (*Boettcher and Jordan*, 2004), which affects the types of earthquakes on the faults (Figure 1.8). For example, earthquake swarms are short-lived sequences of earthquakes in small, localised areas, and are often used to infer aseismic slip (e.g., *Lohman and McGuire*, 2007, *Peng and Gomberg*, 2010, *Kuna et al.*, 2019). Earthquake swarms thus embody the aseismic-seismic interaction on faults. I discuss other aspects of this aseismic-seismic interaction for the rest of this section.

Aseismic-seismic interaction may explain the higher number of foreshocks on oceanic transform faults (Figure 1.9). *McGuire et al.* (2005) found that the ratio of foreshocks to aftershocks was an order of magnitude higher for $M < 6$ earthquakes on East Pacific Rise faults compared to similar sized earthquakes on continental strike slip faults in Southern California. This difference in ratio can be attributed to the very low aftershock productivity of oceanic transforms (15 times lower than continental strike slip faults) (*McGuire et al.*, 2005) and the high number of foreshocks. The number of foreshocks

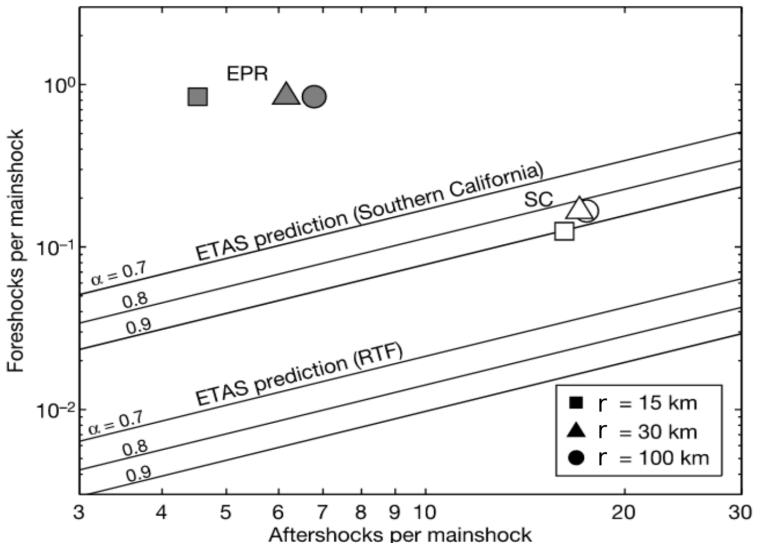

Figure 1.9: The number of aftershocks and foreshocks in regions around the main shock for 19 main shocks on faults on the East Pacific Rise (solid symbols) and 24 main shocks on continental strike-slip faults in Southern California (open symbols). The radius of the region around the earthquake used to define foreshocks and aftershocks is indicated in the legend. Figure from *McGuire et al.* (2005).

could be increased by earthquake swarms, which hint at a more aseismic triggering process for oceanic transforms compared to continental strike slip faults. This difference in earthquake triggering could be caused by serpentinisation on oceanic transform faults encouraging aseismic creep (e.g., *Moyer et al.*, 2018, *Kuna et al.*, 2019), or pore pressure changes in the fault core (*Géli et al.*, 2014).

On a smaller scale, the amount of seismic compared to aseismic slip, the seismic coupling, varies significantly between oceanic transform faults. *Brune* (1968) and *Kanamori and Stewart* (1976) determined that the Romanche and Gibbs fracture zones off the Mid-Atlantic Ridge had 100% seismic coupling, as in all the relative plate motion on these two transform faults was accounted for by seismic slip in earthquakes. Most recent studies, however, find that seismic coupling on oceanic transforms ranges from 5 – 50% (e.g., *Engeln et al.*, 1986, *Cowie et al.*, 1993, *Okal and Langenhorst*, 2000, *Abercrombie and Ekström*, 2001, *Behn et al.*, 2002, *Bird et al.*, 2002, *Boettcher and Jordan*, 2004). Coupling has also been observed to vary along individual faults, such as on the Gofar transform in the East Pacific Rise (*Boettcher and Jordan*, 2004, *Boettcher and McGuire*, 2009, *McGuire et al.*, 2012, *Moyer et al.*, 2018) and the Blanco fault off the coast of Oregon (*Dziak et al.*, 1991, *Braunmiller and Nábělek*, 2008). I examine the effect of this variation of coupling on earthquake stress drops in my work on the Blanco fault (Chapter 2).

Stress drops on oceanic transform faults have a wide range of values. For example,

Allmann and Shearer (2009) found a high average stress drop of 6.0±0.7 MPa for oceanic transform faults compared to an average stress drop of 3.3±0.2 MPa for all interplate earthquakes. *Chen and McGuire* (2016) also found a high average stress drop of 16.2±3.8 MPa, but *Moyer et al.* (2018) found stress drops of 0.04 - 3.4 MPa, similar to the overall average of interplate earthquakes quoted above. *Boettcher and Jordan* (2004) also found low stress drops of 0.1 - 0.7 MPa for a global set of oceanic transform faults and *Pérez-Campos et al.* (2003) suggested low stress drops for four earthquakes on oceanic transforms. The wide spectrum of stress drops on oceanic transforms indicates that further work is needed to clarify whether oceanic transforms have high earthquake stress drops. I add to this debate by examining stress drops along the Blanco oceanic transform fault (Chapter 2).

The aseismic-seismic interaction on the Blanco fault makes it an interesting example. One aspect of this interaction is low seismic coupling, which suggests that the earthquakes that do occur are influenced by aseismic slip on the fault. The Blanco fault was ideal for examining the effect that aseismic slip has on earthquake behaviour and specifically stress drops, due to the change in seismic coupling along its length (e.g., *Braunmiller and Nábělek*, 2008). I discuss the structure of the Blanco fault and some of its interesting properties in the following section.

1.2.1 The Blanco oceanic transform fault

The Blanco oceanic transform fault is a 350-km long right lateral strike-slip fault which forms a boundary between the Pacific and Juan de Fuca plates. The Blanco fault is approximately six million years old (*Embley and Wilson*, 1992, *Wilson*, 1993) and slips at a rate of 3 - 8 mm/yr (*Willoughby and Hyndman*, 2005). To the north, the boundary continues into the Juan de Fuca spreading ridge, and to the south, the Gorda spreading ridge. To the east, the Juan de Fuca plate subducts underneath the North American plate (Figure 1.10a).

The Blanco fault is composed of five depressions and several small transform segments, with one particular 150-km long transform segment known as the Blanco ridge. These depressions and transform segments, from the southeast end of the fault to the northwest, include: the Gorda depression (GDP), the Blanco ridge (BLR), the Cascadia depression (CAS), the Surveyor depression (SUR), the Parks Plateau fault (PP), the east Blanco depression (EBD) and the west Blanco depression (WBD) (Figure 1.10b). These segments are discussed in detail here.

The Gorda depression (GDP) is a pull-apart basin (*Embley and Wilson*, 1992), which is consistent with its rhomboidal shape (*Mann et al.*, 1983) and the normal-

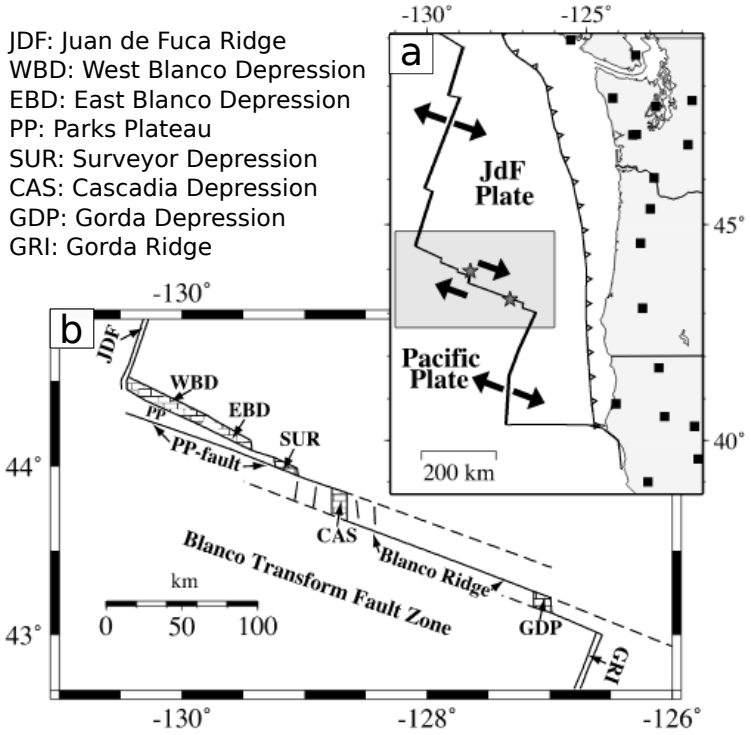

Figure 1.10: Map of the Blanco transform fault zone. (a): Large scale map of Blanco fault in context with local plates. Arrows indicate plate motions and the boundary marked with triangles is a subduction zone. (b): Fault scale map of the different segments of the Blanco fault. Different segments of the fault are marked by annotations defined in the legend and are discussed in the text. Figure modified after *Braunmiller and Nábělek* (2008).

faulting earthquakes within it (*Braunmiller and Nábělek*, 2008). *Embley and Wilson* (1992) suggested that the Gorda depression used to be a spreading segment but has since been replaced by the Gorda ridge.

To the west of the Gorda depression, the 150-km long Blanco ridge (BLR) is the longest strike-slip segment of the Blanco fault. The Blanco ridge has featured 5 out of 7 recorded $M > 6$ earthquakes on the Blanco fault up to 2017, possibly due to the structural complexity created at its eastern end by the intersection with the abyssal hill topography of the Gorda ridge (*Embley and Wilson*, 1992). This complexity may explain the unilateral northwest propagation of these large earthquakes along the fault (*Braunmiller and Nábělek*, 2008). *Kuna et al.* (2019) observed an offset in the locations of these $M > 6$ earthquakes and suggested that the Blanco ridge has two distinct asperities which rupture roughly every 14 years.

The origin of the ridge structure of the Blanco ridge is unclear. Some studies suggest that extensive shearing occurred along this section of the fault, allowing penetration of water into the crust and serpentinite diapirism to occur (*Embley and Wilson*, 1992, *Dziak et al.*, 2000, *Kuna et al.*, 2019). *Dziak et al.* (2000) suggested this diapirism to explain a low Bouguer anomaly in gravity data that coincided with the Blanco ridge, similar to the anomaly observed by *Kastens et al.* (1979) for the Tamayo transform fault in the Gulf of California. However, petrological analysis of rocks from the Blanco ridge find no evidence of serpentinite, although this could be due to a low sampling density (*Dziak et al.*, 2000). Serpentinite is a useful and simple explanation for many of the properties of oceanic transform faults, but without further evidence of its presence on the Blanco fault, it should be considered hypothetical.

The eastern edge of the Blanco ridge is defined by the Cascadia depression (CAS). The Cascadia depression is another pull-apart basin which is dominated by normal faulting, and differs from the other depression on the Blanco fault in that it may feature active sea floor spreading. Evidence for this active spreading consists of igneous intrusions and basement doming inferred from seismic reflection data (*DeCharon*, 1989, *Embley and Wilson*, 1992), as well as the morphology of the depression: a central basin surrounded by normal fault blocks which face inwards towards the centre (*Embley and Wilson*, 1992). The magma source for this spreading must be very deep, however, as the intermediate depth of earthquakes indicates a cool crust (*Braunmiller and Nábělek*, 2008) (Figure 1.11). Northwest of the Cascadia depression is the Surveyor depression (SUR), another pull-apart basin with dominant normal faulting but with no evidence for active sea floor spreading (*Embley and Wilson*, 1992, *Braunmiller and Nábělek*, 2008).

Southwest of the Surveyor depression and striking parallel to the main Blanco fault strand, the Parks Plateau (PP) structure is less understood than the other segments of the Blanco fault. The Parks Plateau has been described as both an active (*Delaney et al.*, 1981, *Braunmiller and Nábělek*, 2008) or former (*Embley and Wilson*, 1992, *Dauteuil*, 1995) transform fault. This segment may have a more complicated history though, as rock sampling identified volcanoclastic sediments (*Juteau et al.*, 1995).

The most western segments of the Blanco fault are the east (EBD) and west Blanco depressions (WBD). The east Blanco depression is another pull-apart basin (*Braunmiller and Nábělek*, 2008) but the west Blanco depression is more complex. *Braunmiller and Nábělek* (2008) identified three possible transform faults from three groups of slip vectors in the west Blanco depression and *Juteau et al.* (1995) observed striated fault planes during dives in the area. The possible transform faults and lack of normal faulting within the depression suggest that it is not a pull-apart basin or a spreading ridge, but instead has a complex history of ongoing changing structure (*Embley and Wilson*, 1992).

Although the structure of individual segments is interesting, the most interesting property for my work is the variation in seismic coupling along the fault. The sum of the slip of all the earthquakes on the Gorda, Cascadia, Surveyor, and East Blanco depressions accounts for only 15% of the plate motion, which suggests a large amount of aseismicity (*Braunmiller and Nábělek*, 2008). *Braunmiller and Nábělek* (2008) also identified that the northwestern half of the fault has very low coupling, whilst the southeastern half has higher coupling. This change in coupling is the major property I investigate using stress drops on the Blanco fault (Chapter 2). I use these stress drops to infer the link between the variation in coupling along the fault and the thermal structure.

1.2.2 Thermal and velocity structure of the Blanco fault

The complex structure of the Blanco fault complicates thermal models of the crust and mantle below the fault. The lower temperature areas of thermal models suggest where earthquake are likely to occur, but the temperature structure below the Blanco fault depends on whether the Cascadia depression is an active spreading centre. *Braunmiller and Nábělek* (2008) modelled temperatures underneath the Blanco fault using a simple half-space cooling model which ignored the possible sea floor spreading at the Cascadia depression (Figure 1.11a). This model constrains the maximum depth of seismic slip at the 600°C isotherm, which is consistent with experimental work on olivine (e.g., *Pinkston and Kirby*, 1982, *Boettcher et al.*, 2007) and with previous work on other oceanic transform faults (e.g., *Engeln et al.*, 1986, *Abercrombie and Ekström*,

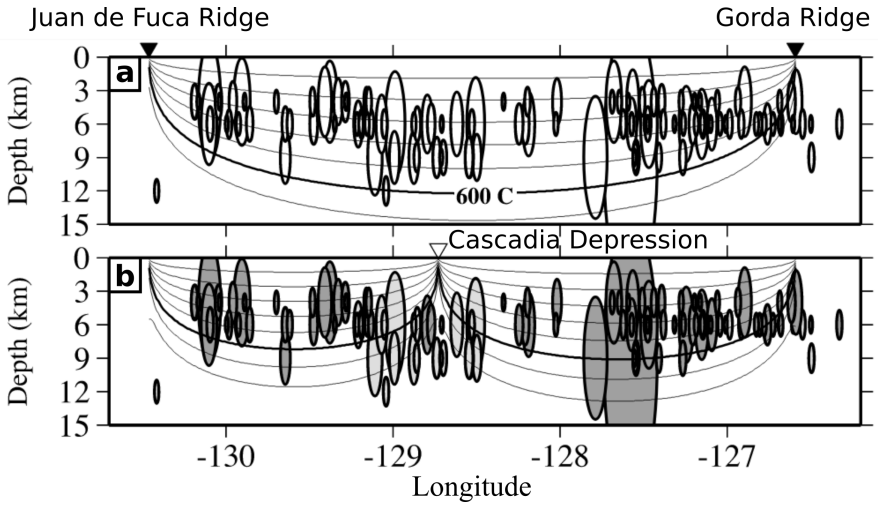

Figure 1.11: Two different cooling models for the Blanco fault. (a): Half space cooling model which ignores the possible spreading centre at the Cascadia depression. (b): Half space cooling model including the possible spreading centre at the Cascadia depression. Earthquake rupture areas are plotted as ellipses. Isotherms are marked by grey lines in 100°C increments. Figure modified after *Braunmiller and Nábělek* (2008).

2001). *Braunmiller and Nábělek* (2008) also considered another model which includes sea floor spreading at the Cascadia depression, which causes thermal upwelling underneath the Cascadia depression at the centre of the fault (Figure 1.11b). This model appears to be contradicted by earthquake locations in the centre of the fault, which are deeper than the 600°C isotherm. *Braunmiller and Nábělek* (2008) justify this by suggesting a deep magma source for the thermal upwelling. *Kuna et al.* (2019) also found that earthquakes were deeper than the modelled 600°C isotherm, although they attributed it to hydrothermal cooling.

These thermal models are challenged by the results of *Byrnes et al.* (2017), who examined the velocity structure of the mantle below the Blanco fault. They identified low shear wave velocities under the northwest section of the Blanco fault, and slightly high shear wave velocities under the southeast section (Figure 1.12). They infer mantle upwelling below the northwest section of the Blanco fault, which is consistent with petrological work which found that melt is formed beneath the Blanco fault (*Gaetani et al.*, 1995). This upwelling would significantly affect the depth of isotherms in the thermal models of *Braunmiller and Nábělek* (2008).

On a larger scale, *Porritt et al.* (2011) examined the deep velocity structure underneath the Cascadia subduction zone using ambient noise tomography along the west coast of the U.S.. They observed a split in the subducting slab of the Juan de Fuca plate underneath the North American plate, which matches the continuation of the Blanco fault to the west U.S. coast. They infer that this continuation is a weak zone

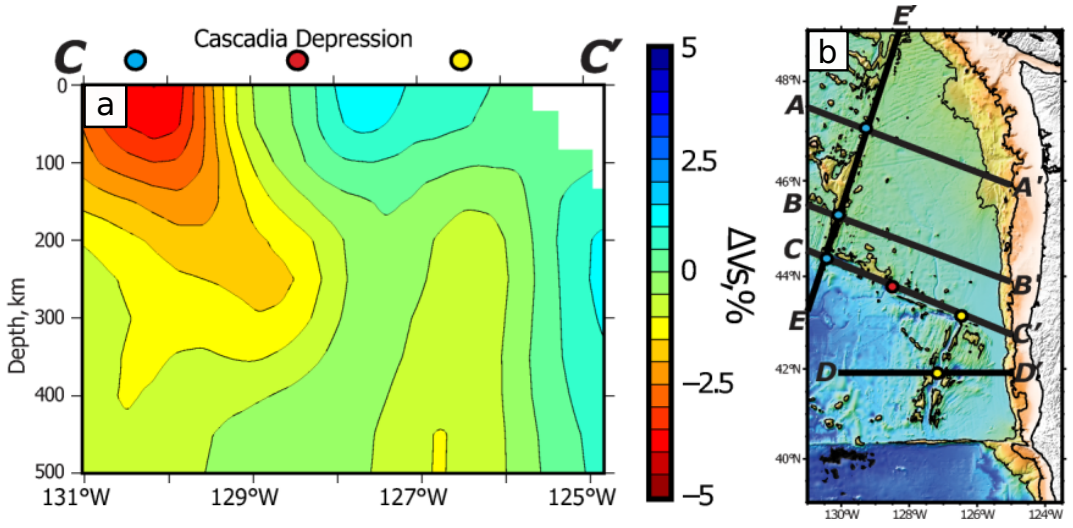

Figure 1.12: (a): Shear wave velocity change (ΔV_S) along profile C to C' in (b) along the strike of the Blanco fault using the model of *Byrnes et al.* (2017). The average shear wave velocity change is positive on the southeast segment of the fault and negative on the northwest segment of the fault. (b): Map of the region showing the location of the C - C' profile. Figure modified after *Byrnes et al.* (2017).

which allows increased melting and therefore a higher heat production. This result is compatible with the findings of *Byrnes et al.* (2017), although the study areas of the two studies do not significantly overlap to confirm this.

The complex thermal structure of the Blanco fault may be linked to the seismic coupling, as I discuss in my work on the Blanco fault (Chapter 2). As discussed earlier, if a fault is highly coupled then it primarily releases energy through earthquakes rather than aseismic slip. *Dziak et al.* (1991) identified generally low coupling along the Blanco fault, and with a variation between the northeast and southwest segments of the fault, with 3.8% and 14.1% of moment released seismically for each segment respectively. *Kuna et al.* (2019) and *Braunmiller and Nábělek* (2008) also identified low average coupling along the fault, although *Braunmiller and Nábělek* (2008) noted that the variation in coupling along the fault can be partially explained by different seismic zone widths and earthquake frequency-size distributions along the fault. I investigate the effect of this variation in coupling on earthquake properties on the Blanco fault.

The properties of the Blanco fault make it an interesting prospect to investigate. The structure of the Blanco fault is complex on a surface level, with five depressions and a 150-km long transform segment which features the largest earthquakes. This complexity may relate to the interaction of seismic and aseismic slip on the Blanco fault, as in its coupling, but the direct cause of slow aseismic slip or slow earthquakes is still not understood. One way to understand this interaction is to look at patterns

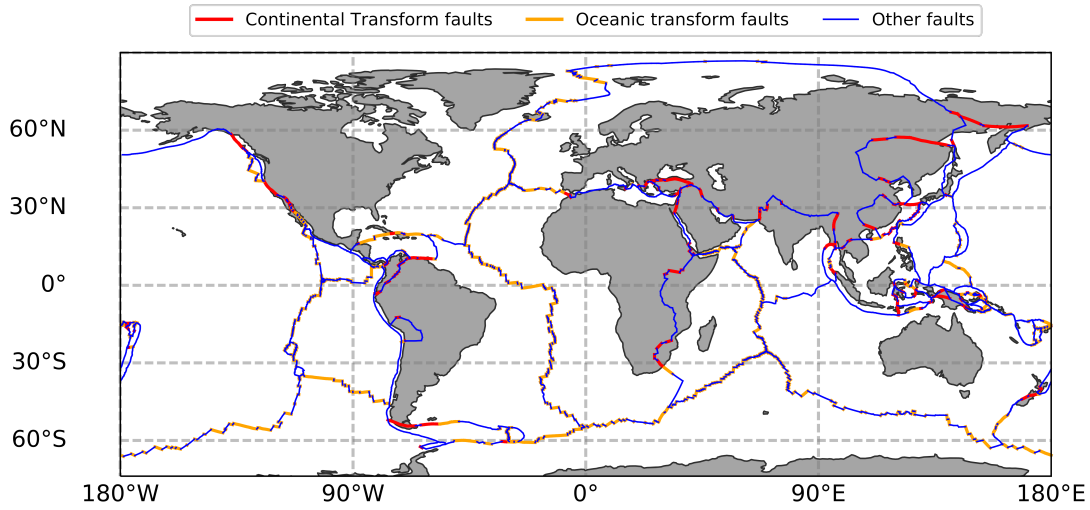

Figure 1.13: Global map of faults coloured by type. Continental strike slip faults are red, oceanic transform faults are orange, and all other fault types are dark blue. Fault segment locations and types were taken from *Bird* (2003).

of earthquake properties in areas of high and low aseismic slip, and use these patterns to infer the conditions which lead to more aseismic slip. I chose to examine the effects of seismic coupling on earthquake stress drops on the Blanco fault (Chapter 2), to investigate the influence of aseismic slip on the stress on a fault.

1.3 Continental strike slip faults

One of the reasons I chose to study the Blanco fault was due to the relative lack of research performed into earthquake properties on oceanic transforms, mainly due to the distance from seismic stations. The opposite is true for the continental counterpart of oceanic transforms - continental strike slip faults. Continental strike slip faults occur globally (*Bird et al.*, 2002) (Figure 1.13) and are one of the most intensely studied types of plate boundaries, as demonstrated by the extensive work on the San Andreas (e.g., *Bakun and Lindh*, 1985, *Zoback et al.*, 1987, *Abercrombie*, 1995, *Nadeau and Johnson*, 1998, *Bakun et al.*, 2005) and North Anatolian faults (e.g., *Barka*, 1992, *Stein et al.*, 1997, *Şengör et al.*, 2005, *Hearn et al.*, 2009, *Taylor et al.*, 2016). Continental strike slip faults can be hundreds of kilometres long and host up to M 8 earthquakes (e.g., *Martínez-Garzón et al.*, 2015). Their shallow depth and proximity to large population centres makes them crucial to study.

Continental strike slip faults also feature aseismic-seismic interaction, although to a lower level than oceanic transform faults as indicated by the higher seismic coupling of continental strike slip faults (*Behn et al.*, 2002). Indeed, the first case of aseismic creep was identified on the San Andreas fault in 1960 (e.g., *Scholz*, 2002). Aseismic creep has

since been identified on many continental strike slip faults (*Aytun*, 1982, *Allen et al.*, 1991, *Prioul et al.*, 2000, *Azzaro et al.*, 2001, *Galehouse and Lienkaemper*, 2003). One advantage of studying continental strike slip faults is that it is easier to use data from GPS or InSAR than on oceanic transform faults. Using GPS and InSAR helps identify long term aseismic slip on a fault, and allows in-depth study of the post-seismic aseismic "afterslip" associated with large earthquakes (e.g., *Smith and Wyss*, 1968, *Bucknam et al.*, 1978, *Bilham*, 1989, *Marone et al.*, 1991, *Donnellan and Lyzenga*, 1998, *Miyazaki et al.*, 2004, *Hsu et al.*, 2006, *Chlieh et al.*, 2007, *Ingleby and Wright*, 2017).

Continental strike slip faults and oceanic transform faults also have significant differences in earthquake stress drops. Earthquakes on continental strike slip faults have stress drops of 0.1 - 100 MPa (e.g., *Abercrombie and Leary*, 1993, *Allmann and Shearer*, 2007, *Chen and Shearer*, 2013), which is similar to oceanic transform faults (Sec. 1.2). However, differences in methods and assumptions make comparing absolute stress drops between studies difficult (Sec. 1.1.1). Fortunately, *Allmann and Shearer* (2009) compared stress drops for continental strike slip faults and oceanic transforms using the same analysis method, and found that continental strike slip earthquakes had an average stress drop of 3.58 ± 0.64 MPa, almost a factor of 2 lower than the average stress drop of 6.03 ± 0.68 for oceanic transform earthquakes. It is unclear what causes this difference in stress drop, but one possibility is that oceanic transform earthquakes have exceptionally low rupture velocities compared to continental strike slip fault earthquakes (e.g,. *Beroza and Jordan*, 1990, *McGuire et al.*, 1996). An alternative explanation could be that earthquakes on oceanic transform faults are mainly triggered by aseismic slip, whereas continental strike slip faults are mainly triggered by other earthquakes. Aseismic slip builds stress slowly on asperities which could allow asperities on oceanic transform faults more time to heal, and therefore they would have a higher strength and a higher stress drop when they eventually rupture.

The San Andreas fault is the most thoroughly studied continental strike slip fault, striking along the west coast of the U.S. through California and into Mexico (Figure 1.14). The San Andreas fault has featured many $M > 5$ earthquakes over the last 100 years (*Ellsworth et al.*, 1981), with its largest magnitude recorded earthquake occurring approximately 100 years ago - the 1906 San Francisco earthquake which killed up to 3000 people (*Hansen and Condon*, 1989) and caused $11 billion of damage (adjusted for inflation) (*Algermissen*, 1972). The length of time since that earthquake suggests that the San Andreas is due another large earthquake (*Ellsworth et al.*, 1981), which would be devastating for the west coast of California, one of the most economically important regions in the United States.

The most studied area of the San Andreas fault is the Parkfield region. The Parkfield

region seems to feature $M > 6$ repeating earthquakes, which led to a long term study to see if earthquakes could be successfully predicted (*Bakun and Lindh*, 1985). Although the 2004 M_W 6 earthquake arrived after the predicted year of 1993 (*Bakun et al.*, 2005), this work spurred many advances in understanding earthquakes including the link between repeating earthquakes and aseismic slip (Sec. 1.4.1). The failure of the prediction experiment also serves to illustrate an important concept: earthquakes can be incredibly complex, and sometimes exhibit unexpected behaviours. A good example of this is the 2010 M_W 7.2 El Mayor-Cucapah earthquake.

1.3.1 The 2010 M_W 7.2 El Mayor-Cucapah earthquake

The 4th April 2010 M_W 7.2 El Mayor-Cucapah earthquake was unusual for the region of Baja California, Mexico. The 2010 El Mayor-Cucapah earthquake occurred within a restraining bend of the San Andreas fault, which has featured several large earthquakes on the Laguna Salada and Cerro Prieto faults (*Fletcher et al.*, 2014). The epicentre was located between the large right lateral fault systems in California and the spreading centre region of the Gulf of California (*Kroll et al.*, 2013). The 2010 earthquake was unusual in that it did not rupture any of the known larger faults which accommodate approximately 90% of the fault motion (*Fletcher et al.*, 2014), but instead ruptured a series of 9 or more smaller faults 1 - 3 km away from these larger faults (e.g., *Fletcher et al.*, 2014, *Hauksson et al.*, 2011, *Huang et al.*, 2017b) (Figure 1.14). The complexity of this rupture and other recent ruptures (e.g, *Lay et al.*, 2018, *Stirling et al.*, 2017, *Zhang et al.*, 2012, *Fletcher et al.*, 2014) suggests that seismic hazard calculations must take into account the possibility of multi-fault ruptures.

The El Mayor-Cucapah earthquake was a 120-km long bilateral rupture which ruptured 55 km southeast towards the Gulf of California and 65 km northwest towards the U.S. (e.g., *Wei et al.*, 2011, *Kroll et al.*, 2013). The rupture had a dextral strike slip mechanism to the southeast, and a mix of dextral strike slip and normal faulting to the northwest. The earthquake ruptured southeast for the first 16 s, then propagated northwest for several seconds before rupturing bilaterally 20 s after the initiation of rupture (*Uchide et al.*, 2013). The rupture process of the El Mayor-Cucapah earthquake is further complicated by a possible 15-s long normal faulting event which preceded the main rupture (*Hauksson et al.*, 2011, *Wei et al.*, 2011). *Fletcher et al.* (2014) have extensively mapped the surface rupture of the El Mayor-Cucapah earthquake and found slip on at least seven different faults through the region due to the earthquake, and may have identified triggered slip on a number of other faults in the Yuha Desert region (e.g., *Rymer et al.*, 2011, *Kroll et al.*, 2013).

Several slip models have been created for the El Mayor-Cucapah earthquake using

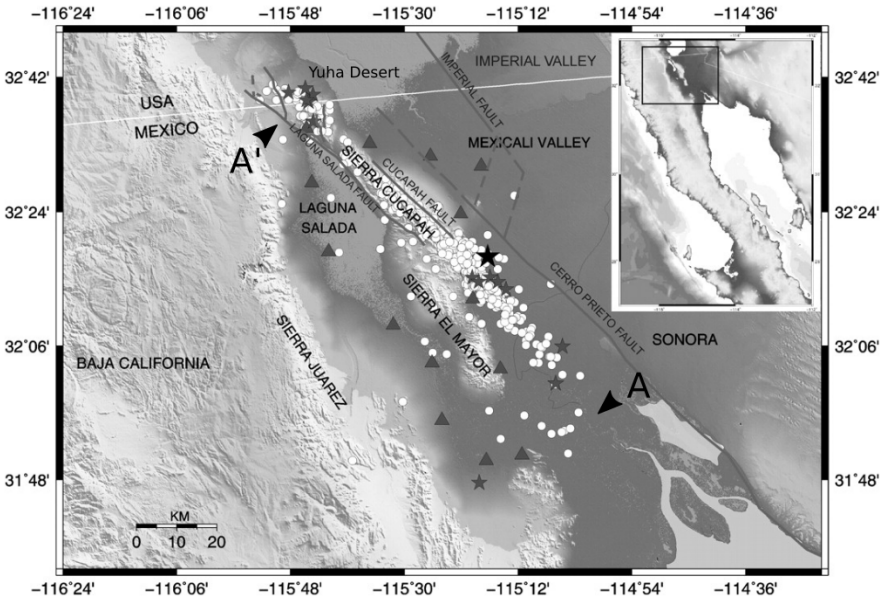

Figure 1.14: Map of the region surrounding the 2010 El Mayor-Cucapah earthquake. Faults are marked by thick solid or dashed grey lines. The epicentre of the El Mayor-Cucapah earthquake is marked by the black star. Smaller grey stars are aftershocks with $M > 4.5$ and white dots indicate smaller aftershocks. Main shock epicentre and aftershocks were located by the Red Sísmica del Noroeste de México using the local station array (triangles). Assuming that the aftershock locations indicate the rupture area of the earthquake, the 2010 El Mayor-Cucapah earthquake does not appear to be on any of the nearby major faults. Triangles marked A and A′ indicate the rough beginnings and ends of slip models in Figures 1.15 and 1.16. Figure modified after *Castro et al.* (2011).

a combination of geodesy, seismology and remote-sensing data (Figure 1.15). These slip models vary from single fault geometries (*Rodríguez-Pérez et al.*, 2012, *Mendoza and Hartzell*, 2013), four faults (*Wei et al.*, 2011, *Uchide et al.*, 2013), and up to nine faults (*Huang et al.*, 2017b). All of these slip models have relatively consistent overall fault geometry. The consistency between the models indicates that while the El Mayor-Cucapah earthquake was complex and ruptured several faults of different orientations, the majority of slip took place on one or two southeast-northwest striking near-vertically dipping faults.

Several studies have also modelled the post-seismic slip of the El Mayor-Cucapah earthquake (e.g., *Gonzalez-Ortega et al.*, 2014, *Dickinson-Lovell et al.*, 2017). Post-seismic deformation occurs by several mechanisms which include fluid flow induced by pressure changes caused by coseismic stress release (poroelastic rebound), the viscoelastic relaxation of the crust and mantle, and aseismic creep otherwise known as afterslip. Afterslip is another example of the interaction between aseismic slip and earthquakes, as it may affect the occurrence of aftershocks (e.g., *Hsu et al.*, 2006, *Perfettini and Avouac*, 2007).

Dickinson-Lovell et al. (2017) modelled the post-seismic slip of the El Mayor-Cucapah earthquake and found that post-seismic slip is dominated in the far-field and long-term by viscoelastic flow or relaxation, similar to the results of other studies (e.g., *Pollitz et al.*, 2012, *Rollins et al.*, 2015, *Hines and Hetland*, 2016). Immediately after the earthquake, in the near field, afterslip made the largest contribution to the 10 – 40 cm of post-seismic slip with a small component of poroelastic rebound (*Gonzalez-Ortega et al.*, 2014). Most of the afterslip was located at the edges of areas with high coseismic slip. I will examine the relationship between afterslip and aftershocks in the following section.

1.3.2 Foreshocks and aftershocks of the El Mayor-Cucapah earthquake

Foreshocks and aftershocks are smaller magnitude earthquakes that occur before and after a large earthquake, respectively. The pattern in their occurrence is often linked to aseismic precursors in the case of foreshocks (e.g., *Bouchon et al.*, 2011, *Kato et al.*, 2012, *Chen and Shearer*, 2013, *Jansen et al.*, 2019), or afterslip in the case of aftershocks (e.g., *Gonzalez-Ortega et al.*, 2014, *Zhu and Miao*, 2015, *Wu et al.*, 2017). In this way, foreshocks and aftershocks reflect the interaction between aseismic creep and earthquake properties. However, there are several other mechanisms that affect the properties of foreshocks and aftershocks.

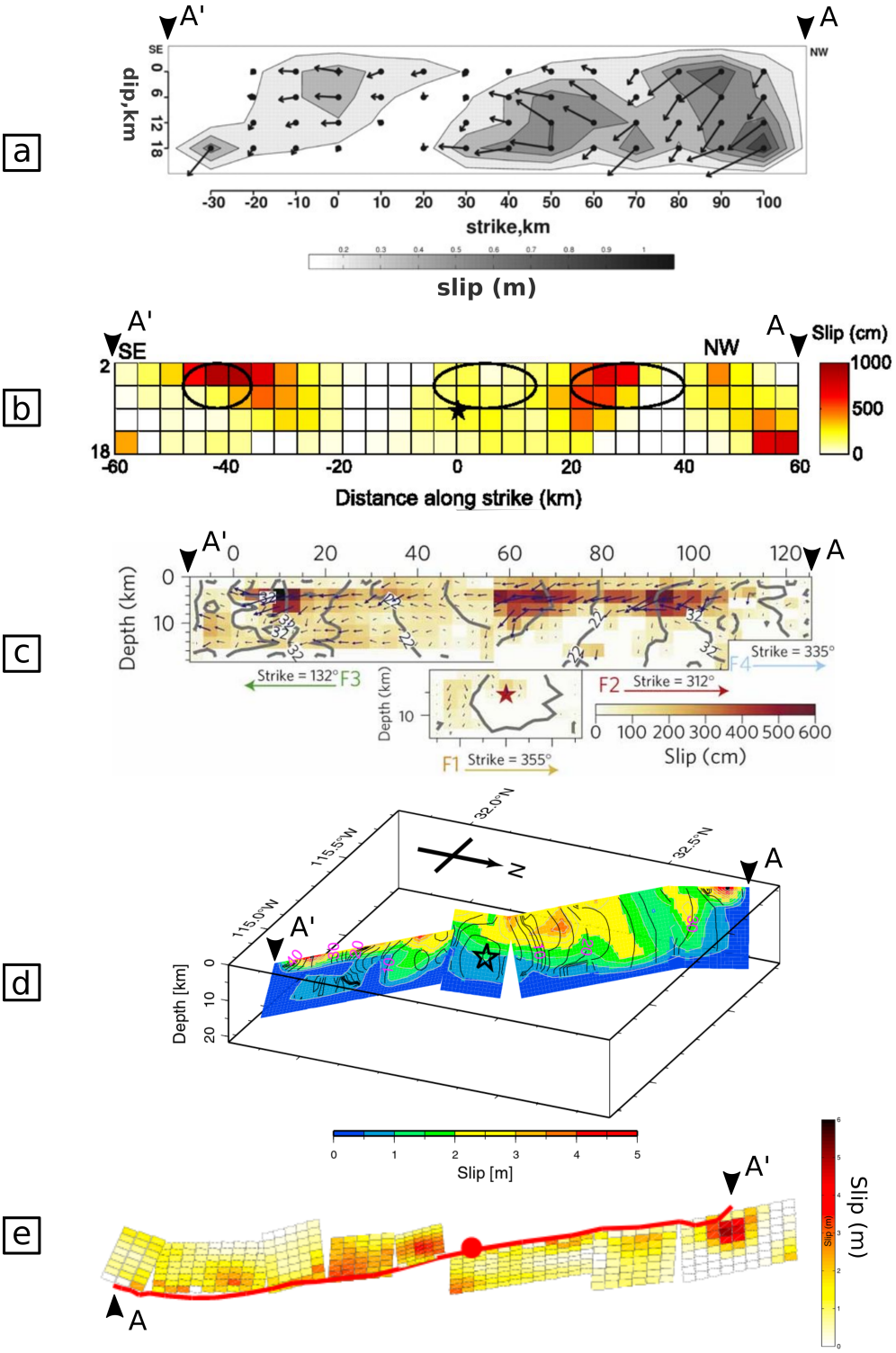

Figure 1.15: Slip models of the 2010 El Mayor-Cucapah earthquake from (a): *Rodríguez-Pérez et al.* (2012), (b): *Mendoza and Hartzell* (2013), (c): *Wei et al.* (2011), (d): *Uchide et al.* (2013), and (e): *Huang et al.* (2017b). Triangles marked A and A′ indicate the rough location of the southeast and northwest ends of the slip models located on Figure 1.14. Figures have been modified from their originals.

Whilst aftershocks occur with nearly all major earthquakes, foreshocks are far less common and therefore more difficult to examine (e.g., *Jones and Molnar*, 1979, *Abercrombie and Mori*, 1996, *Reasenberg*, 1999, *Yoon et al.*, 2019) (Figure 1.9). There are two main models for foreshock occurrence: a) foreshocks trigger each other, or b) aseismic slip triggers the foreshocks (e.g., *Seif et al.*, 2018, *Yoon et al.*, 2019). Both usually involve some form of earthquake migration. Many studies examine foreshock migration with time and make observations that support either the foreshock triggering (e.g., *Helmstetter and Sornette*, 2003a, *Felzer et al.*, 2004, *Herman et al.*, 2016) or the aseismic slip model (e.g., *Dodge et al.*, 1996, *Kato et al.*, 2012, *Chen and Shearer*, 2013, *Kato and Nakagawa*, 2014).

The triggering mechanism for aftershocks is also unclear. The most obvious triggering mechanism for aftershocks is the main shock. Such a relationship could explain why aftershocks are often located on the edge of high slip patches of the main shock (e.g., *Peng and Zhao*, 2009, *Yamada et al.*, 2010, *Kato and Nakagawa*, 2014, *Wu et al.*, 2017, *Wetzler et al.*, 2018, *Yabe and Ide*, 2018) (Figure 1.16). Alternatively, afterslip could serve as a triggering mechanism for aftershocks (e.g., *Perfettini and Avouac*, 2007, *Helmstetter and Shaw*, 2009, *Peng and Zhao*, 2009, *Gonzalez-Ortega et al.*, 2014, *Zhu and Miao*, 2015, *Huang et al.*, 2017a, *Wu et al.*, 2017). Note that dynamic triggering, viscoelastic relaxation, and fluid diffusion are also possible triggering mechanisms (*Scholz*, 2002, *Wright et al.*, 2013, *Wu et al.*, 2017).

Further evidence for afterslip as a driving mechanism for aftershocks of large earthquakes can come from aftershock migration with time (e.g., *Wesson*, 1987, *Peng and Zhao*, 2009, *Lengliné et al.*, 2012, *Huang et al.*, 2017a, *Ross et al.*, 2017, *Perfettini et al.*, 2018). For example, *Peng and Zhao* (2009) observed large scale migration of aftershocks after the 2004 M_W 6.0 Parkfield earthquake, and inferred a correlation between the location of aftershocks and the post-seismic deformation. It is important to emphasise, however, that without an independent measurement of afterslip such as GPS or InSAR, afterslip may not be the only cause of aftershock migration. Aftershock migration may also be caused by fluid flow similar to induced seismicity (e.g., *Bosl and Nur*, 2002, *Miller et al.*, 2004, *Malagnini et al.*, 2012), or may reflect the stress migration of a cascading model of aftershocks (e.g., *Helmstetter and Sornette*, 2003b, *Marsan and Lengline*, 2008).

The foreshock and aftershock behaviours in the El Mayor-Cucapah sequence show similar patterns to the observations above. The foreshocks in the El Mayor-Cucapah sequence occur in two clusters roughly a week and a day before the main shock, with magnitudes of M 1.5 - 4.4 (*Hauksson et al.*, 2011). Any migration of these foreshocks is difficult to observe as there are only roughly 40 recorded foreshocks, but *Chen and*

Shearer (2013) suggest fast migration along the main fault plane for the earlier cluster and a slower northward migration for the cluster immediately before the main shock, both of which are compatible with a precursory aseismic transient event.

Aftershocks are far more numerous than foreshocks in the El Mayor-Cucapah sequence, with over 10,000 aftershocks compared to roughly 40 foreshocks (*Hauksson et al.*, 2011, *Kroll et al.*, 2013). Despite the high number of aftershocks, few studies have examined the migration of aftershocks in the El Mayor-Cucapah sequence. *Castro et al.* (2011) examined aftershock locations, and found several rapid migrations within the first five hours after the main event, although they infer these migration patterns from very few earthquakes. The Yuha Desert region (Figure 1.14) to the north of the main rupture has been examined extensively, with similar migration speeds to the velocity of aseismic afterslip observed from GPS (*Ross et al.*, 2017). On the other hand, *Kroll et al.* (2013) did not observe any migration of aftershocks in the Yuha Desert. Other areas near the El Mayor-Cucapah earthquake also saw increased rates of seismicity (e.g., *Kroll et al.*, 2013, *Meng and Peng*, 2014), although this is likely due to static and dynamic triggering by the main shock. I chose to study the properties of aftershocks of the El Mayor-Cucapah earthquake sequence to look into the relation between aseismic afterslip and seismic aftershocks.

Another reason I chose to study the El Mayor-Cucapah earthquake sequence is the possible link between main shock slip and aftershock locations. Aftershocks appear to concentrate on the edges of areas of high slip during the main shock (e.g., *Peng and Zhao*, 2009, *Yamada et al.*, 2010, *Rietbrock et al.*, 2012, *Kato and Nakagawa*, 2014, *Wu et al.*, 2017, *Wetzler et al.*, 2018, *Yabe and Ide*, 2018). The same also appears to be true for the El Mayor-Cucapah earthquake (e.g., *Wei et al.*, 2011, *Gonzalez-Ortega et al.*, 2014, *Huang et al.*, 2017b) (Figure 1.16). One can infer from this clustering that aftershocks do not occur in areas of high slip as these areas have already released their stress through the main shock. On the other hand, some aftershocks do occur within the high slip regions of large earthquakes (e.g., *Yamada et al.*, 2010, *Wei et al.*, 2011, *Gonzalez-Ortega et al.*, 2014, *Urano et al.*, 2015, *Wu et al.*, 2017). If aftershocks occur on the edges of high main shock slip regions and within high slip regions, is there a significant difference in their stress drops? I attempt to analyse the variation in stress drops of aftershocks depending on their location in relation to the main shock slip in Chapter 3.

Stress drops of aftershocks may be higher in regions of high slip (e.g., *Yamada et al.*, 2010, *Urano et al.*, 2015, *Yamada et al.*, 2017, *Moyer et al.*, 2018), or might not (e.g., *Sumy et al.*, 2017). It is not clear, however, what the pattern of stress drops of aftershocks should be. Should the stress drops of aftershocks in high slip regions be

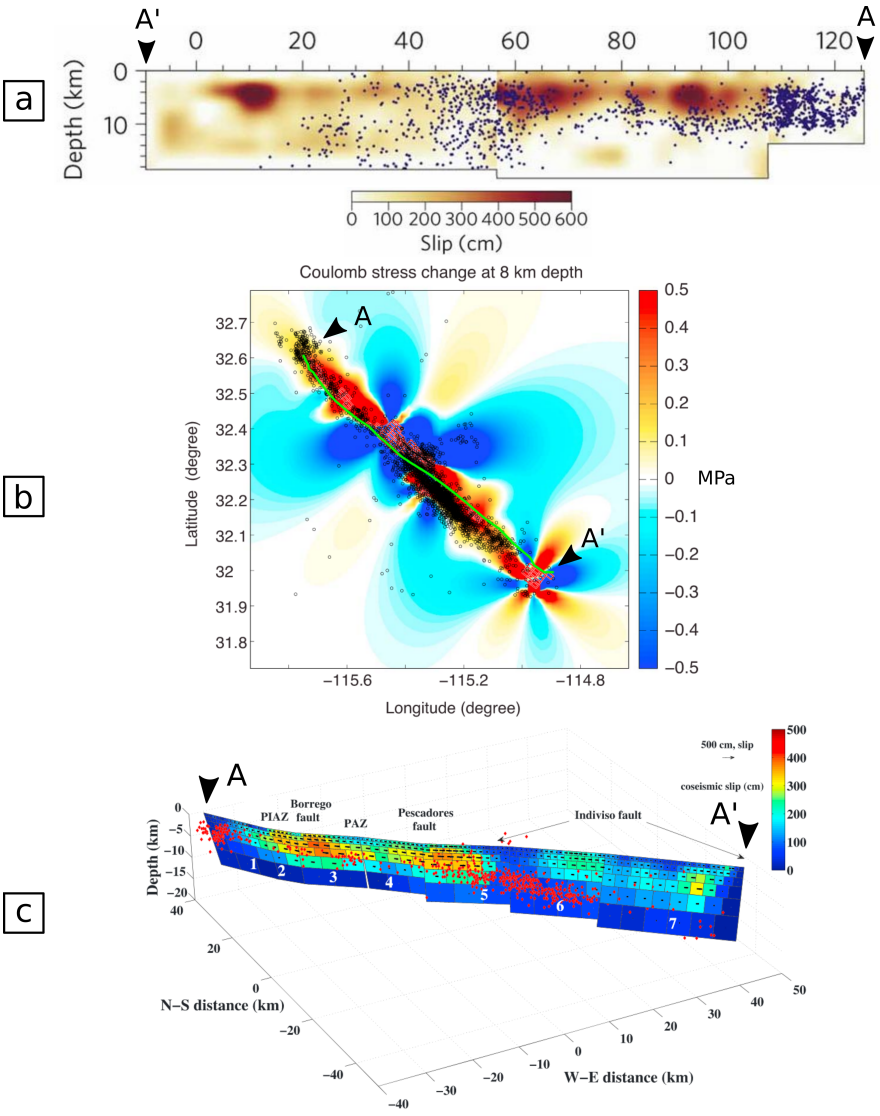

Figure 1.16: Aftershocks plotted against slip models of the 2010 El Mayor-Cucapah earthquake. Aftershocks are plotted as (a): blue, (b): black, and (c): red dots. (a): Slip model of *Wei et al.* (2011) plotted with aftershocks. (b): Coulomb stress change for a set depth of 8 km using the slip model of *Huang et al.* (2017b). Aftershocks mostly occur in areas with a positive Coulomb stress change. (c): Aftershocks against an unpublished slip model as modified after *Gonzalez-Ortega et al.* (2014). Faults and regions such as the Puerta Accommodation Zone (PAZ) and Paso Inferior Accommodation Zone (PIAZ) are marked. Triangles marked A and A′ indicate the rough location of the southeast and northwest ends of the slip models located on Figure 1.14. Figures have been modified from their originals.

low as the asperity will not have had time to heal since the main shock? Or should the aftershocks in high slip regions have high stress drops as the aftershocks are occurring on asperities which did not rupture in the main shock and therefore must be very strong? I add to this debate by examining the stress drops of aftershocks in the 2010 El Mayor-Cucapah earthquake sequence (Chapter 3) and how the slip of the main shock and the aseismic creep of afterslip affect the properties of aftershocks. Understanding the properties of these aftershocks is important for seismic hazard analysis, especially if high stress drop earthquakes which have been linked to higher ground motions (e.g., *Bindi et al.*, 2018) should be expected near the areas which are most affected by the larger earthquake.

1.4 Repeating earthquakes

Repeating earthquakes are earthquakes that repeatedly rupture the same patch of a fault. In a sequence of repeating earthquakes, the individual earthquakes are within a few tenths of a magnitude unit, have similar source time functions and therefore recorded waveforms, and are co-located - on the same rupture patch with similar rupture extents. Repeating earthquake sequences have a wide range of magnitudes of M 0 - 4 and recurrence intervals of months to years (e.g., *Nadeau and Johnson*, 1998, *Lengliné and Marsan*, 2009). These sequences have been identified in many different tectonic environments (e.g., *Schaff and Richards*, 2004) including strike-slip faults (e.g., *Nadeau and Johnson*, 1998, *Schaff et al.*, 1998, *Peng and Ben-Zion*, 2005, *Templeton et al.*, 2008, *Lengliné and Marsan*, 2009, *Schmittbuhl et al.*, 2016), subduction zones (e.g., *Igarashi et al.*, 2003, *Zhang et al.*, 2008, *Uchida and Matsuzawa*, 2011, *Kato et al.*, 2012, *Yamashita et al.*, 2012, *Yu*, 2013, *Kato and Nakagawa*, 2014, *Ye et al.*, 2014, *Dominguez et al.*, 2016, *Hatakeyama et al.*, 2017, *Gardonio et al.*, 2018, *Okuda and Ide*, 2018), triple junctions (e.g., *Chen and McGuire*, 2016, *Materna et al.*, 2018), arc continent collision boundaries (e.g., *Chen et al.*, 2008) and low angle normal faults (e.g., *Valoroso et al.*, 2017). An example of a repeating earthquake sequence is shown in Figure 1.17. In Chapter 4, I apply a new method to identify repeating earthquakes and to study their interaction with fault properties. In the following section, I discuss the properties of repeating earthquakes.

In older literature, repeating earthquakes are often referred to as doublets or multiplets (e.g., *Poupinet et al.*, 1984, 1996, *Baisch and Bokelmann*, 2001). Some of the older doublets identified in the literature may be part of longer earthquake sequences which were not identified because the sensitivity and quality of detection instruments was too low at the time.

Repeating earthquakes are a useful instrument to analyse the properties of the

subsurface. For example, *Poupinet et al.* (1984) used a pair of repeating earthquakes to look at the temporal variation in seismic velocity structure at depth by looking at the change in travel time, and *Zhang et al.* (2008) adopted a similar approach to measure the rotation of the inner core. Alternatively, one can look at changes in repeating earthquake rates due to events such as landslides (*Bell*, 2018).

Repeating earthquake rates also respond to large earthquakes. *Lengliné and Marsan* (2009) observed variation in recurrence intervals of earthquakes sequences after the 2004 M_W 6.0 Parkfield earthquake. They observed sequences that stopped completely after the Parkfield earthquake without recurring in the three years they examined after the earthquake. They also observed sequences that sped up after the Parkfield earthquake and then slowed down with time, similar to the Omori decay of aftershocks (*Omori*, 1894, *Utsu*, 1961). These Omori-like repeating sequences appear to be relatively common (e.g., *Schaff et al.*, 1998, *Wu et al.*, 2014, *Kim et al.*, 2016, *Schmittbuhl et al.*, 2016, *Hatakeyama et al.*, 2017). Some sequences followed a similar pattern but initiated only after the main shock, similar to "burst-type" repeaters observed elsewhere (e.g., *Igarashi et al.*, 2003, *Templeton et al.*, 2008, *Turner et al.*, 2013, *Yu*, 2013, *Schmittbuhl et al.*, 2016). Finally, *Lengliné and Marsan* (2009) observed that some sequences were completely unaffected by the Parkfield earthquake. These behaviours may be correlated with loading and unloading of different repeating asperities by the Parkfield earthquake, although *Lengliné and Marsan* (2009) found that the stress changes induced by the large earthquake must be very heterogeneous to explain the dense patterns of the four behaviours. Other studies have also observed that large events trigger repeating earthquake sequences through dynamic or static stresses (e.g., *Chen et al.*, 2010, *Chen and Shearer*, 2013, *Wu et al.*, 2014, *Dominguez et al.*, 2016).

But if the recurrence intervals of earthquakes within a repeating sequence change in response to the stress changes of a large earthquake, how do repeating earthquake sequences continually occur without nearby large magnitude earthquakes? One possible mechanism is aseismic slip, which could induce the stress changes needed to trigger repeating earthquakes. Aseismic slip can occur at a constant rate for decades (e.g., *Hussain et al.*, 2016, *Loveless and Meade*, 2016, *Xu et al.*, 2018), which would explain the consistency of recurrence intervals of sequences over equally long time frames (e.g., *Lengliné and Marsan*, 2009). *Nadeau and Johnson* (1998) were one of the first studies to suggest a link between repeating earthquakes and aseismic slip and inferred that repeating sequences could be used to measure how much aseismic slip was occurring in a region. I discuss the derivation of this link in the following section.

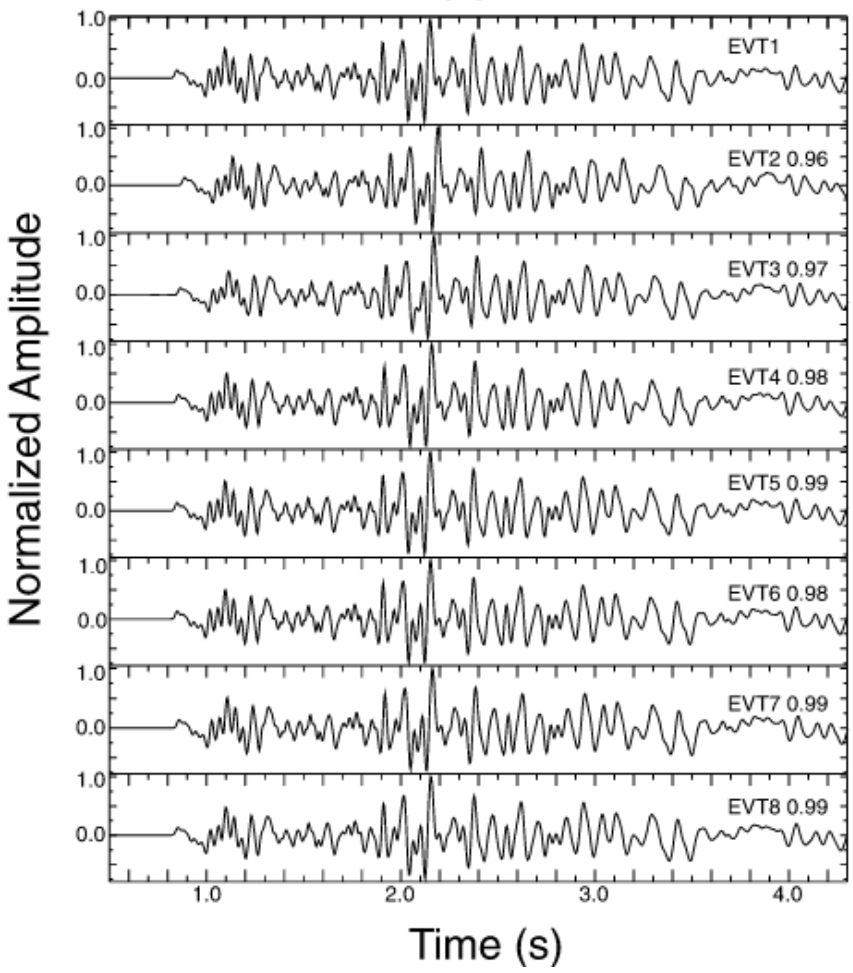

Figure 1.17: An example of co-located repeating earthquakes within a sequence recorded at the same station in Parkfield, California. Cross correlation coefficients with the first event (EVT1) are given in the top right of each subplot. Recurrence intervals between events vary from 2 months to 3 years. Figure modified after *Kim et al.* (2016).

1.4.1 The moment scaling problem

Nadeau and Johnson (1998) observed that repeating earthquakes in Parkfield, California had longer recurrence intervals than expected and therefore lower slip rates than the tectonic slip rate. To understand their approach, one must consider how repeating earthquakes should behave in terms of their moment M_0 and recurrence interval t_r.

The equation for moment and stress drop $\Delta\sigma$ (Equation (1.2)) can be expanded by assuming a circular rupture (*Brune*, 1970) where r is the radius:

$$M_0 = \pi r^2 \mu \tilde{\delta}, \tag{1.7}$$

$$\Delta\sigma = \frac{7\pi\mu\tilde{\delta}}{16r}. \tag{1.8}$$

Then, assuming that the seismic slip rate of repeating earthquakes must be equal to the long term tectonic slip rate, the average slip $\tilde{\delta}$ is $\tilde{\delta} = t_r V_L$ where t_r is the recurrence interval and V_L is the loading velocity. Substituting $t_r V_L$ for the slip, and solving Equations (1.7) and (1.8) for r yields:

$$\sqrt{\frac{M_0}{\pi\mu t_r V_L}} = \frac{7\pi\mu t_r V_L}{16\Delta\sigma}. \tag{1.9}$$

Which leads to:

$$t_r = \frac{M_0^{\frac{1}{3}} \Delta\sigma^{\frac{2}{3}}}{1.81\mu V_L}. \tag{1.10}$$

Therefore, the recurrence intervals of repeating earthquakes should scale as $t_r \propto M_0^{\frac{1}{3}}$ if the seismic slip of repeating earthquakes is equal to the tectonic slip rate. Note that this assumes that stress drop is independent of magnitude which seems to be valid (Sec. 1.1.2).

In contrast to this theoretical scaling, *Nadeau and Johnson* (1998) found that recurrence intervals of repeating earthquakes in Parkfield, California, scaled as $t_r \propto M_0^{0.17}$ (roughly $M_0^{\frac{1}{6}}$) (Figure 1.18), which suggests there is a problem with the assumptions used to obtain the $M_0^{\frac{1}{3}}$ scaling in Equation (1.10). The most obvious assumption to question is that the seismic slip rate of repeating earthquakes is comparable to the tectonic slip rate of the region, and a possible slip deficit is indeed the focus of the majority of the explanations for the difference in recurrence interval-moment scaling. *Nadeau and Johnson* (1998), however, used a different approach.

Nadeau and Johnson (1998) suggested that the stress drop of repeating earthquakes decreases with increasing moment, and that the smallest repeating earthquakes they

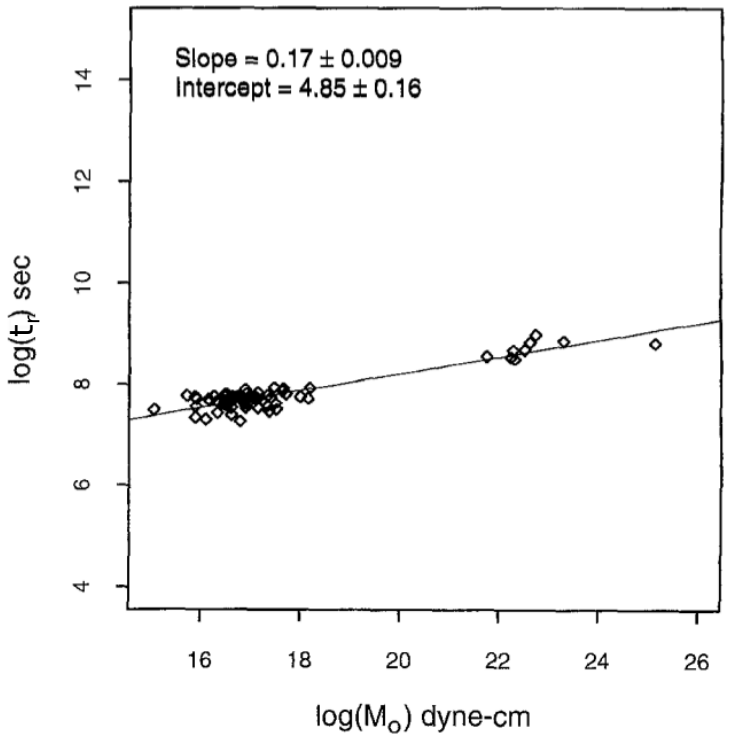

Figure 1.18: Average recurrence intervals versus moments for repeating earthquake sequences on a log-log scale as identified by *Nadeau and Johnson* (1998). The slope of 0.17 annotated in the upper left indicates that recurrence intervals scale as $M_0^{0.17}$. Figure from *Nadeau and Johnson* (1998).

identified had stress drops of hundreds to thousands of megapascals. These extremely high stress drops required a fault that was stronger than typical laboratory rock estimates (*Beeler et al.*, 2001) and had a highly heterogeneous variation in strength. One can infer from this that repeating earthquakes occur on small and strong asperities on the fault, leading to very high stress drops (Figure 1.19a). The main problem with this explanation is that stress drops of earthquakes with similar magnitudes to those studied by *Nadeau and Johnson* (1998) do not approach the high stress drops (roughly 1000 MPa) required to explain the slip deficit of repeating earthquakes, instead averaging around 0.1 – 100 MPa (e.g., *Imanishi et al.*, 2004, *Allmann and Shearer*, 2007, *Abercrombie*, 2014). Further work has suggested that varying the rigidity of the rock to create high strength asperities and looking at non-spatially averaged stress drops may achieve the high stress drops required, but the viability of this approach is still unclear (e.g., *Nadeau et al.*, 2004, *Dreger et al.*, 2007, *Kim et al.*, 2016).

Beeler et al. (2001) tested the hypothesis of *Nadeau and Johnson* (1998) by examining stress drops of repeating earthquakes. They found the stress drops of repeating earthquakes were 2 - 3 orders of magnitude lower than required to explain the slip deficit. Instead, *Beeler et al.* (2001) described an alternative explanation for the slip deficit (Figure 1.19b). They allowed repeating asperities to continuously creep and harden with slip until a threshold stress where rupture occurs. If the coefficient of this slip hardening is higher than the elastic loading stiffness, then very little interseismic aseismic slip occurs on the asperity. If the slip hardening coefficient is similar to the stiffness, then there is significant aseismic slip on the asperity. If the slip hardening coefficient is smaller than the stiffness, then the asperity will slip completely aseismically with no earthquakes. Assuming the slip hardening coefficient is independent of the radius of the asperity and the elastic loading stiffness is proportional to one over the radius, the ratio of seismic slip compared to the total slip on the asperity should increase with the earthquake moment as $M_0^{\frac{1}{3}}$. Thus the interseismic aseismic slip is high for small repeating earthquakes and accounts for the slip deficit on repeating asperities. The model of *Beeler et al.* (2001) challenges the assumption that the slip of these patches is completely seismic. Note however, that *Beeler et al.* (2001) acknowledge that there is no experimental evidence to support slip hardening, and they assume that the strength of the earthquake rupture patch is reset to a consistent strength over multiple loading cycles.

Aseismic slip is an important component of many of the explanations of the slip deficit of repeating earthquakes. Similar to the work of *Beeler et al.* (2001), *Chen and Lapusta* (2009) and *Cattania and Segall* (2019) suggest that the slip deficit of repeating earthquakes is accounted for by aseismic slip in the interseismic and preseismic periods. These two studies use rate and state friction (e.g., *Dieterich*, 1978, *Dieterich*

and Kilgore, 1994, *Marone*, 1998, *Scholz*, 2002) to model velocity-weakening asperities surrounded by a larger velocity-strengthening region. *Chen and Lapusta* (2009) demonstrated that a model with a small velocity-weakening, potentially seismogenic, patch within a larger, velocity strengthening creeping region can make up for this slip deficit (Figure 1.19c). In their model, the velocity-weakening patches of repeating earthquakes experience interseismic aseismic creep due to penetration of aseismic slip from the surrounding velocity strengthening region, which explains the slip deficit in the recurrence interval-moment scaling relation. Note that *Chen and Lapusta* (2009) also attributed some of the aseismic slip to the post-seismic period of repeating earthquakes. The post-seismic period cannot contain much of the aseismic slip to explain the slip deficit, as observed by the study of *Hawthorne et al.* (2016) of repeating earthquakes in Parkfield using strainmeter data.

Cattania and Segall (2019) used a similar model of a velocity-weakening asperity within a large creeping region, but they found that the recurrence interval-moment scaling was explained by different behaviours depending on the size of the asperity relative to the characteristic nucleation dimension r_∞ (Figure 1.19d). The $M_0^{\frac{1}{6}}$ scaling for small asperities with radii $< 4.3r_\infty$ is caused by a breakdown of self-similarity (therefore decreasing stress drop with decreasing moment) due to the finite nucleation size. The scaling for asperities with radii $> 4.3r_\infty$ is due to the large size of the patches, which allow partial ruptures and aseismic slip within the asperity, the opposite of the larger seismic slip for large asperities inferred by *Beeler et al.* (2001). *Okuda and Ide* (2018) may have observed partial rupturing within larger patches as they identified repeating earthquake sequences with $M \leq 4$ located within the rupture area of a larger M 4.8 sequence. Note that the approaches of *Chen and Lapusta* (2009) and *Cattania and Segall* (2019) rely on the larger velocity-strengthening region that surrounds the velocity-weakening asperity, as this causes creep to slowly propagate into the asperity before a major rupture.

Sammis and Rice (2001) and *Anooshehpoor and Brune* (2001) also used aseismic creep to explain the unexpected recurrence interval-moment scaling of repeating earthquakes, but in a different form to the previous examples. *Sammis and Rice* (2001) suggested that repeating earthquakes occur on small *weak* asperities that are located on the border between a locked patch and a creeping patch which are both much larger than the repeating asperity (Figure 1.19e). This model results in slip velocity shielding for the small repeating asperity where the high slip rate of the larger locked patch makes up most of the slip deficit and the small asperity has a much lower slip rate. In this model, the $M_0^{\frac{1}{6}}$ scaling is a result of the stress scaling with distance from the boundary of the larger asperity. Taking x as the distance from the boundary of the larger locked asperity and a as the radius of the repeating asperity, the stress concentration

scales as $x^{-\frac{1}{2}}$ which means that the average stress across the small repeating asperity scales as $a^{-\frac{1}{2}}$. Therefore the recurrence interval will be proportional to $a^{\frac{1}{2}}$, and thus $M_0^{\frac{1}{6}}$. One of the problems with this hypothesis is that it predicts large locked regions on creeping faults with streaks of small repeating earthquakes around their edges, and there is no evidence for this behaviour on creeping faults such as Parkfield (*Chen and Lapusta*, 2009). There is, however, possible evidence of this in Japan where repeating earthquakes concentrate around the asperities of larger earthquakes (e.g., *Igarashi et al.*, 2003, *Uchida et al.*, 2003, *Yamashita et al.*, 2012). It is not clear whether these locations in Japan are adjacent to large creeping areas though, or whether the larger earthquake merely affects the behaviour of repeating earthquakes that are within its high slip areas in a different way to those around the edges.

Anooshehpoor and Brune (2001) used a different shielding-based model to explain the recurrence interval-moment scaling (Figure 1.19f). They hypothesised that repeating earthquakes occur on small *strong* asperities that are located in a larger creeping region, which is in turn surrounded by an even larger locked region. This concentric structure of locked-creeping-locked asperities provides slip velocity shielding on the small repeating asperity, resulting in a lower slip rate than the tectonic slip rate and the $M_0^{\frac{1}{6}}$ scaling.

I test a different hypothesis to all of the above in Chapter 4, where I suggest that large faults are made of smaller sub-faults. As slip scales with fault length (e.g., *Watterson*, 1986, *Walsh and Watterson*, 1988, *Cowie and Scholz*, 1992, *Dawers et al.*, 1993, *Scholz et al.*, 1993, *Schultz et al.*, 2008, *Carvell et al.*, 2014, *Xu et al.*, 2016), I infer that the recurrence interval-moment scaling is explained by the lower slip rates on the smaller sub-faults which host the repeating earthquakes. I test this new hypothesis to see whether the recurrence interval-moment scaling of repeating earthquakes reflects the amount of aseismic slip or simply reflects the properties of the fault. Some studies have used repeating earthquakes to infer the amount of aseismic slip in a region (e.g., *Nadeau and Johnson*, 1998, *Nadeau and McEvilly*, 1999, *Igarashi et al.*, 2003, *Meng et al.*, 2015, *Schmittbuhl et al.*, 2016, *Uchida et al.*, 2016, *Materna et al.*, 2018), but if my hypothesis is correct then the amount of aseismic slip cannot be inferred from repeating earthquakes. Thus it could be dangerous to use estimates of aseismic slip from repeating earthquakes to estimate seismic hazard (e.g., *Bürgmann et al.*, 2000, *Schmidt et al.*, 2005), or to judge whether regions are locked or creeping from the presence of repeating earthquakes.

Note, however, that repeating earthquakes in general do seem well correlated with the location of aseismic slip. For example, *Valoroso et al.* (2017) observed repeating earthquakes in the Northern Appennines, Italy, and found they clustered well with the

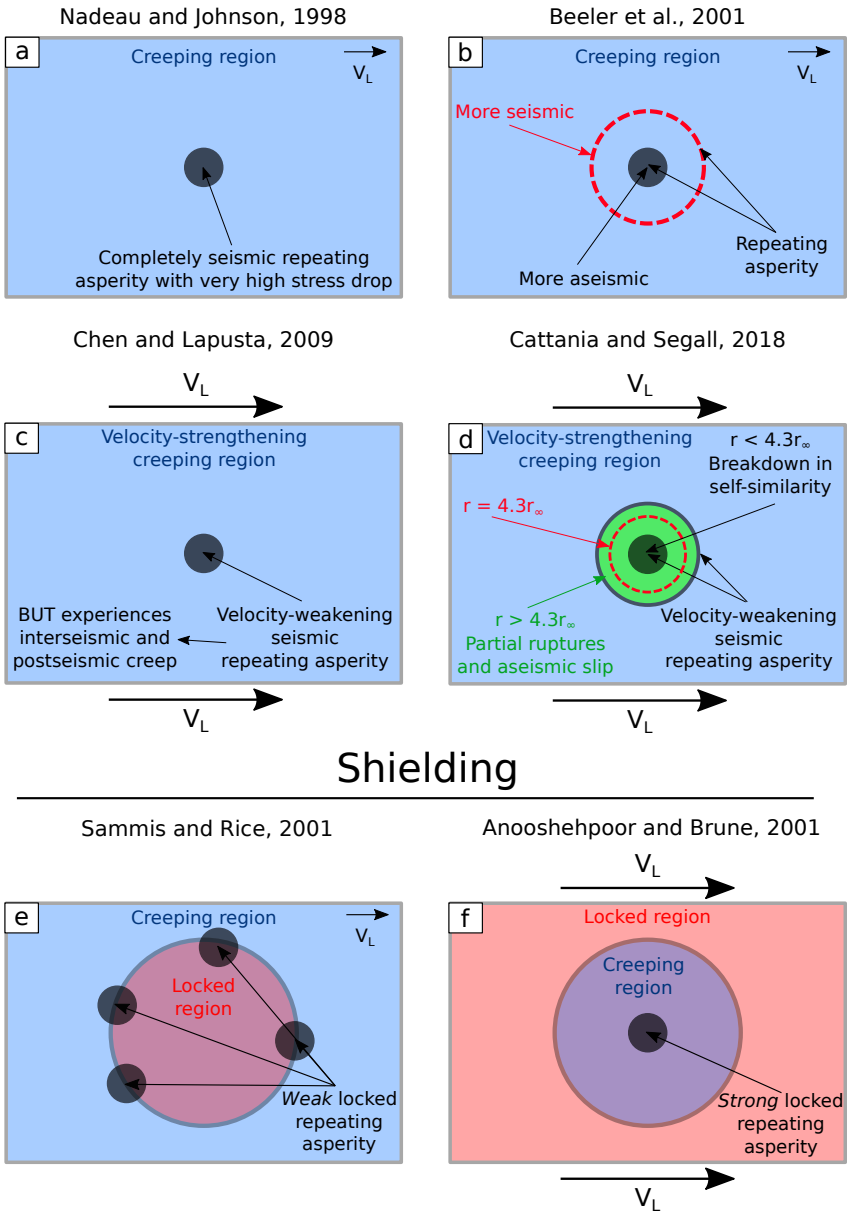

Figure 1.19: Diagrams of six of the different hypotheses to explain the unexpected recurrence interval-moment scaling of repeating earthquakes. These hypotheses include (a): *Nadeau and Johnson* (1998), (b): *Beeler et al.* (2001), (c): *Chen and Lapusta* (2009), (d): *Cattania and Segall* (2019), (e): *Sammis and Rice* (2001), and (f): *Anooshehpoor and Brune* (2001). Full details are given in the text.

aseismic creep identified from geodesy. Other studies find similar patterns of correlation between repeating earthquakes and geodetically inferred aseismic slip (e.g., *Nadeau et al.*, 1995, *Schaff et al.*, 1998, *Nadeau and McEvilly*, 1999, *Bürgmann et al.*, 2000, *Matsuzawa et al.*, 2002, *Igarashi et al.*, 2003, *Uchida et al.*, 2003, *Nadeau et al.*, 2004, *Peng and Ben-Zion*, 2005, *Chen et al.*, 2008, *Lengliné and Marsan*, 2009, *Uchida and Matsuzawa*, 2011, *Schmittbuhl et al.*, 2016, *Gardonio et al.*, 2018), but some do find an anti-correlation (e.g., *Dominguez et al.*, 2016). However, it is unclear whether repeating earthquakes occur only due to aseismic slip or whether aseismic slip increases the stress on the repeating earthquakes and speeds up the nucleation process, similar to the process observed for some earthquakes near large earthquakes (e.g., *Lengliné and Marsan*, 2009). This is difficult to test, but it is important to eliminate other possible explanations for the recurrence interval-moment scaling, to confirm the connection between repeating earthquakes and aseismic slip.

I test my hypothesis using a simple approach to identify repeating earthquakes from earthquake locations and rupture size, without cross correlation. This simple approach for repeating earthquakes can easily be applied to large catalogs of earthquakes, and is much faster than the conventional cross-correlation based approach (e.g., *Nadeau and Johnson*, 1998, *Lengliné and Marsan*, 2009).

1.5 Aims and objectives of my thesis

There are two main aims of my thesis. The first aim of my thesis is to examine how properties of the fault can affect properties of earthquakes. I add to our understanding of earthquake stress drops by studying the Blanco fault (Chapter 2) and the El Mayor-Cucapah earthquake sequence (Chapter 3), and suggest how repeating earthquakes may be diagnostic of fault properties (Chapter 4).

The second aim is to apply new methods to existing problems in the field of seismology. I test the phase coherence method (*Hawthorne and Ampuero*, 2017, *Hawthorne et al.*, 2018, *Williams et al.*, 2019) to obtain earthquake stress drops. I also identify repeating earthquakes using a simpler method than in previous work. These methods have different advantages and disadvantages to more established approaches and depend on different aspects of the analysis. I hope that by establishing these methods and proving their effectiveness, future studies can use them to analyse earthquake properties and fault properties from a new perspective.

To fulfill these aims, my specific objectives are to:

1. Test and develop the phase coherence method for estimating stress drops. Here, I

test the viability of the phase coherence method for different regions, and evaluate the factors that can affect it.

2. Obtain stress drops for the Blanco oceanic transform fault and compare them with seismic coupling along the fault. I add to the sparse number of studies of earthquake stress drops on oceanic transform faults by investigating how the properties of the Blanco fault, specifically the seismic coupling and aseismic slip along it, affect the values of stress drops along the fault.

3. Examine how stress drops of aftershocks of the 2010 M_W 7.2 El Mayor-Cucapah earthquake vary with the slip of the main shock and with time. I examine whether the stress drops of aftershocks vary with time to evaluate the influence of post-seismic slip on earthquake properties.

4. Use a simple approach to identify repeating earthquakes and check whether it correctly identifies repeating earthquakes. This approach would greatly speed up and simplify the analysis of repeating earthquakes.

5. Determine whether the recurrence intervals of repeating earthquakes scale with moment as $M_0^{\frac{1}{6}}$ due to varying slip rates on subfaults. I suggest an explanation for the recurrence interval-moment scaling problem of repeating earthquakes where repeating earthquakes occur on fault strands with slip rates that scale with the length of the fault strand. I test whether this hypothesis explains the unusual recurrence interval-moment scaling of repeating earthquakes in Parkfield, California.

1.6 Thesis roadmap

In Chapter 2, I investigate the stress drops of earthquakes on the Blanco fault, off the coast of Oregon, U.S., using the phase coherence method. This work has been published in *Williams et al.* (2019), but is modified for this thesis. This study is one of the first to use the phase coherence method to calculate stress drops and to calculate stress drops on the Blanco fault. It is also one of the few studies to compare earthquake stress drops with the seismic coupling along a fault. I find that the stress drops are high on areas that are highly coupled, as in areas that release most of their moment through earthquakes. This link between coupling and stress drop could be linked to the temperature structure below the Blanco fault, where higher temperatures reduce the depth of the seismogenic zone and allow less time for healing resulting in lower stress drops in less coupled segments of the fault.

In Chapter 3, I use the phase coherence method to find stress drops of aftershocks in the El Mayor-Cucapah earthquake sequence in Baja California, Mexico. In this study,

I develop the phase coherence method further by applying it to both the P wave and the S wave of earthquakes. I obtain stress drops from this analysis and compare them with the slip of the main shock, as well as looking for a temporal trend to compare with post-seismic afterslip. I also compare the P wave and S wave results to look for any systematic differences. I find that the stress drops of aftershocks of the El Mayor-Cucapah earthquake do not appear to vary with post-seismic aseismic slip. I also observe that the S wave has similar results to the P wave so the S wave is a viable alternative to the P wave for earthquakes with noisy high frequencies.

In Chapter 4, I use a simple approach to identify and investigate repeating earthquakes in Parkfield, California. I identify repeating earthquakes using only their locations and magnitudes, and observe that they follow the same recurrence interval-moment scaling relation of $M_0^{\frac{1}{6}}$ as observed in other studies of repeating earthquakes. I then test whether this unexpected recurrence interval-moment scaling can be explained by repeating earthquakes occurring on small sub-faults with low slip rates. If this is true, the scaling exponent of repeating earthquake ratios should be $\frac{1}{3}$ for sequences on the same fault and $\frac{1}{6}$ for sequences on different faults. I find that this hypothesis may be correct because the scaling exponent of recurrence interval ratios with moment ratios is $\frac{1}{3}$ for closely-spaced sequences on the same fault, and $\frac{1}{6}$ for widely-spaced sequences on different faults. If this hypothesis is true, then it may be inappropriate to infer aseismic slip from repeating earthquakes.

In Chapter 5, I discuss what the results of my thesis imply for the relationship between earthquake properties and fault properties or aseismic slip, as well as what the new methods I have established can help achieve in the field of seismology. I use the stress drops I calculate for the Blanco fault and the 2010 El Mayor-Cucapah earthquake, and the results of the repeating earthquake analysis, to examine the influence of aseismic slip or fault properties on earthquake properties. I discuss the virtues and problems of the phase coherence method. I examine the simple method for identifying repeating earthquakes and discuss its limitations. Finally, I outline the key findings of my thesis.

Chapter 2

Stress drops of earthquakes on the Blanco oceanic transform fault from inter-station phase coherence

"Creation is an act of sheer will."

John Hammond, Jurassic Park

2.1 Background and Motivation

Oceanic transform faults exhibit a range of slip behaviors that are still poorly understood (Sec. 1.2). They often host large amounts of aseismic slip (e.g., *Bird et al.*, 2002, *Boettcher and Jordan*, 2004, *Materna et al.*, 2018) and highly repetitive similar ruptures (e.g., *Wolfson-Schwehr et al.*, 2014, *Ye et al.*, 2014). Earthquakes on oceanic transform faults also display a wide variation in stress drops, with both unusually high stress drops (e.g., *Allmann and Shearer*, 2009, *Chen and McGuire*, 2016) and some of the lowest recorded stress drops (e.g., *Pérez-Campos et al.*, 2003) (Sec. 1.1.2). Stress drops may also vary between areas with more or less aseismic slip (*Moyer et al.*, 2018). But these behaviors remain poorly understood, as only a modest number of studies have examined earthquake properties on these faults because they are often far from observing stations.

In this chapter, I add to our understanding of earthquakes on oceanic transform

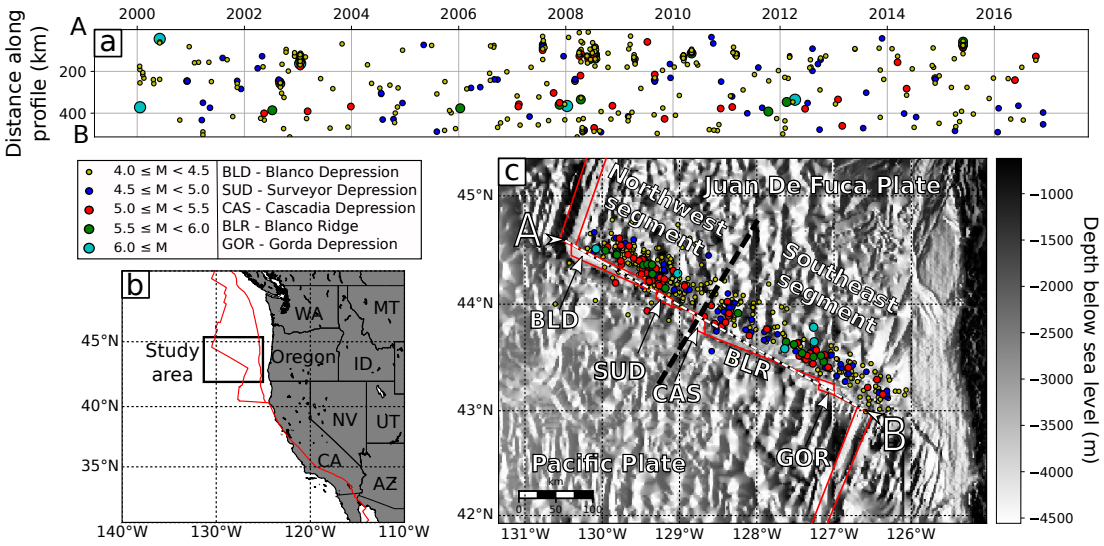

Figure 2.1: (a): Locations and times of $M \geq 4.0$ earthquakes on the Blanco fault along profile marker in (c). (b): Position of study area relative to North America. (c): Earthquakes and tectonic structure of the Blanco fault. The fault trace is marked in red with four bathymetric depressions (BLD, SUD, CAS, GOR) and the Blanco Ridge section of the transform fault (BLR) labeled. The white and black dashed line indicates the profile used for (a) from A to B. The fault structure was taken from *Braunmiller and Nábělek* (2008). Bathymetry was obtained from ETOPO1 (*Amante and Eakins*, 2009), and earthquake locations are reported in the National Earthquake Information Center (NEIC) catalog.

faults by examining stress drops of offshore earthquakes on the Blanco fault, an oceanic transform fault off the coast of Oregon, U.S. (Figure 2.1). I develop and use a method introduced by *Hawthorne et al.* (2018), which is a modified form of rupture directivity analysis (e.g., *Velasco et al.*, 1994, *Mori*, 1996, *Somerville et al.*, 1997, *Tan and Helmberger*, 2010, *Kane et al.*, 2013). This phase coherence-based method provides an alternative and complementary approach to the commonly used spectral amplitude-based method, as the methods take different approaches to derive rupture extent. With the phase coherence approach, I note that because earthquakes have finite areas, seismic waves are generated at various locations in the rupture and therefore have different travel times to different recording stations. This travel time variation creates differences in the apparent source time functions among the recording stations. I measure differences in apparent source time functions at a range of frequencies, or seismic wavelengths. These measurements can be used to infer the rupture extent and stress drop of an earthquake. In this chapter, I determine and take the steps necessary to use this method at long distances.

I use the phase coherence technique to calculate stress drops for $M \geq 5.0$ earthquakes on the Blanco fault, offshore of Oregon, U.S.. I begin by describing the fault, the earthquakes to be considered, and the stations to be used. I then describe the phase coherence method and use it to calculate stress drops. I identify factors that

may reduce the coherence, such as inaccurate trace alignment and different earthquake path effects, and accept only results that will not be significantly affected by these factors. Finally, I analyse the acceptable results and discuss their implications for the properties of the Blanco fault.

2.2 Blanco fault

The Blanco fault is a right-lateral oceanic transform fault between the Pacific and Juan de Fuca plates. The fault slips at 3 - 8 mm/yr (*Willoughby and Hyndman*, 2005) and is split into four transform segments and four topographic depressions (Figure 2.1; Sec. 1.2.1) (*Dziak et al.*, 1991, *Braunmiller and Nábělek*, 2008). The transform segments host mostly strike-slip earthquakes, and the depressions feature normal faulting events (*Braunmiller and Nábělek*, 2008).

Dziak et al. (1991) noted that the southeastern half of the Blanco fault, east of the Cascadia Depression (CAS on Figure 2.1), hosts the largest-magnitude earthquakes and has a higher seismic moment release rate than the northwestern half. They inferred that the southeastern half has less aseismic slip and releases a higher fraction of its moment in earthquakes. *Braunmiller and Nábělek* (2008) identified a similar large-scale variation in their more detailed investigation. In this chapter, I will investigate how stress drops vary between the more and less seismic halves of the Blanco fault.

Note, however, that both estimates of seismic coupling have implicit uncertainties. *Dziak et al.* (1991) estimate the seismic coupling by comparing the cumulative moment rate of earthquakes with magnitudes greater than 4 since 1966, with the expected tectonic release rate derived from the apparent plate motion rate of 6 cm/yr. *Braunmiller and Nábělek* (2008) estimate the seismic coupling by computing the cumulative seismic slip rates from the moments of $M \geq 4.4$ - 4.5 earthquakes between 1964 and 2005, and comparing the summed seismic slip rate with the tectonic slip rate. These approaches both assume that the recent earthquake catalog represents the rate of earthquakes on the Blanco fault accurately, but it is possible that particularly large earthquakes could occur on the Blanco fault which have not been recorded historically. Given the Blanco fault's offshore location and the 150-km long Blanco Ridge segment, it is plausible that a M 7 - 7.5 or larger earthquake with a rupture length of over 100 km (*Wells and Coppersmith*, 1994) could have occurred within the last few centuries without being recorded. This hypothetical large earthquake would increase the apparent seismic coupling of the Blanco fault, and could mean that the seismic coupling estimates made by *Dziak et al.* (1991) and *Braunmiller and Nábělek* (2008) underestimate the true coupling of the Blanco fault.

Dziak et al. (1991) also assume a seismogenic width of 10 km, which could be an overestimate. *Braunmiller and Nábělek* (2008) considered the effect of an additional spreading centre on the temperature isotherms below the Blanco fault and found that the 600°C isotherm, which is often associated with the brittle-ductile transition (*Abercrombie and Ekström*, 2001, *Boettcher et al.*, 2007, *He et al.*, 2007), may occur at a shallow depth of 7 km on the Blanco fault. If *Dziak et al.* (1991) used this smaller width then their estimates of seismic coupling may increase, and could explain some of the difference between the estimates of coupling from *Braunmiller and Nábělek* (2008) (e.g. fully coupled on the southeast segment) and the much lower estimates of *Dziak et al.* (1991) (e.g. 14.1% coupled on the southeast segment).

2.3 Earthquake catalog and initial data processing

I initially consider 398 $M \geq 4.0$ earthquakes that occurred on the Blanco fault between 2000 and 2016, as identified in the National Earthquake Information Center (NEIC) earthquake catalog. The 398 earthquakes in the catalog are scattered in a 20 - 30 km wide band that follows the fault trace, but shifted northeast of where the fault appears in the bathymetry (Figure 2.1). This scatter and northeast shift in earthquake locations may be related to uncertainty in arrival time picks and problems with the velocity model, respectively (*Dziak et al.*, 1991, *Braunmiller and Nábělek*, 2008). Indeed, *Kuna et al.* (2019) used high quality ocean bottom seismometer (OBS) data to relocate events on the Blanco Ridge (BLR on Figure 2.1), and found that the events in 2012 and 2013 relocated onto the bathymetric expression of the fault with very little scatter. I perform my own event relocation later to reduce the effects of the initial location uncertainty on the results.

Earthquakes on the Blanco fault are recorded by seismic networks along the west coast of North America. I use data from a number of networks, whose data are available via the IRIS (Incorporated Research Institutions for Seismology) and the NCEDC (Northern California Earthquake Data Center). A detailed table of networks used is available in Table A.1.

I initially consider data from stations within 780 km (7 degrees) of the earthquake locations (Figure 2.2). I use the obspy mass downloader to obtain seismic waveforms for events in the Blanco event catalog (*Beyreuther et al.*, 2010). I analyse vertical component seismograms from these stations, as I use the first-arriving P wave. I pick the P arrival using a recursive short-term-average/long-term-average algorithm (*Withers et al.*, 1998, *Trnkoczy*, 1999) in the 1 - 10 Hz frequency band. The window for the P arrival was selected based on a simulated P arrival from the TauP program (*Crotwell et al.*, 1999) with the iasp91 Earth model (*Kennett and Engdahl*, 1991).

With the P wave pick obtained, I detrend each original trace and apply a Hanning taper to both ends of the trace. I remove the instrument response with a bandpass filter of 0.05 - 20 Hz applied. Then I detrend the traces again and resample to 100 Hz. I discard traces with signal to noise amplitude ratios less than 3 in the 0.5 - 5 Hz frequency band. All initial processing was performed using ObsPy (*Beyreuther et al.*, 2010).

2.4 Theoretical basis of the phase coherence method

I use the processed data to compute earthquake rupture extents and stress drops. I use a recently developed method (*Hawthorne et al.*, 2018), in which I analyse the similarities and differences of seismograms recorded at various stations. To understand this approach, consider two stations to the south and west (S and W) of an earthquake as shown in Figure 2.3. The illustrated earthquake ruptures outward from the hypocentre (black dot) so that its two asperities A (blue) and B (red) rupture simultaneously, but at locations separated by half the rupture diameter D. Asperities A and B are equidistant from the southern station S, so their signals arrive at S at the same time, creating a single peak in the apparent source time function (ASTF). Asperity B is closer to the western station W, so the signal from B arrives at W earlier than the signal from A. This time shift results in two peaks in the ASTF that are separated by time $\frac{1}{2}D/V_P$: by the separation distance divided by the P wave velocity in the rupture area. In my analysis, I will examine differences in the ASTFs observed at a range of stations to determine how much ASTF peaks could be shifted by intra-source travel time differences. I will use the inferred shifts to estimate the earthquake rupture extents.

However, to analyse ASTFs of real earthquakes, I must first remove the path effects. I use an empirical Green's function approach (similar to, e.g., *Dreger et al.* 2007, *Harrington and Brodsky* 2009, *Wei et al.* 2013, *Taira et al.* 2014). I note that the seismogram $d_{ij}(t)$ recorded at station j due to earthquake i can be approximated as a convolution of an apparent source time function $s_{ij}(t)$ and a Green's function $g_j(t)$:

$$d_{ij}(t) = s_{ij}(t) * g_j(t). \tag{2.1}$$

Note that I assume that the Green's function retains the same shape across the earthquake rupture area.

If I have two earthquakes ($i = 1$ and $i = 2$) with the same Green's function g_j, then I can eliminate the *phases* of the Green's functions Fourier coefficients by calculating

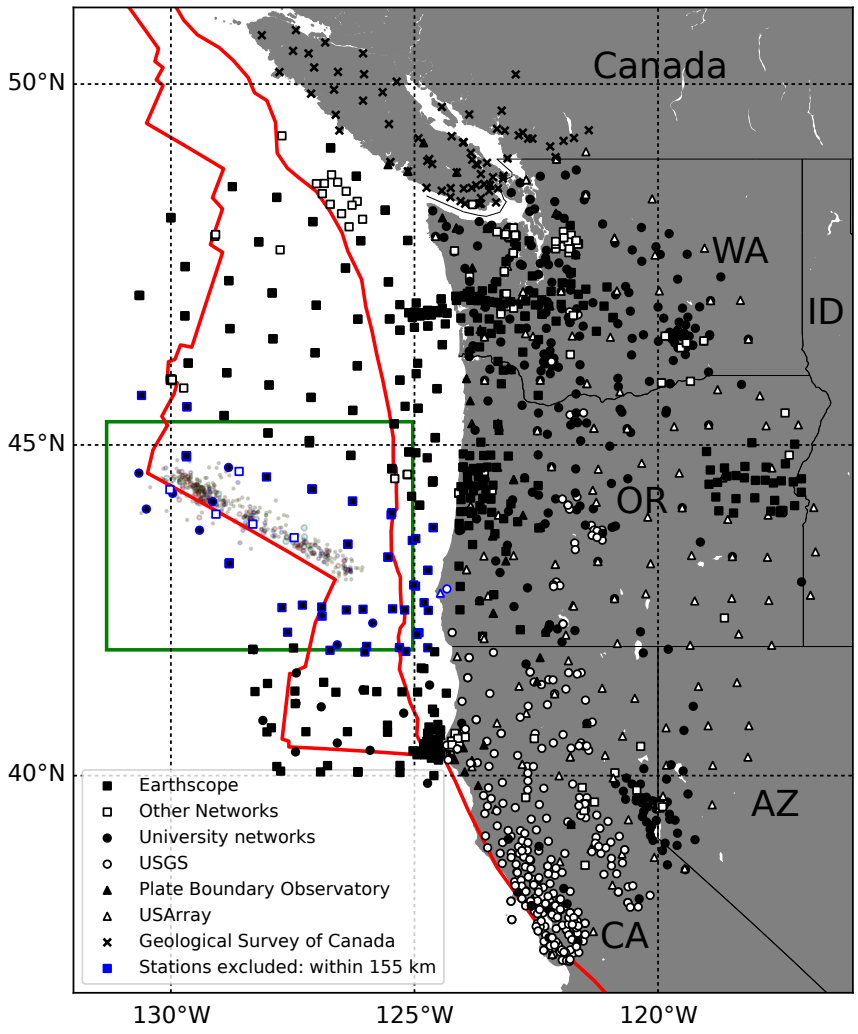

Figure 2.2: Stations used in my analysis. Blue symbols indicate stations that were sometimes excluded to avoid the S wave arrival in my 5-s analysis window. Networks run by the United States Geological Survey (USGS) are grouped. "Other networks" are networks from which I used fewer than 16 stations. Some networks have been grouped for plotting purposes. U.S. states are indicated by the two letter codes. The earthquake catalog from Figure 2.1 is plotted as translucent circles.

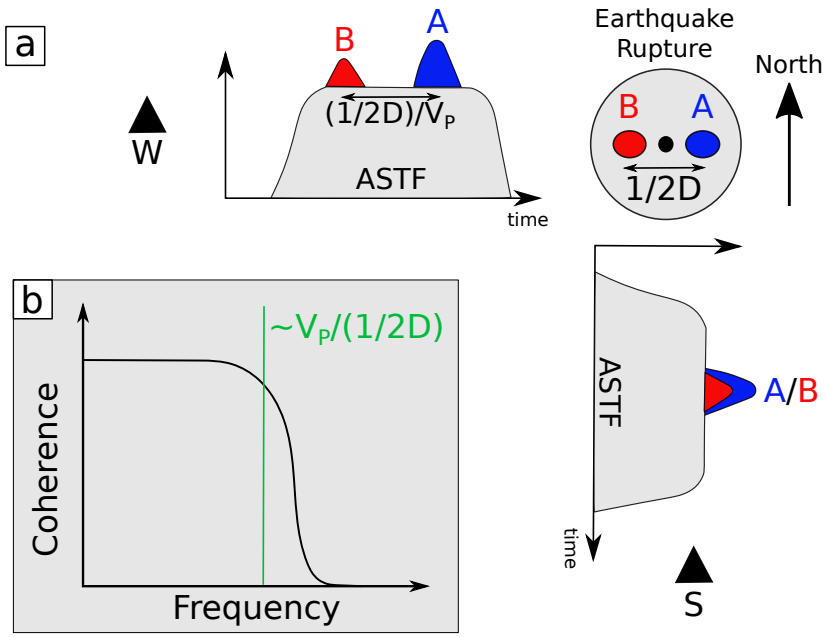

Figure 2.3: (a): Conceptual diagram of apparent source time function variation by station. The grey circle in the top right is the rupture area of a hypothetical earthquake, with the hypocentre marked by the black circle. The earthquake ruptures outwards from the centre, and A and B are asperities within the rupture area which rupture simultaneously but at locations separated by half the rupture diameter D. The apparent source time functions (ASTFs) illustrate the differences in arrival times between signals from A and B. At the western station (W), the signals from A and B are separated in time by $\frac{1}{2}D/V_P$ where V_P is the P wave velocity. (b): A hypothetical phase coherence spectrum for this conceptual case. The phase coherence is between the ASTFs at the western and southern stations and decreases at a frequency roughly equivalent to $V_P/\frac{1}{2}D$.

the cross-spectra $\hat{x}_j$ at station j (*Hawthorne and Ampuero*, 2017):

$$\hat{x}_j = \hat{s}_{1j}\hat{g}_j * \hat{s}_{2j}\hat{g}_j = \hat{s}_{1j}^*\hat{s}_{2j}|\hat{g}_j|^2. \tag{2.2}$$

Here $\hat{s}_{ij}(f)$ is the Fourier transform of $s_{ij}(t)$ and $\hat{g}_j(f)$ is the Fourier transform of $g_j(t)$, and I have dropped the frequency indexing for readability. Since $\hat{g}_j$ appears in Equation (2.2) only via its absolute value, the phases of the cross-spectra $\hat{x}_j$ depend only on the relative phases of the ASTFs of the earthquake.

As noted above, I seek to quantify how much the ASTFs of the earthquake vary across stations due to the finite rupture areas. I focus on differences in phase and use a robust estimate of the inter-station similarity: the inter-station phase coherence

$$C_p = \frac{2}{N(N-1)} \sum_{j=1}^{N} \sum_{l=j+1}^{N} \mathrm{Re}\, \frac{\hat{x}_j^* \hat{x}_l}{|\hat{x}_j^* \hat{x}_l|} \tag{2.3}$$

$$= \frac{2}{N(N-1)} \sum_{j=1}^{N} \sum_{l=j+1}^{N} \mathrm{Re}\, \frac{\hat{s}_{1j}\hat{s}_{1l}^*\hat{s}_{2l}\hat{s}_{2j}^*}{|\hat{s}_{1j}\hat{s}_{1l}^*\hat{s}_{2l}\hat{s}_{2j}^*|}, \tag{2.4}$$

where there are N stations, and I average coherence over $(N-1)*N/2$ station pairs. Equation (2.4) assumes that the two earthquakes have identical Green's functions. With that assumption, C_p provides a measure of the similarity of their ASTFs.

I can compute C_p and thus the ASTF similarity for a range of frequencies, or seismic wavelengths. The ASTFs should appear different when the arrival time variation due to the finite rupture extent causes a significant shift in phase. If I consider very long periods, the arrival time variations are a small fraction of the period and thus should not cause a significant shift in phase, so the phases of the ASTFs are similar and C_p is high. At short periods, on the other hand, the travel time variations can be a significant fraction of the period, and thus cause significant shifts in phase and low C_p. The largest travel time variation is proportional to the finite rupture extent of the larger earthquake of the pair, the largest possible distance between generated seismic waves. Therefore, I can calculate the finite rupture extent of the earthquake by identifying the period at which C_p decreases, which should be $F_{scal}D/V_P$: the travel time across the rupture multiplied by a scaling factor F_{scal}.

In order to systematically analyse a range of earthquakes, I define the frequency at which C_p decreases below 0.5 as the falloff frequency f_f. *Hawthorne et al.* (2018) used synthetics to verify that f_f is inversely proportional to the rupture extent of an earthquake, though they always analysed groups of earthquakes. In a later section, I analyse a suite of individual earthquake ruptures. I find that given the earthquakes'

locations, the iasp91 velocity model (*Kennett and Engdahl*, 1991), and the land-based station distribution, $f_f = 1.2V_P/D$, where $V_P = 8.04$ km/s is the P wave speed in the oceanic upper mantle.

Once I have estimated f_f and computed rupture extents for a range of earthquakes, I compute their stress drops $\Delta\sigma$. I assume an elliptical slip distribution (*Eshelby*, 1957) and couple the earthquake rupture radii with moments M_0 obtained from the magnitudes of the NEIC earthquake catalog:

$$\Delta\sigma = \frac{7}{16}\frac{M_0}{\left(\frac{1}{2}D\right)^3}. \tag{2.5}$$

2.4.1 Comparing the phase coherence approach with spectral amplitude analysis

The phase coherence method is sensitive to different earthquake properties than methods that extract corner frequencies from an earthquake's frequency-domain amplitudes (e.g., *Shearer et al.*, 2006, *Allmann and Shearer*, 2007, 2009). The phase coherence method is most sensitive to the P wave travel time across the rupture area, and has limited sensitivity to the earthquake's rupture speed and duration (*Hawthorne et al.*, 2018). Spectral amplitude analysis methods, on the other hand, are more sensitive to the rupture speed and duration as well as to the P wave travel time across the rupture area (e.g., *Kaneko and Shearer*, 2014) (Sec. 1.1.1). In the future, implementing both of these methods may allow one to extract more information about many individual earthquakes: to quickly estimate both the rupture area and the rupture velocity (Sec. 5.3.1).

2.5 Implementing the phase coherence method on the Blanco fault

2.5.1 Forming earthquake pairs, earthquake relocation, and trace alignment

Before computing stress drops, I must perform a number of processing steps on my data. As a first step, I identify pairs of earthquakes that are potentially closely spaced and could have similar path effects. Since the catalog earthquake locations are uncertain and scattered in a 20-km wide region around the fault zone, I identify all earthquake pairs which have locations separated by less than 20 km. This identification

gives 4636 earthquake pairs, which include 388 unique earthquakes.

Next, I need to align the recordings of these earthquakes. To do so, I relocate the earthquakes in each pair relative to each other using a subset of the seismograms: those with high signal to noise ratios and well-constrained arrival times. To identify the high-quality data, I first bandpass the seismograms between 0.5 and 6 Hz, and cross-correlate a 5-s window beginning on the P wave arrival to align the traces, removing any traces with a signal to noise power ratio less than 20 in that time window. I then compare the first two seconds of the aligned 5-s windows to assess whether the signals are aligned and similar. I identify the traces that have cross-correlation coefficients larger than 0.6 in the 2-s windows, and extract the relative arrival times from the pairs of seismograms.

I use these arrival times to grid search for the relative earthquake locations. I fix the origin time and location of the higher-magnitude event in each pair and grid search for the best-fitting horizontal location and origin time of the smaller event, with depths fixed at 10 km for both events. For each proposed event location and time, I calculate the predicted P arrival times using ray tracing (*Crotwell et al.*, 1999) and the 1-D Earth velocity model iasp91 (*Kennett and Engdahl*, 1991). I compute an L1-norm misfit between the predicted and original estimated differential times from my alignment. In calculating the misfit, I exclude values larger than 0.1 s, as these appear to be due to inaccurate P arrival picks. I compute the final misfit without these outliers.

I use the location and origin time indicated by the minimum misfit to predict the relative arrival times for all traces, including some that were not used in the locations search. Then I use these times to align the seismograms. I note, however, that some seismograms contain significant noise, so as a final check I compute the cross correlation coefficient for a 2-s window beginning on the P arrival filtered between 0.5 and 6 Hz. In my stress drop calculations, I use only those seismograms with correlation coefficients higher than 0.6.

This cross correlation coefficient thresholding is important because it removes noisy traces and assesses whether the path effects are similar - whether I can remove the Green's functions' phases by computing the inter-earthquake phase coherence. But I should note that I have had to use a relatively low cross-correlation threshold compared with some spectral amplitude analysis studies (e.g., *Dreger et al.*, 2007, *Abercrombie*, 2014, 2015), as I compute the cross-correlation at frequencies that may be above the corner frequencies of the earthquakes because the data at lower frequencies is too noisy to use. The low threshold does not seem to strongly affect the results, however, I obtain similar patterns in earthquake stress drops when I use a higher cross-correlation

threshold of 0.8, though I obtain stress drops for fewer earthquakes as there are fewer viable stations (Table A.2, Figure A.1, and Figure A.2). The higher cross-correlation threshold also increases my estimates of median stress drop by roughly 30%.

2.5.2 Calculating the phase coherence

Once I have aligned the traces, I can remove the Green's functions and examine the inter-station ASTF similarity following the steps outlined in Section 2.4. For each earthquake pair, I extract a 5 s window from the aligned traces (Figure 2.4a - d) and compute the cross spectra (Equation (2.2)). The phases of some of the cross-spectra for one earthquake pair are shown in Figure 2.4e. The cross spectra are similar in the 1 - 3 Hz band, and as expected, the inter-station phase coherence is high in that band (Figure 2.4f). It falls off at higher frequencies because the cross-spectra phases start to differ. To estimate uncertainties on the coherence, I bootstrap by selecting 1000 subsets of stations with replacement for each earthquake pair. I then calculate the phase coherence for each subset of stations (Equation (2.4)) and derive 95% confidence limits from the overall distribution. The 95% confidence limits are illustrated by the shaded blue area in Figure 2.4(f).

I follow these steps to calculate coherence as a function of frequency for 1043 earthquake pairs that have more than 10 stations which pass the cross correlation threshold of 0.6. Additional examples of phase coherence profiles and falloff frequency picks are shown in Figures A.3 - A.9. For each earthquake pair, I identify the falloff frequency f_f: the frequency at which coherence falls below 0.5, as defined earlier. In identifying f_f, I require that the f_f occurs at a frequency higher than that of the maximum coherence, because low frequency noise throughout the dataset creates artificially low coherence at low frequencies, which would result in incorrect low falloff frequencies.

2.6 Results and Uncertainty assessment

2.6.1 Initial results and uncertainties

I obtain falloff frequencies for 1043 earthquake pairs (22% of my initial earthquake pairs), which include 161 unique events with magnitudes between M 4.2 - 6.0. I use these falloff frequencies and moments from the earthquake catalog to calculate initial stress drops (Equation (2.5)), and plot the results in Figure 2.5. When an earthquake is included in multiple pairs, I take the maximum among the pairs as the best estimate of the falloff frequency, since each value can be biased lower than its true value because of poor alignment or spatially varying Green's functions, as discussed later.

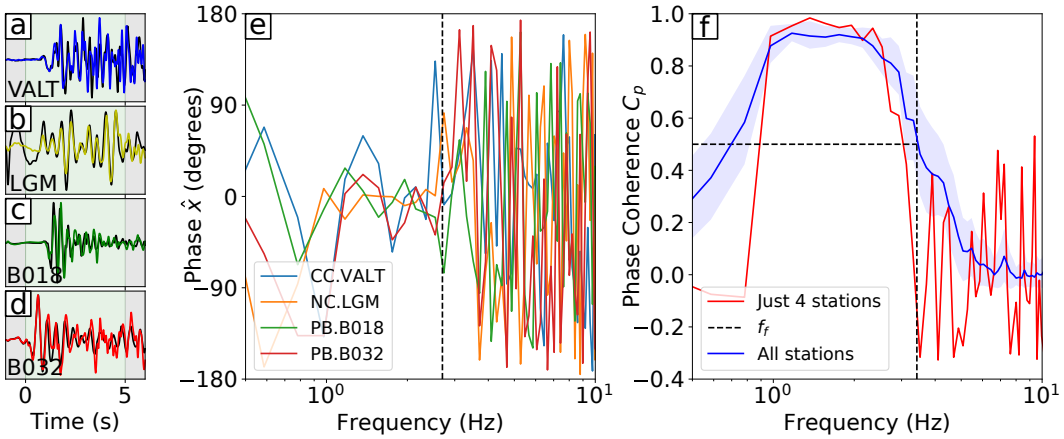

Figure 2.4: An illustration of the phase coherence method using an example earthquake pair. (a) - (d): Aligned traces from an earthquake pair recorded at 4 individual stations. The green window indicates the time window I used to calculate the cross-spectra and phase coherence. (e): Phase of the cross-spectra for each station. Phase spectra are similar in the 1 - 3 Hz band, with the falloff frequency identified from the phase coherence plotted as a dashed black line. (f): Inter-station phase coherence for the four stations in (a) - (d) (red) and all stations recording this event pair (blue with 95% confidence limits shaded), demonstrating the effect of averaging the coherence over stations. Coherence is high in the same frequency band that cross-spectra phases were similar in, resulting in a falloff frequency of roughly 3.4 Hz at a coherence threshold of 0.5. The apparent falloff frequency from the coherence using all stations is similar. Low frequencies have low phase coherence due to energetic low frequency noise in the data set.

In these initial results, the falloff frequency appears to decrease as magnitude increases. Such a decrease is expected, as larger earthquakes typically have larger diameters (e.g., *Báth and Duda*, 1964, *King and Knopoff*, 1968, *Chinnery*, 1969, *Kanamori and Anderson*, 1975, *Wells and Coppersmith*, 1994). However, the rate of decrease with magnitude cannot be directly interpreted from these data points, since each falloff frequency estimate could be affected by a range of factors including (1) incorrect trace alignment (Sec. 2.6.2), (2) differences in earthquake path effects (Sec. 2.6.3), (3) differences in focal mechanisms (Sec. 2.6.4), (4) a limited range of station azimuths (Sec. 2.6.5), and (5) depth phases in the phase coherence time window (Sec. 2.6.6). In the following sections, I evaluate how each factor could modify the coherence.

2.6.2 Incorrect trace alignment

The coherence I calculate can be reduced from its true value if the seismograms of the two earthquakes in a pair are poorly aligned. Here I estimate the alignment uncertainty using a loop closure approach. Then I use synthetics to examine how much the alignment error could reduce the inter-earthquake coherence.

To assess the accuracy of my alignment, I consider groups of 3 closely spaced earthquakes and examine the relationships between their arrival times. Consider, for exam-

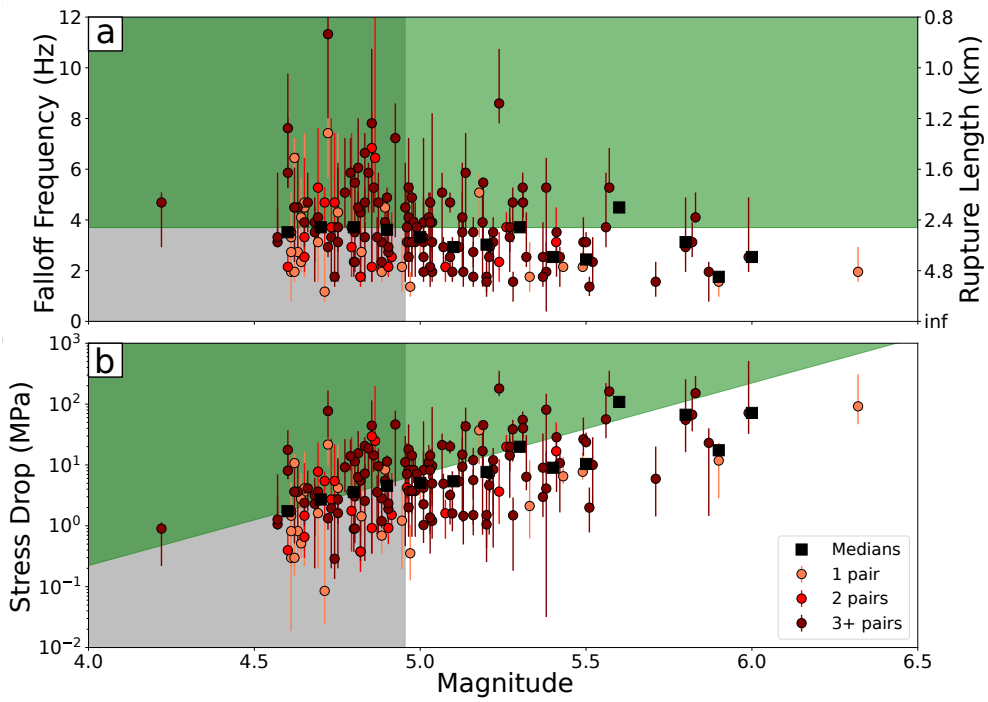

Figure 2.5: Initial unfiltered results for falloff frequency and stress drop variation with magnitude for 161 events. Values on (a) and (b) are coloured by number of event pairs available for each event. Note that small magnitude value shifts of less than 0.05 have been applied to differentiate between data points. Body wave magnitudes were translated to moment magnitude using the magnitude relation from *Braunmiller and Nábělek* (2008). Lower bounds on falloff frequencies have been limited to 1 Hz due to significant low frequency noise, which produces the stepping effect of lower uncertainties on stress drops in (b). The grey shaded area highlights earthquakes with $M < 5.0$ which are unlikely to have correct falloff frequencies as discussed in the text. The green shaded area indicates falloff frequencies I cannot reliably derive according to the alignment uncertainty, which is discussed in the text. Medians for 0.1 magnitude bins are plotted as squares.

ple, the arrival times of three earthquakes at station j: t_{1j}, t_{2j}, and t_{3j}. If these arrival times are correct, then the sum of the relative arrival times, or the loop closure $t_{loop,j}$, should close to zero:

$$t_{loop,j} = (t_{1j} - t_{2j}) - (t_{3j} - t_{2j}) - (t_{1j} - t_{3j}) = 0. \tag{2.6}$$

I find that 80% of loop closures are within 0.1 s of zero when all 3 events in the loop are within 4 km of each other. Such loop closure accuracy implies that 80% of relative arrival time uncertainties for aligned seismograms are within 0.06 s ($0.1/\sqrt{3}$) of zero. The inferred distribution of arrival time errors is illustrated in the histograms shown in Figures A.11 - A.13. Note that I assess only the alignment of earthquakes within 4 km of each other because I will discard results from more widely spaced earthquake pairs in the next section, as they have more variable path effects.

To determine how my alignment uncertainty affects the estimated coherence, I consider the coherence of a template earthquake with itself, after shifting the seismograms by various amounts. I take an earthquake from my dataset and copy its seismograms. Then I pick a set of travel time shifts from the loop closure distribution, apply these shifts to seismograms of the copied event, and calculate the coherence. I repeat this process for 1000 sets of time shifts and use the resulting 1000 coherence profiles to calculate the median phase coherence (black on Figure 2.6). I find that, on average, the added alignment errors reduce the phase coherence to less than 0.5 at frequencies of 3.7 Hz and above. Note that this frequency threshold is less than 0.2 times the minimum Nyquist frequency (20 Hz) for all but 9 of the 1434 stations I used. My coherence calculations appear limited by the accuracy of the earthquake relocations, not by the data quality at high frequencies. For further understanding, I also compute the coherence profiles that would be expected if the alignment errors are chosen from various normal distributions. I find that when the alignment error is larger (colored lines on Figure 2.6), coherence falls off at a lower frequency.

The results above imply that my average alignment uncertainty is likely to reduce perfect coherence ($C_p = 1$) to a coherence of 0.5 by a frequency of 3.7 Hz. Thus when the coherence profiles of real earthquake pairs decrease at frequencies around or above 3.7 Hz, it is unclear whether the falloff in C_p comes from the earthquake's rupture extent or from the average alignment uncertainty. I mark the range of falloff frequencies that are hard to interpret with the green shaded area in Figure 2.5.

This frequency threshold is especially problematic for smaller earthquakes, which are likely to have higher falloff frequencies. I find in Figure 2.5 that many $M < 5.0$ earthquakes have falloff frequencies near to or larger than 3.7 Hz. Since those values are

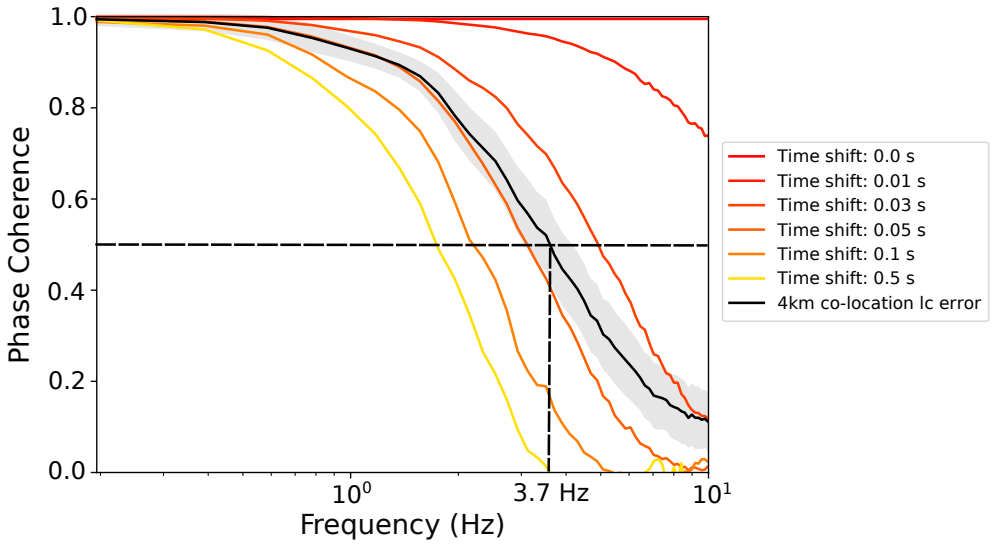

Figure 2.6: Inter-station phase coherence results for an event with itself, but with varied forced alignment shift. The black line shows maximum phase coherence derived from loop closures (lc) only for loops where all 3 events are within 4 km, with the grey shaded area indicating 95% confidence limits.

hard to interpret, I will exclude $M < 5.0$ events from my discussion and interpretation of Blanco fault earthquakes, and I mark $M < 5.0$ in grey on Figure 2.5.

2.6.3 Differences in earthquake path effects

Another possible bias on falloff frequency comes from earthquake spacing. For my analysis to work, the earthquakes must be co-located so that the path effects will be removed in the cross-spectra calculation for each station. If path effects differ at frequencies lower than the falloff frequency, they will not be removed and I will obtain an apparent falloff frequency that is unrelated to the earthquake's rupture extent, even if each event has similar ASTFs at all stations. Such path effect differences are likely to be larger and more problematic for more widely spaced earthquakes.

I have examined coherence profiles for a number of earthquake pairs with various separations. Examples for a range of inter-earthquake distances are shown in Figure 2.7. Empirically I find that the coherence profiles remain relatively consistent among earthquake pairs as long as the events are within 4 km of each other. I note, however, that it is difficult to be sure that the path effects are consistent for any pair of earthquakes, so any falloff frequency I estimate should be considered to be a lower bound on the true falloff frequency.

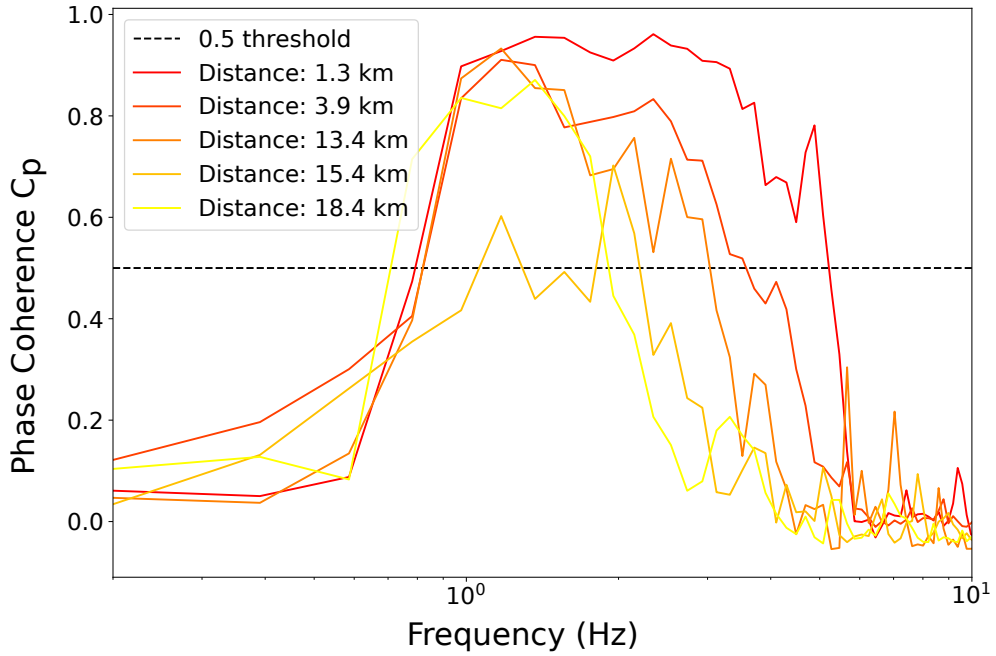

Figure 2.7: Phase coherence spectra for a single event with multiple pairs. The distance between each pair is quoted in the legend, and is estimated using the relative event relocation approach (Sec. 2.5.1). The dashed black line is the coherence threshold of 0.5 which I use to pick falloff frequencies. This figure illustrates that as the distance between events decreases, the falloff frequency increases.

2.6.4 Differences in focal mechanisms

Coherence profiles can also be affected by the focal mechanisms of earthquakes in my pairs. Earthquakes with different focal mechanisms will give rise to different seismograms, even when the earthquakes have the same ASTFs or small rupture areas. Such focal mechanism-induced differences can reduce coherence and result in an incorrect falloff frequency.

Previous analysis of earthquakes on the Blanco fault suggests that focal mechanisms are unlikely to vary significantly on a 4-km length scale. *Braunmiller and Nábělek* (2008) observed that strike-slip mechanisms dominate on transform segments of the Blanco fault, while normal mechanisms are more common within depressions. They found that slip vectors varied by less than 20° along the fault, which suggests that my coherence estimates are unlikely to be reduced due to focal mechanisms.

2.6.5 Limited range of station azimuths

It is not only differences in the earthquakes that can affect the phase coherence, but properties of the station distribution as well. The basis of the phase coherence method is that I search for ASTF variations caused by varying source-station travel

times, which differ due to the stations' azimuths and the rupture directivity (e.g., *Mori*, 1996, *Somerville et al.*, 1997). However, in my analysis, I have a limited azimuthal distribution of stations; most stations are located at azimuths between 20 and 70° (Figure 2.2). To determine how this limited azimuthal range could affect my rupture extent estimates, I collaborated with my supervisor, Jess Hawthorne, to examine how the falloff frequencies of synthetic ruptures vary with the azimuthal range of stations.

The synthetic ruptures were created following the approach of *Hawthorne et al.* (2018). The synthetic events have heterogeneous slip distributions and rupture bilaterally at velocities of 0.8 times the shear wave speed. Seismic waves due to these ruptures were propagated through the iasp91 1-D velocity model (*Kennett and Engdahl*, 1991) to estimate apparent source time functions for each station in the station distribution for a typical earthquake pair. These apparent source time functions were then convolved with synthetic Green's functions created from random noise from a normal distribution, to create synthetic earthquake traces. The cross-spectra and phase coherence was then computed between the traces of each synthetic rupture and a smaller synthetic rupture. From the phase coherence, the falloff frequency of the larger synthetic rupture can be estimated. Figure 2.8 shows the falloff frequencies obtained from synthetic ruptures with a range of diameters.

The falloff frequencies are roughly 1.2 V_P/D for the representative station distribution used for earthquakes on the Blanco fault, where V_P is 8.04 km/s, the P wave velocity in the oceanic upper mantle, as well as for a few additional representative azimuthal distributions. Note that if one uses randomly distributed stations on the surface of a homogeneous half space, f_f is 1.1 V_P/D (Figures A.14 - A.16).

To understand why the scaling factor F_{scal} is higher for my station set, imagine that an earthquake contains two concurrent bursts of slip at either ends of its rupture extent. If those slip bursts are recorded at stations located at 0 and 180° azimuth from the rupture, I would see two peaks in the source time function, where each peak relates to the signal from a slip burst. The time between these peaks is equal to the travel time across the rupture. For stations perpendicular to the rupture, the time between these peaks is approximately zero (Figure 2.3 and Figure A.17).

In the inter-station phase coherence method, I compute the coherence between the ASTFs of stations. Stations that are closely spaced have similar arrival times of the slip burst peaks and roughly the same apparent source time function. Stations that are widely spaced have different arrival times of the peaks and thus different apparent source time functions. The maximum difference in arrival times of the peaks that these widely spaced stations can have is the travel time across the rupture. The inter-station

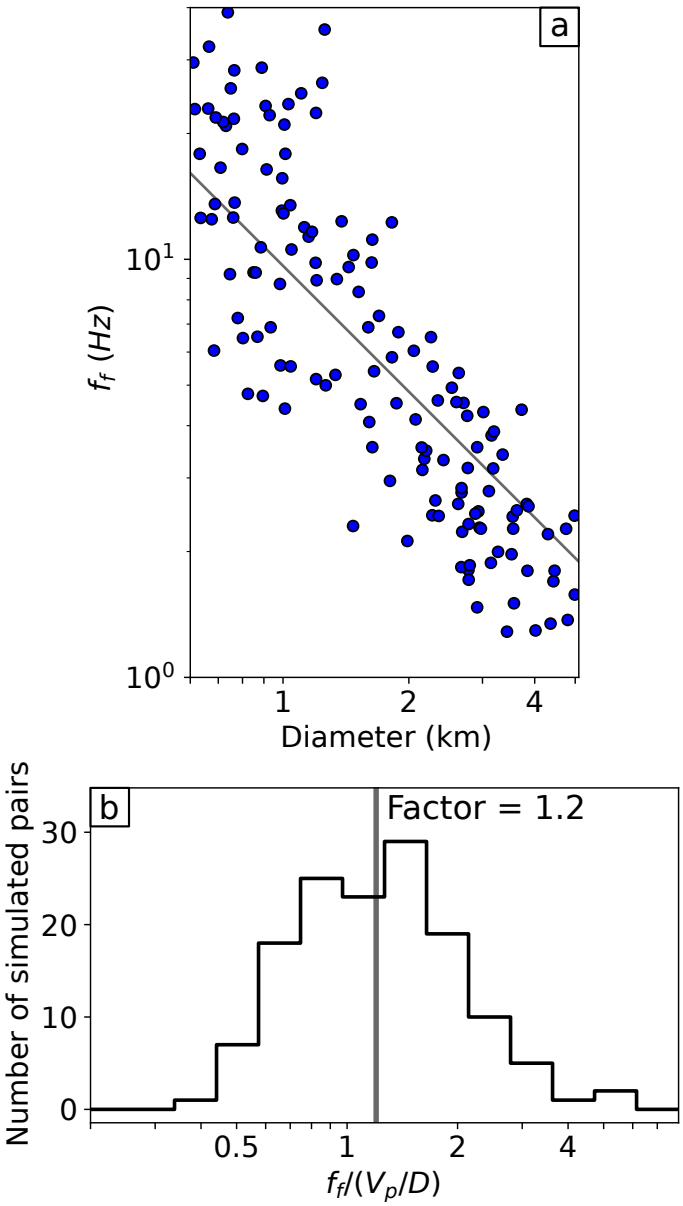

Figure 2.8: (a): Falloff frequencies obtained from synthetic ruptures for a range of rupture diameters. (b): Histogram of falloff frequencies normalized by V_P/D, where V_P is 8.04 km/s, the P wave velocity of the upper mantle. The median of the normalized falloff frequencies plots at 1.2, which defines the scaling factor I use in my calculations of the rupture extent.

coherence thus falls off at a frequency that scales with one over the travel time across the rupture.

With randomly distributed stations, I average the coherence between many widely and closely spaced station pairs and find that coherence falls off at a frequency of 1.1 V_P/D. But for my narrow azimuthal range of stations, I have lots of station pairs that are closely spaced. I find that the coherence falls to 0.5 at a frequency of 1.2 V_P/D, on average, with a larger F_{scal} because of the concentration of closely spaced stations. So I assume that the falloff frequency f_f is 1.2 V_P/D when I interpret my estimated f_f in terms of earthquake diameter.

Another approach to visualise the effect that azimuthal variation of stations has on the scaling factor F_{scal} is to compute the falloff frequency of a synthetic earthquake using stations with varying differences in azimuth between them, as demonstrated in Figure 2.9. For an azimuthal difference greater than 45°, the falloff frequency is relatively unaffected by increasing azimuthal difference. At differences less than 45°, the falloff frequency is increased significantly which will cause inaccuracies in my estimated stress drops. Most of the stations I use in my earthquake pairs are concentrated between 20 and 70° azimuth, so may cause increased falloff frequencies, which I correct using the higher scaling factor of 1.2. If I had a much wider azimuthal range of stations, then the scaling factor would be closer to 1.1. On the other hand, even with a wide azimuthal range of stations, the scaling factor can still be increased if most of those stations are within a narrow azimuthal range with few outliers, as I found in Chapter 3.

2.6.6 Depth phases in the phase coherence time window

In my coherence analysis, I use a 5-s time window focused on the P arrival. But other phases, such as the depth phases pP and sP, also arrive in this time window. To assess how the depth phases could affect the phase coherence, consider an earthquake i recorded at stations j, each with a P arrival followed Δt_{ij} seconds later by a pP arrival.

If the local earth structure is relatively simple, so that most complexity in the Green's function arises well away from the source, the pP-phase can be approximated as a time-shifted version of the P arrival, with the same source time function so that the seismogram d_{ij} is (e.g., *Letort et al.*, 2015)

$$d_{ij}(t) = (s_{ij}(t) + Y s_{ij}(t + \Delta t_{ij})) * g_j(t), \tag{2.7}$$

where Y is a real number that accounts for the reflection coefficient and amplitude of

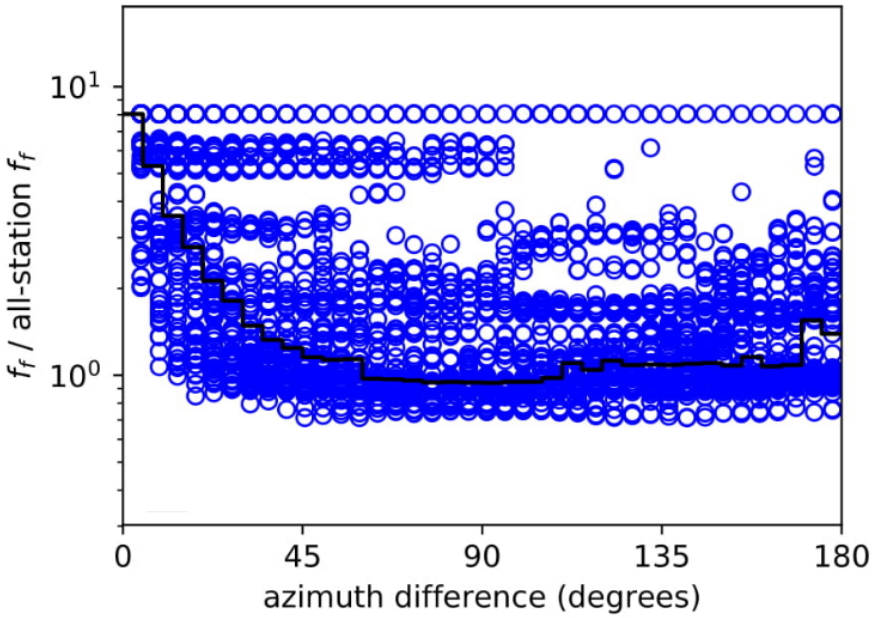

Figure 2.9: Coherence falloff frequency versus azimuthal difference between stations, where the falloff frequency has been computed from coherence between station cross spectra. The solid black line indicates the median falloff frequency in windows of 5°. The median falloff frequency is stable for azimuthal differences between 45° and 180° and increases dramatically for differences less than 45°.

the pP-phase, s_{ij} is the ASTF, and g_j is the Green's function of the P arrival.

When I compute the cross-spectra at a single station j (Equation (2.2)) for a pair of earthquakes ($i = 1$ and $i = 2$), I obtain

$$\hat{x}_j = |\hat{g}_j|^2(\hat{s}^*_{1j} + Y\hat{s}^*_{1j}e^{-if\Delta t_{1j}})(\hat{s}_{2j} + Y\hat{s}_{2j}e^{if\Delta t_{2j}}) \tag{2.8}$$

$$= |\hat{g}_j|^2\hat{s}^*_{1j}\hat{s}_{2j}(1 + Ye^{-if\Delta t_{1j}})(1 + Ye^{if\Delta t_{2j}}). \tag{2.9}$$

These calculations reveal that the pP arrival does change the cross spectra; the two terms in parentheses in Equation (2.9) represent a phase shift for each station resulting from the pP arrivals for each earthquake, which have different time shifts Δt_{1k} and Δt_{2k}.

In my C_p calculations, however, I am not interested in the phase of any individual $\hat{x}_j$, but in how the time shifts Δt_{ij} are likely to differ among stations. I compute Δt_{ij} using ray tracing and find it is roughly constant (< 0.01 s) for both pP and sP at stations in the 175 - 800 km distance range and for earthquake depths from 0.5 - 20 km (Figure A.18). If Δt_{ij} is consistent across stations j for each event i, then the phase shift of the cross-spectra $\hat{x}_j$ due to the depth phase arrival will also be consistent across stations, and the phase coherence $\hat{x}_j\hat{x}^*_l$ between two stations j and l will be

unchanged. Therefore I exclude stations within 175 km of each earthquake before calculating coherence and stress drop, to keep coherence high even if the analysed time windows include secondary arrivals.

Note that if the 5-s window of analysis is not long enough to capture the entire apparent source time function of the depth phases, then the phase may differ between apparent source time functions resulting in an artificially decreased coherence. This truncation of the apparent source time functions is also a problem generally for the phase coherence method, and it is often prudent to use a longer time window to ensure the entire source time function is captured. On the other hand, a longer time window here may increase the risk of including water multiples in the time window. Water multiples are arrivals which reflect multiple times off the seabed, and arrive later than conventional depth phases due to the slower velocity of the medium they travel through. Fortunately, the high source-receiver distance for my work on the Blanco fault means that water multiples are unlikely to arrive in the 5-s window I use for my analysis.

2.6.7 Final stress drop results

In the sections above, I examined how several factors could modify the phase coherence. I (1) assessed resolvable falloff frequencies given the uncertainty in my trace alignment, (2) analysed how coherence changes with inter-earthquake distance, (3) considered the impact of focal mechanisms, (4) identified appropriate rupture diameter-falloff frequency calibration given the azimuthal distribution of stations, and (5) showed that depth phases are unlikely to influence the coherence in my case. I found that I can identify earthquake pairs with well-resolved coherence by considering only events within 4 km of each other and by noting that falloff frequencies above 3.7 Hz are likely to be unresolvable. This 3.7-Hz resolution limit suggests that I cannot interpret $M < 5.0$ earthquakes due to their high falloff frequencies. After imposing these thresholds, I am left with 298 pairs created from 124 unique events, including 61 $M \geq 5.0$ earthquakes (Figure A.19, Table A.3). Their falloff frequencies and stress drops are shown in Figure 2.10.

2.7 Analysing stress drops on the Blanco fault

2.7.1 Average stress drop

The median stress drop of the 61 $M \geq 5.0$ earthquakes with well-resolved coherence falloffs is 8 MPa. I compute the uncertainty on the median stress drop by bootstrapping the earthquakes included and by sampling the stress drop probability distributions for

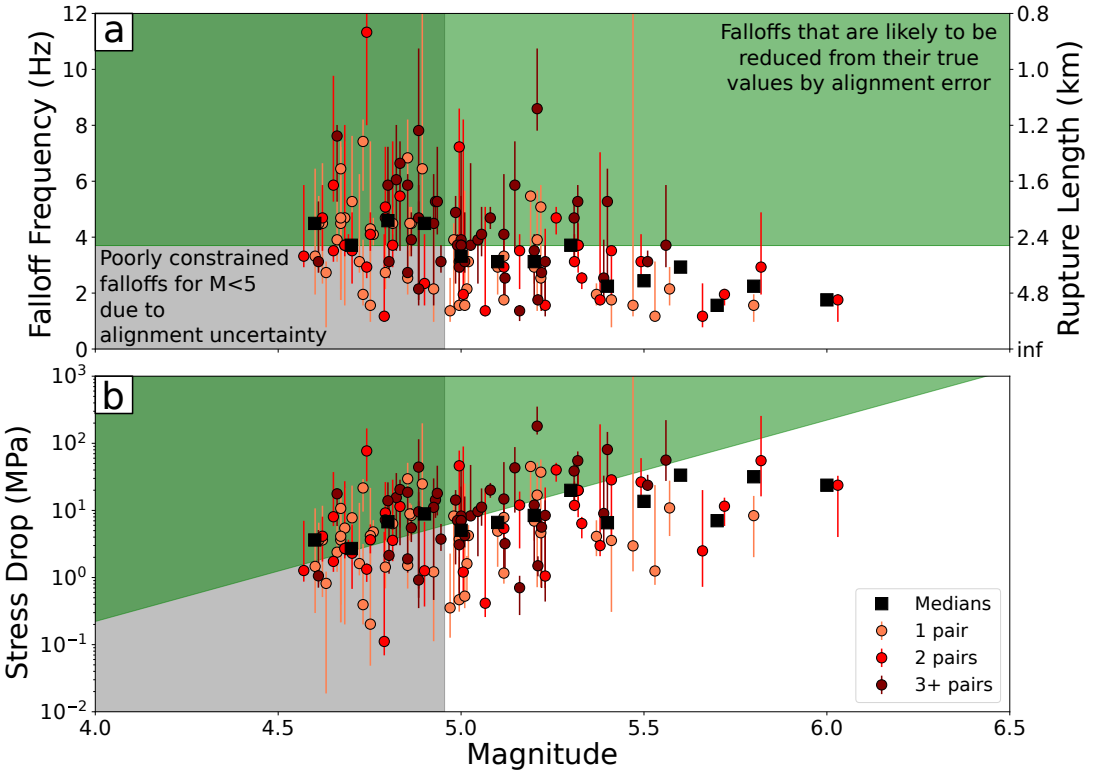

Figure 2.10: (a): Falloff frequencies against magnitude for 124 events. (b): Stress drops plotted against magnitude for the same events. Note that magnitudes have been shifted by values less than 0.05 to differentiate between data points. Earthquakes with $M < 5.0$ which are unlikely to have the correct falloff frequency are highlighted by the grey shaded area on the plot. The 3.7 Hz limit on reliable falloff frequencies due to the alignment uncertainty is indicated by the green shaded area. Results are colored by the number of earthquake pairs available for each measurement. Medians for 0.1 magnitude bins are plotted as squares.

individual earthquakes, which I obtained earlier by bootstrapping the stations used (Sec. 2.5.2). For each bootstrap sample, I choose a random subset of the earthquakes with replacement, and recalculate the median using the stress drops picked from the individual earthquakes' probability distributions. I resample 100,000 times and find 95% confidence limits of 6 and 12 MPa on the median stress drop.

The median stress drop for the Blanco fault found here is higher than values found in some previous studies of oceanic transform faults. *Boettcher and Jordan* (2004) found values of 0.1 - 0.7 MPa for a global set of faults, and *Moyer et al.* (2018) found values of 0.04 - 3.4 MPa for the East Pacific Rise transform faults, but my median stress drop is similar to the 6.03±0.68 MPa median stress drop obtained in the global study of oceanic transform faults by *Allmann and Shearer* (2009). However, note that comparing absolute values of stress drops between studies can be prone to error, as different rupture models and analysis methods are used. The difficulty in comparing stress drops between studies means I can suggest only that the median stress drop for the Blanco fault appears to be within an order of magnitude of previous estimates for oceanic transform faults.

In comparing my stress drops with previous results, I also note that the stress drops I calculate here are lower bounds on the true stress drops, because the falloff frequencies are lower bounds on the true falloff frequency. Some of these falloff frequencies may be lower than their true values because of poor trace alignment, or variable Green's functions.

On the other hand, my data limit my ability to examine low stress drop earthquakes. Low frequency noise in the dataset means I cannot identify falloff frequencies below 1 Hz. Indeed, I exclude such earthquakes from my analysis with my initial cross-correlation threshold. The exclusion of low falloff frequency and thus low stress drop earthquakes from my analysis results in an overestimated median stress drop.

Note that I include all earthquake pairs in my analysis and do not throw out any earthquake pairs with a small difference in magnitude between them. Tests with synthetic ruptures (Figure A.14) indicate that the falloff frequency is independent of the relative earthquakes' sizes, so long as the ruptures have heterogeneous and different slip distributions. However, any repeating earthquakes with similar slip distributions in the catalog will be assigned inappropriately high falloff frequencies and stress drops with my approach, as such earthquakes could have high coherence at frequencies above the true falloff frequency (*Nadeau and Johnson*, 1998, *Dreger et al.*, 2007). To check for such a bias, I tried excluding pairs with only 0.1 or 0.2 magnitude unit differences, but the median stress drop and stress drop patterns remain unchanged (Table A.4).

The effects of alignment uncertainty and low frequency noise create a narrow resolution band of falloff frequencies between 1 and 4 Hz. This range of allowed falloff frequencies creates a small apparent increase in stress drop with magnitude in Figure 2.10. But since that increase is not robust, I do not discuss it further. Most previous studies have found magnitude-independent stress drops (e.g., *Abercrombie*, 1995, *Mori et al.*, 2003, *Shearer et al.*, 2006, *Chen and Shearer*, 2011, *Uchide et al.*, 2014, *Chen and McGuire*, 2016, *Abercrombie et al.*, 2017).

2.7.2 Spatial variation of stress drops

I also examine how stress drops vary with location along the fault. As noted in the Blanco fault section, *Dziak et al.* (1991) and *Braunmiller and Nábělek* (2008) found that the seismic moment release varied along the Blanco fault, with the northwest segment (west of the Cascadia Depression - see Figure 2.11) and southeast segment accommodating 3.8% and 14.1% of moment in earthquakes, respectively. I separate the fault into these two segments and calculate median stress drops of the $M \geq 5.0$ earthquakes on each segment. The 30 $M \geq 5.0$ events on the NW segment have a median stress drop of 6 MPa (with bootstrap-based uncertainties of 4 to 11 MPa), and the 31 events on the SE segment have a median of 11 MPa (6 to 22 MPa). The two best-fitting median stress drops imply that stress drops on the SE segment are higher by a factor of 1.7, though the 95% confidence intervals allow factors between 0.8 and 3.5.

When interpreting the stress drop ratios, it is important to note that the median stress drops represent averages of individual stress drops that are highly scattered (Figure 2.11a). Some of the scatter in individual stress drops is likely real inter-earthquake variation which is sampled by my bootstrap-based uncertainty estimate. But some of the scatter is likely an artefact of the analysis method. My uncertainty estimates account for some of that scatter; I account for noise and station distribution when I create probability distributions for individual earthquakes by bootstrapping the stations included in the analysis. However, there are two sources of bias that I do not account for in my uncertainty estimates. As noted in the last section, stress drops could be biased low by poor trace alignment or inappropriate empirical Green's functions but the median stress drops could be biased high because I am unable to analyse earthquakes with f_f below 1 Hz. I do find a similar stress drop ratio of 2.1 (with 95% confidence limits of 0.8 and 4.7) using seismograms that passed a cross correlation coefficient threshold of 0.8 as discussed in an earlier section. Those similar ratios suggest that the trace alignment and location scatter are not significantly affecting my results. But I would still urge caution in interpreting the factor of difference I find, due to its high uncertainty.

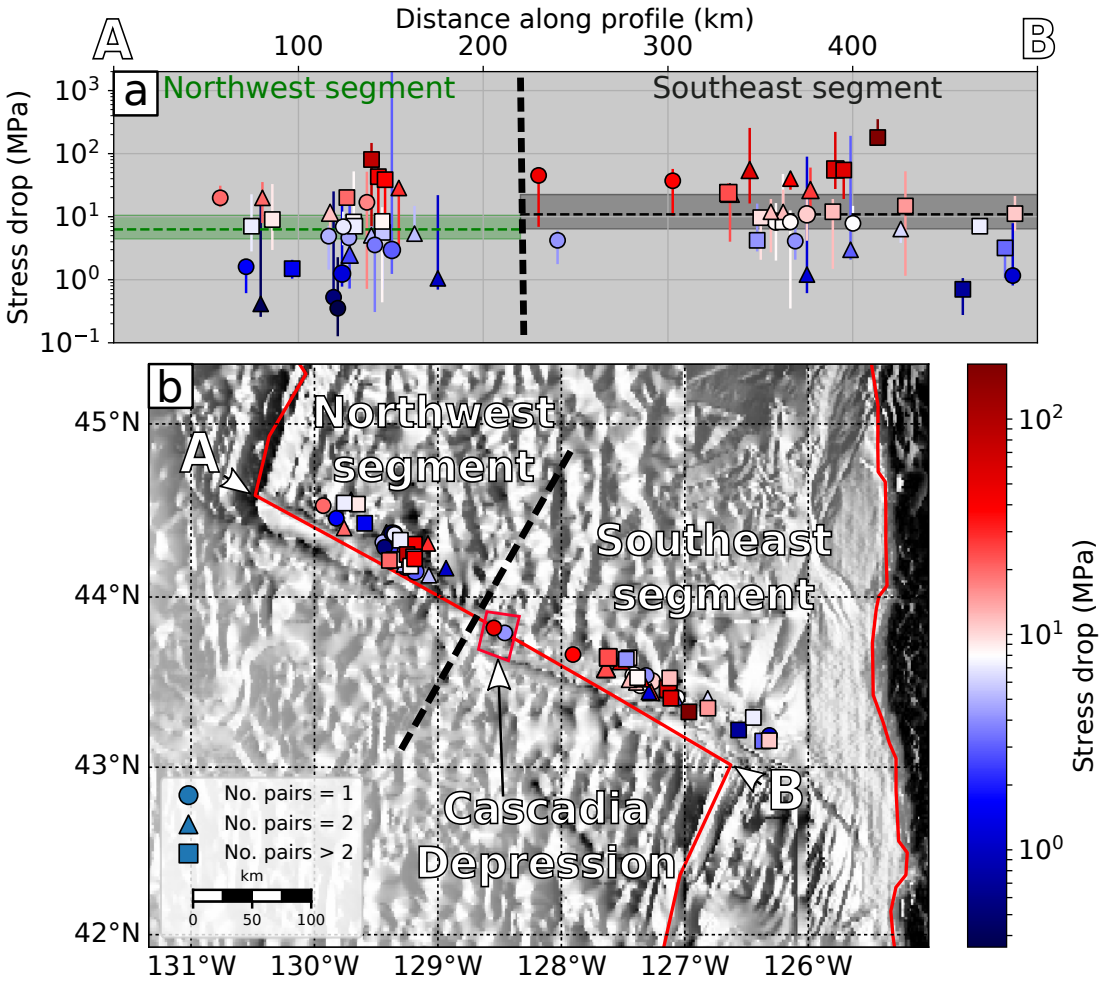

Figure 2.11: (a): Stress drops for $M \geq 5.0$ earthquakes on the Blanco fault plotted along the fault from A to B. The thick black vertical dashed line in the centre of the plot indicates cutoff point I defined between the northeast and southwest segments (derived from the Cascadia Depression shown as the red square in (b)). Stress drops are colored by amplitude. Symbols indicate the number of earthquake pairs that were available for each measurement. The median stress drops for the northwest and southeast segments are shown by the dashed horizontal green and black lines, respectively. The shaded areas around these medians show the 95% confidence limits. (b): Stress drops for $M \geq 5.0$ earthquakes on the Blanco fault plotted in map view.

Despite the uncertainty on my stress drop estimates, it is interesting to note that *Moyer et al.* (2018) identified a similar spatial variation in stress drops for East Pacific Rise transform faults, where stress drops were a factor of 2 larger in higher seismic moment release areas. They explained their results using the model of *Hardebeck and Loveless* (2018), where creeping faults had reduced strength and therefore lower stress drops. Another possible explanation for higher stress drops occurring on more seismic segments is that the lower stress drops on the NW segment could arise due to reduced fault healing, related to a shorter seismic cycle and thinner seismogenic zone. *Byrnes et al.* (2017) identified a negative shear wave velocity anomaly below the NW segment of the Blanco fault and a positive anomaly beneath the SE segment, which could indicate mantle upwelling beneath the NW segment. The suggested mantle upwelling under the NW segment could lead to a smaller seismogenic zone, and therefore a shallower transition to velocity-strengthening behaviour under the NW segment.

The transition to velocity-strengthening frictional sliding and thus to aseismic creep is thought to be temperature dependent, occurring at 500 - 600 °C on transform faults (*Abercrombie and Ekström*, 2001, *Boettcher et al.*, 2007, *He et al.*, 2007, *Braunmiller and Nábělek*, 2008). If the temperature of the NW segment is higher due to increased heat flow, aseismic creep will occur at a shallower depth within the fault zone, and the seismogenic zone will be smaller. A smaller seismogenic zone can be loaded more quickly by aseismic slip at depth, and thus is more likely to have a shorter earthquake cycle. The shorter seismic cycle of asperities would allow less time for the fault to heal (*Marone et al.*, 1995, *Niemeijer and Spiers*, 2006, *Hauksson*, 2015), and thus reduce its ability to accommodate high stresses. The limited fault strength may allow only lower stress drops on the more aseismic NW segment.

2.8 Conclusions

I have demonstrated the applicability of the phase coherence method (*Hawthorne et al.*, 2018) to obtain stress drops for $M \geq 5.0$ earthquakes on the Blanco fault. I considered how the coherence estimates are affected by various factors, including incorrect trace alignment, differences in earthquake Green's functions, differences in focal mechanisms, a limited range of station azimuths, and depth phases in the analysis time window. To account for these factors, I first identified the range of falloff frequencies that are resolvable given my alignment uncertainty. I found empirically that differences in Green's functions are minimal for earthquakes within 4 km. I noted that focal mechanisms are unlikely to vary in my data set, and calibrated my rupture diameter estimates to falloff frequency given the azimuthal distribution of stations for my events. Finally, I showed that depth phases are unlikely to influence the coherence for oceanic

earthquakes observed at distances of several degrees.

Within these constraints, I was able to estimate stress drops of 61 $M \geq 5.0$ earthquakes on the Blanco fault. Future comparisons of these or other coherence-based stress drops with stress drops derived from spectral amplitude analysis may provide insight into earthquake rupture dynamics and allow one to constrain more earthquake properties, as the various techniques have different sensitivities to the rupture properties and local wavespeeds.

I found a median stress drop of 8 MPa (with 95% confidence limits of 6 to 12 MPa) for the 61 $M \geq 5.0$ earthquakes on the Blanco fault with well-resolved coherence falloffs. This median is similar to or higher than other estimates on oceanic transform faults (*Boettcher and Jordan*, 2004, *Allmann and Shearer*, 2009, *Moyer et al.*, 2018). The median stress drop is a factor of 1.7 (0.8 to 3.5) higher on the more seismically active southeast segment of the Blanco fault. This factor of difference should be carefully considered due to the scatter of individual stress drop, and the large uncertainty in the factor itself. Nevertheless, I note that one possible explanation for the lower stress drops on the more aseismic segment, which were also observed on the East Pacific Rise (*Moyer et al.*, 2018), is that the more aseismic segment has higher temperatures, which lead to a shallower seismogenic zone, a shortened seismic cycle, less time for healing and thus less potential for large strength and stress drop in the earthquakes.

Chapter 3

Estimating the stress drops of aftershocks of the 2010 M_W 7.2 El Mayor-Cucapah earthquake using the phase coherence method on P and S waves

"My bugs don't have bugs."

Eoin Colfer, Artemis Fowl

3.1 Introduction

In Chapter 2, I examined the stress drops of earthquakes on the Blanco fault using the newly developed phase coherence method. I observed a slight increase in stress drops with increasing moment and decreasing aseismic slip but could not examine whether stress drops depend on depth because of the poorly resolved earthquake depths. Here I use the phase coherence method to examine stress drops of aftershocks of the El Mayor-Cucapah earthquake. I examine whether stress drops depend on moment and depth of the earthquake. I also examine whether stress drops vary with the decreasing post-seismic aseismic slip rate following the main earthquake (*Gonzalez-Ortega et al.*, 2014). I further develop the phase coherence method by applying it to the P wave and the S wave to determine whether the S wave would be a viable alternative to the P

wave.

The behaviour of stress drops of aftershocks varies for different large earthquakes. Aftershocks have been observed to have higher stress drops within high slip regions of the 2007 *M* 6.9 Noto Hanto earthquake (*Urano et al.*, 2015) or around the high slip regions of the 2006 M_W 6.7 Kīholo Bay earthquake (*Yamada et al.*, 2010). On the other hand, aftershocks have also been observed to have similar stress drops in high slip and low slip regions of the 2011 M_W 5.7 Prague earthquake (*Sumy et al.*, 2017). Aftershocks' stress drops also appear to vary with time as well as the slip of the main shock. For example, *Sumy et al.* (2017) observed that the stress drops of aftershocks increased with time after the 2011 M_W 5.7 Prague earthquake, but *Abercrombie* (2014) observed that the stress drops of aftershocks decreased rapidly immediately after the 2004 *M* 6 Parkfield earthquake before increasing to match stress drops of the background seismicity. Any change in the stress drops of aftershocks with time after the main shock could be caused by the post seismic slip which occurs after many large earthquakes (e.g., *Smith and Wyss*, 1968, *Bucknam et al.*, 1978, *Donnellan and Lyzenga*, 1998, *Hsu et al.*, 2006, *Ingleby and Wright*, 2017). It is thus important to investigate the stress drops of aftershocks to improve our understanding of the influence of aseismic slip on the stress conditions of earthquakes. Here I investigate how stress drops of earthquakes interact with aseismic slip by examining the stress drops of aftershocks of the 2010 M_W 7.2 El Mayor-Cucapah earthquake.

The 4 April 2010 M_W 7.2 El Mayor-Cucapah earthquake ruptured 120 km along a series of faults in northeastern Baja California, Mexico. The northern end of this series of faults extends into southern California, U.S. (*Fletcher et al.*, 2014). The faults ruptured by the 2010 earthquake are located close to the boundary between the North American and Pacific tectonic plates, in a region often referred to as the "Big Bend" (Figure 3.1). The Big Bend is a restraining bend of the strike slip San Andreas fault system between the strike slip fault to the north and the spreading centre in the Gulf of California in the south (*Wei et al.*, 2011, *Kroll et al.*, 2013, *Fletcher et al.*, 2014). The El Mayor-Cucapah earthquake was unusual for the Big Bend region because the earthquake did not rupture the larger faults such as the Laguna Salada and Cerro Prieto faults but instead ruptured a series of smaller faults (Figure 3.2). The larger faults were previously thought to accommodate most of the relative plate motion between the Pacific and North American plates (e.g., *Fletcher et al.*, 2014). Despite not rupturing the larger faults, the El Mayor-Cucapah earthquake was the largest event in the Big Bend region in 120 years (*Hough and Elliot*, 2004, *Kroll et al.*, 2013).

The 2010 El Mayor-Cucapah earthquake caused up to 9 m of slip (e.g., *Wei et al.*, 2011, *Mendoza and Hartzell*, 2013) with components of dextral strike slip and normal

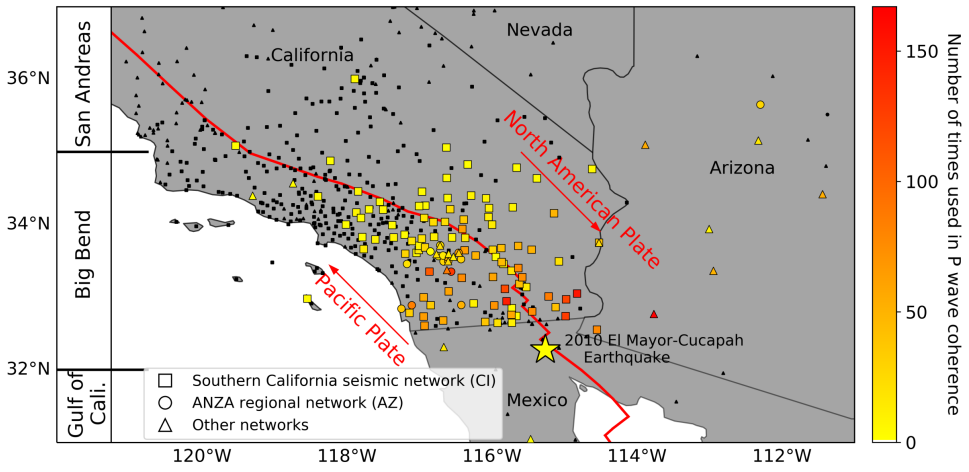

Figure 3.1: The tectonic setting of the 2010 M_W 7.2 El Mayor-Cucapah earthquake and locations of stations which recorded the aftershocks of the earthquake. The El Mayor-Cucapah earthquake epicentre is plotted as a yellow star. Large scale tectonic regions are outlined on the left of the plot. The approximate tectonic plate boundary is plotted in red, with the directions of plate motion indicated by the red arrows. Stations used in my analysis are plotted by network. Some networks have been grouped for plotting purposes. The colour of the stations indicates the number of earthquake pairs that used this station to analyse the P wave using the inter-station phase coherence method. In total, 272 earthquake pairs were analysed. Stations indicated by the small black symbols were not used because of their low signal-to-noise ratios.

faulting (*Hauksson et al.*, 2011). The slip of the earthquake was distributed over a bilateral rupture which extended to the southeast and northwest away from the epicentre (e.g., *Wei et al.*, 2011, *Rodríguez-Pérez et al.*, 2012, *Kroll et al.*, 2013, *Uchide et al.*, 2013). The El Mayor-Cucapah earthquake ruptured in a southeastern direction for the first 16 s and then ruptured bilaterally for the remainder of its 52-s duration (*Uchide et al.*, 2013). The segment southeast of the epicentre was relatively simple: it was 55 km long, mostly dextral strike slip and primarily along a single fault (*Kroll et al.*, 2013). The segment northwest of the epicentre was more complex: it was 65 km long, featured dextral strike slip and normal faulting components and ruptured multiple faults (*Kroll et al.*, 2013). The earthquake also triggered further slip in nearby regions including in the Yuha Desert to the north (e.g., *Rymer et al.*, 2011, *Kroll et al.*, 2013) and along the Laguna Salada fault (*Fletcher et al.*, 2014).

There are several models of the slip distribution of the El Mayor-Cucapah earthquake (e.g., *Wei et al.*, 2011, *Rodríguez-Pérez et al.*, 2012, *Mendoza and Hartzell*, 2013, *Uchide et al.*, 2013, *Huang et al.*, 2017b). These models are similar even though they range from single fault models (e.g., *Rodríguez-Pérez et al.*, 2012, *Mendoza and Hartzell*, 2013) to complex 9-fault ruptures (e.g., *Huang et al.*, 2017b). I focus on the slip models of *Wei et al.* (2011) and *Mendoza and Hartzell* (2013) because these two models are available in the SRCMOD database (*Mai and Thingbaijam*, 2014) and because these

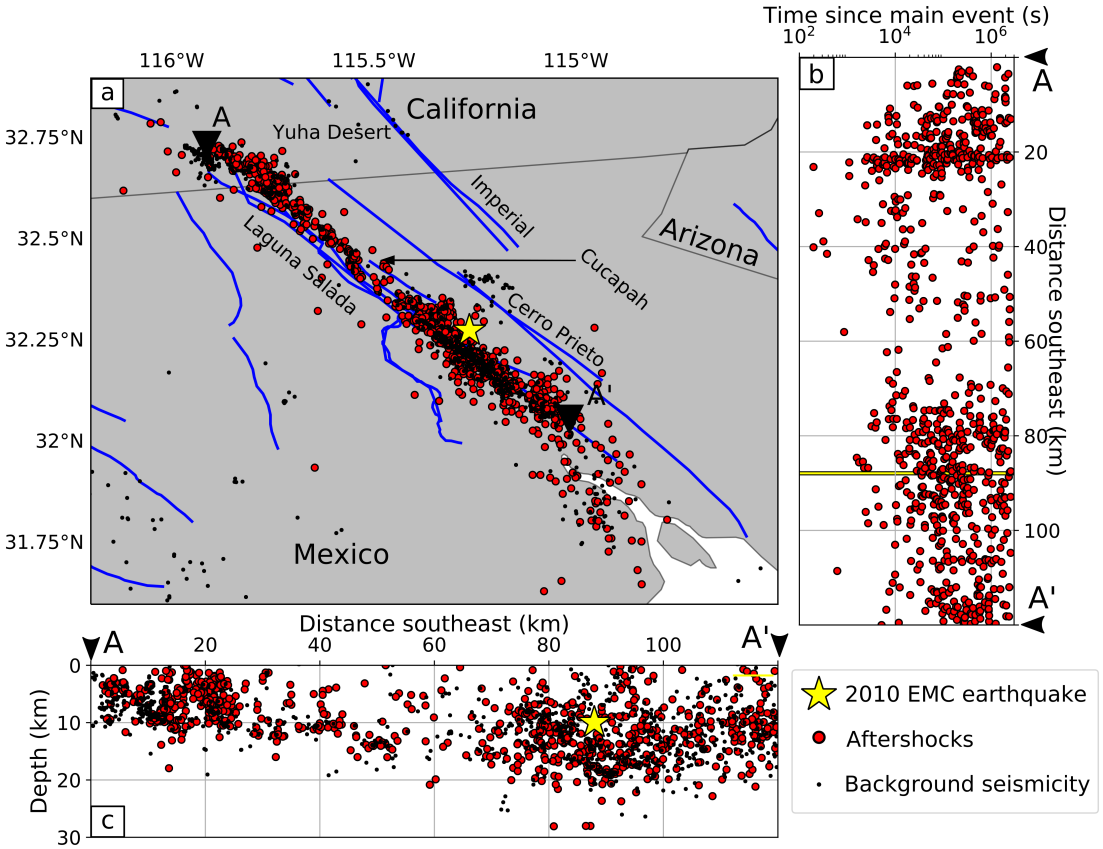

Figure 3.2: The local fault structure and aftershocks of the 2010 El Mayor-Cucapah earthquake. (a): A map of the local fault structure and the $M \geq 3$ aftershocks (red dots) around the El Mayor-Cucapah earthquake (yellow star). Faults from the Global Earthquake Model Global Active Faults project (*Christophersen et al.*, 2015) are plotted in blue. Notable faults are labelled. Small black dots are $M \geq 3$ earthquakes that occurred between the end of the 31-day aftershock period and the 31st December 2018. The triangles marked A and A′ are the start and end of the fault profile used in the other subplots and later figures. (b): Locations of aftershocks along the fault profile with time since the El Mayor-Cucapah main shock. The location of the El Mayor-Cucapah main shock is marked by the yellow line. (c): The depths of aftershocks and later earthquakes plotted along the fault profile.

models have similar slip distributions to the other models of the El Mayor-Cucapah earthquake.

Wei et al. (2011) performed a finite-fault inversion of measurements of the 2010 earthquake including data from seismology, geodesy and remote sensing. They found that most of the main shock slip occurred on two faults striking southeast to northwest with minor slip on two smaller faults striking roughly north-south (Figure 3.3a - 3.3b). *Mendoza and Hartzell* (2013) performed a similar finite-fault inversion of teleseismic P waveforms of the 2010 earthquake. They obtained a simple slip model consisting of one fault striking southeast to northwest (Figure 3.3c - 3.3d). Both models include two patches of high slip: one patch roughly 20 km northwest of the epicentre and another patch roughly 40 km southeast of the epicentre. I attempt to examine whether the stress drops of aftershocks in regions of high slip are systematically different to the stress drops of aftershocks of regions of less slip for the 2010 El Mayor-Cucapah earthquake.

The 2010 El Mayor-Cucapah earthquake was preceded by roughly 40 M 1.5 - 4.4 foreshocks and followed by over 10,000 $M \geq$ -0.1 aftershocks (*Castro et al.*, 2011, *Hauksson et al.*, 2011, *Kroll et al.*, 2013, *Ross et al.*, 2017). The aftershocks were mostly distributed over the entire rupture area but some aftershocks occurred outside of the rupture area in the Gulf of California and north of the Mexico-U.S. border. Here I obtain the stress drops of some of these aftershocks and compare them to the post-seismic slip of the El Mayor-Cucapah earthquake.

The post-seismic slip of the 2010 El Mayor-Cucapah earthquake occurred in the same direction as the coseismic displacement (*Gonzalez-Ortega et al.*, 2014). *Gonzalez-Ortega et al.* (2014) found that the early slip near the earthquake could be explained by afterslip and estimated the distribution of post-seismic slip using Global Positioning System (GPS) data. They also observed that the post-seismic slip rate decayed with time. I contrast the decay in post-seismic slip rate with the stress drops of aftershocks to investigate how aseismic slip affects the stress drops of earthquakes.

Here I obtain stress drops of aftershocks of the 2010 El Mayor-Cucapah earthquake using the inter-station phase coherence method (*Williams et al.*, 2019). I examine the variation of stress drops of the aftershocks with moment and depth. I observe that stress drops may slightly increase with moment but do not appear to vary with depth. I also observe that the stress drops of aftershocks do not significantly change with time after the main shock. I use the phase coherence method on both the P wave and the S wave and find that the S wave is a viable alternative to the P wave.

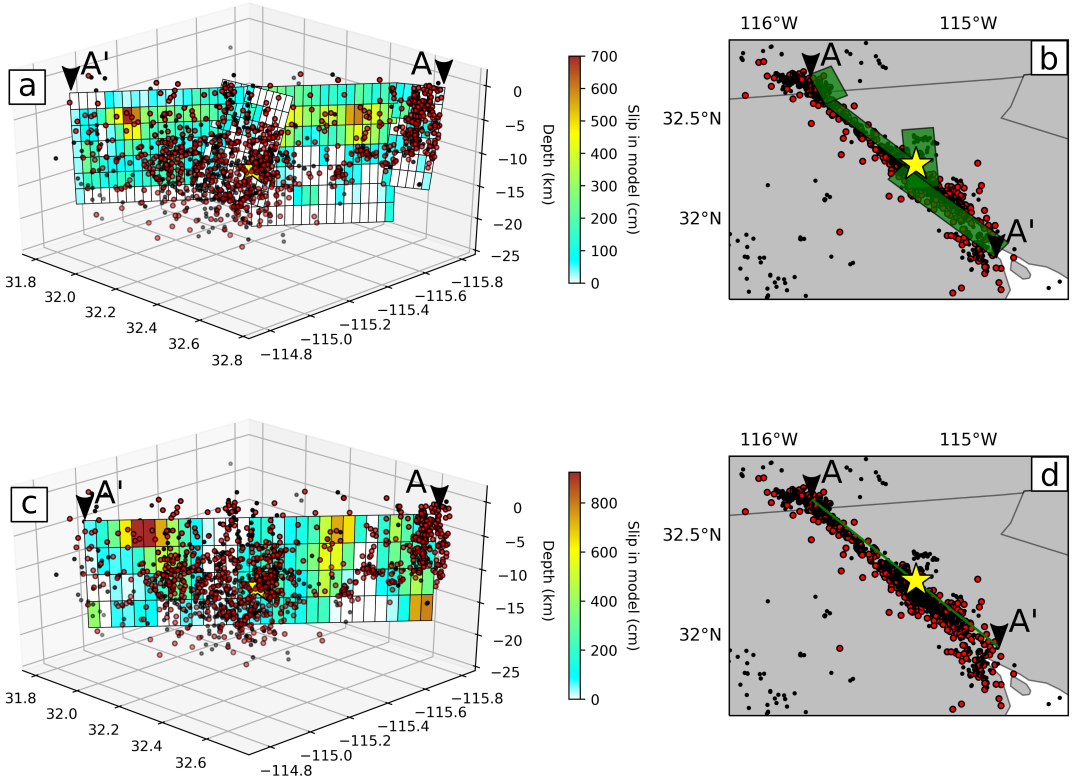

Figure 3.3: Slip models and nearby earthquakes for the 2010 El Mayor-Cucapah earthquake. Aftershocks (red circles), earthquakes which occurred between the end of the 31-day aftershock period and the 31st December 2018 (black circles), and the hypocentre of the 2010 El Mayor-Cucapah earthquake (yellow star) are plotted on the slip models of (a): *Wei et al.* (2011) and (c): *Mendoza and Hartzell* (2013). The slip of the different slip models is coloured following the colour bars to the right of the plot. The earthquakes and slip models are also plotted in map view in (b) and (d). The horizontal extent of each fault in each slip model is outlined by the green squares. The triangles marked A and A′ define the northwest and southeast extent of the slip models.

3.2 Data: Aftershocks of the 2010 El Mayor-Cucapah earthquake

I identify the aftershocks of the 2010 El Mayor-Cucapah earthquake using the Southern California Seismic Network (SCSN) earthquake catalog from 1981 to 2018, as relocated by *Hauksson et al.* (2012). This catalog includes approximately 1,250,000 earthquakes in southern California which were relocated using absolute and differential travel-time picks. Some earthquakes in this catalog were also relocated using 2-D and 3-D velocity models. I select the aftershocks of the 2010 El Mayor-Cucapah earthquake by defining a region around the main shock based on the slip models of *Wei et al.* (2011) and *Mendoza and Hartzell* (2013) (Table B.1). I select earthquakes in this region that occurred less than 31 days after the main event. I accept only $M \geq 3$ earthquakes because their data have higher signal-to-noise ratios. I thus select 948 $M \geq 3$ aftershocks (Figure 3.2). I also select 4464 $M \geq 3$ earthquakes in this region from 31 days after the main shock until the 31st December 2018 to use as reference earthquakes, which I will employ to remove the Green's function from the earthquakes of interest later in this chapter (Sec. 3.3.3).

The earthquakes in the catalog of *Hauksson et al.* (2012) have average location uncertainties of 0.75 km horizontally and 1.25 km vertically which is equivalent to a 3-D location accuracy of roughly 1.5 km. The catalog of *Hauksson et al.* (2012) shares 153 aftershocks with the catalog of *Kroll et al.* (2013). The catalog of *Kroll et al.* (2013) has smaller location uncertainties of 0.04 km horizontally and 0.12 km vertically. There is no significant shift in the average locations of aftershocks in these catalogs, so I use the more accurate locations from the catalog of *Kroll et al.* (2013) when an aftershock appears in both catalogs.

The aftershocks are recorded by over 300 stations within 4.5° distance in southern California and the surrounding areas (Figure 3.1). These stations belong to a range of networks (Table B.2) including the Southern California Seismic Network operated by the California Institute of Technology and the United States Geological Survey (USGS) and the ANZA seismic network operated by the University of California; San Diego. 90% of these stations have sampling rates of 100 Hz and a maximum resolvable frequency of 40 Hz that is significantly higher than the expected falloff frequencies of the $M \geq 3$ earthquakes examined here. I analyse both the P wave and S wave, so I use the vertical and horizontal components from each station. I use the east component as the horizontal component. Some stations have only a vertical component, so there are over 300 stations available for the P wave but fewer than 200 stations available for the S wave.

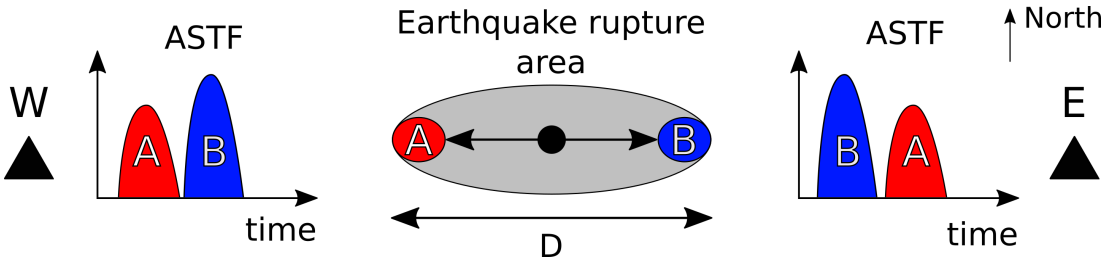

Figure 3.4: Conceptual diagram of the phase coherence method. The epicentre of the earthquake is marked by the black dot, and the rupture area is outlined by the grey oval, with the diameter of the rupture D. The earthquake ruptures bilaterally from the epicentre, ending at the rupture patches marked A (red) and B (blue) at the western and eastern ends of the rupture, respectively. The signals from each rupture patch are marked by the same colours in the apparent source time functions (ASTF) for each of the western (W) and eastern (E) stations indicated by triangles. Patch B slips more than patch A as indicated by the higher amplitude of the signal from B in the ASTFs. Note that both patches rupture at the same time. Diagram is not to scale.

3.3 Method

I use the inter-station phase coherence method to estimate stress drops of the aftershocks of the 2010 El Mayor-Cucapah earthquake. Here I outline the concept of the phase coherence method. I also describe the processing that I perform before using the method.

3.3.1 Concept of the phase coherence method

The phase coherence method uses the variation of apparent source time functions to determine the rupture extent of an earthquake (e.g., *Hawthorne and Ampuero*, 2017, *Hawthorne et al.*, 2018, *Williams et al.*, 2019). To understand how the phase coherence method works, consider an earthquake which ruptures bilaterally with two rupture patches, A and B, at the western and eastern ends of the rupture, respectively (Figure 3.4). Note that patch B has a higher amplitude signal because it contains more slip than patch A.

The arrival times of signals from each of these patches will change depending on the distance and azimuth between the patches and the recording station. Stations at opposite ends of the rupture will have the largest difference in apparent source time functions. Consider the apparent source time function (ASTF) of the eastern station (E on Figure 3.4). The signal from patch B arrives first as that patch is closest to the station. The signal from patch A arrives later because that patch is farther away from the station. The ASTF of the eastern station thus has two peaks: the larger, earlier peak of the signal from patch B and the smaller, later peak of the signal from patch A. The ASTF of the western station (W on Figure 3.4) also has two peaks, but the smaller

peak of patch A arrives earlier than the larger peak of patch B because A is closer to the station than B. The difference in the arrival time of the signals of the patches at a single station is due to the travel time of the signal across the rupture e.g. the signal from A travels across the rupture to the eastern station, and the signal from B travels across the rupture to the western station. The travel time across the rupture is the diameter of the rupture D divided by the wave propagation velocity V_W. Therefore one can estimate the diameter of the rupture by comparing the ASTFs of different stations.

The ASTFs of the eastern and western stations are similar at periods longer than the difference in travel time between the signals from A and B. The ASTFs differ at periods shorter than the difference in travel time because the signals of different patches occur at different times within the ASTFs. I measure the similarity of the ASTFs by comparing the phase between the ASTFs using the phase coherence. If I computed the phase coherence between the ASTFs at the western and eastern stations, I would observe a high coherence at periods longer than the difference in travel time. I would observe a decrease in coherence at periods shorter than the difference in travel time. This decrease in coherence occurs at a period or frequency known as the falloff frequency f_f. The falloff frequency reflects the difference in travel time between patches of an earthquake. The maximum difference in travel time between patches of an earthquake will be the travel time across the rupture. Therefore the falloff frequency can be used to estimate the rupture extent of an earthquake.

To examine the differences in ASTFs in real data, however, the ASTFs of each station must be isolated. A real earthquake signal $d_{ij}(t)$ may be modelled as:

$$d_{ij}(t) = s_{ij}(t) * g_{ij}(t), \tag{3.1}$$

where i indexes the earthquake and j indexes the station. Here $s_{ij}(t)$ is the apparent source time function of the earthquake and $g_{ij}(t)$ is the Green's function which describes the effect of the path between earthquake and recording station. To isolate the apparent source time function, the Green's function must be removed from the earthquake signal.

One approach to remove the Green's function is to use an earthquake which is co-located with the initial earthquake in an approach often referred to as the empirical Green's function approach (e.g., *Hough and Dreger*, 1995, *Mori et al.*, 2003, *Shearer et al.*, 2006, *Allmann and Shearer*, 2007, *Abercrombie*, 2014). The signal from the co-located earthquake will follow the same path to each station as the signal from the initial earthquake and thus will have the same Green's function. The phase of the Green's function can be removed by cross correlating the signal of the initial earthquake ($i = 1$) with the signal of the co-located earthquake ($i = 2$) to form the cross spectrum $\hat{x}_j$

at station j:

$$\hat{x}_j = \hat{s}_{1j}\hat{g}_j * \hat{s}_{2j}\hat{g}_j = \hat{s}^*_{1j}\hat{s}_{2j}|\hat{g}_j|^2, \tag{3.2}$$

where $\hat{s}_{1j}$ is the Fourier transform of $s_{1j}(t)$ and the frequency indexing has been dropped for readability. The Fourier transform of the Green's function $\hat{g}_j$ appears in the cross spectrum as its absolute value, so the phases of the cross spectrum depend only on the difference in phases between the apparent source time functions $\hat{s}_{1j}$ and $\hat{s}_{2j}$.

The cross spectra at different stations (j and l) can be compared to estimate the difference in phases of apparent source time functions using the inter-station phase coherence C_p:

$$C_p = \frac{2}{N(N-1)} \sum_{j=1}^{N} \sum_{l=j+1}^{N} \mathrm{Re}\, \frac{\hat{x}^*_j \hat{x}_l}{|\hat{x}^*_j \hat{x}_l|} \tag{3.3}$$

$$= \frac{2}{N(N-1)} \sum_{j=1}^{N} \sum_{l=j+1}^{N} \mathrm{Re}\, \frac{\hat{s}_{1j}\hat{s}^*_{1l}\hat{s}_{2l}\hat{s}^*_{2j}}{|\hat{s}_{1j}\hat{s}^*_{1l}\hat{s}_{2l}\hat{s}^*_{2j}|}, \tag{3.4}$$

where there are N stations and the coherence is averaged over $N*(N-1)/2$ pairs of stations. The phase coherence is computed for a range of frequencies.

The phase coherence will decrease, or fall off, when the ASTFS start to differ among stations. As noted earlier, that falloff frequency f_f is proportional to one over the travel time across the rupture of the larger earthquake of the earthquake pair. The falloff frequency can be used to obtain the diameter of the rupture D assuming a circular rupture (*Brune*, 1970). The rupture diameter is calculated using $D = F_{scal}\frac{V_W}{f_f}$ where F_{scal} is a scaling factor estimated used synthetic ruptures that calibrates the apparent falloff frequency for the azimuthal range of stations and V_W is the wave propagation velocity. With more stations in a wider azimuthal range, there will be a larger variation in ASTFs and the apparent falloff frequency will require a lower F_{scal} to estimate the rupture diameter (Sec. 3.4.4). Note that the propagation velocity of the wave V_W will depend on the velocity structure of the region of interest.

The rupture diameter can be used to estimate the stress drop $\Delta\sigma$ assuming an elliptical slip distribution (*Eshelby*, 1957):

$$\Delta\sigma = \frac{7}{16}\frac{M_0}{\left(\frac{1}{2}D\right)^3}, \tag{3.5}$$

where $\frac{1}{2}D$ is the radius of the earthquake and the moment M_0 is obtained from the magnitude of the earthquake.

I use the phase coherence method to identify variations in apparent source time

functions of the aftershocks of the 2010 El Mayor-Cucapah earthquake and thus estimate the rupture extents and stress drops of these aftershocks.

3.3.2 Initial processing of the data

Before analysing the recorded data for each event, I identify the P wave and S wave arrivals and remove data which have low signal-to-noise ratios (SNRs). I also perform some initial processing steps on the data before using the phase coherence method

I use the vertical components and east components of seismic stations to analyse the P wave and S wave, respectively. I identify the P wave and S wave arrival for each component at each station using the Akaike Information Criterion Derivative (AICD) (e.g., *Morita and Hamaguchi*, 1984) picking method from the PhasePicker module (*Chen and Holland*, 2016). Initially, the picking method uses autoregression to predict the amplitude of a signal. The Akaike Information Criterion determines the quality of the fit of the predicted amplitude from autoregression to the actual amplitude of the signal. The AICD detects changes in the quality of fit. The AICD thus identifies large differences in the predicted amplitude and the actual amplitude of a signal as are evident in the P wave arrival. The resulting arrivals appear to be accurate to within a few tenths of a second from visual inspection of traces with high SNRs.

I identify the P wave arrival using the AICD picking method on a 12-s time window filtered between 3 and 20 Hz and centred on the P wave arrival time predicted using raytracing (*Crotwell et al.*, 1999) through the iasp91 1-D Earth velocity model (*Kennett and Engdahl*, 1991). For traces where there was no detectable P wave arrival, I rerun the picking process using a lower picking threshold and a shorter time window for calculating the moving average used for autoregression. The lower threshold encourages the picking approach to pick a less clear arrival. I use the same approach to find the S wave arrival in a 24-s time window centred on the predicted S wave arrival time. I use a longer window to identify the S wave as the predicted S arrival seemed less accurate from visual comparisons with the data. I use a narrower time window for the S wave for some traces to avoid including the P wave arrival in the window.

I perform several other initial steps after picking the arrivals. I detrend each seismic trace, taper 5% of the start and end of the trace, and apply a bandpass filter between 0.05 Hz and 40 Hz. Then I correct for the instrument response and resample at 100 Hz. All initial processing is performed using ObsPy (*Beyreuther et al.*, 2010).

Note that I choose not to rotate the seismograms into the transverse component, but instead use the east component. For my work in Chapter 2, rotation of seismograms

was not important as most of the energy of the P wave that I was analysing arrives on the vertical component. However, most of the energy of the S wave will appear on the transverse component as SH energy due to the loss of energy from the SV phase through reflections and conversions at layer boundaries (e.g., *Bormann et al.*, 2002). Thus, in most cases the recorded seismograms should be rotated into a new reference frame featuring the transverse component, which is aligned in a direction perpendicular to the incoming wave. On the other hand, most of the stations I use here are to the north of the analysed earthquakes (Figure 3.7), and so the east component is roughly equivalent to the transverse component. This assumption also seems to agree with my results, with the S wave and P wave having very similar stress drops from the phase coherence method (Section 3.5.6). It is still possible, however, that the east component is different enough to the transverse component that rotation may make some difference to my results to the S wave, so in future rotation should be performed before analysing the S wave.

3.3.3 Identifying co-located earthquake pairs and aligning traces

To remove the path effects, or Green's functions, I need to identify earthquakes with similar Green's functions. I identify pairs of earthquakes as co-located if they are within some distance threshold horizontally and vertically. If I use a longer distance threshold, then I would identify more pairs of earthquakes but the Green's functions of these earthquakes may differ and reduce the falloff frequency. If I use a shorter distance threshold then the number of earthquake pairs with different Green's functions may be reduced, but the number of stress drops would also be reduced. The 1.5-km uncertainties on the locations of earthquakes in the catalog of *Hauksson et al.* (2012) also mean that using a shorter distance threshold may discard some earthquake pairs that are actually co-located. I choose to use a 2-km co-location threshold. The 2-km threshold helps mitigate the number of earthquakes with different Green's functions and is above the uncertainty of earthquake locations in the catalog, whilst also leaving enough results to interpret. Note that this co-location threshold is larger than the rupture diameters one might expect for $M \geq 3$ earthquakes. The Green's functions of the earthquake may differ and reduce the phase coherence, so the stress drops in this study should therefore be treated as lower bounds on the true stress drop.

After identifying pairs of earthquakes with similar Green's functions, I also need to make sure that the magnitudes of each earthquake in a pair are sufficiently different. If the smaller earthquake in the co-located pair has a similar magnitude to the larger earthquake, then it may also have a larger rupture extent. The falloff frequency for the earthquake pair would then describe the rupture extent of the smaller earthquake rather than that of the larger earthquake. To reduce the number of earthquake pairs

where the rupture extent of the smaller earthquake affects the falloff frequency, I accept pairs of earthquakes only when the magnitude of the smaller earthquake is 0.3 or more magnitude units smaller than the magnitude of the larger earthquake.

To increase the number of aftershocks which have viable falloff frequencies, I use earthquakes from 31 days after the 2010 El Mayor-Cucapah main shock to the 31st December 2018 as the smaller earthquakes in earthquake pairs. In total, there are 1942 co-located pairs of earthquakes which include 632 unique aftershocks. Note that a few of these pairs still have falloff frequencies which are affected by the rupture extent of the smaller earthquake (Sec. 3.4.7).

For each earthquake pair and each of the P and S wave arrivals, I align the traces of each station using normalised cross correlation. The alignment of these traces must be accurate to ensure that poor alignment does not introduce a phase shift and decrease the phase coherence. To align the traces, I first bandpass filter the traces between 3 and 20 Hz. Then I cross-correlate a 2-s window of each trace beginning 0.3 s before the arrival. The window includes 0.3 s before the arrival to allow for uncertainties in the picked arrivals. I shift the 2-s window and identify the best alignment of the traces as the shift with the highest cross correlation coefficient. I accept stations with maximum cross correlations coefficients of greater than or equal to 0.7. This cross correlation coefficient threshold should select traces which have clear arrivals. Using a cross correlation coefficient threshold also helps select earthquake pairs that have similar path effects. If the path effects of the two earthquakes are different, then the traces will differ and the cross correlation coefficient will be reduced. Also note, however, that the 3 - 20 Hz frequency band includes frequencies that are higher than the corner frequencies that one might expect for the $M \geq 3$ aftershocks. Using only earthquake pairs which have high cross correlation coefficients at these high frequencies may systematically discard dissimilar earthquakes with lower falloff frequencies and result in artificially high falloff frequencies and stress drops.

I accept stations which have high signal-to-noise ratios for specific frequency bands using an estimate of the signal fraction: $\frac{Signal}{Signal+Noise}$ (e.g. Figure 3.5b). To estimate the signal fraction, I first use a time window of the trace beginning on the arrival which includes the signal (the arrival) and the noise. I take the power spectrum of this window as an estimate of the power spectrum of the signal plus the noise. Next, I use a window before the arrival which includes only the noise. I take the power spectrum of the noise window as an estimate of the power spectrum of the noise. The contribution of the noise to the power spectrum of the arrival window is thus the ratio of the power spectrum of the noise window and the power spectrum of the arrival window, assuming that the noise is consistent for both windows. This ratio is the noise fraction $\frac{Noise}{Signal+Noise}$. The

contribution of the signal to the power spectrum is thus $1 - \frac{Noise}{Signal+Noise}$: the signal fraction $\frac{Signal}{Signal+Noise}$. A signal fraction close to one suggests that the signal contributes most the energy in the window on the arrival, and a signal fraction of zero suggests that the noise contributes most of the energy in the window.

I compute a signal fraction spectrum for each trace at each station. I use the power spectrum of a 2.3-s window beginning 0.3 s before the arrival as the signal and the power spectrum of a 2.3-s window beginning 3.6 s before the arrival as the noise. I compute the ratio of these spectra to obtain the noise fraction and the signal fraction as described above. I accept traces if the average signal fraction is more than 0.6 in the 3 - 6 Hz, 6 - 10 Hz, and 10 - 15 Hz frequency bands.

I also calculate a signal-to-noise ratio in the time domain by comparing the variance of the signal in the window beginning on the arrival with the variance of the noise window. Both windows are bandpass filtered between 3 and 20 Hz. Using a time domain signal-to-noise threshold should select clear arrivals from the dataset. I accept only traces which have a time domain-based SNR of more than 3.

Note that for the calculation of the phase coherence for the S wave, I estimated the signal to noise ratio and signal fraction of my analysis window by comparing the S wave window with the same noise window as I used for the P wave. This approach has the benefit of maintaining consistency in the signal to noise ratio calculation for both the P wave and S wave which allows direct comparison of the P wave and S wave results. On the other hand, it is possible that this approach misrepresents the actual signal to noise ratio. The P wave arrives shortly before the S wave for many of the stations I analyse, and could cause the coherence of the S wave to decrease. It therefore may make sense to treat the P wave as the noise in future work.

3.3.4 Computing the phase coherence and obtaining falloff frequencies

I use the well-aligned and high signal-to-noise ratio data identified above in the phase coherence method. The first step in the phase coherence method is to remove the path effects, or Green's functions, from the signal at each station. I remove the phase of the Green's functions from the data for each station and for each earthquake pair by computing the cross-spectra (Equation (3.2)). I select a 2.3-s window of the signal at each station beginning 0.3 s before the arrival. I taper the 2.3-s window using a multi-taper approach (e.g., *Thomson*, 1982, *Park et al.*, 1987). A multi-taper approach discards less of the signal than more conventional tapers (*Park et al.*, 1987). I compute 10 tapers or Slepian sequences (e.g., *Thomson*, 1982, *Park et al.*, 1987) using a

time half-bandwidth product of 4, which defines the frequency resolution of the tapered signal to be every 0.02 Hz. I avoid using tapers which do not taper down to zero at their edges because these tapers create steps in the tapered data which cause artificial high amplitude spectral signal at higher frequencies. I thus apply four tapers to the 2.3-s window and compute the cross spectrum for each taper. I average over the cross spectra of the tapers to obtain the cross spectrum at each station.

I compute the inter-station phase coherence C_p for each pair of earthquakes using the cross spectra of all available stations (Equation (3.4)). I use the inter-station phase coherence for each earthquake pair to pick the falloff frequency. The falloff frequency is determined by the variation in apparent source time functions. The apparent source time functions vary in response to differences in travel times for signals in the rupture (Sec. 3.3.1) which vary with azimuth. If the azimuthal range of stations is too narrow, then the variation in apparent source time functions will be small and the apparent falloff frequency may be too high to be resolved. To ensure that there is a wide variation in apparent source time functions and a resolvable apparent falloff frequency, I use a maximum of two stations in each bin of 10° azimuth. I also require that the azimuthal range of stations spans at least 120° (Sec. 3.4.4). I accept earthquake pairs with eight or more stations that pass these thresholds. An example of P wave and S wave phase coherence is shown in Figure 3.5a.

I compare the coherence profiles obtained from the data with the "synthetic noise-adjusted coherence" for each earthquake pair. The synthetic noise-adjusted coherence uses the signal fraction to estimate how much a given coherence would be reduced because of the signal-to-noise ratio. I can therefore use the synthetic noise-adjusted coherence to pick the falloff frequency. This approach avoids picking a falloff frequency where the coherence decreases due to the decrease in signal-to-noise ratio for higher frequencies.

To calculate the synthetic noise-adjusted coherence, I consider that the phase coherence contains three components: coherent signal, incoherent signal, and random noise. The coherent signal is the parts of the ASTFs that are the same between stations. The amplitude of the coherent signal can be estimated by multiplying the coherence by the signal fraction. The incoherent signal is the part of the ASTFs which vary between stations. The amplitude of the incoherent signal can be estimated by multiplying one minus the coherence by the signal fraction and a random distribution of noise. The random noise is the noise that appears in a trace and hides the signal that I want to examine and decreases the coherence through random phase shifts. The amplitude of the random noise is estimated by multiplying the noise fraction (one minus the signal fraction) by a random distribution of noise. I add hypothetical amounts of the coherent

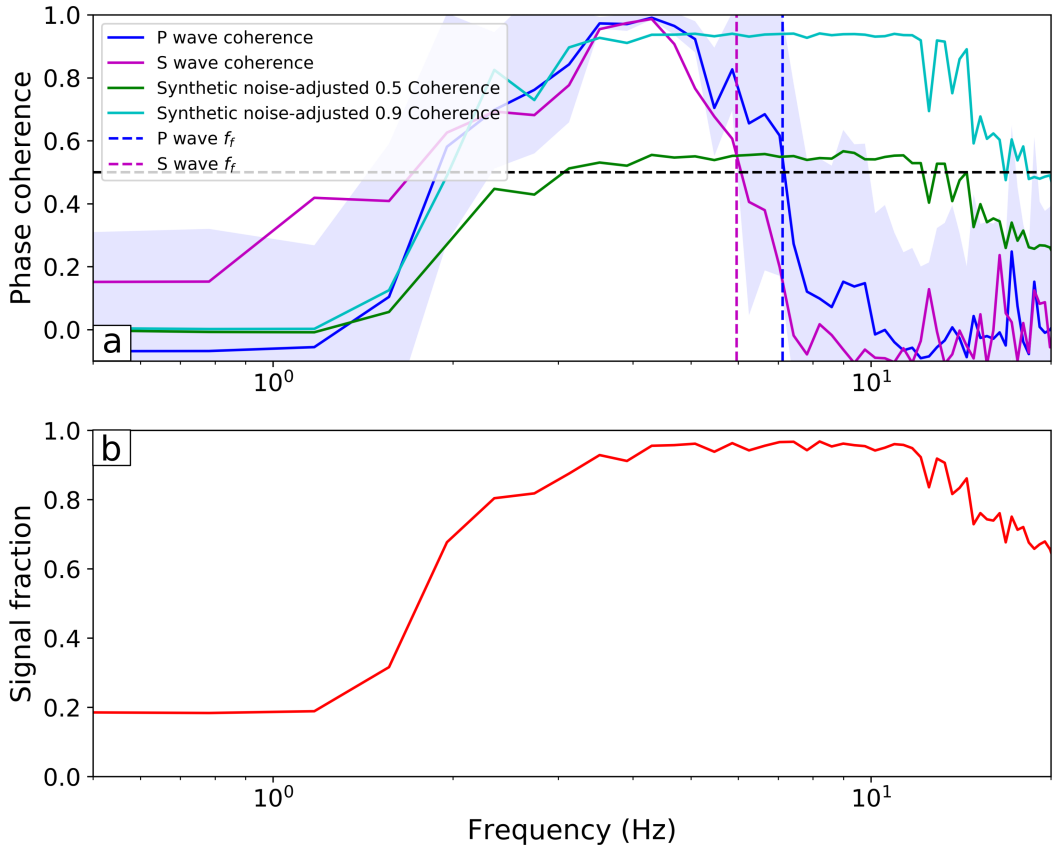

Figure 3.5: An example of the P wave and S wave coherence and the signal fraction for a M 3.83 event with a M 3.44 event. (a): Phase coherence of the P wave (blue) and the S wave (magenta). Confidence intervals on the P wave coherence estimates are indicated by the shaded blue regions. Synthetic noise-adjusted coherences are marked in cyan (adjusted coherence of 0.9) and green (adjusted coherence of 0.5). The falloff frequency obtained using the synthetic noise-adjusted 0.5 coherence for each analysed wave is marked by the blue dashed line for the P wave and the magenta dashed line for the S wave. The black dashed line illustrates a constant coherence of 0.5. (b): The signal fraction of the P wave coherence (red) for this earthquake pair.

signal, incoherent signal, and random noise together to determine the synthetic noise-adjusted coherence. I estimate the synthetic noise-adjusted coherence for a constant coherence of 0.5 and 0.9 at all frequencies using the coherence and signal fraction of each earthquake pair (e.g. Figure 3.5a).

Using the synthetic noise-adjusted coherence, I can pick a falloff frequency of an earthquake which is less biased by the change in signal-to-noise ratio with frequency. I pick the falloff frequency as the frequency at which the phase coherence decreases below the synthetic noise-adjusted 0.5 coherence. I require that the falloff frequency fulfils several conditions to minimise the effect of noise. First, I require that the falloff frequency is higher than the frequency of maximum phase coherence to prevent the

falloff frequency being picked at noisy frequencies below 2 Hz (e.g. Figure 3.5b). I also require that the next four higher frequencies above the potential falloff frequency are below the synthetic noise-adjusted 0.5 coherence to prevent the falloff frequency being picked at single frequencies with particularly low SNRs. Finally, I compute a more precise falloff frequency by interpolating the coherence between the first frequency that fulfils my requirements and the previous frequency, because the coherence is sampled only every 0.4 Hz due to the 2.3-s time window. Note that my results may be biased towards higher falloff frequencies and therefore higher stress drops because falloff frequencies below 2 Hz are usually unresolvable due to the low signal-to-noise ratio.

Comparing the synthetic noise-adjusted coherence with the observed coherence also allows earthquakes which do not have resolvable falloff frequencies to be excluded. If the observed phase coherence of an earthquake pair falls off at a similar frequency to the synthetic noise-adjusted 0.9 coherence, then the falloff frequency of that earthquake pair is controlled by the change in the signal fraction, not by the rupture extent of the larger earthquake. I visually exclude pairs where the observed coherence falls off close to the same frequency as the synthetic noise-adjusted 0.9 coherence (e.g., Figure 3.9). I perform this exclusion visually to try and reduce the number of earthquake pairs that were removed. Using an automatic threshold would remove most earthquake pairs with high falloff frequencies, and that would bias the stress drops to lower values.

I estimate 95% confidence limits on each falloff frequency by bootstrapping the stations used in the inter-station phase coherence. For each earthquake pair, I randomly select $N_{75\%}$ stations with replacement, where $N_{75\%}$ is 75% of the initial number of stations used. I recalculate the phase coherence using this new station set. I select 1000 new station sets and obtain 1000 estimates of the phase coherence. I compute the median and standard deviation of these 1000 coherence profiles at each frequency. I subtract twice the standard deviation from the median at each frequency to estimate the 2.5% confidence limit on the phase coherence and add twice the standard deviation to the median at each frequency to estimate the 97.5% confidence limit. From these limits (e.g. blue shaded regions on Figure 3.5a), I pick the 95% confidence limits on the falloff frequency of each earthquake pair. Note that I accept only earthquake pairs which have resolvable confidence limits on the falloff frequency. For example, if the 2.5% confidence limit on phase coherence for an earthquake pair does not fulfil the conditions required to pick the falloff frequency, then I do not use that earthquake pair.

3.4 Results: Falloff frequencies and stress drops

I obtain falloff frequencies f_f for earthquake pairs using the phase coherence method for both the P wave and S wave. In total, I find falloff frequencies for 272 earthquake

pairs by analysing the P wave and 171 earthquake pairs by analysing the S wave out of a possible 1942 co-located earthquake pairs.

I select the falloff frequencies from earthquake pairs and group them by the larger event in the earthquake pair. I obtain an estimate of the falloff frequency of each larger earthquake by examining the scatter of falloff frequencies for the earthquake pairs. The scatter in the falloff frequencies is caused by effects including variation in the co-location of each earthquake pair, differences in the azimuthal range of stations used, and random variations in slip distributions between earthquakes. I estimate the falloff frequency of each larger earthquake by taking the maximum of the falloff frequencies from the available earthquake pairs. I take the maximum to mitigate the reduction in falloff frequency caused by poorly co-located earthquake pairs (Sec. 3.4.2). I use the 95% confidence limits of the maximum falloff frequency as the 95% confidence limits on the falloff frequency of the earthquake. Note, however, that taking the maximum falloff frequency may bias the falloff frequency of some earthquake pairs higher than the true falloff frequency, as some of the scatter in the falloff frequency will be caused by variations in the azimuthal range of stations. If the falloff frequency is biased high, then the stress drop is also biased high. Thus my results should be considered with caution, especially for higher magnitude earthquakes with lower falloff frequencies that are more likely to be biased high by the maximum falloff frequency approach.

After computing the maximum falloff frequency, I obtain falloff frequencies for 74 earthquakes using the P wave and 51 earthquakes using the S wave. 42 earthquakes have falloff frequencies for the P and S wave.

I obtain the rupture diameter for each earthquake from the falloff frequency by computing $F_{scal}\frac{V_W}{f_f}$, where F_{scal} is a scaling factor and V_W is the wave propagation velocity. The wave propagation velocity is obtained from the 1-D models of P and S wave velocities used by *Wei et al.* (2011) in their model of the El Mayor-Cucapah earthquake (Table B.3). I select the appropriate wave propagation velocity for the depth of each earthquake being analysed. The scaling factor F_{scal} accounts for the variation in apparent source time functions resolved by the azimuthal distribution of stations. The scaling factor thus adjusts the apparent falloff frequency to reflect the true rupture diameter. I compute the scaling factor for the P wave and S wave using a representative distribution of stations and synthetic ruptures as described in Sec. 3.4.4. I obtain scaling factors F_{scal} of 1.49 and 2.32 for the P wave and the S wave respectively.

I estimate the stress drop of each earthquake using the rupture diameter and the earthquake moments (Equation (3.5)). To obtain the moment of each earthquake, I

calibrate the magnitudes of earthquakes in the catalog to moment magnitudes using the equation $M_W = 0.754M_L + 0.88$ (*Ross et al.*, 2016). I calculate the earthquake moments from these moment magnitudes. I determine 95% confidence limits on the stress drop by calculating the rupture diameter and stress drop from the 95% confidence limits on each falloff frequency.

The 95% confidence limits estimated above, however, do not account for several sources of uncertainty in the falloff frequency. These sources of uncertainty include the accuracy of trace alignment (Sec. 3.4.1), the difference in Green's functions between earthquakes (Sec. 3.4.2), the variation in focal mechanisms between earthquakes (Sec. 3.4.3), the variation in the azimuthal range of stations (Sec. 3.4.4), the inclusion of depth phases in the analysis time window (Sec. 3.4.5), the use of repeating earthquakes in earthquake pairs (Sec. 3.4.6), and the use of small earthquakes with unexpectedly large diameters (Sec. 3.4.7). I discuss each of the sources of uncertainty in the following sections. Note that the effects of some of these factors have been accounted for in my processing steps and the following sections justify some of the thresholds used in my analysis.

3.4.1 Accuracy of trace alignment

One of the most significant limitations on the phase coherence in my work on the Blanco fault was the accuracy of trace alignment (Sec. 2.6.2). Poorly aligned traces cause a decrease in the phase coherence at a frequency lower than the falloff frequency. I estimate the effect of trace alignment on coherence for the aftershocks of the El Mayor-Cucapah earthquake by estimating loop closures for each station and arrival (Sec. 2.6.2).

To understand loop closures, consider the arrival times at a single station j for three earthquakes (i = 1, 2, and 3): t_{1j}, t_{2j}, and t_{3j}. If these three earthquakes form co-located pairs with each other, the relative alignment times at station j for each pair should sum to form the loop closure $t_{loop,j}$:

$$t_{loop,j} = (t_{1j} - t_{2j}) - (t_{3j} - t_{2j}) - (t_{1j} - t_{3j}) = 0, \tag{3.6}$$

which will be close to zero if the alignment is accurate. The alignment error for each station can be estimated as $t_{loop,j}/\sqrt{3}$.

I obtain a distribution of loop closures and estimates of the alignment error for both the P and S wave (Figures B.1 - B.4). I use the estimates of the alignment error to examine the effect that the uncertainty in the alignment will have on the phase

coherence. I compute the phase coherence of an event with a copy of itself with the traces of the copy misaligned by time shifts randomly picked from the distribution of alignment errors. The coherence of an event with itself should be exactly one at all frequencies so any decrease in the coherence will be caused by the alignment uncertainty. I calculate the phase coherence of the event with itself 1000 times using 1000 randomly selected sets of time shifts. I calculate the median and standard deviation of the coherence of these 1000 estimates for each frequency. I compute the 2.5% confidence limit by subtracting twice the standard deviation from the median of the coherence at each frequency. I compute the 97.5% confidence limit by adding twice the standard deviation to the median of the coherence at each frequency. The obtained alignment uncertainty estimates are shown in Figure 3.6.

The alignment uncertainty does not appear to significantly reduce the coherence at frequencies below 20 Hz for either the P or the S wave. The falloff frequencies of the $M \geq 3$ earthquakes I examine here are likely lower than 20 Hz, so the alignment uncertainty is not a significant problem for the aftershocks of the El Mayor-Cucapah earthquake.

3.4.2 Difference in earthquake path effects

Another factor which can reduce the phase coherence is the difference in earthquake path effects. Earthquakes that are not co-located have different path effects, or Green's functions. If the Green's functions differ, then the phase coherence can be reduced at lower frequencies than the falloff frequency. It is thus important that earthquakes are co-located with similar Green's functions to prevent any effect on the falloff frequency. In Chapter 2, I assumed earthquakes within 4 km were co-located to account for the uncertainty in locations of earthquakes on the Blanco fault. In this chapter, I assume that earthquakes within 2 km are co-located because the earthquake locations in the catalog of earthquakes for southern California and Baja California are accurate to 1.5 km on average (*Hauksson et al.*, 2012).

Nonetheless, some of the earthquake pairs analysed here may be far enough apart that their Green's functions differ. If the Green's functions of the earthquakes in a pair are different, then the difference in path effects may introduce a shift in phase at a frequency which depends on the distance between the earthquakes. For example, if two earthquakes are 2 km apart then the Green's functions will be similar at wavelengths significantly longer than this distance but will begin to differ for wavelengths that are similar to this distance. The frequency f of a wavelength λ of 2 km is roughly 3 Hz using $V_P = f\lambda$ and a P wave velocity V_P of 6.16 km/s. The phase coherence of frequencies above 3 Hz thus may be reduced because of the difference in Green's functions. If the

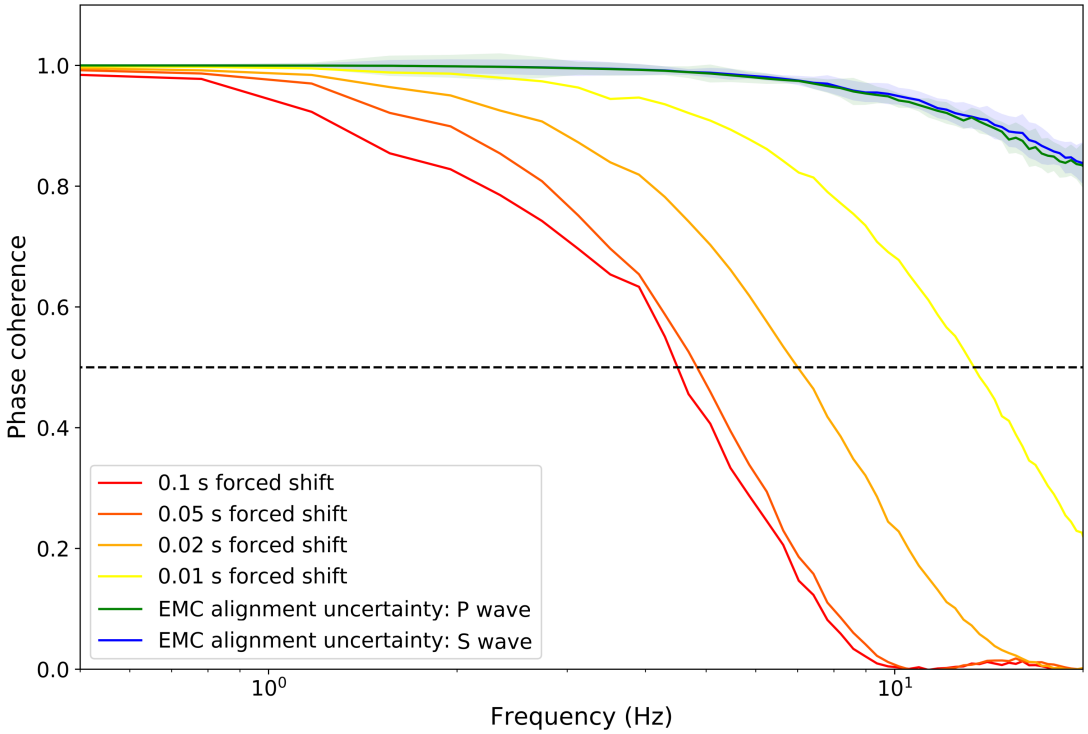

Figure 3.6: The effect of alignment uncertainty on phase coherence for the El Mayor-Cucapah (EMC) aftershocks. Forced alignment shifts from 0.01 - 0.1 s are plotted as yellow to red lines. Red lines indicate a higher forced alignment shift. The effect of alignment for the results of the P wave and S wave coherence are plotted as green and blue lines respectively. The 95% confidence intervals on the effect of alignment uncertainty for each arrival are indicated by the shaded areas of the same colour. The dashed black line indicates a constant coherence of 0.5.

phase coherence is reduced, then the falloff frequency may be reduced from its true value. I identified an example of this effect in Figure 2.7 where the falloff frequency increases with decreasing distance between earthquakes in pairs.

Due to the location uncertainty, it is difficult to tell which earthquake pairs are too far apart, so I cannot remove falloff frequencies which are biased low due to different Green's functions. Instead, I take the maximum falloff frequency available for each larger earthquake. The maximum falloff frequency should be the falloff frequency which is least affected by any reduction in phase coherence caused by a difference in Green's functions. There is no guarantee that the maximum apparent falloff frequency is the true falloff frequency, however, so the falloff frequencies obtained here should be considered lower bounds on the true falloff frequency of each earthquake.

3.4.3 Variation in focal mechanism

The focal mechanisms of earthquakes in pairs may also differ. The 2010 El Mayor-Cucapah earthquake had components of two different focal mechanisms: strike slip and normal faulting (e.g., *Wei et al.*, 2011). The presence of a complex focal mechanism for the main shock suggests that the focal mechanisms of aftershocks could vary along the fault plane. Different earthquake focal mechanisms will have different moment tensors and thus different seismograms at a particular station. The phase coherence of two earthquakes with different focal mechanisms will thus fall off at a low apparent falloff frequency even if the earthquakes are otherwise similar. I accept only earthquake pairs which are co-located within 2 km. That selection should reduce the number of pairs of earthquakes with different focal mechanisms. Note, however, that I do not know whether I have excluded all possible pairs of earthquakes where the focal mechanisms differ, so the falloff frequencies obtained here should be treated as lower bounds on the true falloff frequencies.

3.4.4 Azimuthal range of stations

To estimate a falloff frequency which corresponds to the rupture diameter of an earthquake, the azimuthal range of stations used must capture the variation of apparent source time functions caused by the rupture diameter. A narrow azimuthal range of stations (e.g. stations within 30°) will have less variation in the apparent source time functions. The apparent falloff frequency would thus require a large scaling factor to adjust it to the rupture diameter. A wider azimuthal range of stations (e.g. stations within 90°+) will have a large variation in the apparent source time functions. The apparent falloff frequency would thus require a smaller scaling factor to adjust it to the rupture diameter.

Although the aftershocks of the 2010 El Mayor-Cucapah earthquake were recorded on stations at a wide range of azimuths (Figure 3.1), these stations are concentrated in line with the strike of the main shock. Most of the stations which pass the SNR and cross correlation thresholds are within a narrow 10 - 20° azimuthal range relative to the fault strike. The apparent source time functions for stations in this narrow range are similar, so using stations mostly within this narrow range would result in high falloff frequencies that would require a high scaling factor to calibrate them to the rupture diameter. The high apparent falloff frequencies would also be unresolvable for this dataset due to the decrease in SNR for higher frequencies (e.g. Figure 3.5b). To increase the variation in apparent source time functions and reduce the apparent falloff frequencies, I allowed a maximum of two stations in each bin of 10° azimuth. I also required that each earthquake pair had a range of stations spanning 120° azimuth.

I estimate the scaling factor F_{scal} which calibrates the apparent falloff frequency for the azimuthal distribution of stations using a representative distribution of stations. To estimate the representative distribution of stations, I separate stations into 10° azimuthal bins for each analysed pair of earthquakes. The azimuths of the stations are estimated relative to the strike of the fault which is roughly 45° anticlockwise from north. For each azimuthal bin, I determine the percentage of earthquake pairs which have stations in the bin. I accept azimuthal bins where at least 50% of the earthquake pairs have stations. For each bin, I select the most commonly used stations until I have the median number of stations for the bin. I combine the stations from each bin to form the representative azimuthal distribution of stations. I do not allow stations to appear multiple times in the representative distribution. The representative station distribution for the results of the P wave is wider than the results of the S wave and is more evenly distributed in azimuth (Figure 3.7). The wider and more even distribution of stations for the P wave suggests that the P wave will require a lower scaling factor than the S wave to calibrate the apparent falloff frequencies to correspond to the rupture diameter.

After obtaining the representative distribution of stations, I pick a representative earthquake location at the northwestern end of the El Mayor-Cucapah rupture (black star on Figure 3.7) which represents the location of the majority of the earthquakes with resolvable stress drops. I recalculate the azimuths and estimate take-off angles of the distribution of stations relative to this earthquake location. I use these azimuths and take-off angles to estimate the scaling factor.

To estimate the scaling factor for the representative azimuthal distribution of stations, I create a series of synthetic ruptures with varying radii using the same approach as *Hawthorne et al.* (2018). The synthetic ruptures have heterogeneous slip distri-

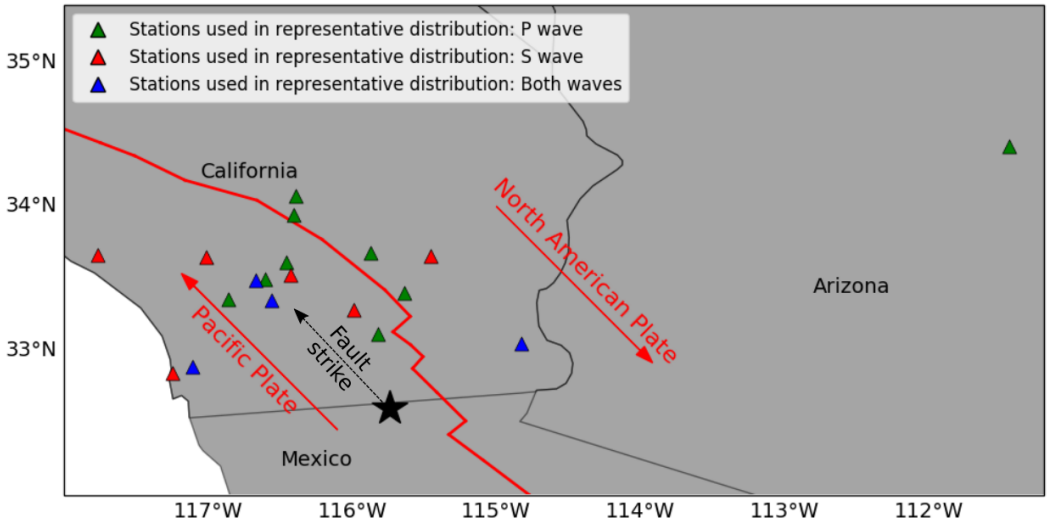

Figure 3.7: Representative stations distributions for the results of the P wave and S wave. The representative distribution of stations for the results of the P wave are indicated by green triangles. The representative distribution of stations for the results of the S wave are indicated by red triangles. Stations that appear in the representative distribution of stations for both the P wave and the S wave are indicated by blue triangles. The location of the earthquake chosen to represent the majority of my results is denoted by the black star. U.S. states are outlined by the grey lines. A rough tectonic plate boundary is drawn in red with relative plate motions annotated. A rough fault strike is shown by the dashed arrow.

butions and rupture bilaterally at a rupture speed equivalent to 90% of the S wave velocity. For each point on the slip distribution, the travel time to each station in the representative station distribution is computed using the wave propagation velocity. I use a propagation velocity of 6.16 km/s for the P wave and 3.56 km/s for the S wave which are average velocities for the 1-D velocity model used by *Wei et al.* (2011) in their model of the 2010 El Mayor-Cucapah earthquake (Table B.3). The resulting travel times produce varying apparent source time functions at each station depending on the azimuth and take-off angle of the signal to the station. A synthetic Green's function is also added to the signal at each station by convolving the apparent source time function with a series of random values picked from a normal distribution. This convolution produces traces for each synthetic rupture at each station. The cross spectrum is then estimated between the traces for each synthetic rupture and another synthetic rupture with a smaller radius at each station. These cross spectra are used to calculate the inter-station phase coherence. Finally, the apparent falloff frequency for each synthetic rupture is estimated from the phase coherence.

I estimate the apparent falloff frequency for 100 synthetic ruptures with diameters of 600 - 4000 m. I compare the apparent falloff frequency with the actual rupture diameter. The difference between the apparent falloff frequency and the actual rupture diameter

indicates the scaling factor F_{scal} that must be applied to calibrate the apparent falloff frequencies to the true diameter for these ruptures. I find scaling factors of 1.49 and 2.32 for the representative stations distributions of the P wave and S wave analysis, respectively (Figures 3.8 and B.5). These factors are similar to those obtained in previous work (e.g., *Hawthorne et al.*, 2018, *Williams et al.*, 2019).

3.4.5 Depth phases in the analysis window

One of the sources of uncertainty I considered for the Blanco fault was the arrival of depth phases in the analysed time window (Sec. 2.6.6). Depth phases feature the same source time function as the main arrival, and the variation in relative arrival time between the depth phases and the main arrival may produce differences in phase between apparent source time functions and thus reduce the phase coherence. In Chapter 2, I prevented depth phases decreasing the phase coherence by using stations that were 175 - 800 km from the earthquakes on the Blanco fault. The depth phases for stations in this distance range had constant relative arrival times to the P wave arrival and thus did not cause a phase shift and the associated decrease in coherence.

Here I analyse P and S waves and use a shorter 2.3-s time window starting 0.3 s before the arrival. I test whether depth phases that arrive immediately after the P and S wave will arrive in the 2.3-s window, and whether these depth phases will have varying relative arrival times that will reduce the phase coherence. I calculate synthetic arrival times for the pP, sP, pS, and sS depth phases using TauP (*Crotwell et al.*, 1999) and the velocity model for the region around the El Mayor-Cucapah earthquake from *Wei et al.* (2011) (Table B.3). I find that the pP and sP depth phases arrive in the 2.3-s time window after the P wave arrival for earthquakes shallower than 6 km. The pS depth phase does not arrive in the 2.3-s window after the S wave arrival for any earthquakes shallower than 20 km and stations within 500 km. The sS depth phase arrives within the 2.3-s window after the S wave arrival for earthquakes shallower than 6 km. For the pP, sP and sS depth phases, the relative arrival times of the depth phases vary compared to the associated main arrival for stations that are less than 175 km away. The variation in these relative arrival times may reduce the phase coherence.

The variation in relative arrival times of the depth phases affects approximately 50% of the stations in my analysis because the stations are less than 175 km from the El Mayor-Cucapah aftershocks. These stations tend to have high signal-to-noise ratios because of their proximity to the earthquakes, so I cannot discard the closer stations without compromising the number of falloff frequencies I obtain. Since I choose not to discard closer stations, the depth phases may reduce the phase coherence for earthquakes shallower than 6 km. However, I observe no systematic difference in falloff

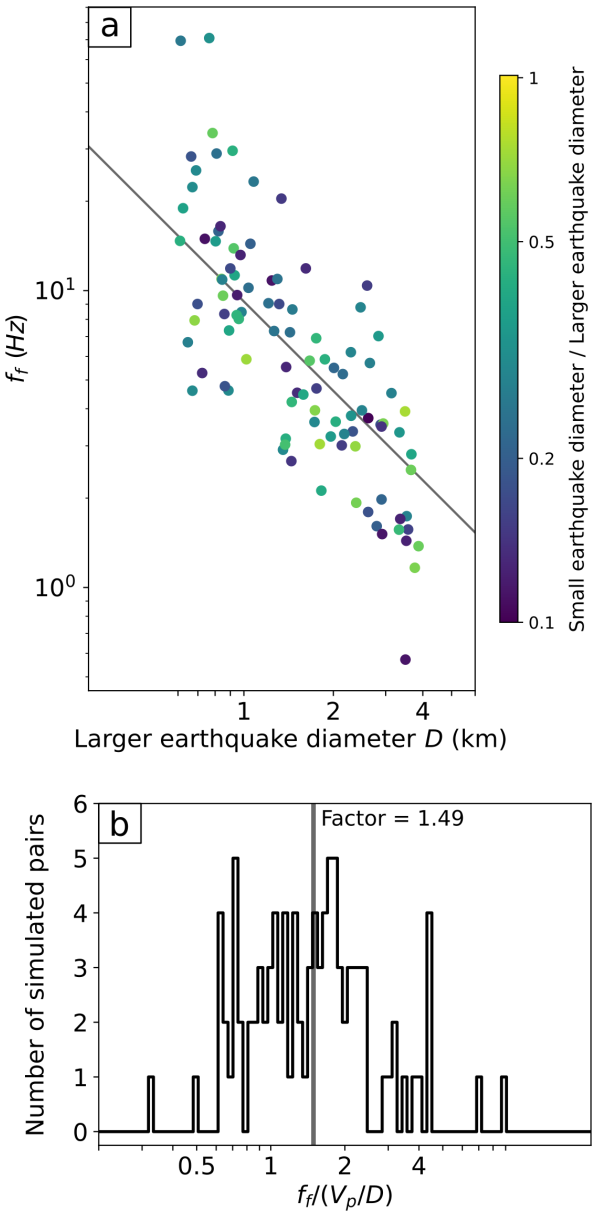

Figure 3.8: The effect of the representative station distribution on synthetic falloff frequencies of varying earthquake radii for the P wave. The representative station distribution is picked as described in the text. (a): Synthetic falloff frequencies for different earthquake diameters. Points are coloured by the ratio of the diameters of the smaller and larger earthquakes in the pair. The grey line is the log-log fit for the change in synthetic falloff frequencies with diameter. (b): Histogram of the factor F_{scal} required to obtain the actual rupture length from the apparent falloff frequency of each synthetic earthquake. The grey line indicates the median factor of the histogram, which is 1.49 for the P wave.

frequency with earthquake depth (Figure B.6) which suggests that depth phases do not have a significant effect on the phase coherence for this dataset.

3.4.6 Repeating earthquakes

The falloff frequency of the phase coherence of some earthquake pairs may not reflect the rupture extent of the larger earthquake of the pair. For example, some co-located earthquakes may be repeating earthquakes. Repeating earthquakes rupture the same patch of the fault with near-identical slip distributions (Sec. 1.4). If the slip distributions are near-identical, then the signals from each point on the slip distribution will arrive at roughly the same time for each earthquake at each station. The apparent source time functions (ASTFs) of each earthquake at each station will therefore be near-identical, and the variation of ASTFs of each earthquake will also be near-identical. The difference in phase of the ASTFs of each earthquake will thus be almost constant for all stations. The inter-station phase coherence method measures variation in these differences in phase between stations, so a non-varying phase difference between stations will cause high coherence at high frequencies. The falloff frequency of the phase coherence will therefore not relate to the rupture extent of the larger earthquake.

One can observe examples of the effect of repeating earthquakes where one larger earthquake has multiple earthquake pairs. The phase coherence spectra for a larger earthquake using several smaller earthquakes is shown in Figure 3.9. The pairs with high falloff frequencies (blue lines) are possible pairs of repeating earthquakes. The coherence of these pairs falls off at a high frequency, and that falloff may reflect the decrease in signal fraction. The pairs with lower falloff frequencies (green lines) are normal pairs of earthquakes which fall off at a lower frequency than the signal fraction. Falloff frequencies obtained from repeating earthquake pairs do not represent the rupture extent of the larger earthquake, so I visually exclude them from my analysis by comparing the phase coherence with the synthetic noise-adjusted 0.9 coherence (Sec. 3.3.4). Note that visually excluding earthquakes with falloff frequencies that match the signal fraction will preferentially exclude earthquakes with high falloff frequencies and high stress drops.

3.4.7 Smaller earthquakes with large rupture extents

I identified earthquake pairs where the smaller earthquakes have 0.3 units or more smaller magnitudes than the magnitude of the larger earthquake. The magnitude depends on the moment M_0 of an earthquake, which in turn depends on the shear modulus μ, the rupture area A, and the averaged slip on the fault due to the earthquake $\tilde{\delta}$ following $M_0 = \mu A \tilde{\delta}$. Therefore, a lower magnitude earthquake can have a larger rupture

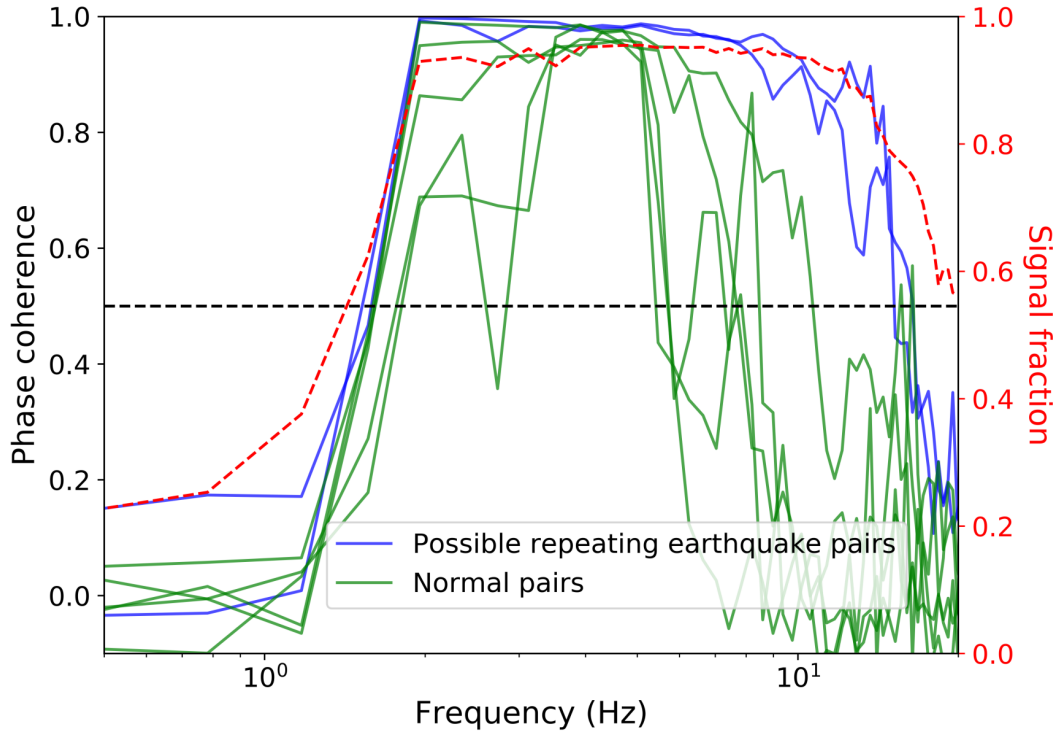

Figure 3.9: S wave coherence for a M 3.68 earthquake with smaller M 3.05 - 3.5 earthquakes. The average signal fraction is plotted as a red dashed line. A constant coherence of 0.5 is shown by the black dashed line. The coherence spectra shown in blue have much higher falloff frequencies than most of the earthquake pairs, and therefore could be repeating earthquakes. The spectra shown in green have relatively consistent falloff frequencies which are lower than the falloff frequencies of the blue spectra.

extent than a higher magnitude earthquake if the slip varies significantly between the two earthquakes. If the lower magnitude earthquake has a larger rupture extent, then the falloff frequency of the phase coherence between these events will reflect the rupture extent of the lower magnitude event rather than the higher magnitude event.

I observe several cases in my analysis where the smaller earthquake in a pair has a longer rupture extent than the larger earthquake. For example, Figure 3.10 includes phase coherence spectra for several earthquake pairs for a single larger earthquake. Most of the spectra have falloff frequencies higher than 10 Hz, but one earthquake pair has a lower falloff frequency of roughly 6 Hz. The difference between the falloff frequency of this earthquake pair and the falloff frequencies of the other pairs suggests that the lower falloff frequency does not correspond to the rupture diameter of the supposedly larger earthquake.

I visually exclude pairs with particularly low falloff frequencies compared to other earthquake pairs with the same larger earthquake. Removing the pairs with particular low falloff frequencies is difficult to automate because the falloff frequency of an earthquake will vary by a few tens of percent due to variations in the azimuthal range of stations for different earthquake pairs or due to complexity in the slip distribution. Excluding pairs where the smaller earthquake has a longer rupture extent is also impossible to do if a larger earthquake has only one or two co-located earthquakes. The falloff frequencies of earthquakes with few pairs should thus be considered with caution.

3.4.8 Summary of steps to account for the effect of uncertainties on stress drops

In the above sections, I identified several sources of uncertainty in the estimated falloff frequencies. I estimated the alignment uncertainty from the aligned traces and found that the observed falloff frequencies should not be affected by the alignment (Sec. 3.4.1). I also discussed how different Green's functions between earthquakes can decrease the coherence (Sec. 3.4.2). I use a co-location threshold of 2 km which should reduce the number of earthquake pairs where the difference in Green's functions is a problem. I also take the maximum falloff frequency to obtain a falloff frequency as close to the true falloff frequency as possible for earthquakes where the difference in Green's functions may be a problem. The co-location threshold of 2 km also helps mitigate any possible cases of earthquakes pairs having different focal mechanisms (Sec. 3.4.3). I encouraged a wider azimuthal range of stations with a wide variation in apparent source time functions by allowing only two stations per 10° bin of azimuths. I also required that each earthquake pair has an azimuthal range of stations that spans at least 120° (Sec. 3.4.4). I determined scaling factors using synthetic ruptures of 1.49 and 2.32 for

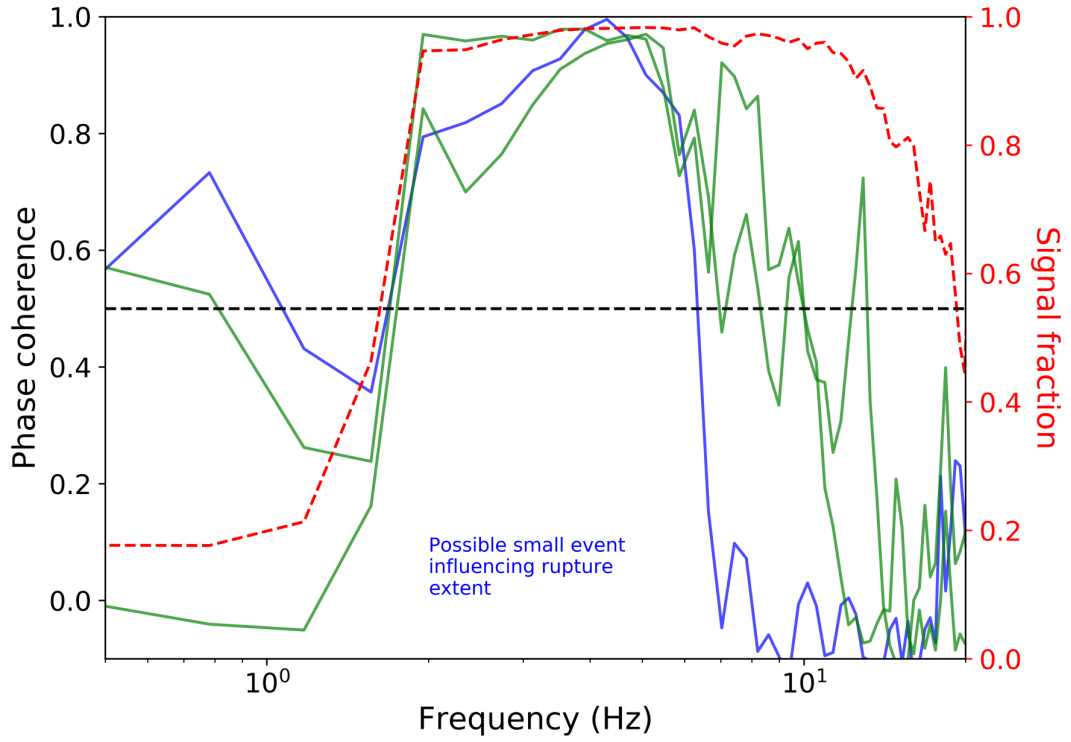

Figure 3.10: S wave coherence for a M 3.37 earthquake with smaller M 3.0 - 3.1 earthquakes. The average signal fraction is plotted as a red dashed line. A constant coherence of 0.5 is plotted as the black dashed line. The phase coherence of the larger earthquake with the M 3.0 earthquake plotted in blue has a lower falloff frequency than the other earthquake pairs.

the P and S waves, respectively. I identified that depth phases do not appear to reduce the phase coherence for this study (Sec. 3.4.5)

I also examined how variations in the rupture extent of the smaller earthquake may affect the falloff frequency of the larger earthquake in the earthquake pair. I visually excluded any examples where repeating earthquakes appeared to significantly increase the falloff frequency of a larger earthquake by looking at the consistency of falloff frequencies among earthquake pairs (Sec 3.4.6). I also visually excluded earthquake pairs where an unexpectedly long rupture length of the smaller earthquake in the pair appeared to affect the falloff frequency (Sec. 3.4.7). Generally, I found that the effects of some of the sources of uncertainty described above indicate that the falloff frequencies in this study are lower bounds on the true falloff frequency.

After imposing the azimuthal range thresholds, taking the maximum falloff frequency for each larger earthquake, and visually excluding earthquake pairs where the coherence appears to be affected by the rupture extent of the smaller earthquake in the pair, I determine the final falloff frequencies and stress drops. I discuss these falloff frequencies and stress drops in the following section.

3.5 Discussion

I examined the stress drops of aftershocks of the 2010 M_W 7.2 El Mayor-Cucapah earthquake using the phase coherence method. Here I discuss these stress drops and examine how they vary with different earthquake properties and with aseismic slip. I also compare the results of the phase coherence method using the P wave and the S wave, and I evaluate whether the S wave is a viable alternative to the P wave.

3.5.1 Computing the median stress drop

I obtain falloff frequencies and stress drops for 74 M 3.4 - 4.7 earthquakes using the phase coherence method on the P wave (Figure 3.11). I estimate median falloff frequencies and stress drops for each 0.2 magnitude unit bin. I also estimate 95% confidence limits for each median. To estimate the 95% confidence limits on the median falloff frequency, I select each earthquake in the magnitude bin. I then randomly select a falloff frequency for each earthquake from the 1000 estimates obtained earlier by bootstrapping stations. I recompute the median falloff frequency using the selected falloff frequencies for each earthquake. I repeat this 1000 times to obtain 1000 realisations of the median falloff frequency of the magnitude bin. I then take the 2.5% and 97.5% confidence limits from these 1000 realisations to represent the uncertainty on the

median falloff frequency.

For the median stress drops in each magnitude unit bin, I use the same process as above but calculate the stress drop using each randomly selected falloff frequency from each earthquake. I then recompute the median stress drop. I repeat this 1000 times and obtain 1000 realisations of the median stress drop. I pick the 2.5% and 97.5% confidence limits in the median stress drop from these 1000 realisations. I use this approach to calculate the median stress drops in all the following analyses.

I use the process above to estimate the median stress drop of all the aftershocks of the El Mayor-Cucapah earthquake used in the phase coherence method. I find a median stress drop of 1.7 MPa, with 95% confidence limits of 1.2 MPa and 2.2 MPa. The median stress drop is similar to the median stress drop of 1.57 MPa estimated by *Shearer et al.* (2006) in their large scale study of earthquakes throughout southern California, but it is lower than the median stress drop for other studies of strike slip faults in California (e.g., *Jones and Helmberger*, 1998, *Mori et al.*, 2003, *Allmann and Shearer*, 2007, *Hardebeck and Aron*, 2009, *Abercrombie*, 2014). The median stress drop is also lower than the 5.62 MPa average stress drop estimated by *Chen and Shearer* (2013) for the first five days of El Mayor-Cucapah aftershocks, and it is lower than the 3.54±0.64 MPa global average stress drop for continental strike slip faults estimated by *Allmann and Shearer* (2009).

Although the median stress drop estimated here appears to be lower than many previous estimates, it is important to remember that I obtain lower bounds on the stress drops of earthquakes and therefore might expect a systematically lower stress drop. It is also difficult to compare absolute values between studies because of possible differences in assumptions. The studies cited above use spectral corner frequency-based methods to estimate the stress drops of earthquakes. The stress drops from spectral corner frequency-based methods depend strongly on the rupture velocity, whereas the stress drops from the phase coherence method depend strongly on the wave propagation velocity. The rupture velocity is usually assumed to be 75 - 90% of the S wave velocity (e.g., *Madariaga*, 1976, *Shearer et al.*, 2006, *Allmann and Shearer*, 2007, *Hardebeck and Aron*, 2009, *Abercrombie*, 2014, *Abercrombie et al.*, 2017) and is not validated by modelling the earthquakes. These rupture velocities may not be accurate given the possibility of earthquakes with rupture velocities faster than the shear wave velocity (e.g. *Xia et al.*, 2004, *Bouchon et al.*, 2001, *Robinson et al.*, 2006) and earthquakes with particularly low rupture velocities (e.g., *Kanamori and Stewart*, 1976, *Okal and Stewart*, 1982, *Pérez-Campos et al.*, 2003). On the other hand, the wave propagation velocity is known to within 10%. The difference in median stress drop between this study and previous studies could be partially due to inaccurate rupture velocities in

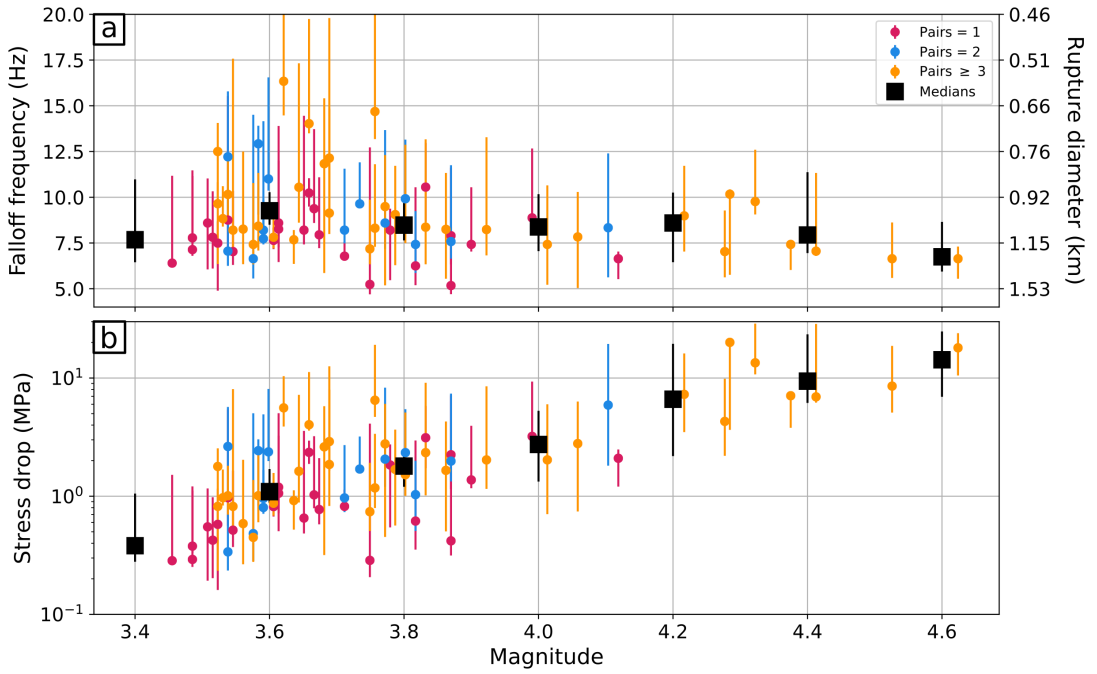

Figure 3.11: Falloff frequencies (a) and stress drops (b) against magnitude of aftershocks of the 2010 El Mayor-Cucapah earthquake using the P wave. The points are coloured by the number of pairs used to obtain the maximum falloff frequency as described in the legend. The error bars on each point are 95% confidence limits on each falloff frequency and stress drop estimated by bootstrapping stations. Median falloff frequencies and stress drops in 0.2 magnitude unit bins are plotted as black squares. The error bars on these medians are 95% confidence limits computed as described in the text.

previous studies. It is also possible that the phase coherence method obtains a more accurate rupture extent than spectral corner frequency-based methods, which I discuss in further detail in Sec. 5.3.1.

3.5.2 Dependence of stress drops on moment

The falloff frequencies decrease slightly with increasing earthquake magnitude. Such a decrease is expected as the rupture extent should increase with magnitude. However, the falloff frequency does not decrease as much as one might expect assuming that the rupture extent rapidly increases with magnitude (*Wells and Coppersmith*, 1994), so the stress drops appear to increase with magnitude and therefore moment (Figure 3.11b). This moment dependence differs from the lack of dependence observed by most studies (e.g., *Abercrombie*, 1995, *Mori et al.*, 2003, *Shearer et al.*, 2006, *Allmann and Shearer*, 2007, 2009, *Chen and Shearer*, 2011, *Uchide et al.*, 2014, *Cocco et al.*, 2016, *Abercrombie et al.*, 2017). I observed a similar increase in stress drops with moment in Chapter 2 but attributed that slight moment dependence to the narrow resolution band of falloff frequencies created by the poor alignment accuracy and low frequency

noise. It is possible that the moment dependence observed here is also artificially created. I use a co-location threshold of 2 km which may allow earthquakes pairs that have different Green's functions. These pairs will have decreased phase coherence and a lower apparent falloff frequency. The falloff frequencies of lower magnitude earthquakes are more likely to be reduced because of their generally higher true falloff frequencies. Thus, the low co-location threshold may create an artificially shallow dependence of falloff frequency on magnitude and therefore the increase of stress drop with magnitude. It is also possible that the apparent moment dependence of stress drops is coincidental. I find stress drops for only 12 $M > 4$ earthquakes, and the stress drops for these earthquakes could be coincidentally high. More stress drops and further work are required to test whether the moment dependence of stress drops is robust.

3.5.3 Dependence of stress drops on depth

I also examine the variation in the stress drops of aftershocks of the 2010 El Mayor-Cucapah earthquake with depth. Many previous studies observe that stress drops increase with the earthquake depth (e.g., *Jones and Helmberger*, 1996, *Hardebeck and Hauksson*, 1997, *Shearer et al.*, 2006, *Allmann and Shearer*, 2007, *Baltay et al.*, 2011, *Chen and Shearer*, 2013, *Oth*, 2013, *Uchide et al.*, 2014, *Goebel et al.*, 2015, *Chen and McGuire*, 2016), but some studies observe no dependence of stress drops on depth (e.g., *Jin et al.*, 2000, *Kinoshita and Ohike*, 2002, *Mori et al.*, 2003, *Allmann and Shearer*, 2009, *Abercrombie et al.*, 2017, *Goebel et al.*, 2017, *Wu and Chapman*, 2017). Some studies suggest that the increase of stress drop is artificial and can be removed by accounting for the increase in S wave velocity and therefore rupture velocity with depth (e.g., *Allmann and Shearer*, 2009, *Abercrombie et al.*, 2017, *Goebel et al.*, 2017). Increasing the rupture velocity reduces the rupture extent, so increasing the rupture velocity with depth will account for the increase in stress drop with depth. Here I account for the increase in wave propagation velocity with depth by varying the propagation velocity used to obtain the rupture diameter and the stress drop. I choose the wave propagation velocity for each earthquake based on the depth of the earthquake and the velocity model used by *Wei et al.* (2011) in their slip model of the El Mayor-Cucapah earthquake (Table B.3).

To test whether the depth dependence of stress drops changes using a depth-varying wave propagation velocity, I also estimate stress drops using a constant average wave propagation velocity of 6.16 km/s (Figure 3.12a). I compare these stress drops with the stress drops estimated using a depth-varying wave propagation velocity (Figure 3.12b). I estimate a log-linear line of best fit for the change in median stress drops with depth for each subplot using an L2-norm. Using a constant average velocity, I observe a slight increase in stress drops with depth. Using a depth-varying velocity, I observe a decrease

in stress drops with depth. The change in the depth dependence of stress drops using different velocity models does not agree with previous results which observed a uniform stress drop using a depth-varying velocity. The change in dependence may suggest, however, that using a depth-varying velocity is important as it will significantly alter the stress drops of earthquakes.

The decrease in stress drops with depth observed here differs from the increase in stress drops with depth that many previous studies observe (e.g., *Jones and Helmberger*, 1996, *Hardebeck and Hauksson*, 1997, *Shearer et al.*, 2006, *Allmann and Shearer*, 2007, *Baltay et al.*, 2011, *Chen and Shearer*, 2013, *Oth*, 2013, *Uchide et al.*, 2014, *Goebel et al.*, 2015, *Chen and McGuire*, 2016) and differs from what one might intuitively expect. From physical intuition, one might expect the stress drops to increase with depth as the normal stress increases. If the normal stress increases, then the frictional strength will also increase. Thus the stress drop should increase with depth. I do not observe an increasing stress drop with depth which suggests that the stress drop is not controlled by the change in the normal stress.

The decrease in stress drop with depth could reflect the change in seismic coupling. One might expect the coupling to decrease with depth as the temperature increases and the crust behaves more ductilely. Perhaps the stress drops decrease following the same relation between stress drops and coupling that I observed for the earthquakes on the Blanco fault in Chapter 2. On the other hand, *Kuna et al.* (2019) observed no change in the stress drops between the more coupled crust and the less coupled mantle for earthquakes on the Blanco fault. Their results suggest that the change in coupling with depth does not have a strong effect on the stress drops of earthquakes.

It is also possible that the depth dependence of stress drops simply reflects the change in the number of resolvable earthquakes with depth. The three deepest median stress drops use only one earthquake each. A single earthquake does not accurately represent the average stress drop. Indeed, excluding these three medians would likely result in a relatively constant stress drop with depth. The change in median stress drops with depth also appears to be directly related to the change in earthquake magnitude for each depth bin. The relative variation of median stress drops with depth is strikingly similar to the change in average earthquake magnitude for each bin (Figure 3.13).

I also estimate 95% confidence limits on the slope of the line of best fit for the depth-independent and depth-dependent velocity plots. To estimate 95% confidence limits on the gradient of this line of best fit, I randomly select a median stress drop for each bin from the 1000 estimates used to estimate the 95% confidence limits on the median. I then compute the line of best fit for these new medians. I repeat this 1000 times to

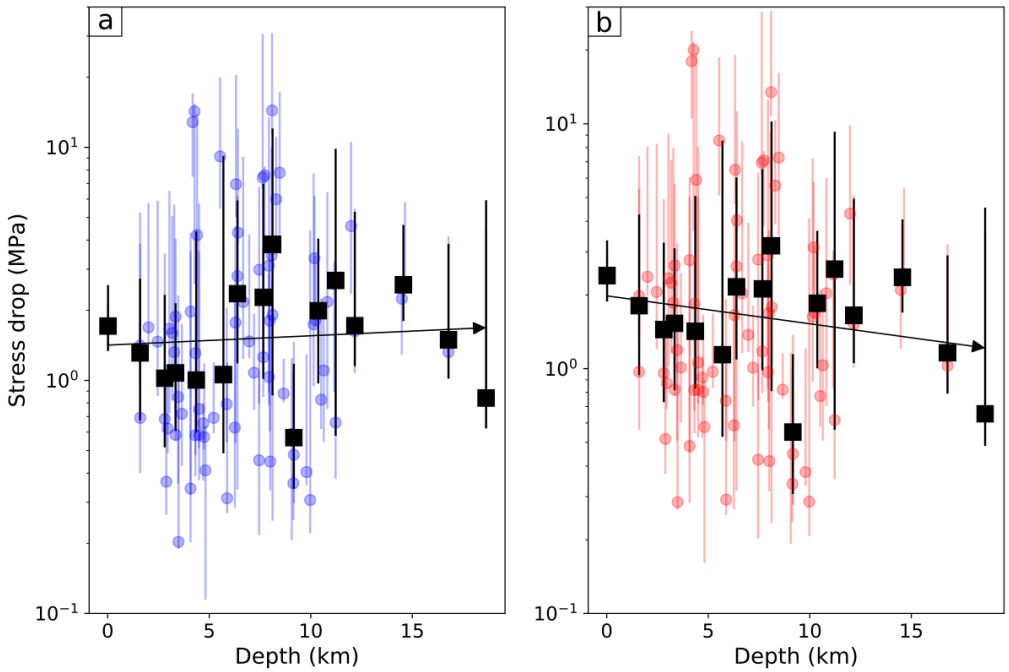

Figure 3.12: Stress drops of El Mayor-Cucapah aftershocks versus depth where the P wave velocity used for each earthquake is (a): constant at 6.16 km/s which is the average P wave velocity from the velocity model of *Wei et al.* (2011) and (b): increases with depth following the velocity model used by *Wei et al.* (2011) (Table B.3). Error bars on the stress drops indicate 95% confidence limits estimated by bootstrapping stations. These stress drops were obtained by analysing the P wave. Median stress drops in 2 km depth bins are plotted as black squares. The error bars on these medians are 95% confidence limits. The median stress drops and 95% confidence limits are calculated using the approach described in the main text. The fitted black arrows show the trend of increasing stress drop with increasing depth for (a), and decreasing stress drop with depth for (b).

obtain 1000 estimates of the gradient and obtain 95% confidence limits on the gradient. I observe 95% confidence limits on the log-linear slope of the depth-independent velocity stress drops with depth of -0.008 and 0.024. I observe 95% confidence limits on the log-linear slope of the depth-dependent velocity stress drops with depth of -0.024 and 0.011. Clearly, the trends for the stress drops using depth dependent and depth-independent velocities are poorly resolved. Considering the poorly resolved median stress drops at depth, the effect of earthquake magnitude on the average stress drop in each depth bin, and the poorly resolved slopes of the change of stress drop with time, the depth dependence of stress drops for the aftershocks of the El Mayor-Cucapah earthquake is not well-resolved and I do not discuss it further in this chapter.

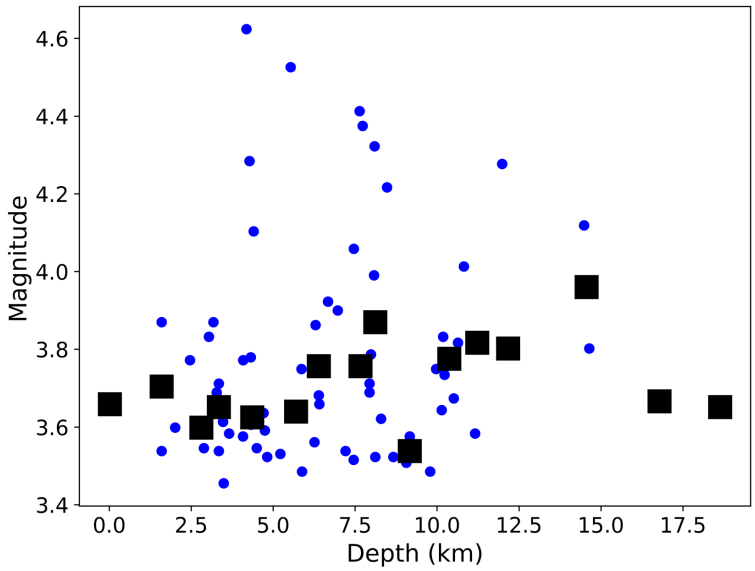

Figure 3.13: Magnitudes of earthquakes analysed using the P wave versus depth (blue circles). Black squares are median depths and magnitudes in depth bins of 2 km.

3.5.4 Spatial variation of stress drops

The low number of results also affects my ability to examine the spatial variation of stress drops. Here I attempt to compare the median stress drops for each segment of the slip model of *Wei et al.* (2011), but the majority of my results are located on the northwestern end of the El Mayor-Cucapah rupture (Figure 3.14). There are few earthquakes to the southeast which have viable falloff frequencies because of their lower signal-to-noise ratios and narrow azimuthal ranges of stations. Still, I calculate the median stress drops using the approach in Sec. 3.5.1. I allow only earthquakes that are within the region of the slip model which I define as latitudes south of 32.73° and longitudes east of -115.8°. I assign each earthquake to the closest segment. I calculate a median stress drop of 1.8 MPa (95% confidence limits of 0.9 and 3.6 MPa) for the 2 earthquakes on Segment 1 on Figure 3.14. There are no events on Segment 2. I calculate a median stress drop of 2.0 MPa (1.0, 3.4) for the 12 earthquakes on Segment 3. Finally, I calculate a median stress drop of 1.8 MPa (1.2, 2.6) for the 39 earthquakes on Segment 4. There is no clear variation in the median stress drop along the fault. On the other hand, there are only 14 earthquakes on the more southeastern segments of the slip model, so the lack of variation in median stress drops along the fault is not robust. A larger number of stress drops would be required in order to assess the spatial variation in stress drops.

The lack of viable stress drops on the southeastern section of the rupture means I cannot look for the change in the stress drops of aftershocks with the slip of the main shock. The stress drops that I do obtain are also almost exclusively for earthquakes

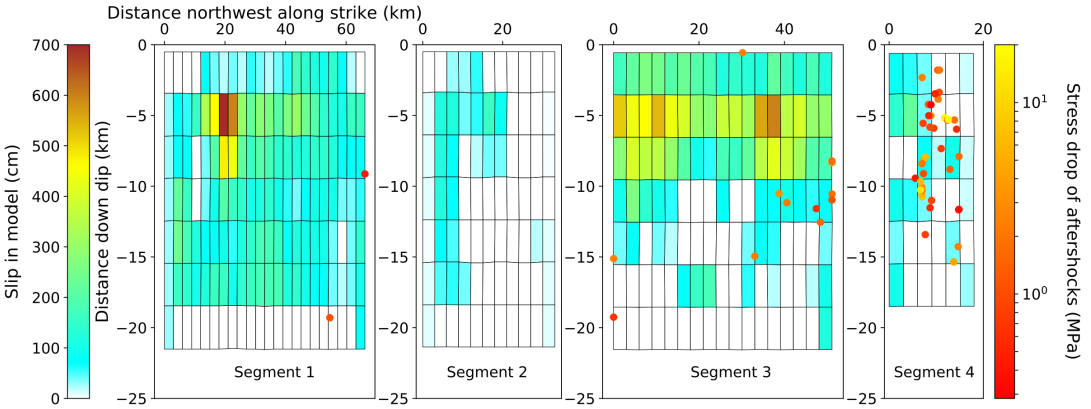

Figure 3.14: Stress drops of aftershocks (coloured dots) projected onto the slip model (coloured rectangles) of *Wei et al.* (2011). These stress drops were obtained by analysing the P wave. The stress drop of each aftershock is indicated by the colour bar on the right of the figure. The slip of the slip model is indicated by the colours of the slip segments and the colour bar on the left of the figure. Segment 1 is the most southeastern segment of the slip model shown in Figure 3.3a, and the number of the segment increases as you move northwest on the slip model. Only stress drops of earthquakes inside of the region of the slip model are allowed which is defined as latitudes south of 32.73° and longitudes east of -115.8°.

located on low slip patches of the main shock. One might expect the stress drops of aftershocks on high slip patches to be difficult to obtain because aftershocks tend to concentrate around these patches (e.g., *Peng and Zhao*, 2009, *Yamada et al.*, 2010, *Kato and Nakagawa*, 2014, *Wu et al.*, 2017, *Wetzler et al.*, 2018, *Yabe and Ide*, 2018). Indeed, *Wei et al.* (2011) observed that the aftershocks of the El Mayor-Cucapah earthquake are concentrated around high slip patches. There were, however, several aftershocks on these high slip patches (Figure 3.3) but they did not pass the signal-to-noise thresholds.

3.5.5 Variation of stress drops with aseismic slip

I examine whether the stress drops of aftershocks change with the decreasing post-seismic aseismic slip rate observed by *Gonzalez-Ortega et al.* (2014) (Figure 3.15). I calculate moving averages using a window of five values for the 31 days of interest after the main shock. For each window, I estimate the median stress drop using the approach in Sec 3.5.1. I estimate a line of best fit in log-log space of the median stress drops and time using an L2-norm.

I observe that the median stress drop slightly increases with time and therefore increases with decreasing post-seismic aseismic slip rate. The increase in median stress drop with time may disagree with the study of *Chen and Shearer* (2013), who observed a slight decrease in earthquake stress drop with time over the first 5 days following the El Mayor-Cucapah main shock. The increase in stress drop with decreasing aseismic slip may reflect the same behaviour of earthquake stress drops and aseismic slip that

I observed in the earthquakes on the Blanco fault. For the Blanco fault, I found that stress drops were higher on the less coupled northwestern half of the fault which has more aseismic slip. If I observe the same relation between aseismic slip and stress drops here, then it may suggest the properties of earthquakes can be altered by nearby aseismic slip. Note, however, that aftershocks are more likely to be triggered by the stress released by the main shock than by the post-seismic slip (*Hardebeck et al.*, 1998, *Kilb et al.*, 2002, *Cattania et al.*, 2015).

The increase in stress drops with time for the El Mayor-Cucapah aftershocks also varies depending on the analysis. If I examine the change in the stress drops of the S wave with time, then I observe a decrease in stress drops with time (Figure B.9). On the other hand, I experiment with different moving average windows when computing the median stress drop (Sec. B.8) and find no change in the trend of increasing stress drop with time. I also estimate 95% confidence limits on the slope of the line of best fit in log-log space following the same approach as described in Sec. 3.5.3. I obtain 95% confidence limits of -0.28 and 0.25 for the log-log slope of the stress drops with time for the P wave, and 95% confidence limits of -0.45 to 0.18 for the log-log slope of the results of the S wave. The significant range of these limits indicates that the trend of changing stress drops with time is not robust for the results of either the P wave or the S wave. It also suggests that the observed stress drops do not change significantly with time or decreasing post-seismic aseismic slip rate.

However, the lack of a significant trend of stress drops with aseismic slip is also interesting. One might expect that stress drops of aftershocks would be higher when the aseismic slip rate was highest immediately after the main earthquake. The high aseismic slip rate and stressing rate may encourage the rupture of strong asperities which would increase the median stress drop. The lower aseismic slip rate later after the main earthquake may be unable to encourage the rupture of strong asperities and would result in a lower median stress drop. I do not observe this pattern of decreasing stress drop with decreasing aseismic slip rate which suggests that the interaction of aseismic slip and earthquake properties is more complex than this simplistic model.

Note, however, that I use only 74 earthquakes to examine the change in stress drops with aseismic slip rate. It is possible that this is not enough earthquakes to reliably resolve the change in earthquake stress drops with the aseismic slip rate. Future work might examine the behaviour of stress drops with aseismic slip in more detail by using a dataset with a higher signal-to-noise ratio and stations closer to the rupture. It would also be interesting to see whether the interaction of aftershocks and aseismic slip could be tested for other large earthquakes, as post-seismic slip is a fairly common phenomenon (e.g., *Smith and Wyss*, 1968, *Bucknam et al.*, 1978, *Donnellan and Lyzenga*,

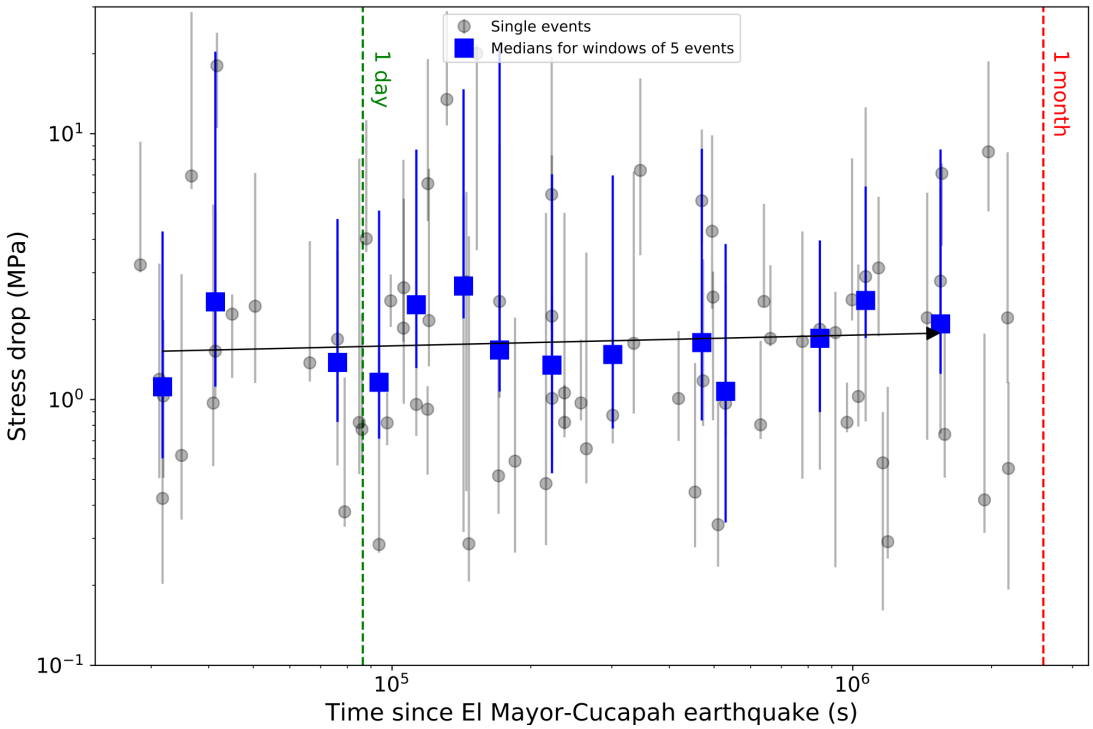

Figure 3.15: Stress drops of the aftershocks of the El Mayor-Cucapah earthquake plotted against the time since the earthquake. These stress drops were obtained by analysing the P wave. Median stress drops of windows including five values are plotted as black squares. These medians were calculated following the approach described in the text. The 95% confidence limits on these medians are shown by the error bars and are calculated as described in the text. The L2-norm line of best fit is plotted as the black arrow.

1998, *Hsu et al.*, 2006, *Ingleby and Wright*, 2017).

3.5.6 Applying the phase coherence method to the S wave

In this study, I tested whether the S wave can be used in the phase coherence method and whether it is a viable alternative to the P wave. I ran the same analysis for the S wave as the P wave using the same signal-to-noise ratio filtering and the same azimuthal range requirements. I thus estimated falloff frequencies for 51 events with the S wave, somewhat lower than the 74 events with estimated falloff frequencies using the P wave. I find falloff frequencies for fewer events for the S wave than the P wave mostly because of the difficulty in picking the S wave on noisy traces. Because the S wave often occurs within the coda of the P wave, the arrival can be difficult to identify and therefore difficult to align. The number of stations that pass the cross correlation coefficient threshold of 0.7 is therefore reduced compared to the P wave. The lower number of stations also reduces the azimuthal range of stations which reduces the number of events that pass the threshold of a minimum 120° azimuthal range. The difference in the azimuthal range of stations is clear in Figure 3.7 where the representative distribution

of stations for the S wave is narrower than the representative distribution for the P wave. The narrow representative distribution of stations for the S wave also means that the variation in apparent source time functions for the available stations is low, so the scaling factor F_{scal}, which calibrates apparent falloff frequencies to the true rupture diameter to account for the variation in apparent source time functions, is particularly high. I used synthetics as described in Sec. 3.4.4 to obtain a scaling factor of 2.32 for the S wave which is higher than scaling factors in previous studies (e.g., *Hawthorne et al.*, 2018, *Williams et al.*, 2019).

I compare the falloff frequencies and stress drops of the P wave and S wave in Figure 3.16. The lower propagation velocity of the S wave means that the difference in apparent source time functions caused by the rupture extent of an earthquake will occur at lower frequencies. Thus the falloff frequencies of the S wave should be systematically lower than the P wave. I indeed observe that the falloff frequency of the S wave is systematically lower than the P wave for the 42 events that have S wave and P wave results (Figure 3.16a). I also observe that the stress drops of the S wave are similar to the P wave, with the absolute differences between the S wave and P wave stress drops mostly below 2.5 MPa (Figure 3.16c). The consistency of these stress drops suggests that the difference in scaling factor between the waves is well resolved. The overall median stress drop of 1.6 MPa (with 95% confidence limits of 1.3 - 2.2 MPa) for the S wave is similar to the median stress drop of 1.7 (1.2, 2.2) MPa observed for the P wave. I also observed a similar change in depth dependence of stress drops for constant and depth-varying velocity (Figure B.7). The dependence of stress drop on time, however, shows a decreasing stress drop with time (Figure B.9).

The similar stress drops of the S wave and P wave and the systematically lower falloff frequencies for the results of the S wave suggests that the phase coherence method can also be applied to the S wave. The S wave is therefore a viable alternative to the P wave if the signal-to-noise ratio is low enough to obscure the P wave arrival so that the P wave cannot be picked and aligned. However, note that if the P wave cannot be aligned well, it is unlikely that the S wave will fare better. The arrival of the S wave often occurs in the coda of the P wave so is difficult to pick and align even before considering general noise conditions. The coda of the P wave can also act as noise for the phase coherence of the S wave. The coda of the P wave contains many arrivals which feature the apparent source time function. The variation in relative time between the S wave arrival and the arrival of these coda waves causes a shift in phase which varies for different stations similar to the effect of depth phases (Sec. 3.4.5). The S wave is still a useful alternative, however, especially if the noise is random and occurs at particularly high frequencies which will affect the higher falloff frequencies of the P wave more than the lower falloff frequencies of the S wave.

Comparing the stress drops determined using the P wave and S wave phase coherence could be useful for examining the uncertainty involved in the phase coherence approach. For example, the absolute difference between the P wave and S wave stress drops in Figure 3.16c appears to generally increase with increasing magnitude, with a median absolute difference of 0.6 MPa. This possible increase in the absolute difference with magnitude suggests that the possible dependence of stress drops with magnitude may not be robust, but it is also interesting that the P and S wave stress drops are similar at low magnitudes. In Section 3.5.2, I suggested that the falloff frequencies of lower magnitude earthquakes might be artificially reduced by the low colocation threshold, resulting in a reduced stress drop. Considering that the S wave should have a lower falloff frequency than the P wave, the similarity between the stress drops of the P wave and S wave suggests that the stress drops for lower magnitude earthquakes are not as affected by the colocation threshold as I previously speculated.

3.6 Conclusions

I used the phase coherence method to obtain stress drops for 74 $M \geq 3$ aftershocks of the 2010 El Mayor-Cucapah earthquake. I observed a median stress drop of 1.7 MPa (with 95% confidence limits of 1.2 - 2.2 MPa) which is lower than most previous studies. The lower median stress drop could be linked to inappropriate low rupture velocities in previous studies and the strong dependence of stress drops on rupture velocity for results from spectral corner frequency-based methods. I observed a slight increase in stress drops with moment which is the opposite of previous observations of no moment dependence of stress drops. I also observe a decrease in stress drops with increasing depth, but this trend is not robust. The stress drops of the aftershocks may also increase with time since the main earthquake. This increase with time occurs as the post-seismic slip rate decreases which suggests that aseismic slip may influence the properties of earthquakes. This trend is not robust, however, and further work is needed to test the interaction between aseismic slip and earthquake stress drops.

I also further developed the phase coherence method by using it on the P wave and the S wave of aftershocks of the El Mayor-Cucapah earthquake to test whether the S wave is a viable alternative to the P wave. I found falloff frequencies for 42 earthquakes using both the P and S wave. The falloff frequencies of the S wave are systematically lower than the P wave as expected. The stress drops are also similar which indicates the azimuthal factors are appropriate. The similarity in the stress drops of the P wave and the S wave suggests that the S wave is a viable alternative to the P wave for the phase coherence method. Future work can use the S wave to avoid using a P wave where the arrival is unclear or where there is high frequency noise that obscures the

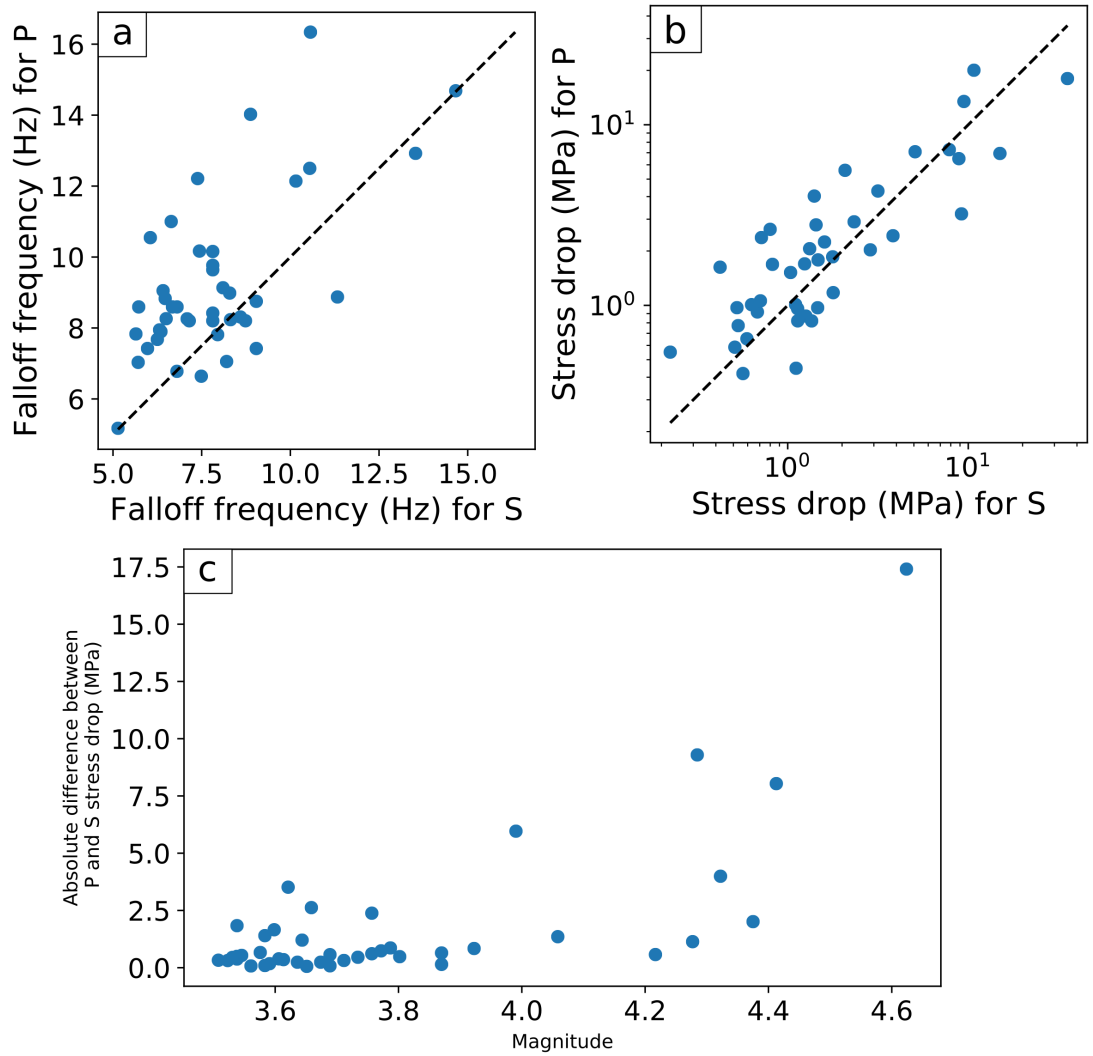

Figure 3.16: Falloff frequencies (a) and stress drops (b) from the analysis of the P wave and S wave compared against each other. The median absolute difference between P and S wave stress drops is shown in (c). The dashed black lines indicates where the falloff frequencies and stress drops would be equal between the two sets of results.

higher falloff frequency of the P wave.

Chapter 4

The long recurrence intervals of small repeating earthquakes may be due to the slow slip rates of small fault strands

"Your scientists were so preoccupied with whether or not they could, they didn't stop to think if they should."

Ian Malcolm, Jurassic Park

4.1 Introduction

Repeating earthquakes are earthquakes that repeatedly rupture particular patches of faults (*Nadeau and Johnson*, 1998, *Uchida and Bürgmann*, 2019). They are recognized via their similar waveforms and consistent rupture area, and are often used to track the slip rate of the creeping faults that host them (e.g., *Nadeau and Johnson*, 1998, *Nadeau and McEvilly*, 1999, *Igarashi et al.*, 2003, *Meng et al.*, 2015, *Schmittbuhl et al.*, 2016, *Uchida et al.*, 2016, *Materna et al.*, 2018). Repeaters have been used to track slip rates on strike-slip faults (e.g., *Nadeau and Johnson*, 1998, *Schaff et al.*, 1998, *Peng and Ben-Zion*, 2005, *Templeton et al.*, 2008, *Lengliné and Marsan*, 2009, *Schmittbuhl et al.*, 2016), subduction zones (e.g., *Igarashi et al.*, 2003, *Zhang et al.*, 2008, *Yamashita et al.*, 2012, *Yu*, 2013, *Ye et al.*, 2014, *Dominguez et al.*, 2016, *Hatakeyama et al.*, 2017), thrust faults (e.g., *Chen et al.*, 2008), and triple junctions (e.g., *Chen*

and McGuire, 2016, *Materna et al.*, 2018), but the physics that controls the recurrence rates of repeaters remains poorly understood.

If all of the slip on repeating earthquake patches accumulates in earthquakes, the cumulative earthquake slip should match the long-term fault slip rate and the slip per earthquake should equal the slip rate times the recurrence interval of the repeating earthquake. However, observed repeating earthquakes occur less often than one would expect given long-term slip rates estimated from geodesy and geology (e.g., *Nadeau and Johnson*, 1998, *Nadeau et al.*, 2004, *Chen et al.*, 2007, *Lengliné and Marsan*, 2009).

This slip or recurrence interval discrepancy is especially large for small repeating earthquakes. Observed repeater recurrence intervals t_r scale with moment M_0 as $M_0^{0.17}$ (*Nadeau and Johnson*, 1998, *Nadeau et al.*, 2004, *Chen et al.*, 2007, *Lengliné and Marsan*, 2009) but if earthquakes are assumed to have magnitude-independent stress drops (e.g., *Shearer et al.*, 2006, *Allmann and Shearer*, 2007, 2009), the slip per earthquake should scale as $M_0^{\frac{1}{3}}$. And if earthquakes accommodate all the slip on a given patch, the recurrence interval is equal to the slip per earthquake divided by the long term slip rate. The predicted t_r thus scales as $M_0^{\frac{1}{3}}$ (*Nadeau and Johnson*, 1998, *Beeler et al.*, 2001) (Sec. 1.4.1) and decreases more quickly with decreasing moment than the observed t_r.

Nadeau and Johnson (1998) were the first to identify the $M_0^{0.17}$ recurrence interval-moment scaling. They and later authors suggested that smaller repeating earthquakes could have higher or more heterogeneous stress drops (e.g., *Nadeau et al.*, 2004, *Dreger et al.*, 2007, *Kim et al.*, 2016). However, stress drops of these earthquakes are observed to be independent of magnitude (e.g., *Allmann and Shearer*, 2007) and much lower than *Nadeau and Johnson* (1998) suggested (e.g., *Imanishi et al.*, 2004, *Abercrombie*, 2014).

The correct physical model for repeaters remains unclear, and a range of models have been proposed. Repeating earthquakes could have long recurrence intervals because some of the slip on repeating earthquake patches accumulates aseismically or via partial ruptures in postseismic, interseismic, or preseismic periods (*Beeler et al.*, 2001, *Chen and Lapusta*, 2009, *Cattania and Segall*, 2019). Alternatively, repeating earthquakes could have long recurrence intervals because they occur within regions of low slip rate or low stressing rate. Earthquakes could occur in the rupture area of larger earthquakes (*Anooshehpoor and Brune*, 2001), on the border of a larger locked asperity (*Sammis and Rice*, 2001), or within a cluster of asperities (*Johnson and Nadeau*, 2002).

Here I seek to test the latter models: to assess whether spatially variable slip rates

could create the long recurrence intervals of repeating earthquakes. I also suggest another potential origin for spatially variable slip rates: earthquakes could also occur on an array of fault strands of various lengths which together constitute the main fault. The slip rate on each strand is smaller than the regional slip rate, as the regional rate is a sum of all of the strands' slip rates. The slip on these strands is affected by complex geometry and interaction between faults, but geological observations and modelling imply that the slip accumulated on a given fault strand scales linearly with the length of the strand (e.g., *Watterson*, 1986, *Walsh and Watterson*, 1988, *Marrett and Allmendinger*, 1991, *Gillespie et al.*, 1992, *Cowie and Scholz*, 1992, *Dawers et al.*, 1993, *Scholz et al.*, 1993, *Clark and Cox*, 1996, *Schlische et al.*, 1996, *Fossen and Hesthammer*, 1997, *Kim and Sanderson*, 2005, *Schultz et al.*, 2008, *Bergen and Shaw*, 2010, *Torabi and Berg*, 2011, *Kolyukhin and Torabi*, 2012, *Schultz et al.*, 2013, *Carvell et al.*, 2014, *Xu et al.*, 2016).

If all fault strands form at the same time, the shorter fault strands should have lower slip rates than the longer fault strands. To understand the origin of the assumption that all fault strands form at the same time, consider that the common model for fault formation is coalescence, where a larger fault forms through the coalescence of a series of smaller cracks (*Scholz*, 2002). If a larger fault is made of a series of smaller cracks which feature less slip and lower slip rates, the slip rate of the larger fault would be the sum of the slip rates of the smaller cracks. It is plausible then that slip rate of a fault might be proportional to fault length.

I may thus hypothesise that small earthquakes have especially long recurrence intervals because they are small enough to occur on short fault strands which have low slip rates. The lower slip rates on these short fault strands could result in a reduced apparent recurrence interval-moment scaling. To show that the $M_0^{0.17}$, or $M_0^{\frac{1}{6}}$, recurrence interval scaling can be achieved via varying fault slip rates, I define $V_L(M_0)$ to be the slip rate on a fault which hosts earthquakes with moment M_0. I also hypothesise that

$$V_L(M_0) \propto M_0^{\frac{1}{6}}, \tag{4.1}$$

and insert this velocity scaling into relation between recurrence interval and moment described in Equation (1.10):

$$\begin{aligned} t_r &= A\frac{M_0^{\frac{1}{3}}}{V_L(M_0)}, && (4.2)\\ &= A\frac{M_0^{\frac{1}{3}}}{M_0^{\frac{1}{6}}}, && (4.3)\\ &= AM_0^{\frac{1}{6}}, && (4.4) \end{aligned}$$

where A is a constant equal to $\frac{\Delta\sigma^{\frac{2}{3}}}{c^{\frac{1}{3}}k^{\frac{2}{3}}\mu}$ and c is a constant. Thus the unexpected recurrence interval-moment scaling of repeating earthquakes may be because the slip rate of faults scales with $M_0^{\frac{1}{6}}$. Note that I assume μ is constant; any scaling of μ with the size of the earthquakes will also affect recurrence interval-moment scaling.

I can also describe an expected relation between the dimension of the earthquakes and the loading velocity. Earthquake moment is $M_0 = \mu A\tilde{\delta}$ and stress drop appears constant with magnitude (Sec. 1.1.2), which implies that $M_0 \propto D^3$, and that the loading velocity V_L scales with earthquake diameter D as:

$$V_L(M_0) \propto M_0^{\frac{1}{6}}, \tag{4.5}$$

$$V_L(D) \propto D^{\frac{1}{2}}. \tag{4.6}$$

Here D is the diameter of an earthquake with moment M_0, and V_L is the slip rate of a fault that typically hosts earthquakes with diameter D and moment M_0. As I assume that smaller earthquakes are more likely to occur on smaller fault strands, the scaling of loading velocity with earthquake diameter is likely similar to the scaling of loading velocity with fault strand length.

This hypothetical scaling of loading velocity with fault strand length may also have a physical basis. Whilst many studies have observed that the maximum displacement of a fault scales linearly with the length of the fault (e.g., *Gillespie et al.*, 1992, *Dawers et al.*, 1993, *Schlische et al.*, 1996), some studies have observed that the maximum displacement scales with the square root of fault length (e.g., *Fossen et al.*, 2007, *Schultz et al.*, 2008). It is plausible then that the slip rate of a fault scales with the square root of fault length, assuming that the slip rate scales linearly with the maximum displacement of a fault. Assuming that the rupture diameter of earthquakes on a fault scales linearly with the fault length due to larger earthquakes occurring on larger faults, it thus seems plausible that the slip rate scales with the square root of earthquake diameter, from which one may derive that slip rate is proportional to $M_0^{\frac{1}{6}}$.

Small earthquakes may thus have especially long recurrence intervals because they are small enough to occur on short fault strands which have low slip rates. There may be no discrepancy in slip on a local scale, and slip may scale as $M_0^{\frac{1}{3}}$ on each fault strand (blue lines on Figure 4.1b). One might infer a slip deficit on a regional scale only because the repeating earthquake rate is compared with the regional slip rate, which is the sum of the slip rates on the collection of fault strands (green dashed line on Figure 4.1b).

Here I test the hypothesis that fault strand- or segment-dependent slip rates create

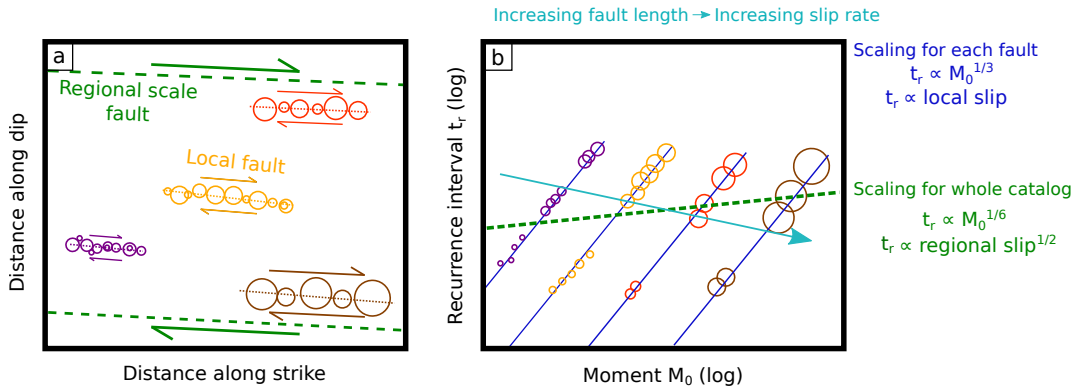

Figure 4.1: Conceptual model of my hypothesis. (a): Map view of earthquake sequences (circles) on different fault strands (dotted lines) within a regional scale fault (green dashed line). Larger fault strands have higher slip rates (larger arrows) and can host larger earthquakes (larger radii). (b): Hypothetical recurrence interval versus moment plots for earthquake sequences that could exist on each fault strand. The solid blue lines indicate a $M_0^{\frac{1}{3}}$ scaling of recurrence intervals on each fault strand while the dashed green line illustrates a $M_0^{0.17}$ scaling that might be observed by considering all the earthquakes together.

the $M_0^{0.17}$ recurrence interval scaling of repeating earthquakes. I note that if spatially variable slip rates create the $M_0^{0.17}$ scaling, that scaling should be apparent among widely spaced earthquake sequences. But closely spaced sequences should respond to the same local slip rate and thus have a scaling closer to $M_0^{\frac{1}{3}}$. So I compare the recurrence intervals of closely and widely spaced earthquake sequences near Parkfield, California.

4.2 Data: Repeating earthquake sequences

I search for distance-dependent scaling using two datasets from Parkfield, California.

4.2.1 Earthquake sequences identified by Lengliné and Marsan, 2009

I analyse a catalog of repeating earthquake sequences identified by *Lengliné and Marsan* (2009). The catalog includes 334 repeating earthquake sequences composed of 2414 M 0.94 – 3.19 earthquakes that occurred between 1984 and 2007. *Lengliné and Marsan* (2009) formed these sequences by requiring repeating earthquakes to have similar waveforms, 70% horizontal source overlap, and a magnitude difference of less than or equal to 0.2 magnitude units compared to any of the earthquakes in the sequence. Many of these sequences were perturbed by the 2004 M_W 6.0 Parkfield earthquake, however, so I truncate the catalog 1 day before the 2004 event and thus analyse 220 sequences composed of 1540 earthquakes (Figure 4.2). I assume that the earthquake rate is stable in the 1984 – 2004 time interval.

4.2.2 Two-earthquake sequences from the relocated NCSN catalog

I also identify pairs of co-located earthquakes, which I describe as 2-earthquake sequences, directly from the Northern California Seismic Network (NCSN) earthquake catalog, as relocated by *Waldhauser and Schaff* (2008) and *Waldhauser* (2009). I select a subset of this catalog in the 90-km long area shown in Figure 4.2 (coordinates in Table C.1) and exclude any earthquakes with depths shallower than 4 km as their depths are more poorly resolved (Figure 4.2). I analyse earthquakes between 1984 and 2004, again stopping 1 day before the 2004 Parkfield event. The analysed relocated catalog consists of 5255 events with magnitudes of M 0.15 – 4.9.

To begin, I calculate the earthquake moments M_0 from the reported catalog magnitudes, assuming $M_0 = 10^{1.6M+9.05}$ Nm (*Wyss et al.*, 2004). I use the moment to estimate earthquake rupture radius r, assuming an elliptical slip distribution (*Eshelby*, 1957) and a stress drop $\Delta\sigma$ of 10 MPa, as has been inferred for the Parkfield area (e.g., *Imanishi et al.*, 2004, *Allmann and Shearer*, 2007, *Abercrombie*, 2014):

$$r = \left(\frac{7}{16} \frac{M_0}{\Delta\sigma} \right)^{\frac{1}{3}}. \tag{4.7}$$

Next, I use a simple approach to identify 2-earthquake sequences of repeating earthquakes – earthquakes that rupture the same area – without using waveform correlation. For each earthquake in the catalog, I search for the next earthquake in time that is located within one rupture radius horizontally and vertically, and which has a magnitude within 0.3 magnitude units. I allow a 34-m uncertainty on the horizontal location and an 80-m uncertainty on the vertical location. These uncertainties are the 95% confidence limits for relative location errors in the relocated catalog (*Waldhauser*, 2009; catalog version 201112.1). I require that one earthquake in each 2-earthquake sequence has a magnitude greater than M 1.3, to avoid selecting sequences which have skipped an event. Earthquakes with $M < 1.1$ may be missing from the catalog, as a frequency-magnitude plot suggests a Gutenberg-Richter distribution with a roll-off at magnitudes below 1.1 (Figure C.1).

This search for similar earthquakes identifies 1230 2-earthquake sequences. Note that the analysis of these sequences assumes that all of these co-located events are repeating earthquakes. This assumption seems acceptable for the Parkfield region; up to 55% of small earthquakes in smaller-scale studies of this region have been identified as repeating earthquakes using waveform correlation analysis (*Nadeau et al.*, 2004), and isolated events are excluded by the relative location requirements.

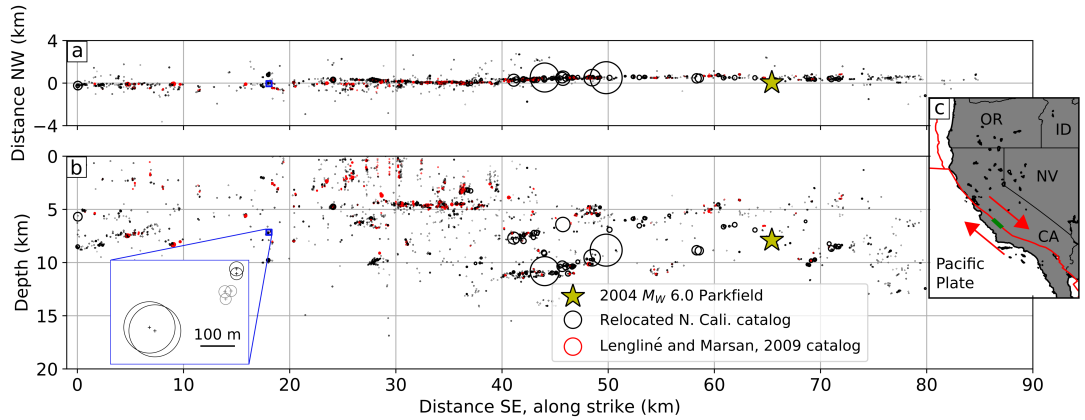

Figure 4.2: (a): NCSN earthquake locations in map view along the Parkfield segment of the San Andreas Fault. Earthquakes after the day before the 2004 M_W 6 earthquake are excluded. Earthquakes that appear in the catalog of *Lengliné and Marsan* (2009) are marked in red. The hypocentre of the 2004 M_W 6 earthquake is marked by the yellow star. (b): Earthquake locations along strike versus depth. The inset plot demonstrates two example 2-earthquake sequences (black circles) identified using the simple approach discussed in the text. The third obvious cluster of earthquakes did not meet my criteria (grey circles). The radii of these earthquakes is calculated in the text. (c): Larger scale view of study area (green) in global context.

4.3 Method and Results

4.3.1 Analysing earthquake sequences in the Lengliné and Marsan catalog

I begin by analysing the median recurrence intervals and moments of each sequence in the catalog of *Lengliné and Marsan* (2009) (light grey dots on Figure 4.3a). The moment is calculated from the NCSN magnitudes using the calibration of *Wyss et al.* (2004), as described above. I also compute and plot the median recurrence intervals and moments in various moment bins (black squares on Figure 4.3a). I compute 95% confidence limits on the median recurrence intervals by jackknifing the sequence catalog. In each of 2000 realisations, we remove 20% of the sequences and recompute the median recurrence interval and moment for each moment bin. The error bars in Figure 4.3a indicate 95% confidence limits derived from these realisations.

I use these uncertainty estimates when I estimate the best-fitting recurrence interval-moment slope, or scaling exponent γ. When fitting γ, I weight each point by one divided by the variance implied by the 95% confidence limits on each point. I then jackknife again to estimate uncertainties on the scaling exponent. I recalculate the best-fitting exponent 1000 times, excluding 20% of the earthquake catalog each time. The slope of the relation between these median recurrence intervals and moment bins in log-log space is equal to the scaling exponent γ of the recurrence interval-moment relation

discussed earlier ($t_r \propto M_0^{\gamma}$). The slope γ should be equal to $\frac{1}{3}$ if all earthquakes have the same stress drop and the slip per earthquake is equal to the regional slip rate multiplied by the recurrence interval. Given the limited number of sequences in the catalog of *Lengliné and Marsan* (2009), the recurrence interval-moment scaling exponent is poorly constrained at 0.15 (95% confidence limits of 0.13 and 0.20) but is consistent with the shallower $\gamma = \frac{1}{6}$ scaling, which is equivalent to the $\gamma = 0.17$ identified by *Nadeau and Johnson* (1998).

I want to know if the recurrence interval-moment scaling is different for closely and widely spaced earthquake sequences. As noted in the introduction, if closely spaced earthquake sequences are sensitive to similar slip rates, recurrence intervals may locally scale as $M_0^{\frac{1}{3}}$ even though widely spaced sequences show a $M_0^{0.17}$ scaling, on average. So I consider pairs of earthquake sequences. For each pair, I calculate the ratio of the median recurrence intervals of the sequences and the ratio of the median moments.

The recurrence interval and moment ratios of earthquakes should follow the same scaling as the recurrence intervals and moments. Suppose I analyse two repeating earthquake sequences labelled a and b, which have median recurrence intervals $t_{r,a}$ and $t_{r,b}$ and moments $M_{0,a}$ and $M_{0,b}$. These sequences occur on asperities with loading velocities of $V_{L,a}$ and $V_{L,b}$. If I compute the ratio of the recurrence intervals of the two sequences, it should scale with the ratio of moments and loading velocities following the same recurrence interval-moment scaling as in Equation (1.10):

$$\frac{t_{r,a}}{t_{r,b}} = \frac{A M_{0,a}^{\frac{1}{3}} V_{L,b}}{A M_{0,b}^{\frac{1}{3}} V_{L,a}} \tag{4.8}$$

$$= \left(\frac{M_{0,a}}{M_{0,b}}\right)^{\frac{1}{3}} \frac{V_{L,b}}{V_{L,a}}, \tag{4.9}$$

where I assume that A is the same for the two sequences.

When the two earthquakes are part of the same fault strand and the loading velocity is homogeneous over the whole strand, the recurrence intervals tend to

$$\frac{t_{r,a}}{t_{r,b}} = \left(\frac{M_{0,a}}{M_{0,b}}\right)^{\frac{1}{3}}. \tag{4.10}$$

If the two events are part of two fault strands with two distinct velocities, the "normal" $\frac{t_{r,a}}{t_{r,b}} \propto \left(\frac{M_{0,a}}{M_{0,b}}\right)^{\frac{1}{3}}$ scaling will disappear. If the loading velocity scales with moment $M_0^{\frac{1}{6}}$ as described above, the ratios will scale as $\frac{t_{r,a}}{t_{r,b}} \propto \left(\frac{M_{0,a}}{M_{0,b}}\right)^{\frac{1}{6}}$.

All the ratios between sequences in the catalog of *Lengliné and Marsan* (2009)

are plotted in Figure 4.4a (grey dots). Next, I bin and examine the scaling of ratios by inter-sequence distance. I compute the inter-sequence distance by computing the distance between the median locations of each earthquake sequence. For each distance bin, I compute the median recurrence interval ratios and median moment ratios for various moment ratio bins (coloured symbols with error bars). Finally, I estimate the recurrence interval-moment scaling for each distance bin by fitting lines in log-log space through the median recurrence interval ratios.

I compute 95% confidence limits on the median recurrence interval ratios by jackknifing the sequence catalog as above. The error bars in Figure 4.4a indicate 95% confidence limits derived from the 1000 realisations of the jackknifed catalog. I use the uncertainty estimates when I estimate the best fitting slopes, or scaling exponent γ, for the median recurrence interval ratios and moment ratios for each distance bin, using the same approach as the simpler recurrence interval-moment slope calculation.

To ensure high-quality statistics, I prefer to consider only medians in distance and moment bins that include at least 20 sequences with at least 10 sequences that figure in the numerators of the moment ratios and at least 10 sequences that figure in the denominators of the moment ratios. I plot medians that do not fulfil these requirements with open symbols and dashed error bars, and where possible I do not use them in the exponent calculation. The catalog of *Lengliné and Marsan* (2009) includes a limited number of sequences, however, and none of the distance bins of interest meet this 20 sequence requirement. For completeness, I nevertheless compute scaling exponents for these distance bins using the available (poorly constrained) medians and plot them with open symbols in the inset panel in Figure 4.4a. All of the confidence intervals on these scaling exponents include 0.17 and exclude $\frac{1}{3}$, but the confidence interval width is likely underestimated due to the low number of sequences used in the jackknifing.

4.3.2 Analysing 2-earthquake sequences in the relocated NCSN catalog

I perform a similar analysis for the 2-earthquake sequences identified in the NCSN catalog. I first calculate the time between the earthquakes in each sequence – the recurrence interval – and plot it against the average moment of the sequence (Figure 4.3b). I then estimate the scaling exponent of the calculated recurrence intervals with moment using the same approach as above. The scaling exponent of these calculated recurrence intervals with moment is 0.18 (95% confidence limits of 0.16 and 0.20), similar to the $M_0^{0.17}$ scaling of recurrence intervals of repeating earthquakes obtained from waveform correlation by *Nadeau and Johnson* (1998).

I again want to compare each earthquake sequence with closely and widely spaced sequences, so I compute recurrence interval and moment ratios for all possible sequence pairs. I estimate the distance between these sequences as the distance between the locations of the first events in the 2-earthquake sequences. I experiment with different approaches for estimating the distance between sequences and find no significant impact on my results (Figures C.18 and C.19). I do not want to compare 2-earthquake sequences that are part of the same longer sequence, however, so I exclude ratios of sequences that are within 200 m and 0.3 magnitude units of each other. Then I compute median recurrence interval ratios and moment ratios for a range of moment ratio and distance bins, and calculate 95% confidence intervals (error bars) and the best-fitting scaling exponent using jackknifing, following the same procedure as for the catalog of *Lengliné and Marsan* (2009). In each of 1000 jackknifed realizations, I remove 20% of the earthquake catalog, exclude any 2-earthquake sequences that have lost an earthquake, and recompute recurrence interval ratios, moment ratios, and scaling exponents.

I next fit lines to the median recurrence interval ratios and moment ratios to obtain scaling exponents for each distance bin. The scaling exponents obtained for earthquakes separated by more than 100 m are scattered around 0.17 and include 0.17 in their 95% confidence intervals (Figure 4.4b). The 0 - 100 m distance bin is an exception, however. It has a best-fitting scaling exponent of 0.3 and includes $\frac{1}{3}$ within its uncertainty intervals.

4.3.3 Testing for bias in the analysis

I repeat my analysis with a range of modifications to check that the observed recurrence interval-moment scaling is not biased by the approach. Full details and discussion are available in Appendix C. I test whether the result changes if I modify the bin widths (Figure C.2) and the averaging method (Figure C.3). I also exclude 2-event sequences with recurrence intervals of less than one month to try and avoid any effect of aftershocks (Figure C.4), extend the buffer period before the Parkfield earthquake to 6 months (Figure C.6), and attempt to avoid any bias in the recurrence intervals due to end of the earthquake catalog (Figure C.7). Finally, I take the earthquake location uncertainty into account (Figure C.8), change the stress drop assumed to estimate earthquake radii to align with a global estimates of stress drop (e.g., *Allmann and Shearer*, 2009) (Figures C.9 and C.10), and attempt to track sequences from the NCSN locations (Figure C.11). In these tests, the exponent for the 0 - 100 m distance bin remains elevated but is up to 0.1 lower than the previous scaling exponent. It has best-fitting values between 0.23 and 0.3, and according to the jackknife probabilities, it has a 75 - 95% chance of exceeding the average exponent of the other distance bins.

4.3.4 Validation with synthetic earthquake catalogs

To check that the code and methodology are appropriate, I analyse several synthetic catalogs as generated by Jessica Hawthorne. First, I consider a synthetic catalog where repeating earthquakes have recurrence intervals that scale as $M_0^{0.17}$. The analysis recovers this $M_0^{0.17}$ scaling, with some scatter (Figure C.22). Uncertainty-induced scatter in the scaling exponent is evenly distributed above and below 0.17 in all distance bins.

I also analyse a catalog of earthquakes on multiple fault strands, where recurrence interval scales as $M_0^{\frac{1}{3}}$ on each fault strand and the slip rate of each strand scales with its length. This catalog simulates the scenario suggested in Figure 4.1. As expected, I retrieve a scaling exponent of close to $\frac{1}{3}$ for the lower distance bin and a reduced exponent of close to 0.17 for the wider distance bins in these catalogs (Figure C.23).

4.4 Discussion

I analysed the recurrence interval-moment scaling of repeating earthquakes in two earthquake catalogs. The scaling exponents obtained by analysing the sequences catalog of *Lengliné and Marsan* (2009) appear to be inconsistent with spatially dependent slip rates, as the scaling exponents are scattered around 0.17 and do not vary with the distance between repeating earthquake sequences. As I note above, however, this catalog usually has less than 10 unique sequences in the numerator and denominator of each moment ratio and distance bin and therefore a large uncertainty on the scaling exponents which is not necessarily captured in the jackknifing.

The scaling exponents obtained from 2-earthquake sequences in the NCSN catalog are better resolved, and they are consistent with spatially dependent slip rates. The 2-earthquake sequences within 100 m of each other give a high scaling exponent with a best-fitting value of 0.3 obtained from 1878 pairs of sequences. The 95% confidence intervals on the exponent of 0.25 - 0.34 include $\frac{1}{3}$: the value expected when constant-stress drop repeaters occur in response to a locally uniform slip rate, without allowing for aseismic slip. The 2-earthquake sequences which are 100 - 250 m apart also give an elevated exponent of 0.2, with 95% confidence limits of 0.16 - 0.24. More widely spaced sequences give scaling exponents close to the 0.17 value identified previously (e.g., *Nadeau and Johnson*, 1998, *Nadeau et al.*, 2004, *Chen et al.*, 2007). The change in scaling could indicate that the background slip rate changes with location and that smaller earthquakes occur on regions of the fault with lower slip rate or lower stressing rate (*Anooshehpoor and Brune*, 2001, *Johnson and Nadeau*, 2002).

The jackknife-based uncertainties suggest a distance-dependent change in scaling

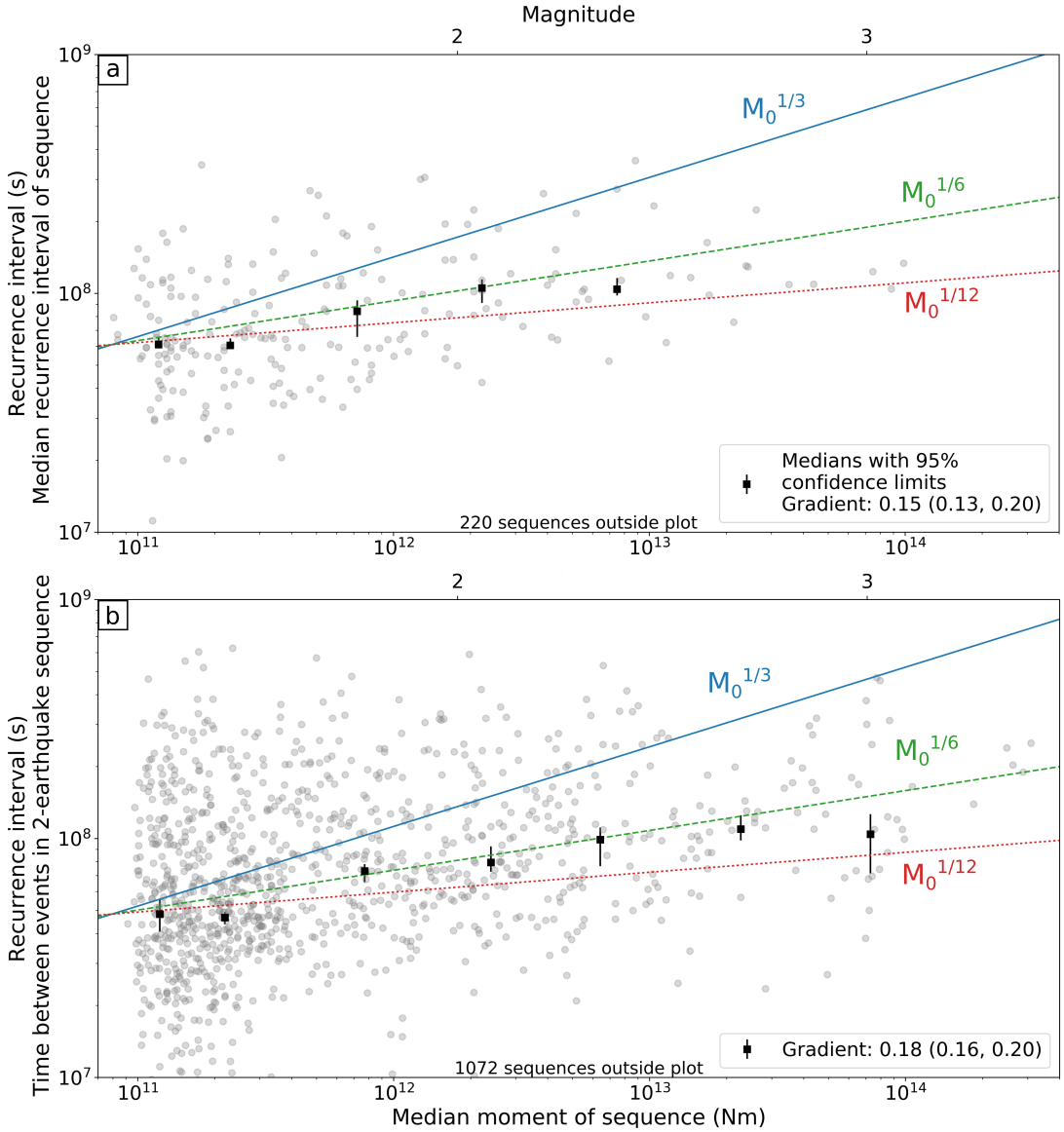

Figure 4.3: Median recurrence interval versus median moment for sequences from (a): the repeating earthquakes catalog of *Lengliné and Marsan* (2009) and (b): the relocated northern California catalog (*Waldhauser and Schaff*, 2008, *Waldhauser*, 2009) on a log-log scale. Individual values are plotted as red circles, with medians for moment bins shown as black squares. The error bars on the medians indicate 95% confidence limits, which were estimated via jackknifing (details in the text). The t_r scaling relations of $M_0^{\frac{1}{3}}$, $M_0^{\frac{1}{6}}$ ($M_0^{0.17}$), and $M_0^{\frac{1}{12}}$ are plotted as solid blue, dashed green, and dotted red lines respectively.

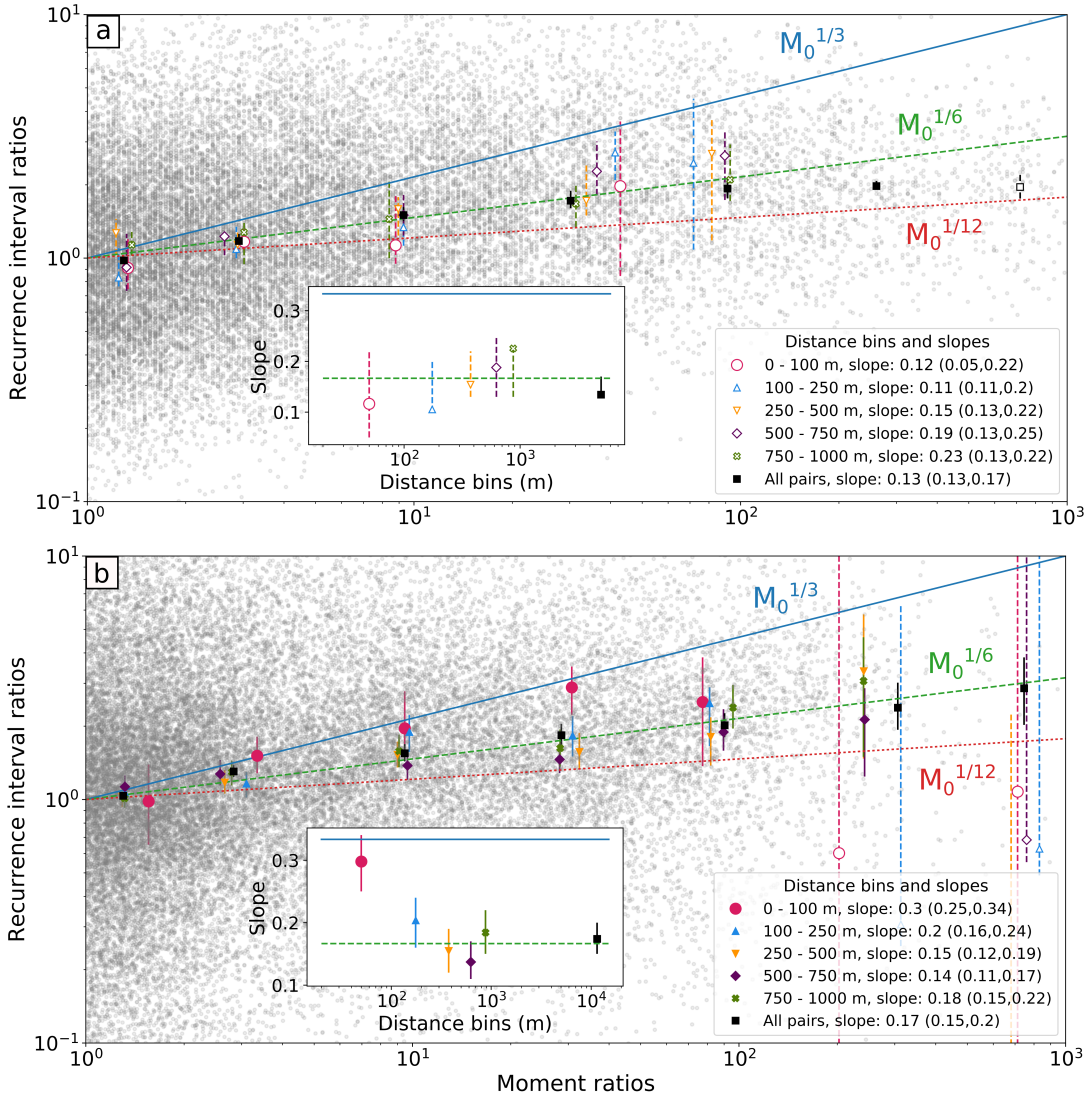

Figure 4.4: Recurrence interval ratios versus moment ratios (small red circles) for pairs of sequences in (a): the catalog of *Lengliné and Marsan* (2009) and (b): the relocated NCSN catalog (*Waldhauser and Schaff*, 2008, *Waldhauser*, 2009). The medians of sequences in different moment ratio and distance bins are plotted with varying colors and symbols, as described in the legend. Open symbols with dashed error bars are bins which did not contain at least 10 unique pairs in the numerator and denominator of the ratios. Those points are excluded from the slope calculation. Inset plots: slopes for various distance bins. Slopes with open symbols have been calculated using only points with open symbols, so have large uncertainties that are not captured by the 95% confidence limits. Recurrence interval scaling relations are as in Figure 4.3. Error bars represent 95% confidence limits are calculated using jackknifing as described in the text.

exponent with greater than 99% probability. However, these uncertainties may not include all sources of error, and in some of the tests for biases on the NCSN catalog, I found that the 0 - 100 m scaling exponent could be close to 0.17 within uncertainty. For example, I found a scaling exponent of 0.23 (0.16 - 0.32) when I attempted to track longer sequences from the NCSN locations (Figure C.11). Nevertheless, I note that in all of the tests on the NCSN catalog, the 0 - 100 m distance bin had the largest exponent (Figures C.2 - C.15).

The change in scaling at distances of 0 - 200 m is consistent with my use of primarily M 1 - 2.5 earthquakes, which have diameters around 10 - 100 m. Such earthquakes could frequently occur on fault strands with lengths of 100 m or less. It may be that when I compare earthquake sequences within 200 m of each other, I am usually comparing sequences on the same fault, but when I compare earthquakes more than 200 m apart, I am usually comparing sequences on different faults (e.g., *Waldhauser et al.*, 2004), which could have different slip rates.

The results of this study suggest that spatially dependent slip rates are a viable explanation of the scaling of the recurrence intervals of repeating earthquakes with moment. This explanation would imply that the scaling first identified by *Nadeau and Johnson* (1998) reflects the properties of the fault system, not the properties of the earthquakes themselves. The results may indicate that one can further probe the fault system and learn about its fault strands and slip rates by examining the timing and spacing of repeating and non-repeating earthquakes.

It is also worth considering the physical basis of these fault strands, and it is useful to begin by discussing the origin of faults and their structure. Faults do not form by simply fracturing more rock, but appear to form by coalescence of a series of smaller cracks (e.g., *Scholz*, 2002). As cracks coalesce to form the larger fault, the fault creates shear zones between further cracks and the fault continues to lengthen. Through this process, faults grow and continue to accumulate slip, forming a narrow core along their length where the majority of their slip occurs. This fault core is surrounded by a wider damage zone, where the width of this damage zone increases with the displacement on the fault, so older faults which have slipped more such as the San Andreas fault will have large damage zones than other younger faults. Within these damage zones are a series of deformation bands and smaller, secondary slip surfaces. Perhaps the smaller, low slip rate faults that must be present for repeating earthquakes to be accurately explained by the hypothesis investigated here are secondary slip surfaces within the damage zone of the larger Parkfield fault. Without further physical evidence in the form of lab or field measurements, however, it is unclear that the nature of repeating earthquakes can be explained using the smaller, low slip rate faults that I suggest here.

The results in this chapter should be interpreted with caution. I analyse only one region here, and I use a simple approach to identify repeating earthquakes. There remain several other viable explanations for the recurrence interval scaling. The scaling could result from aseismic slip (*Anooshehpoor and Brune*, 2001, *Beeler et al.*, 2001, *Sammis and Rice*, 2001, *Chen and Lapusta*, 2009), partial ruptures of repeater patches (*Cattania and Segall*, 2019), or highly heterogeneous stress drops (*Nadeau and Johnson*, 1998).

4.5 Conclusions

With this work, I sought to test the hypothesis that small repeating earthquakes have exceptionally long recurrence intervals because they occur preferentially on fault strands or segments with low slip rates. I examined the recurrence interval-moment scaling of repeating earthquakes in the Parkfield area using the repeating earthquake catalog of *Lengliné and Marsan* (2009) and sequences in the relocated NCSN catalog (*Waldhauser and Schaff*, 2008, *Waldhauser*, 2009) identified using a simple approach. With the catalog of *Lengliné and Marsan* (2009), I obtain a scaling within error of the $M_0^{0.17}$ scaling identified by *Nadeau and Johnson* (1998) for all subsets of the sequences. But with the NCSN location-based sequences, which have better spatial resolution, I recover that scaling only when I consider sequences that are more than 100 m apart. Sequences within 100 m of each other show a scaling close to $M_0^{\frac{1}{3}}$, as would be expected if the earthquakes have magnitude-independent stress drops and keep up with the local fault slip rates. This "normal" local scaling suggests that the observed $M_0^{0.17}$ scaling can be explained by spatially varying slip rates or by a collection of fault strands that have size-dependent slip rates.

Chapter 5

Discussion and conclusions

"There is an art to flying, or rather a knack.
The knack lies in learning how to throw yourself
at the ground and miss."

Douglas Adams, Life, the Universe and Everything

In the previous chapters, I obtained stress drops of earthquakes on the Blanco fault (Chapter 2) and of aftershocks of the 2010 El Mayor-Cucapah earthquake (Chapter 3), and examined the recurrence interval-moment scaling of repeating earthquakes (Chapter 4). I observed that the stress drops of earthquakes may vary because of aseismic slip. I also found that the recurrence interval-moment scaling of repeating earthquakes may reflect the properties of faults that feature the repeating earthquakes. Here, I discuss what these observations may tell us about the interaction of earthquake properties with aseismic slip and fault properties. I evaluate the uncertainties in my analysis and examine how these uncertainties affect my observations. My analysis used new methods to evaluate the properties of these earthquakes. I discuss the advantages and disadvantages that these methods have compared to more conventional approaches.

I begin by discussing the properties of stress drops of earthquakes on the Blanco fault (Chapter 2) and aftershocks of the 2010 El Mayor-Cucapah earthquake (Chapter 3). I examine how the estimated stress drops vary with earthquake moment and aseismic slip on the Blanco fault. I also examine how the stress drops of the El Mayor-Cucapah aftershocks vary with moment, depth and time since the main event (Sec. 5.1). Next, I discuss the relationship between aseismic slip and repeating earthquakes. I discuss whether the unexpected scaling of the recurrence intervals of repeating earthquakes with moment can be explained by spatially varying slip rates (Sec. 5.2).

Then I evaluate the phase coherence method I used in Chapters 2 and 3. I discuss the advantages and disadvantages of the phase coherence method and examine how the method may be used together with commonly used spectral decomposition methods to look at rupture properties such as the rupture velocity (Sec. 5.3.1). I also examine the simplified approach for identifying repeating earthquakes which I used in Chapter 4 (Sec. 5.3.2). I compare the sequences identified by the simple approach with sequences identified using the more computationally expensive cross correlation approach in previous studies to test whether the simple approach correctly identifies repeating earthquake sequences. I describe the advantages of using the simple approach to analyse the properties of repeating earthquakes. Finally, I outline the key findings of my thesis (Sec. 5.4).

5.1 Properties of earthquake stress drops

5.1.1 Comparing average stress drops

I obtain stress drops of earthquakes on the Blanco fault (Chapter 2) and stress drops of the aftershocks of the 2010 M_W 7.2 El Mayor-Cucapah earthquake (Chapter 3). I observe a median stress drop of 8 MPa (95% confidence limits of 6 - 12 MPa) for earthquakes on the Blanco fault and a median stress drop of 1.7 MPa (1.2 - 2.2 MPa) for the aftershocks of the 2010 El Mayor-Cucapah earthquake. The factor of 4.8 higher median stress drop of earthquakes on the Blanco fault suggests that earthquakes on oceanic transform faults may have higher stress drops than earthquakes on continental strike slip faults. Previous studies have also observed that stress drops are systematically higher on oceanic transform faults (*Allmann and Shearer*, 2009), but with a smaller factor of 1.7 difference.

The stress drops of earthquakes on the Blanco fault and aftershocks of the El Mayor-Cucapah earthquake may differ because of a fundamental difference in rupture properties between oceanic transform faults and continental strike slip faults. For example, earthquakes on oceanic transform faults may have systematically shorter rupture extents because of the presence of serpentinite along the fault, which may act as a rupture barrier to limit the rupture extent. The difference in stress drops may also be artificial, however, because of differences in data quality for each study. For example, frequencies lower than 1 Hz tend to have lower signal-to-noise ratios (SNRs) for the data of the earthquakes of the Blanco fault and frequencies lower than 2 Hz have lower SNRs for the data of El Mayor-Cucapah aftershocks. Relatively few of the falloff frequencies of the aftershocks are close to the lower limit of 2 Hz (Figure 5.1). On the other hand, many of the falloff frequencies of the $M > 5$ earthquakes on the Blanco fault are close to 1 Hz. Earthquakes with similar magnitudes, larger rupture extents, and thus lower

falloff frequencies will be unresolvable because of the low SNR at low frequencies. The earthquakes with larger rupture extents will have lower stress drops, so excluding them may artificially increase the median stress drop. Alternatively, perhaps I used inappropriately high wave propagation velocities to estimate the rupture extent. Using more appropriate velocities might eliminate the difference in average stress drops. To eliminate the difference in average stress drop, the wave propagation velocities would need to be equal to 0.8 times the current velocities for the aftershocks of the El Mayor-Cucapah earthquake and 1.1 times the velocity used for the earthquakes on the Blanco fault. Although these changes seem small, they are unlikely given the already low velocities (average 6.16 km/s for the P wave) used for the aftershocks of the El Mayor-Cucapah earthquake and the high velocity (8.04 km/s) used for the earthquakes on the Blanco fault. It is also possible that the difference in average stress drop between the earthquakes on the Blanco fault and the El Mayor-Cucapah aftershocks is real and reflects the moment dependence of stress drops which I discuss later (Sec. 5.1.2).

I can also compare the median stress drops for the Blanco fault and the aftershocks of the El Mayor-Cucapah earthquake with previous estimates of average stress drops for similar tectonic settings. If the median stress drops are similar to these previous estimates then that might suggest that I obtain accurate estimates of the stress drop. The median stress drop of 8 MPa for earthquakes on the Blanco fault is higher than the median stress drop of 3 - 4 MPa (inferred from Figure 5.2) observed by *Kuna et al.* (2019) on the Blanco fault. The 8 MPa median stress drop is also higher than other previous studies of oceanic transform faults which have average stress drops of less than 1 MPa (*Boettcher and Jordan*, 2004, *Moyer et al.*, 2018), but it is within uncertainty of the global average stress drop of 6.03 MPa for oceanic transform faults estimated by *Allmann and Shearer* (2009). On the other hand, the 1.7 MPa median stress drop observed for the aftershocks of the 2010 El Mayor-Cucapah earthquake is lower than the 5.62 MPa average stress drop estimated for the first five days of El Mayor-Cucapah aftershocks by *Chen and Shearer* (2013). The median stress drop for the aftershocks is also lower than the 3.54±0.64 MPa global average stress drop for continental strike slip faults estimated by *Allmann and Shearer* (2009).

The estimates of the median stress drop obtained here differ from estimates in previous studies. The difference in estimates may be because of different assumptions made in my work and previous studies. For example, the stress drops obtained from the phase coherence method are less sensitive to changes in the rupture velocity. Thus assuming an incorrect rupture velocity will not change stress drops obtained using the phase coherence method as much as the stress drops from spectral decomposition methods. The phase coherence method may also obtain a more accurate rupture extent than spectral decomposition methods in some cases (Sec. 5.3.1). It is also important

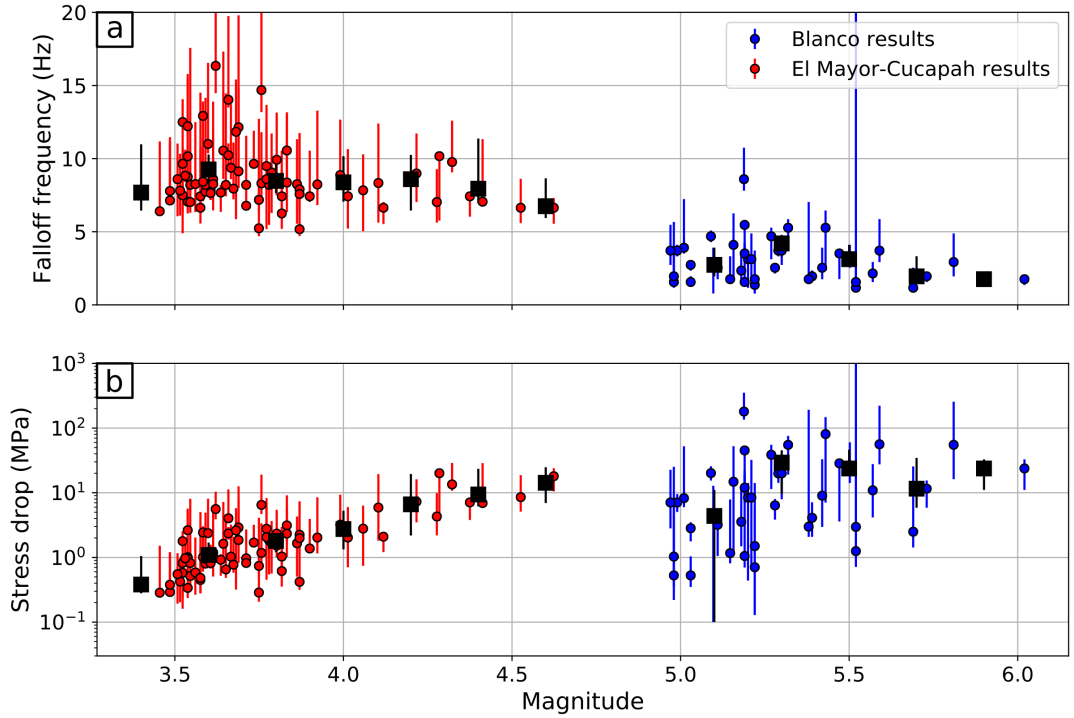

Figure 5.1: (a): Falloff frequencies and (b): stress drops of earthquakes on the Blanco fault (blue circles) and aftershocks of the 2010 El Mayor-Cucapah earthquake (red circles). The results for the aftershocks of the El Mayor-Cucapah earthquake were obtained using the P wave. The uncertainties (error bars) on each value are 95% confidence limits estimated from bootstrapping the stations used in the phase coherence calculation. Median falloff frequencies and stress drops are plotted as black squares in 0.2 magnitude unit bins. The error bars on each median are 95% confidence limits estimated by selecting 1000 samples of bootstrapped falloff frequencies for each earthquake in each magnitude bin.

to note that most of the studies using spectral decomposition methods do not include uncertainties on individual stress drops, so may underestimate the uncertainty in their average stress drops. My median stress drops may thus be within uncertainty of the average stress drops from previous studies. However, it is difficult to determine the cause of the observed difference in stress drops between my work and previous studies without further analysis. One important test would be to obtain stress drops for a set of earthquakes using both the phase coherence method and spectral decomposition methods. With sets of results from each method, it would be easier to identify the cause of the difference between results of each method.

In the following sections, I discuss whether the stress drops of earthquakes estimated in this thesis depend on other earthquake properties, fault properties, and aseismic slip. Note, however, that all these properties affect stress drops concurrently, so the effect of different properties can be difficult to isolate. For example, one might imagine that larger earthquakes occur systematically deeper than smaller earthquakes. If stress drops

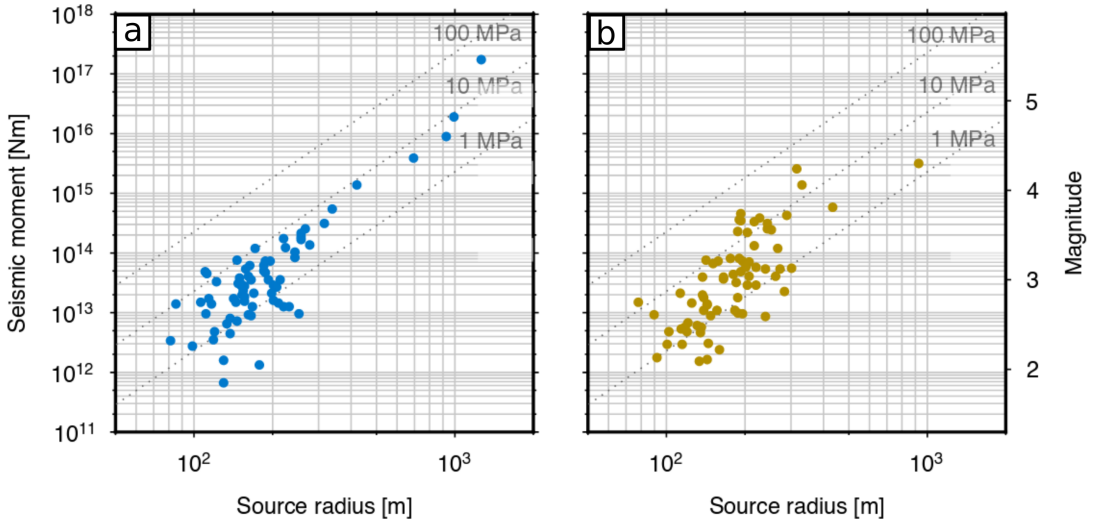

Figure 5.2: Seismic moment versus earthquake radius of earthquakes on the Blanco fault obtained by *Kuna et al.* (2019). Constant stress drops are plotted as dotted lines. Earthquakes are either (a): crustal seismicity or (b): mantle seismicity. Crustal seismicity is shallower than 7 km and mantle seismicity is deeper than 7 km. Figure modified after *Kuna et al.* (2019).

then increase with depth, is this because stress drops increase with depth, or because stress drops increase with magnitude? It is impossible to differentiate between depth and magnitude dependence in this case without further observations. The difficulty in differentiating between the effects of depth and magnitude in the hypothetical case above demonstrates that the results I discuss here should be considered with caution.

5.1.2 Moment dependence

Most studies observe that stress drops do not vary with moment (e.g., *Abercrombie*, 1995, *Mori et al.*, 2003, *Shearer et al.*, 2006, *Chen and Shearer*, 2011, *Uchide et al.*, 2014, *Chen and McGuire*, 2016, *Abercrombie et al.*, 2017, *Yoshida et al.*, 2017). However, I observe a slight increase with moment in the stress drops of earthquakes on the Blanco fault and the stress drops of aftershocks of the El Mayor-Cucapah earthquake (Figure 5.1). I also observe that the median stress drop of earthquakes on the Blanco fault is a factor of 4.8 higher than the median stress drop of the El Mayor-Cucapah aftershocks. The difference in median stress drops may reflect the difference in magnitude between the two studies: the median stress drops was calculated for $M > 5$ earthquakes on the Blanco fault and $M < 4.8$ aftershocks of the El Mayor-Cucapah earthquake.

The change in stress drop with magnitude can be considered more directly by examining the variation in falloff frequency with magnitude. I expect the falloff frequency to decrease with increasing rupture extent and increasing magnitude. I observe that the falloff frequency decreases slightly with magnitude of the aftershocks of the El

Mayor-Cucapah earthquake, but it appears to be relatively constant with magnitude of earthquakes on the Blanco fault (Figure 5.1). The unexpected weak decrease in falloff frequency with magnitude results in stress drops that increase with magnitude. It is possible, however, that the change in falloff frequency with magnitude of each dataset is artificially created by the poor resolution of falloff frequencies in my analysis.

In Chapter 2, I noted that there was a narrow band of resolution for falloff frequencies because of the large alignment uncertainty and low frequency noise. The large alignment uncertainty allowed only falloff frequencies lower than 4 Hz to be resolved. On the other hand, the noise at low frequencies allowed only falloff frequencies higher than 1 Hz to be resolved. This narrow band of resolution may artificially create the constant falloff frequencies with magnitude of earthquakes on the Blanco fault.

In Chapter 3, I used a co-location threshold of 2 km to select pairs of earthquakes to analyse because of the uncertainty in earthquake locations. Using this co-location threshold may allow earthquakes with different Green's functions to be included in pairs. These variable Green's functions can reduce the phase coherence and cause a lower apparent falloff frequency. Lower magnitude earthquakes will be more likely to have a reduced apparent falloff frequency because of their generally higher true falloff frequencies. The weak co-location threshold may thus introduce an artificially shallow dependence of falloff frequency on magnitude and thus an artificial increase of stress drop with magnitude.

On the other hand, it is worth considering whether stress drops may indeed increase with the magnitude of an earthquake. Although I suggest here that the moment dependence is artificial, *Kuna et al.* (2019) also observed a slight increase in stress drops with moment (Figure 5.2). There is also some evidence that moment dependence can occur for individual regions (*Cocco et al.*, 2016). One might imagine, therefore, that higher magnitude earthquakes may have higher stress drops in particular regions. Indeed, many earthquake properties such as the slip (e.g., *Candela et al.*, 2011, *Cocco et al.*, 2016) and fracture energy (the energy used to create the new fault surface) (e.g., *Cocco and Tinti*, 2008, *Cocco et al.*, 2016) appear to be scale-dependent and therefore moment-dependent, so why do observations generally find that the stress drop is independent of moment? One hypothesis is that some frictional properties of a fault, such as the yield stress, follow some statistical, spatial distribution which is scale independent. The stress drop reflects the heterogeneity of stress on a fault, so the stress drop is also scale independent (e.g., *Andrews and Barall*, 2011, *Candela et al.*, 2011, *Cocco et al.*, 2016). Another simplistic view is that because stress drop is proportional to $\frac{\mu A \bar{\delta}}{r^3}$, and the rupture area A depends on the radius r^2 and slip scales with earthquake size, the stress drop does not depend on moment (Sec. 1.1.2). The moment-independence

of stress drops is a fundamental constraint on our understanding of earthquake physics which must be solved before we can claim that we understand the physical process of earthquakes. The slight moment dependence I observe in my results highlights the work still needed to fully understand the dependence of stress drops on moment.

It is also important to take into account that I obtained stress drops of only 61 earthquakes on the Blanco fault and 74 aftershocks of the 2010 El Mayor-Cucapah earthquake. The observed slight moment dependence is therefore based on relatively few measurements. To examine the moment dependence in more detail would require more and better resolved falloff frequencies and stress drops. But the presence of moment dependence in my results suggests that it would be worthwhile to investigate the moment dependence in future. It would be interesting to see whether the stress drops from the phase coherence method and spectral corner frequency-based methods would both depend on moment, or whether the dependence appears because of a difference between the two methods (Sec. 5.3.1).

5.1.3 Depth dependence

In some studies, stress drops appear to increase with depth (e.g., *Jones and Helmberger*, 1996, *Hardebeck and Hauksson*, 1997, *Shearer et al.*, 2006, *Allmann and Shearer*, 2007, *Baltay et al.*, 2011, *Chen and Shearer*, 2013, *Oth*, 2013, *Uchide et al.*, 2014, *Goebel et al.*, 2015, *Chen and McGuire*, 2016). These studies assume a constant rupture velocity at all depths and therefore a uniform S wave velocity at all depths. However, several studies have observed that the depth dependence of their stress drops vanished if they used an S wave velocity that increased with depth (e.g., *Allmann and Shearer*, 2009, *Abercrombie et al.*, 2017, *Goebel et al.*, 2017). The increase in S wave velocity with depth increases the rupture velocity with depth. A higher rupture velocity results in shorter rupture extents for deeper earthquakes. Shorter rupture extents means lower stress drops. Thus, the increase in stress drops with depth may be removed by using a depth-dependent S wave velocity.

I could not investigate the dependence of stress drops on depth for earthquakes on the Blanco fault because the depths of the earthquakes were poorly resolved (Table A.3), but I did examine the stress drops of the El Mayor-Cucapah aftershocks for depth dependence. Note that I vary the P wave velocity here as I use the propagation wave velocity in the phase coherence method rather than the rupture velocity. I found that the stress drops of the El Mayor-Cucapah aftershocks increased slightly with depth when I used a depth-independent P wave velocity (Figure 3.12a). I found that the stress drops decreased slightly with increasing depth when I used a depth-dependent P wave velocity (Figure 3.12b). However, I estimated the 95% confidence limits on

the slopes of the log-linear lines of best fit for stress drops with depth using both depth-independent and depth-dependent velocity. I estimated 95% confidence limits of -0.008 and 0.024 for the slope of the stress drops using a depth-independent velocity and 95% confidence limits of -0.024 and 0.011 for the slope of the stress drops using depth-dependent velocities. Both of these trends have poorly resolved slopes and do not indicate a large variation in stress drop with depth. The relative variations in stress drop between medians for individual depth bins may also reflect the increase of stress drops with increasing moment (Sec. 3.5.3).

A lack of variation of stress drops with depth has been observed in previous studies (e.g., *Jin et al.*, 2000, *Kinoshita and Ohike*, 2002, *Mori et al.*, 2003, *Allmann and Shearer*, 2009, *Abercrombie et al.*, 2017, *Goebel et al.*, 2017, *Wu and Chapman*, 2017). My results and the results of these studies are interesting as they suggest that the depth of an earthquake does not affect its stress drop. Such depth-independent stress drops are surprising at first glance, the stress drops should increase with depth because the normal stress increases with depth due to the increasing overburden. If the normal stress increases with depth then the frictional strength of the fault should also increase with depth, and the larger frictional strength could allow for larger stress drops for deeper earthquakes. Another possible explanation of this surprising depth-independence of stress drops could be the variation in pore fluid pressure. The pore fluid pressure may increase with depth at the same rate as the normal stress. The effective normal stress may thus remain uniform with depth, resulting in no change in shear strength and stress drops with depth.

The stress drops of the aftershocks of the El Mayor-Cucapah earthquake suggest that stress drops do not increase with depth in response to increasing normal stress. However, the dependence of stress drops on depth may be affected by the approach I use to estimate the falloff frequency. I accepted the maximum falloff frequency from all available earthquake pairs for a single earthquake as the true falloff frequency of the earthquake. Picking the maximum apparent falloff frequency discards falloff frequencies that are biased low by different Green's functions due to the large 2-km co-location threshold. However, using the maximum falloff frequency may also systematically increase the falloff frequencies of shallow earthquakes. Shallow earthquakes have more earthquake pairs because there is a higher density of earthquakes at shallow depths. Shallow earthquakes are therefore more likely to have a range of apparent falloff frequencies around the true falloff frequency which represents the scatter in apparent falloff frequency caused by small variations in the azimuthal range of stations. The maximum falloff frequency for shallow earthquakes is thus likely to be the highest apparent falloff frequency in the scatter around the true falloff frequency. If all the maximum falloff frequencies sample the highest apparent falloff frequency in the scatter then the relative

variations of stress drops are robust as they are systematically biased high above the true falloff frequency. Deeper earthquakes have fewer earthquake pairs, however, so the scatter of apparent falloff frequencies around the true falloff frequency may not be fully represented. Thus the maximum falloff frequency for deeper earthquakes might not be the highest apparent falloff frequency. Deeper earthquakes may sample systematically lower apparent falloff frequencies than shallow earthquakes, despite the true falloff frequency being similar for both sets of earthquakes. The decrease in median stress drop with depth could thus be artificially created. The three deepest median stress drops also use only a single earthquake. It is unlikely that a single earthquake will accurately represent the median stress drop at depth. Indeed, excluding these three medians would likely result in a relatively constant stress drop with depth. Without better resolution of falloff frequencies and more stress drops, it is difficult to conclude whether the stress drops of aftershocks of the El Mayor-Cucapah earthquake depend on depth.

5.1.4 Variation with aseismic slip

Examining the interaction of aseismic and seismic slip was one of the main aims of my thesis. I examined the stress drops of earthquakes on the Blanco fault and aftershocks of the El Mayor-Cucapah earthquake for interaction with aseismic slip.

Stress drops of earthquakes on the Blanco fault increase with seismic coupling, with a factor of 1.7 (0.8 - 3.5) higher stress drops on the more coupled southeastern half compared to the less coupled northwestern half (*Williams et al.*, 2019). This variation of stress drops with coupling is similar to the factor of 2 higher stress drops on more coupled segments of East Pacific Rise faults observed by *Moyer et al.* (2018) and consistent with the lower stress drops on creeping segments of strike slip faults observed by some studies (e.g., *Jin et al.*, 2000, *Allmann and Shearer*, 2007). On the other hand, *Kuna et al.* (2019) found no systematic difference in stress drops earthquakes in more coupled crust and less coupled mantle.

In Chapter 2, I suggested that the lower stress drops on the less coupled northwestern half of the fault could be linked to a mantle upwelling underneath the fault (*Byrnes et al.*, 2017). I suggested that this mantle upwelling increases the temperature of the crust and reduces the width of the seismogenic zone, reducing the length of the seismic cycle. A shorter seismic cycle means asperities have less time to heal so are weaker and rupture with lower stress drops. But there are alternative mechanisms that may explain the dependence of stress drops on seismic coupling. For example, the low stress drops on the northwestern half of the fault could be due to the complexity of the faulting. The northwestern half of the fault consists of 3 - 4 depressions with short

strike slip segments between them (Figure 1.10b). Some of these depressions include possible normal and strike slip faulting (e.g., *Embley and Wilson*, 1992, *Juteau et al.*, 1995, *Braunmiller and Nábělek*, 2008). The southeastern half has much simpler structure with most of the fault consisting of a single strike slip fault: the Blanco ridge. One might imagine that the complex faulting in the northwestern half of the fault allows penetration of fluids into the crust and that these fluids increase the pore pressure and reduce the effective normal stress. A lower effective normal stress results in a lower shear strength and thus lower stress drops (e.g., *Roland et al.*, 2012, *Moyer et al.*, 2018).

On the other hand, the higher stress drops on the southeastern half of the Blanco fault could be caused by fluid interaction that creates serpentinite. Some forms of serpentinite are stable at low slip rates and normally resist earthquake nucleation. These serpentinites are also unstable at high slip rates and allow earthquakes to nucleate if an external trigger increases the slip rate (*Reinen et al.*, 1991). Strong asperities within serpentinite may remain stable at low slip rates for a long time, allowing them to accumulate high amounts of stress. When the slip rate or stressing rate does increase, for example through dynamic triggering (e.g., *Kilb et al.*, 2000, *Gomberg and Johnson*, 2005, *Velasco et al.*, 2008), the strong asperities experience earthquakes with particularly high stress drops. Serpentinite diapirism under the Blanco ridge has been suggested as the mechanism for the formation of the ridge structure (*Embley and Wilson*, 1992, *Dziak et al.*, 2000, *Kuna et al.*, 2019). Most of the earthquakes on the southeastern half of the Blanco fault occur on the Blanco ridge. The high stress drops on the southeastern half of the Blanco fault may therefore be due to the presence of serpentinite. Note, however, that the presence of serpentinite has yet to validated by physical samples (*Dziak et al.*, 2000).

The variation of stress drops with seismic coupling could also be due to the depth dependence of stress drops on the Blanco fault, which I cannot examine due to the poor resolution of earthquake depths. One might imagine that the earthquakes on the cooler southeastern half of the Blanco fault are systematically deeper than the earthquakes on the warmer northwestern half. These deeper earthquakes could have higher stress drops (e.g., *Jones and Helmberger*, 1996, *Hardebeck and Hauksson*, 1997, *Shearer et al.*, 2006, *Allmann and Shearer*, 2007, *Baltay et al.*, 2011, *Chen and Shearer*, 2013, *Oth*, 2013, *Uchide et al.*, 2014, *Goebel et al.*, 2015, *Chen and McGuire*, 2016). On the other hand, coupling decreases with depth as the temperature increases and the crust behaves more ductilely (e.g., *Brace and Kohlstedt*, 1980, *Sibson*, 1984, *Tse and Rice*, 1986). By this reasoning, if stress drops increase with coupling, then they should decrease with depth. The lack of evidence for decreasing stress drops with depth in the literature suggests that the change in coupling with depth does not affect the stress drops or that the increase of stress drops with depth due to an increase in normal stress (Sec.

1.1.2) is the more dominant effect. Previous work on the Blanco fault (*Braunmiller and Nábělek*, 2008) also suggests that there is no systematic spatial variation in earthquake depths on the Blanco fault (Figure 1.11), so it is unlikely that the depth dependence of stress drops could artificially create the variation of stress drops with seismic coupling.

I also examined whether the stress drops of aftershocks of the 2010 M_W 7.2 El Mayor-Cucapah earthquake varied with the post-seismic aseismic slip rate (Chapter 3). The post-seismic aseismic slip rate appears to decay with time (*Gonzalez-Ortega et al.*, 2014). The stress drops of the aftershocks appear to slightly increase with time when the P wave is analysed (Figure 3.12). If the stress drops increase with time then perhaps they reflect the interaction between aseismic slip and earthquake properties identified in the stress drops of earthquakes on the Blanco fault. However, the stress drops of the aftershocks decrease with time when the S wave is analysed (Figure B.7). I also estimated 95% confidence limits on the slope of the line of best fit in log-log space for the stress drops with time for both the P wave and S wave. I found 95% confidence limits of -0.28 to 0.25 on the slope of the line of best fit for the P wave and 95% confidence limits of -0.45 to 0.18 on the slope of the line of best fit for the S wave. Clearly, the trend of stress drop with time is not well resolved for either set of results. The lack of a consistent trend of stress drops with time between the two sets of results and the poor resolution of the slopes of the two sets of results suggests that there is no systematic change in stress drops with time. The stress drops of the aftershocks thus do not appear to be affected by the decrease in aseismic slip rate.

The lack of significant variation in stress drops of aftershocks of the El Mayor-Cucapah earthquake with the aseismic slip rate is interesting. A physical intuition might lead one to expect the stress drops to decrease with time and decreasing aseismic slip rate. The high aseismic slip rate immediately after the main earthquake may encourage the rupture of strong and weak asperities. Later after the main earthquake, the lower aseismic slip rate may not be able to rupture the strong asperities due to a lower stressing rate, thus decreasing the average stress drop. This relationship between aseismic slip rate and stress drop is not observed in the stress drops of the aftershocks of the 2010 El Mayor-Cucapah earthquake, which suggests that effects other than the aseismic slip rate may affect the earthquake stress drop. One of these effects could be that the main shock increases the pore pressure on some asperities and lowers the pore pressure on others. The asperities with reduced pore pressure will have increased effective normal stress and therefore increased frictional strength which allows them to resist rupture. The asperities with increased pore pressure will have decreased effective normal stress and therefore decreased frictional strength. These weakened asperities will rupture more easily with lower average stress drops. The pore pressure on the weakened asperities may then decrease with time as the pore pressure re-equilibrates

in the fault zone. The decrease in pore pressure will increase the effective normal stress and frictional strength of the weakened asperities. The increase in frictional strength with time may cause the average stress drop of asperities to increase with time. Perhaps this pore pressure effect is acting at the same time as the effect of aseismic slip, and I therefore do not observe any systematic change in stress drop. Note also that the stress changes induced by the main shock are more likely to trigger aftershocks, so the post-seismic slip may not be the main control on the stress drops of aftershocks (*Hardebeck et al.*, 1998, *Kilb et al.*, 2002, *Cattania et al.*, 2015).

If the stress drops of aftershocks of the 2010 El Mayor-Cucapah earthquake do increase with decreasing post-seismic slip, then they may follow the same relation between aseismic slip and earthquakes properties as the increase in stress drops of earthquakes with seismic coupling on the Blanco fault. I suggest a number of mechanisms including strong asperities, serpentinisation, and pore pressure effects to explain the physics behind the change in stress drops with aseismic slip. But several of these mechanisms are likely acting at the same time. The change in stress drops likely reflects the trade-off between these mechanisms. There is also a key difference between the results of Chapters 2 and 3. The variation in stress drops of earthquakes on the Blanco fault appears to be due to the amount of aseismic slip, whereas the variation in stress drops of the El Mayor-Cucapah aftershocks may be due to the change in aseismic slip *rate*. It is not clear whether the effects of increased aseismic slip and increased aseismic slip rate for the two different datasets are related through the same mechanism, and the mechanisms I suggest for each dataset may not explain the variation in the other dataset.

It is also important to remember that I obtain relatively few stress drops here. Future work should aim to significantly increase the number of available measurements to test the robustness of the observed effects of aseismic slip on earthquake stress drops. It would also be interesting to see if the dependence of earthquake stress drops on aseismic slip can be observed elsewhere. For example, one could investigate the relation between stress drops and post-seismic slip on subduction zones following megathrust earthquakes or examine the variation of stress drops with coupling on more faults with creeping and locked segments (e.g., *Jin et al.*, 2000, *Allmann and Shearer*, 2007, *Moyer et al.*, 2018, *Kuna et al.*, 2019). Any dependence of stress drops on aseismic slip must be considered with caution, as the dependence of stress drop on moment, depth, focal mechanism, or other properties could cause an apparent relation between stress drops and aseismic slip.

5.1.5 Assumptions made about stress drop

Throughout this discussion, I make the assumption that if the strength of a fault varies, then I should see low stress drops for earthquakes on weaker areas of a fault, and high stress drops for earthquakes on stronger areas of a fault. In order for this to be true, I make the assumption that the final stress after the earthquake is constant across the region of interest, and therefore that an earthquake with a high stress drop must have ruptured a strong asperity with a high initial shear stress required for rupture. Although this assumption is sometimes used in previous studies (*Hardebeck and Aron*, 2009, *Hauksson*, 2015, *Yoshida et al.*, 2017), it is not clear how accurate it may be. It is difficult to obtain measurements of the stress on a fault especially after a disruptive earthquake, so direct estimates of the initial stress and final stress before and after an earthquake respectively, are uncommon. Thus I make the assumption that the stress drop, which represents the relative change in stress on the fault due to the earthquake, describes the change from some initial stress to a final stress, where the final stress is some minimum stress level that is relatively constant for most rocks.

The constant final stress level that I suggest here may be affected by other factors such as the temperature. Higher temperature rocks are likely to be velocity-strengthening, and therefore slip aseismically when they have stress applied to them (*Abercrombie and Ekström*, 2001, *Boettcher et al.*, 2007, *He et al.*, 2007, *Braunmiller and Nábělek*, 2008). Only at particularly high stress will these rocks slip seismically (e.g., *Scholz*, 2002), and as soon as this stress is partially released, the rock may begin slipping aseismically again. In situations like this, the final stress of the rock after an earthquake may be higher than one would expect for velocity-weakening material, and so this is one illustration of where my assumption of a constant final stress may be inappropriate. Increased temperature may also cause low stress drops by shortening the healing time between earthquakes (*Hauksson*, 2015).

In order for the stress drop to correlate strongly with the fault strength, I must also assume that stress drops are near-complete stress drops, releasing most or all of the stress on a patch of a fault, reducing the shear stress to the dynamic frictional stress. There is some evidence for earthquakes which have complete stress drops (e.g., *Zoback and Beroza*, 1993, *Barton and Zoback*, 1994, *Hasegawa et al.*, 2011, *Ross et al.*, 2017) but other authors have observed possible evidence of earthquakes with partial stress drops (e.g., *Sharma and Wason*, 1994, *Cotton and Campillo*, 1995, *Gibowicz*, 1998). Partial stress drops of earthquakes may occur if the fault locks immediately after the occurrence of an earthquake, when the average dynamic stress for the fault is reduced and the stress drop is not complete (*Brune*, 1970, 1976, *Sharma and Wason*, 1994). Alternatively, if the release of stress in the earthquake is not constant across the

fault, then some regions of the fault may retain higher stress levels after the earthquake (*Brune*, 1970, 1976). It is also possible that the final stress on the fault after an earthquake is lower than the dynamic stress, which is often called the frictional overshoot model(*Savage and Wood*, 1971, *Gibowicz*, 1998).

There is widespread debate on which of these models is the correct approach (e.g., *Savage and Wood*, 1971, *Madariaga*, 1976, *Snoke et al.*, 1983, *Brune*, 1976, *Brune et al.*, 1986, *Smith et al.*, 1991) and some studies even see evidence that multiple models may apply to different regions (e.g., *Gibowicz*, 1998). If complete, partial, and overshoot stress drops are possible, then one cannot infer any information about the strength of faults from the static stress drops derived from earthquakes on those faults. This ambiguity in what stress drops represent is problematic for my analysis, and suggests that the inferences I make about the strength of faults later in this thesis may be incorrect. On the other hand, even with partial stress drops one might still expect some level of correlation with the strength of faults, even if that correlation is much weaker than if stress drops were complete. So, I assume that stress drops are complete for this discussion of this thesis, but it is important to remember that a difference in stress drop may not necessarily reflect a difference in fault strength.

It is also worth considering the effect that other factors may have on the stress drops I estimate here. For example, observations of induced seismicity have suggested that increased pore fluid pressure may result in lower stress drops (e.g., *Chen and Shearer*, 2011, *Goertz-Allmann et al.*, 2011, *Kwiatek et al.*, 2014). Increased pore fluid pressure will reduce the effective normal stress and therefore reduce the frictional strength of a rock (e.g., *Scholz*, 2002). Thus an increased pore fluid pressure may lead to lower stress drops of earthquakes, assuming that the final stress after earthquakes is constant between regions of higher and lower pore fluid pressure. Perhaps the variation in stress drops I observe along the Blanco fault is not related to a hotter crust on one side, but instead to variation in pore fluid pressure along the fault with higher pore fluid pressure on the north west segment of the fault because of its more complex structural history resulting in more damaged and permeable rock.

The change in stress drops along the Blanco fault could also be related to a change in P wave velocity along the fault. The phase coherence method assumes a P wave velocity to obtain the rupture extent from the falloff frequency. For the Blanco fault, I assume a constant P wave velocity of of 8.04 km/s along the fault, whereas in reality the P wave velocity likely varies. A P wave velocity that is a factor of 0.8 lower on the north west segment of the fault compared to the south east segment would be enough to explain the difference in stress drops which I observe in Chapter 2, which is a reasonable change in P wave velocity along the fault. If the velocity structure of

a fault is particularly heterogeneous then it could also explain smaller scale changes in stress drops of earthquakes estimated using the phase coherence method. I do not consider variations in velocity here, so my results should be considered carefully with appreciation of the uncertainties and assumptions involved.

5.2 Aseismic slip and repeating earthquakes

The interaction between aseismic slip and earthquakes can also be seen in repeating earthquakes. Here, I discuss what the results of Chapter 4 can tell us about the interaction of repeating earthquakes with aseismic slip and fault properties. I begin by establishing why repeating earthquakes are commonly associated with aseismic slip. Then I describe my observations of the properties of repeating earthquakes and examine how they might reflect fault properties rather than aseismic slip. I also discuss the assumptions I make in explaining the observations and whether they are appropriate.

To understand why repeating earthquakes have been suggested to be symptomatic of aseismic slip, consider the patch on which a repeating earthquake occurs. If all the slip on the patch accumulates seismically, then the cumulative slip rate of repeating earthquakes on that patch should match the tectonic slip rate, and the recurrence intervals t_r of repeating earthquakes should scale with moment M_0 as $M_0^{\frac{1}{3}}$ (e.g., *Nadeau and Johnson*, 1998, *Beeler et al.*, 2001) following

$$t_r = \frac{M_0^{\frac{1}{3}} \Delta\sigma^{\frac{2}{3}}}{1.81 \mu V_L}, \tag{5.1}$$

where $\Delta\sigma$ is the stress drop, μ is the shear modulus and V_L is the loading velocity. However, observed recurrence intervals of repeating earthquakes scale as $M_0^{0.17}$ (e.g., *Nadeau and Johnson*, 1998, *Nadeau et al.*, 2004, *Chen et al.*, 2007, *Lengliné and Marsan*, 2009). The recurrence intervals of repeating earthquakes are longer than expected for smaller earthquakes which indicates a deficit in the seismic slip of repeating earthquakes compared to the tectonic slip rate.

Several studies have attempted to explain the long recurrence intervals of repeating earthquakes and the deficit in slip between repeating earthquakes and the tectonic slip rate. Some authors suggested that repeating earthquakes have high stress drops (*Nadeau and Johnson*, 1998) or that repeating earthquakes occur in regions of low slip rate or stressing rate (*Anooshehpoor and Brune*, 2001, *Sammis and Rice*, 2001, *Johnson and Nadeau*, 2002). The most commonly accepted explanations, however, use aseismic slip on the repeating earthquake patch to account for the deficit in slip (*Beeler et al.*, 2001, *Chen and Lapusta*, 2009, *Cattania and Segall*, 2019). Some studies have thus

used repeating earthquakes as a proxy for aseismic slip to estimate the seismic hazard (e.g., *Bürgmann et al.*, 2000, *Schmidt et al.*, 2005).

In Chapter 4, I presented another explanation for the recurrence interval-moment scaling of repeating earthquakes which does not require aseismic slip. I suggested that a single large fault is likely made up of a series of smaller fault strands. Geological observations imply that the individual shorter fault strands will have accumulated less slip than the longer fault strands (e.g., *Watterson*, 1986, *Walsh and Watterson*, 1988, *Marrett and Allmendinger*, 1991, *Gillespie et al.*, 1992, *Cowie and Scholz*, 1992, *Dawers et al.*, 1993, *Scholz et al.*, 1993, *Clark and Cox*, 1996, *Schlische et al.*, 1996, *Fossen and Hesthammer*, 1997, *Kim and Sanderson*, 2005, *Schultz et al.*, 2008, *Bergen and Shaw*, 2010, *Torabi and Berg*, 2011, *Kolyukhin and Torabi*, 2012, *Schultz et al.*, 2013, *Carvell et al.*, 2014, *Xu et al.*, 2016). Therefore, if I assume that all the fault strands originated at the same time, the shorter strands will have lower slip rates than the longer strands. The unexpected recurrence interval-moment scaling of repeating earthquakes may thus be explained by the spatially varying slip rates of different fault strands.

I tested this hypothesis by examining the scaling of ratios of recurrence intervals of repeating earthquake sequences with ratios of their moments. If sequences occur on the same fault, then they should have the same slip rate and the ratio of their recurrence intervals should scale with the ratio of their moments $M_{0,ratio}^{\frac{1}{3}}$. If sequences occur on different faults, then they should have different slip rates and the ratio of their recurrence intervals should scale with the ratio of their moments $M_{0,ratio}^{\frac{1}{6}}$. I found that the scaling of recurrence interval ratios with moment ratios changed with the distance between repeating earthquake sequences: recurrence interval ratios scaled with moment ratios $M_{0,ratio}^{\frac{1}{3}}$ for closely spaced sequences and scaled with moment ratio $M_{0,ratio}^{\frac{1}{6}}$ for widely spaced sequences. This change in scaling with the distance between sequences suggests that the unexpected recurrence interval-moment scaling of repeating earthquakes could be caused by the variation in slip rate between fault strands on which the repeating earthquake sequences occur. The unexpected recurrence interval-moment scaling of repeating earthquakes could thus reflect the properties of the fault rather than aseismic slip.

However, some of the assumptions I make in the above hypothesis may be inappropriate. For example, it is easy to imagine that larger, well developed faults are older than smaller faults (*Segall and Pollard*, 1983) and have slipped more because they have had more time to accumulate slip, not because they have higher slip rates. If the slip rate does not scale with fault length, then how can the change in recurrence interval-moment scaling with distance be explained? One alternative is that the larger amount of slip on older fault strands could result in decreased stress drops on older

fault strands. If a larger, older fault strand has slipped extensively, then the asperities on the fault surface may be worn away and the fault may be smoother (e.g., *Sagy et al.*, 2007, *Brodsky et al.*, 2011) and have a lower shear strength. If a younger, shorter fault strand has slipped less, then the asperities on the fault surface will be less worn and the fault may be rougher and have a higher shear strength (e.g., *Candela et al.*, 2011). The stress drops of earthquakes on these shorter, rougher fault strands should thus be higher than earthquakes on the longer, smoother fault strands, assuming that the final stress is constant in the region or that stress is heterogeneous and higher on the rougher fault strands. The shorter fault strands are more likely to host smaller earthquakes. When I compare sequences on the same fault strand, the stress drop is similar and does not affect the recurrence interval-moment scaling. When I compare sequences on different fault strands, the stress drop is higher for shorter fault strands and will change the recurrence interval-moment scaling relation. This stress drop-based explanation would allow all fault strands to have the same slip rate.

If stress drop scales with the length of the fault strand, then stress drop should also scale with moment. To obtain the recurrence interval-moment scaling of $M_0^{\frac{1}{6}}$, stress drop $\Delta\sigma$ must scale with $M_0^{-\frac{1}{4}}$ in the relation between recurrence interval and moment (Equation (5.1)) so that:

$$t_r = \frac{M_0^{\frac{1}{3}}(M_0^{-\frac{1}{4}})^{\frac{2}{3}}}{1.81\mu V_L}, \tag{5.2}$$

$$t_r = \frac{M_0^{\frac{1}{3}} M_0^{-\frac{1}{6}}}{1.81\mu V_L}, \tag{5.3}$$

$$t_r \propto M_0^{\frac{1}{6}}. \tag{5.4}$$

It is also interesting to calculate the stress drop of earthquakes of various sizes by substituting the observed average recurrence intervals and earthquake moments from Figure 4.3 into the equation for recurrence interval (Equation (5.1)). First, I rearrange Equation (5.1) for stress drop:

$$\Delta\sigma = \left(\frac{1.81 t_r \mu V_L}{M_0^{\frac{1}{3}}}\right)^{\frac{3}{2}}. \tag{5.5}$$

Then, I assume that the shear modulus μ is 30 GPa (*Dziewonski and Anderson*, 1981) and the average slip rate on the Parkfield segment of the San Andreas fault is 26.2 mm/yr (*Toké et al.*, 2011). I assume that there are X fault segments contributing equally to this slip rate so that the loading velocity V_L on each one is (26.2 mm/yr)/X. I insert the median recurrence interval and moment estimates from the repeating earth-

quake sequences identified in Figure 4.3b. I obtain a stress drop of 300 MPa for a M 1.3 earthquake on a single small fault and a stress drop of 90 MPa for a M 3 earthquake on a single large fault. Alternatively, if there are ten faults then the stress drop of a M 1.3 earthquake is 10 MPa and the stress drop of a M 3 earthquake is 1 MPa. The stress drop consistently decreases with magnitude for any number of faults. The stress drops for a higher number of faults are similar to values estimated in previous studies (e.g., *Imanishi et al.*, 2004, *Allmann and Shearer*, 2007, *Cotton et al.*, 2013, *Abercrombie*, 2014, *Cocco et al.*, 2016) and are not as high as the near-lithostatic stress drops suggested by *Nadeau and Johnson* (1998). On the other hand, stress drops have not been observed to decrease with moment (e.g., *Abercrombie*, 1995, *Mori et al.*, 2003, *Shearer et al.*, 2006, *Chen and Shearer*, 2011, *Uchide et al.*, 2014, *Chen and McGuire*, 2016, *Cocco et al.*, 2016, *Abercrombie et al.*, 2017, *Yoshida et al.*, 2017). The lack of any decrease in stress drop with moment suggests that the unexpected recurrence interval-moment scaling of repeating earthquakes cannot be explained by varying stress drops with fault roughness or age. It is, however, useful to consider and eliminate other explanations for the change in the recurrence interval-moment scaling of repeating earthquakes with the distance between sequences.

If fault strand-dependent slip rates or stress drops cannot explain the change in recurrence interval-moment scaling with distance between repeating earthquake sequences, then what alternatives are available? Perhaps repeating earthquakes occur on strong locked asperities within a larger creeping region (*Anooshehpoor and Brune*, 2001) or occur on a series of clustered asperities (*Johnson and Nadeau*, 2002). Both of these models involve spatially varying slip rates on a fault and smaller earthquakes in slower slipping regions, which might explain the variation in recurrence interval-moment scaling with distance without the assumption of slip rates or stress drops that scale with fault length.

It is also important to consider that there are uncertainties inherent in my analysis, such as whether I correctly identify repeating earthquakes (Sec. 5.3.2). These uncertainties and the limited dataset I use to obtain my results mean that I cannot exclude the other explanations for the unexpected recurrence interval-moment scaling of repeating earthquakes with a high degree of confidence (e.g., *Nadeau and Johnson*, 1998, *Beeler et al.*, 2001, *Sammis and Rice*, 2001, *Chen and Lapusta*, 2009, *Cattania and Segall*, 2019, *Chen and Lapusta*, 2019). I should also note that repeating earthquakes do appear to coincide with aseismic slip where the aseismic slip is inferred from geodesy (e.g., *Nadeau et al.*, 1995, *Schaff et al.*, 1998, *Nadeau and McEvilly*, 1999, *Bürgmann et al.*, 2000, *Matsuzawa et al.*, 2002, *Igarashi et al.*, 2003, *Uchida et al.*, 2003, *Nadeau et al.*, 2004, *Peng and Ben-Zion*, 2005, *Chen et al.*, 2008, *Lengliné and Marsan*, 2009, *Uchida and Matsuzawa*, 2011, *Schmittbuhl et al.*, 2016, *Gardonio et al.*, 2018). The

co-location of repeating earthquakes and aseismic slip suggests that the explanations for the unexpected recurrence interval-moment scaling which use aseismic slip may be reasonable (*Beeler et al.*, 2001, *Chen and Lapusta*, 2009, *Cattania and Segall*, 2019). On the other hand, the geodetic observations of aseismic slip are made over large regions, so it is unclear whether the aseismic slip may control the occurrence of repeating earthquakes on small scales.

The uncertainties in the analysis and the limited dataset in Chapter 4 also mean that further work is needed to test whether the variation in recurrence interval-moment scaling with distance is real. One important test would be whether the variation in scaling can be replicated for other regions and earthquake catalogs. Possible catalogs to investigate would be the global earthquake catalog or induced seismicity catalogs (e.g., *Schoenball and Ellsworth*, 2017), although induced seismicity catalogs may not follow the same relation as natural earthquake catalogs due to their triggering mechanism. For the analysis to work, it is essential that these catalogs have high quality locations. For instance, to see the variation in recurrence interval-moment scaling for $M < 3$ earthquakes, I needed earthquake locations that were accurate to under 100 m to identify the change in scaling for earthquakes that were 100 - 200 m apart. However, if a repeating earthquake catalog is mostly $M > 3$ earthquakes then the scaling variation should be observed at larger distances. Observing the variation in scaling for larger distances between larger earthquakes would suggest that the recurrence interval-moment scaling of repeating earthquakes reflects a fundamental interaction between earthquake properties and fault properties.

5.3 Development of new methods

In my thesis, I developed new methods which I used to obtain stress drops and to identify repeating earthquakes. Here I discuss the uncertainties involved in each method and compare them to pre-existing methods. I also examine how each method could be used in future to improve our knowledge of earthquake properties. I begin by discussing the phase coherence method used to obtain stress drops in Chapter 2 and 3 (Sec. 5.3.1). I then discuss the simple approach for identifying repeating earthquakes used in Chapter 4 (Sec. 5.3.2).

5.3.1 The phase coherence method

I used the phase coherence method (*Hawthorne and Ampuero*, 2017, *Hawthorne et al.*, 2018, *Williams et al.*, 2019) to obtain stress drops of earthquakes on the Blanco fault and aftershocks of the 2010 M_W 7.2 El Mayor-Cucapah earthquake. The phase

coherence method uses variations in apparent source time functions caused by spatially distributed slip to identify the rupture length and thus the stress drop of an earthquake. The phase coherence method provides a new approach to analyse the properties of earthquakes and presents new opportunities for understanding the mechanics of earthquakes. My work in Chapter 2 is some of the first to use and develop the phase coherence method and demonstrates that it can be used to obtain earthquake stress drops. I built upon this foundation in Chapter 3, where I used the phase coherence method on the P wave and the S wave signals and demonstrated that the S wave is a viable alternative to the P wave. Using the S wave may be advantageous for datasets where the signal-to-noise ratio is low and the arrival of the P wave is obscured by noise.

The phase coherence method differs from conventional methods for obtaining stress drops, such as the spectral decomposition and spectral ratio fitting methods (Sec. 1.1.1). Stress drops obtained with the phase coherence method depend only weakly on the rupture velocity but strongly on the propagation velocity, whereas stress drops obtained using conventional methods depend strongly on the rupture velocity. A strong dependence on the wave propagation velocity is more acceptable than a strong dependence on the rupture velocity, as the wave propagation velocity is often estimated through velocity modelling and is reasonably well known (within 10%). The wave propagation velocity may be difficult to choose, however, if different regions of the rupture area have different velocities. The rupture velocity is more uncertain and is often assumed to be 90% of the shear wave velocity (e.g., *Madariaga*, 1976, *Shearer et al.*, 2006, *Allmann and Shearer*, 2007, *Hardebeck and Aron*, 2009). The rupture velocity is also more difficult to measure than the wave propagation velocity. Complete knowledge of the rupture velocity would require detailed modelling of the rupture process of each earthquake (e.g., *Fan and Shearer*, 2015, *Grandin et al.*, 2015). Thus the rupture velocity is more uncertain than the wave propagation velocity and a strong dependence on the rupture velocity is less acceptable than a strong dependence on the wave propagation velocity.

To understand how the phase coherence method depends strongly on the wave propagation velocity and conventional spectral corner frequency-based methods depend strongly on the rupture velocity, consider the approach that the methods use to obtain the rupture extent. The phase coherence method estimates the rupture extent without obtaining a rupture duration, whereas other methods use the rupture duration to infer the rupture extent. The rupture duration may not accurately represent the size of an earthquake, even with the correct rupture velocity. Take, for example, a complex and abnormal rupture shown in Figure 5.3. The rupture begins at the epicentre marked by the black dot and ruptures through segments A, B, C, and D in sequence with 0.2 s between the start of rupture of each segment. The rupture of each segment takes 0.3 s.

The rupture velocity β is 2.7 km/s, 90% of the shear wave velocity of 3 km/s. Spectral corner frequency-based methods which rely on rupture duration will identify a rupture duration of 1.1 s and thus a corner frequency f_c of 0.9 Hz, from which one can calculate a rupture radius r of roughly 1 km using $r = \frac{k\beta}{f_c}$ and assuming a circular rupture (*Brune*, 1970) and that k is 0.32 (*Madariaga*, 1976, *Shearer et al.*, 2006, *Allmann and Shearer*, 2007, 2009, *Abercrombie*, 2014). This estimated rupture radius is twice as large as the true rupture radius of 0.55 km, as using the rupture duration does not take into account complex ruptures.

On the other hand, the phase coherence method examines differences in phase between signals in a rupture. These signals vary in arrival time at different stations due to the direction of rupture propagation, or rupture directivity, but they also vary due to the difference in distance that the signal must propagate through. The phase difference will be largest between the signals from A and C, as they have the largest distance between them. The large distance results in a large difference in propagation time, and thus a large difference in phase, demonstrated on Figure 5.3 by the difference in arrival times of A and C on stations E and W. The falloff frequency of the phase coherence will be around 6 Hz assuming that the P wave velocity is 6 km/s, though it may vary somewhat. The falloff frequency is scaled by a factor F_{scal} which comes from synthetic modelling of earthquakes using an assumed rupture velocity. The scaling factor F_{scal} can vary significantly depending on the rupture velocity e.g. *Hawthorne et al.* (2018) observed that the scaling factor can range from 0.7 to 2.2 using a rupture velocity that was equivalent to 5% and 100% of the shear wave velocity, respectively. An appropriate rupture velocity is thus still important for the phase coherence method, but not as important as an appropriate wave propagation velocity. In this example, the rupture velocity is well known, so the falloff frequency is equivalent to a rupture radius closer to the true value. The difference in estimated rupture radius may explain the higher stress drops I obtain from the phase coherence method. If spectral decomposition methods routinely overestimate the rupture radius, they will also underestimate the stress drop. Note, however, that there will only be a large difference in estimated rupture extents between the two methods for complex or bilateral ruptures; for simple unilateral earthquakes or point sources, both the phase coherence method and spectral corner frequency based methods should obtain similar rupture extents.

I examined the difference between stress drops determined in Chapters 2 and 3 and previous studies in Sec. 5.1. I observed higher stress drops for earthquakes on the Blanco fault than previous estimates (*Boettcher and Jordan*, 2004, *Allmann and Shearer*, 2009, *Moyer et al.*, 2018, *Kuna et al.*, 2019) and lower stress drops for aftershocks of the El Mayor-Cucapah earthquake than previous estimates (*Allmann and Shearer*, 2009, *Chen and Shearer*, 2013). This lack of systematic difference in

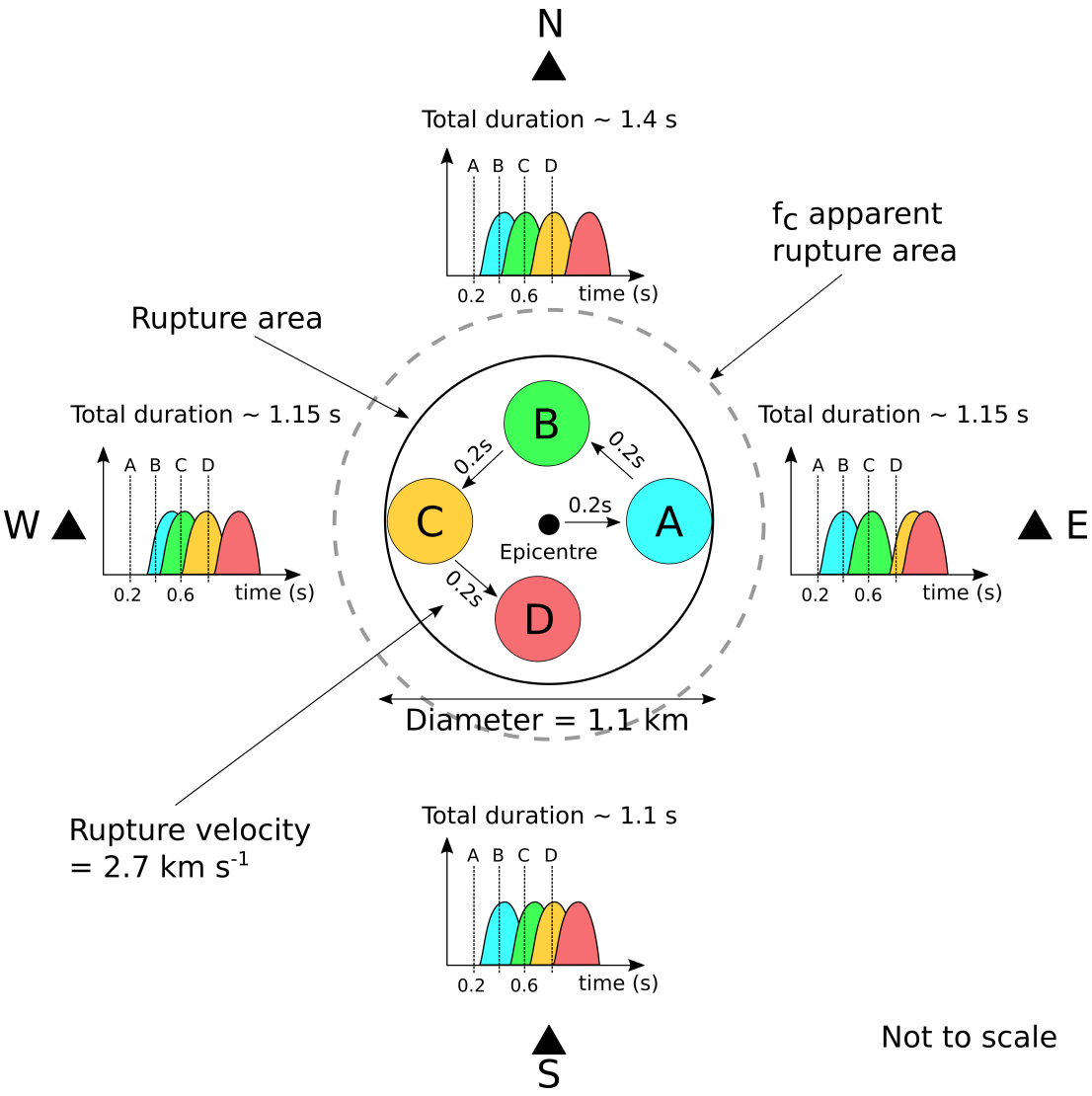

Figure 5.3: The effect of a complex slip distribution on the results of spectral corner frequency-based methods and the phase coherence method. The large black circle indicates the entire earthquake rupture area and the black dot illustrates the epicentre. The four coloured patches marked A-D are different segments of the rupture. Signals at stations (triangles) are plotted through time with the signal from each segment coloured by the colour of the segment. Total durations of the apparent source time function are given for each station. The signal of each segment arrives at a different time in the source time function depending on the relative distance between the segment and the station. Signals from A and C have the largest difference in arrival times between stations as shown by their early or late arrivals at stations E and W. Signals B and D have the next largest difference shown in their arrival times at stations N and S.

stress drops suggests that the phase coherence method does not estimate systematically shorter apparent rupture extents than conventional spectral corner frequency-based methods. Interestingly, I also observe a slight moment dependence of stress drop (Sec. 5.1.2) whereas most previous studies find that stress drops do not depend on moment (e.g., *Abercrombie*, 1995, *Mori et al.*, 2003, *Shearer et al.*, 2006, *Chen and Shearer*, 2011, *Uchide et al.*, 2014, *Chen and McGuire*, 2016, *Abercrombie et al.*, 2017, *Yoshida et al.*, 2017). Perhaps the moment dependence I observe reflects the difference between the phase coherence method and spectral corner frequency-based methods. If larger magnitude earthquakes have more complex ruptures than smaller earthquakes, then one might expect that spectral corner frequency-based methods overestimate rupture extents by increasing amounts as the magnitude of the earthquake increases. The overestimated rupture extents could obscure an increase in stress drop with moment. The phase coherence method, however, would not overestimate the rupture extents so may observe the increase in stress drop with moment. Note, however, that I study only two regions here and relatively few earthquakes, so further work is needed to test the behaviour of the results of the phase coherence method against the behaviour of the results of spectral corner frequency-based methods.

Spectral corner frequency-based methods have several advantages over the phase coherence method, as there are several sources of uncertainty which do not affect these methods as much as they affect the phase coherence method. These sources of uncertainty include the trace alignment (Sec. 2.6.2; Sec. 3.4.1), the noise at higher frequencies, and depth phase arrivals (Sec. 2.6.6; Sec. 3.4.5). The trace alignment is the first step in removing the path effects, and a poor alignment will result in an apparent phase difference between events which reduces the phase coherence at high frequencies. I estimated the accuracy of the trace alignment for the data from earthquakes on the Blanco fault in Figure 2.6. The quality of alignment in that case meant that I could not obtain falloff frequencies which were equal to or above 3.7 Hz, as they may have been systematically biased to lower values by the poor alignment. The quality of alignment depends on the signal-to-noise ratio of the data and the clarity of the arrivals. For example, the alignment uncertainty for the P and S wave in Chapter 3 had less of an effect on lower frequencies than the alignment uncertainty of the P wave in Chapter 2 (Figure 5.4) because I accepted fewer stations with lower signal-to-noise ratios in Chapter 3. Alignment is less important for spectral corner frequency-based methods, as these methods require only a rough window that includes the earthquake source time function, and any minor shifts of the window outside of the arrival will make little difference as long as the window captures most of the earthquake.

High frequency noise has more of an effect on the results of the phase coherence method than the results of conventional spectral corner frequency-based methods. The

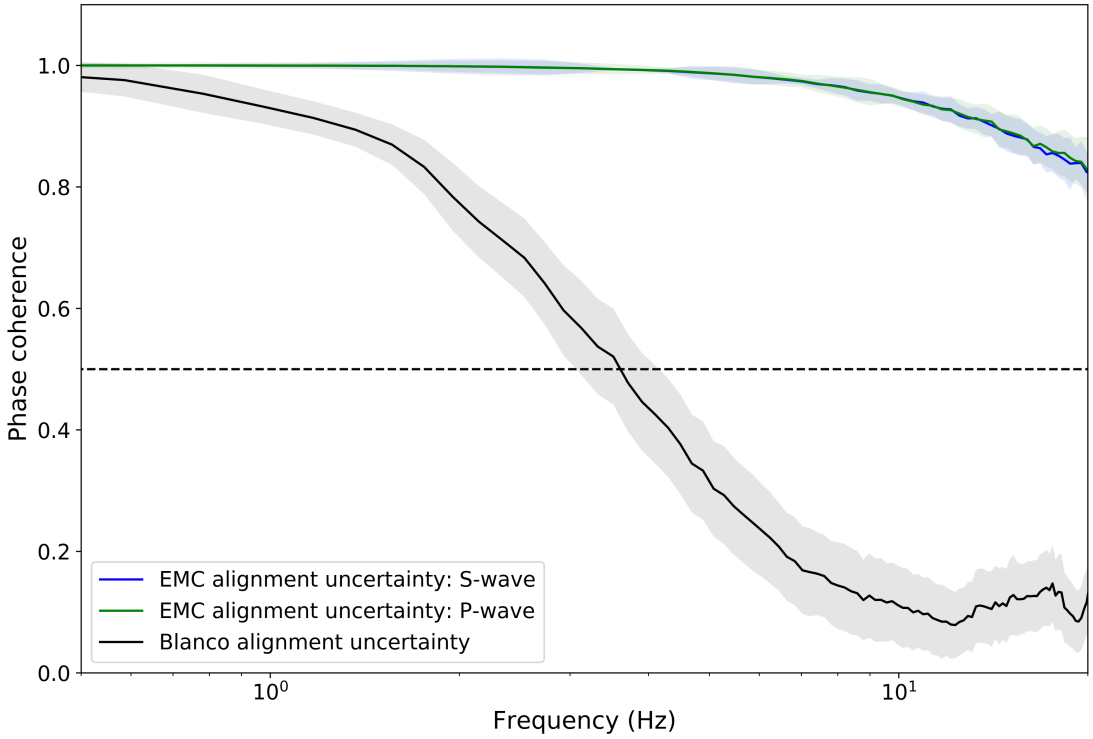

Figure 5.4: The effect of alignment uncertainty on the phase coherence for the results on the Blanco fault (Chapter 2) is plotted in black. The effect of alignment uncertainty from the results of the El Mayor-Cucapah aftershocks for the S wave and P wave (Chapter 3) in blue and green, respectively. The 95% confidence intervals on the effect of alignment uncertainty for each dataset are indicated by the shaded areas. The black dashed line indicates a constant coherence of 0.5 at all frequencies.

falloff frequency of an earthquake tends to be significantly higher than the corresponding corner frequency. Whilst the corner frequency for a M 5 earthquake might be around 1 Hz (Figure 1.2), the falloff frequency of the same earthquake is likely to be around 2 - 4 Hz (e.g., Figure 2.10). Thus the effect of high frequency noise is more of a problem for the phase coherence method. One approach to mitigate this could be to use the S wave rather than the P wave when estimating the falloff frequency of an earthquake. The falloff frequency of the S wave will be lower than the falloff frequency of the P wave because of the slower propagation velocity of the S wave. I analysed both the P wave and S wave in Chapter 3. The results of the S wave were relatively consistent with the results of the P wave, so the S wave may be a viable alternative to the P wave if higher frequencies are particularly noisy.

Depth phase arrivals in the analysed time window of the phase coherence method will also decrease the coherence, and may cause the falloff frequency to be underestimated (Sec. 2.6.6; Sec. 3.4.5). To mitigate this effect, I discarded stations that may include depth phase arrivals in the 5-s window in Chapter 2. I could not discard stations in Chapter 3 because of lower signal-to-noise ratios for more distant stations, so depth phases may have limited the resolution of falloff frequencies of shallow earthquakes in Chapter 3. For spectral corner frequency-based methods, depth phases can cause resonance in the earthquake spectrum estimated using spectral decomposition methods (*Allmann and Shearer*, 2009). *Allmann and Shearer* (2009) also noted, however, that the resonance did not affect their estimated corner frequencies.

Other problems with the phase coherence method can be caused by the smaller earthquakes that larger earthquakes are paired with. If the larger and smaller earthquakes are part of the same repeating earthquake sequence, then the phase coherence will remain high to extremely high frequencies and fall off at a high frequency which does not represent the rupture extent of the larger earthquake (Sec. 3.4.6). On the other hand, if the smaller earthquake has a larger rupture extent than the larger earthquake, then the larger rupture extent of the smaller earthquake will cause the falloff frequency of the earthquake pair. The falloff frequency will thus not correspond to the rupture extent of the larger earthquake (Sec. 3.4.7). Both of these cases change the falloff frequency of the larger earthquake, and both are difficult to identify automatically. Repeating earthquakes can be removed using a phase coherence and signal fraction matching approach, as I did visually in Chapter 3, but identifying which falloff frequencies belong to the smaller earthquake of a pair due to a larger rupture extent is much more difficult. To identify smaller earthquakes which have large rupture extents, the smaller earthquake must feature in pairs with even smaller earthquakes, so that the falloff frequency of the smaller earthquake can be isolated independently of the large earthquake. Alternatively, the large earthquake must have enough consistent

falloff frequency estimates that the falloff frequency of the small earthquake with the large rupture extent does not match the distribution of falloff frequencies and can be excluded. The possibility of repeating earthquakes and small earthquakes with large rupture extents must be considered with caution, and both act as limitations on the use of the phase coherence method. Note, however, that both examples I give here will also cause problems for spectral corner frequency-based methods.

The next step to validate results from the phase coherence method is to apply both phase coherence and spectral corner frequency-based methods to the same dataset. Using these methods together would allow one to look at rupture properties that neither individually allow. As I discussed above, the phase coherence method may find a smaller, more accurate rupture radius than corner frequency methods for some complex ruptures, and comparing the differences in these radii may help to investigate how common complex ruptures are. Comparing the results of different methods may also illustrate variations in the rupture velocity for different earthquakes, as spectral corner frequency-based methods obtain an estimate of the rupture duration, and the phase coherence method estimates the rupture extent. By comparing the rupture duration and extent from the two methods, one can isolate the rupture velocity. The rupture velocity is currently difficult to estimate and involves computing- and time-intensive modelling of the earthquake rupture (e.g., *Fan and Shearer*, 2015, *Grandin et al.*, 2015). Using both methods as described above would simplify this process and may allow the rupture velocity to be estimated for many earthquakes, which could help us to better understand the rupture process.

Future work could also test the resolution of the phase coherence method and whether the method could be useful for problems outside of earthquake seismology. For example, could the method be used on acoustic emissions within a dam to examine the size of any possible cracks? It will be interesting to see new and innovative applications for the phase coherence method and how the method can be used to investigate the physics of earthquake rupture.

5.3.2 Identifying repeating earthquakes without cross correlation

I used a simple approach to identify pairs of repeating earthquakes (two-earthquake sequences) in Chapter 4. The approach is simpler and faster than the usual methods for identifying repeating earthquakes. Most studies (e.g., *Nadeau and Johnson*, 1998, *Lengliné and Marsan*, 2009, *Materna et al.*, 2018) compare the waveforms of earthquakes through cross correlation and select earthquakes with high cross correlation coefficients as repeating earthquakes. Here I identified repeating earthquakes using distance and magnitude thresholds similar to these previous studies but did not examine

the waveforms of earthquakes.

The observation of varying recurrence interval-moment scaling with distance between repeating earthquake sequences discussed earlier (Sec. 5.2) is only reliable if my simple approach correctly identifies repeating earthquakes. The 0.3 magnitude difference threshold and rupture radius-based location threshold I use to identify repeating earthquakes are similar to the approach of *Lengliné and Marsan* (2009) and other repeating earthquake studies (e.g., *Nadeau and Johnson*, 1998, *Peng and Ben-Zion*, 2005, *Chen and McGuire*, 2016, *Materna et al.*, 2018), but the lack of a cross correlation-based threshold could mean some sequences are composed of unrelated earthquakes. To test this, I compared my sequence catalog with the catalog of *Lengliné and Marsan* (2009) (Figure 5.5). I correctly identify 22.5% of the pairs of earthquakes in the sequences catalog of *Lengliné and Marsan* (2009). At first glance, the low proportion of similar pairs suggests that my approach does a poor job of finding repeating earthquakes. However, 60.8% of the pairs in the catalog of *Lengliné and Marsan* (2009) are excluded because I do not use any earthquakes after the 2004 Parkfield earthquake or any earthquakes shallower than 4 km depth, and 4.6% are excluded because I use a higher completeness magnitude of 1.3 compared to the completeness magnitude of 1.2 that *Lengliné and Marsan* (2009) used. The remaining 12.1% of earthquake pairs are not identified because they do not meet the 0.3 magnitude difference threshold or the rupture radius-based location threshold or in some cases because they form earthquake pairs with earlier earthquakes.

If I exclude pairs of earthquakes which were not within my region and magnitude range of interest, then I correctly identify 65% of the pairs of earthquakes. The remaining 35% of earthquake pairs which I failed to identify could be caused by changes in the earthquake magnitude and location in the NCSN catalog in the ten years between the study of *Lengliné and Marsan* (2009) and my study. The simple non-cross correlation based approach identifies over half of the repeating earthquakes found by cross correlation, so does a reasonable job of identifying repeating earthquakes. The simple approach to identify repeating earthquakes also finds a recurrence interval-moment scaling of $M_0^{\frac{1}{6}}$ (Figure 4.3), which is similar to the $M_0^{0.17}$ recurrence interval-moment scaling of repeating earthquakes from previous studies (e.g., *Nadeau and Johnson*, 1998, *Lengliné and Marsan*, 2009).

It is possible that any misidentification of repeating earthquakes is not a problem. Consider that the change in slip rate of fault strands may affect the rate of all earthquakes on the fault strand, and not just recurrence intervals of repeating earthquakes. If this is true then the change in fault scaling with distance may indicate a much more fundamental relation where the slip behaviour of an array of fault strands controls

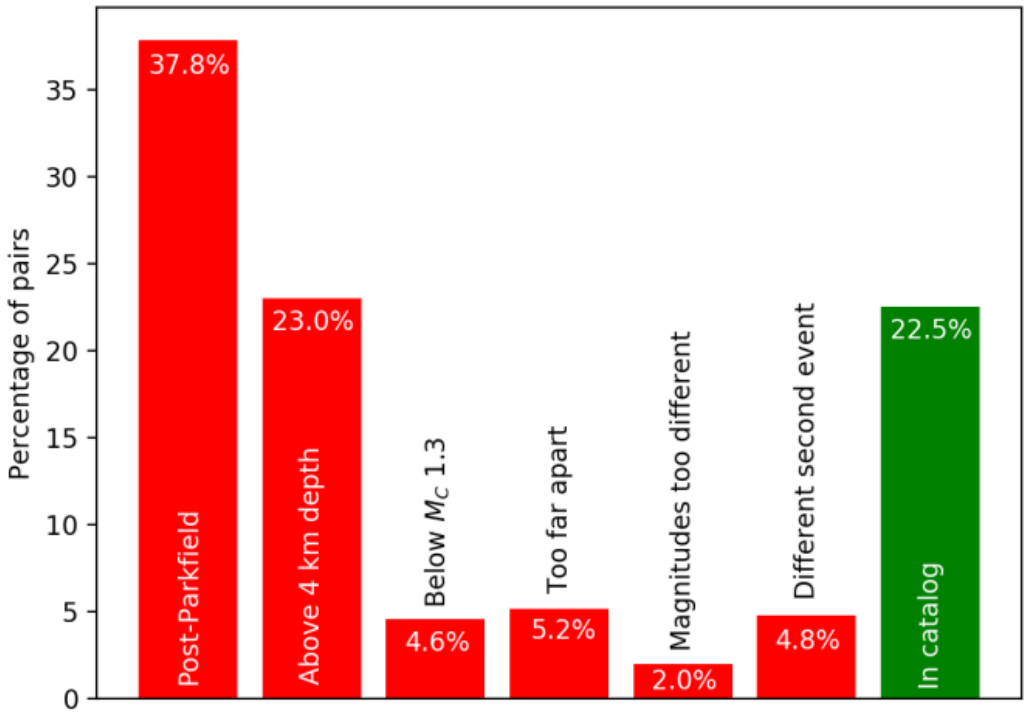

Figure 5.5: The reasons that pairs of earthquakes from the sequences in the catalog of *Lengliné and Marsan* (2009) were excluded from my data analysis. Red bars indicate reasons that pairs were excluded and the green bar indicates the percentage of pairs that were included in the repeating earthquake catalog in my study. From left to right these reasons refer to: one of the earthquakes in the pair being after the 2004 M_W 6.0 Parkfield earthquake, one of the earthquakes being above 4 km depth, both of the earthquakes being below the completion magnitude of 1.3, the earthquakes being too far apart, the difference in earthquake magnitudes exceeding the 0.3 threshold, and the first earthquake of the pair getting paired with an earlier event in the simpler approach.

earthquake occurrence. The change in recurrence interval-moment scaling should then also occur in general earthquake catalogs, not just in repeating earthquake catalogs. If the slip rate depends on the fault strand or spatial location, then seismic hazard estimates should take this into account, and it may allow seismic hazard estimates to be made on a small spatial scale. Note, however, that extensive further testing of this hypothesis is needed before a fundamental relation between fault strands and earthquake occurrence can be inferred.

The approach I used to identify repeating earthquakes is simple and fast and reliably identifies repeating earthquakes when compared with previous studies of the same area. The simplified approach could significantly speed up the identification of repeating earthquakes and allow further investigation into the relation between repeating earthquakes and fault properties in more regions. It may also allow investigation of repeating earthquakes in areas with lower signal-to-noise ratios, as long as the uncertainties on the locations of earthquakes in the catalog are relatively low.

5.4 Conclusions and Key Findings

In this thesis, I used new methods to examine the effect of aseismic slip and fault properties on earthquake properties. I examined the effect of aseismic slip on stress drops of earthquakes on the Blanco fault (Chapter 2) and on stress drops of aftershocks of the 2010 M_W 7.2 El Mayor-Cucapah earthquake (Chapter 3). I obtained these stress drops using the phase coherence method, a new method which uses the variation of apparent source time functions to estimate the rupture extent. I further developed the phase coherence method by applying it in regions with lower data quality, and identified sources of uncertainty that must be counteracted, such as the effect of alignment. I also found that the S wave is a viable alternative to the P wave for applications of the phase coherence method. Using the phase coherence method, I found that the interaction between aseismic slip and stress drops varies between regions, which suggests there is no simple relationship between aseismic slip and earthquake properties.

I also looked at whether the unexpected recurrence interval-moment scaling of repeating earthquakes could be explained using fault strand-dependent slip rates (Chapter 4). I hypothesised that spatially variable slip rates can be used to explain the scaling of recurrence intervals with moments of repeating earthquakes. I detected these repeating earthquakes using a simple approach which does not involve cross correlation. I found that this simple approach identifies the majority of repeating earthquakes identified by previous cross correlation-based approaches. I found that the unexpected recurrence interval-moment scaling of repeating earthquakes may occur because of spatially varying slip rates. Here, I describe the key findings of my thesis and suggest

future work that could test some of the behaviours of earthquake properties that I observed. I also suggest how future work could take advantage of the phase coherence method or the simple approach for detecting repeating earthquakes.

Key Finding 1: Stress drops of earthquakes may depend on the aseismic slip.

In Chapters 2 and 3, I examined the stress drops of earthquakes using the phase coherence method. In Chapter 2, I obtained stress drops of earthquakes along the Blanco fault, off the coast of Oregon, U.S.. My work was some of the first to estimate stress drops of earthquakes on the Blanco fault. The seismic coupling, or proportion of moment released by earthquakes compared to aseismic slip, varies along the Blanco fault, with a more coupled southeastern half of the fault and less coupled northwestern half (*Braunmiller and Nábělek*, 2008). I observed that stress drops were a factor of 1.7 higher for earthquakes on the more coupled southeastern half of the fault, similar to the degree of variation in stress drops on other faults with varying coupling (e.g., *Moyer et al.*, 2018). The factor of difference in stress drops suggests that aseismic slip can affect the properties of earthquakes. I suggested that mantle upwelling under the northwestern segment of the fault (*Byrnes et al.*, 2017) may result in a smaller seismogenic zone, which can be loaded more quickly by aseismic slip and have a shorter seismic cycle. A shorter seismic cycle gives the asperities on the fault less time to heal, reducing their shear strength and thus the stress drop.

In Chapter 3, I obtained stress drops of aftershocks of the 2010 M_W 7.2 El Mayor-Cucapah earthquake. I observed that the stress drops of these aftershocks increased with time since the main shock when analysing the P wave. I also observed that the stress drops of these aftershocks decreased with time since the main shock when analysing the S wave. Both of these trends are low amplitude and not robust. The lack of a systematic change in stress drops with time for both waves suggests that the stress drops do not change with aseismic slip rate.

The variation in the interaction of aseismic slip with stress drops of earthquakes suggests that the interaction is complex and that other factors may change the effect that aseismic slip has on earthquake properties. I suggested several mechanisms for the possible variation in stress drops with aseismic slip including a shorter seismic cycle, the presence of serpentinite, and pore pressure effects. The interaction of aseismic slip and stress drops merits further examination, which could include more data analysis or earthquake modelling. It would be interesting to see if the interaction of aseismic slip and stress drops can be replicated in studies of other faults with varying coupling along their length and if the behaviour of aftershock stress drops is indeed linked to

the post-seismic slip rate.

Key Finding 2: The unexpected scaling of recurrence intervals with moments of repeating earthquakes may be explained by spatially variable slip rates.

In Chapter 4, I tested whether the unexpected recurrence interval-moment scaling of repeating earthquakes in Parkfield, California, can be explained by multiple fault strands within a larger fault zone. I hypothesised that the slip rate on each fault strand increases with its length, assuming that all faults originate at the same time. To test this, I compared the relative recurrence intervals and moments of repeating earthquake sequences with the distance between them. I found that closely spaced sequences, which likely occur on the same fault strand with the same slip rate, follow a recurrence interval-moment scaling of $M_0^{\frac{1}{3}}$, whilst widely spaced sequences, which likely occur on different fault strands with different slip rates, follow a recurrence interval-moment scaling of $M_0^{\frac{1}{6}}$, similar to the unexpected recurrence interval-moment scaling of $M_0^{0.17}$ observed in previous studies (e.g., *Nadeau and Johnson*, 1998, *Lengliné and Marsan*, 2009). The variation in recurrence interval-moment scaling with the distance between sequences suggests that the unexpected recurrence interval-moment scaling can be explained by spatially variable slip rates or slip rates that depend on the length of a fault strand. Thus, perhaps authors should be careful when inferring aseismic slip from the recurrence intervals of repeating earthquakes and should not use the inferred aseismic slip to inform seismic hazard analysis (e.g., *Bürgmann et al.*, 2000, *Schmidt et al.*, 2005).

If slip rates that depend on the length of a fault strand do determine the recurrence intervals of repeating earthquakes, then earthquake properties may be fundamentally determined by fault properties. To explain the recurrence interval-moment scaling, I assumed that the slip rate of the fault strand scales with its length following a power-law distribution. A power-law distribution suggests that fault properties may be self-similar, but this assumption requires further investigation.

The fault strand-dependent slip rate scaling I suggest here to explain the behaviour of repeating earthquakes needs further testing in the lab, testing with earthquake modelling, and supporting observations in the field. One way this scaling could be tested is to apply my approach to other earthquake catalogs, to see if the same recurrence interval-moment scaling variation is observed with the distance between repeating earthquake sequences. These catalogs would need accurate locations to allow the separation of different fault strands. Possible catalogs which would be appropriate include induced seismicity catalogs (e.g., *Schoenball and Ellsworth*, 2017), although these cat-

alogs may not follow the same relation due to the induced nature of their seismicity. It would also be interesting to see if this repeating earthquake behaviour can be replicated in the lab at centimetre to millimetre scales, which would also test whether the power-law scaling of slip rate with the length of a fault strand is correct.

Key Finding 3: Further development of the inter-station phase coherence method.

In Chapters 2 and 3, I used and further developed the inter-station phase coherence method to obtain stress drops of earthquakes (*Hawthorne and Ampuero*, 2017, *Hawthorne et al.*, 2018, *Williams et al.*, 2019). The phase coherence method uses variations in apparent source time functions to estimate the rupture extent of earthquakes, and thus the stress drop. My work is some of the first to use this method to obtain the stress drops of earthquakes and some of the first to test the functionality of the phase coherence method on distant earthquakes using the offshore earthquakes on the Blanco fault in Chapter 2. I also further developed the phase coherence method by applying it to both the P wave and S wave in Chapter 3. I found that the results of the P wave and S wave were relatively consistent which suggests that the S wave may be a useful alternative to the P wave if the higher falloff frequencies of the P wave are obscured by noise at high frequencies.

The phase coherence method has several advantages and disadvantages when compared to conventional spectral corner frequency-based methods. One advantage is that the results of the phase coherence method depend more strongly on the propagation wave velocity in the rupture area than on the rupture velocity. As the propagation wave velocity is normally well known to within 10%, and the rupture velocity is usually assumed to be 75 - 90% of the shear wave velocity, the rupture velocity is more uncertain and therefore a weaker dependence on the rupture velocity may improve the accuracy of stress drop estimates. The phase coherence method may also provide a more accurate estimate of the rupture extent of an earthquake as the method does not rely on the rupture duration, as opposed to spectral corner frequency-based methods which infer the extent from the duration. An example of how using the rupture duration may overestimate the rupture extent of an earthquake is discussed above (Sec. 5.3.1).

However, the phase coherence method also has several sources of uncertainty which do not significantly affect the results of spectral corner frequency-based methods. These uncertainties include the accuracy of trace alignment and the occurrence of depth phases in the analysis window. I discussed how some of the sources of uncertainty can be mitigated in Chapters 2 and 3.

The phase coherence method offers a new approach for examining the properties of earthquakes, which could be combined with existing spectral corner frequency-based methods to look at earthquake properties such as the rupture velocity, which are otherwise difficult to examine. Future work could use these methods together to examine the differences in stress drops estimated using each method and to examine what these differences suggest about the rupture properties of earthquakes such as the rupture velocity.

Key Finding 4: A simple non-cross correlation based approach successfully identifies repeating earthquakes.

In Chapter 4, I identified repeating earthquakes in Parkfield, California, using a simple approach which does not rely on cross correlation of seismic records. I identified pairs of earthquakes as repeating earthquakes if their locations were within one earthquake radius (plus location uncertainty) and within 0.3 magnitude units. Although one might expect this approach to be more error prone due to the lack of cross correlation, I identified similar repeating earthquake sequences to previous work (Figure 5.5). I also observed the same unexpected recurrence interval-moment scaling as previous studies (Figure 4.3) (e.g., *Nadeau and Johnson*, 1998, *Lengliné and Marsan*, 2009).

The simple non-cross correlation based approach for identifying repeating earthquakes appears to correctly identify repeating earthquakes. However, further work is needed to test the performance of the simple approach on other earthquake catalogs, especially those that are of lower quality than the earthquake catalog in Parkfield, California. The simple approach offers an easier and faster approach to examine the behaviour of repeating earthquakes, without the time-consuming process of cross correlating seismic records. Future work may be able to take advantage of this simple approach when waveforms are difficult to cross-correlate due to low signal-to-noise ratios.

5.5 Concluding Remarks

In this thesis I have investigated the interaction of fault properties and aseismic slip with earthquake properties. I have further developed the inter-station phase coherence method for examining the rupture extent and thus the stress drop of earthquakes, which offers a new approach that can be used with existing methods to examine the properties of earthquakes such as the rupture velocity. I used the phase coherence method to obtain some of the first stress drops for earthquakes on the Blanco fault and to estimate stress drops of aftershocks of the 2010 M_W 7.2 El Mayor-Cucapah earthquake. I identified an interaction between aseismic slip and the stress drops of

earthquakes. The stress drops of earthquakes on more coupled segments of the Blanco fault were higher than the stress drops of earthquakes on less coupled segments. The stress drops of aftershocks of the El Mayor-Cucapah earthquake may also increase as the post-seismic slip rate decreases, but this trend is not robust.

I also used a simple approach to identify pairs of repeating earthquakes in Parkfield, California and to investigate the cause of the unexpected recurrence interval-moment scaling of repeating earthquakes. This simple approach finds similar repeating earthquakes to previous cross correlation-based approaches and offers a simpler and faster approach to analyse repeating earthquakes. I found that the recurrence interval-moment scaling of repeating earthquakes varied with the distance between them and thereby showed that the unexpected recurrence interval-moment scaling of repeating earthquakes can be explained by spatially variable slip rates. This explanation suggests that fault properties may fundamentally determine the recurrence intervals and moments of earthquakes.

This thesis has improved our understanding of the interaction of earthquake properties and aseismic slip and has further established the inter-station phase coherence method and the simple method for identifying repeating earthquakes as useful approaches for future investigation of earthquake properties.

Appendix A

Appendix for Chapter 2

A.1 Networks

Here, I give details on the networks I used in this study (Table A.1).

Table A.1: Table of networks used in this study. COLZA/OSU: Central Oregon Locked Zone Array/Oregon State University

Network Code	Full name	Number of stations used	Citation
5E	Cascadia Initiative	10	Anne Trehu (2014): Cascadia Initiative. International Federation of Digital Seismograph Networks. Other/Seismic Network. https://doi.org/10.7914/SN/5E_2014
7A	Cascadia- Keck	10	Scherwath M., Spence G., Obana K., Kodaira S., Wang K., Riedel M., McGuire J., and Collins J., 2011. Seafloor seismometers monitor northern Cascadia earthquakes. Eos, Transactions American Geophysical Union 92(47) pp.421-422.
7D	Cascadia Initiative Community Experiment-OBS component	252	IRIS OBSIP (2011): Cascadia Initiative Community Experiment - OBS Component. International Federation of Digital Seismograph Networks. Other/Seismic Network. https://doi.org/10.7914/SN/7D_2011
BK	Berkeley Digital Seismograph Network	23	Northern California Earthquake Data Center. (2014). Berkeley Digital Seismic Network (BDSN) Data set. Northern California Earthquake Data Center. https://doi.org/10.7932/bdsn
CC	Cascade Chain Volcano Monitoring	34	Cascades Volcano Observatory/USGS (2004): Cascade Chain Volcano Monitoring. International Federation of Digital Seismograph Networks. Other/Seismic Network. https://doi.org/10.7914/SN/CC
CN	Canadian National Seismograph Network	73	Geological Survey of Canada (1989): Canadian National Seismograph Network. International Federation of Digital Seismograph Networks. Other/Seismic Network. https://doi.org/10.7914/SN/CN
HW	Hanford Washington Seismic Network	3	Rohay A.C. Clayton R.E. Sweeney M.D. Devary J.L. and Hartshor D.C. 2010. Annual Hanford Seismic Report for Fiscal Year 2010 (No. PNNL-20084). Pacific Northwest National Laboratory (PNNL) Richland, WA (U.S.).
LI	Laser Interferometer Gravitational-Wave Experiment (LIGO)	1	California Institute of Technology (Caltech) (2000): Laser Interferometer Gravitational-Wave Experiment (LIGO). International Federation of Digital Seismograph Networks. Other/Seismic Network. https://doi.org/10.7914/SN/LI

NC	USGS Northern California Regional Network	264	USGS Menlo Park (1967): USGS Northern California Network. International Federation of Digital Seismograph Networks. Other/Seismic Network. https://doi.org/10.7914/SN/NC
NN	Western Great Basin/Eastern Sierra Nevada	42	University of Nevada (UNR Reno) (1971): Nevada Seismic Network. International Federation of Digital Seismograph Networks. Other/Seismic Network. https://doi.org/10.7914/SN/NN
NV	Neptune Canada	5	Ocean Networks Canada Data Archive, http://www.oceannetworks.ca, Oceans Networks Canada, University of Victoria, Canada. Downloaded on December 1st 2016.
OO	Ocean Observatories Initiative	12	Rutgers University (2013): Ocean Observatories Initiative. International Federation of Digital Seismograph Networks. Other/Seismic Network. https://doi.org/10.7914/SN/OO
PB	Plate Boundary Observatory Borehole Seismic Network	50	UNAVCO
PN	Princeton Earth Physics Project - Indiana	1	n/a
PO	Portable Observatories for Lithospheric Analysis and Research Investigating Seismicity	26	Eaton D.W. Adams J. Asudeh I. Atkinson G.M. Bostock M.G. Cassidy J.F. Ferguson I.J. Samson C. Snyder D.B. Tiampo K.F. and Unsworth M.J., 2005. Investigating Canada's lithosphere and earthquake hazards with portable arrays. Eos Transactions American Geophysical Union 86(17) pp.169-173.
TA	USArray Transportable Array (National Science Foundation (NSF) EarthScope Project)	148	IRIS Transportable Array (2003): USArray Transportable Array. International Federation of Digital Seismograph Networks. Other/Seismic Network. https://doi.org/10.7914/SN/TA
UO	University of Oregon Regional Network	15	Pacific Northwest Seismic Network
US	United States National Seismic Network	6	Albuquerque Seismological Laboratory (ASL)/USGS (1990): United States National Seismic Network. International Federation of Digital Seismograph Networks. Other/Seismic Network. https://doi.org/10.7914/SN/US

UW	Pacific Northwest Seismic Network	216	University of Washington (1963): Pacific Northwest Seismic Network. International Federation of Digital Seismograph Networks. Other/Seismic Network. https://doi.org/10.7914/SN/UW
WR	California Division of Water Resources	9	n/a
X1	Development and Testing of a Deep-Water, Acoustically-Linked, Moored- Buoy Seafloor Observatory	1	Frye D. Freitag L. Collins J. Grund M. Ware J. Detrick R. Johnson R. Lilley M. Wilcock W. LaBonte A. and Brown K. 2004, December. Deployment of a Deep-Water Acoustically-Linked Moored Buoy Observatory on the Nootka Fault off Vancouver Island. In AGU Fall Meeting Abstracts.
X4	Active Fault Mapping	15	Recep Cakir (2016): Active Fault Mapping. International Federation of Digital Seismograph Networks. Other/Seismic Network. https://doi.org/10.7914/SN/X4_2016
X9	Plate Boundary Evolution and Physics at an Oceanic Transform Fault System (Blanco transform)	5	Oregon State University
XA	Monitoring seismicity associated with a possible asperity on the Cascadia megathrust (COLZA/OSU)	7	Anne Trehu and Mark Williams (2008): Monitoring seismicity associated with a possible asperity on the Cascadia megathrust. International Federation of Digital Seismograph Networks. Other/Seismic Network. https://doi.org/10.7914/SN/XA_2008
XD	Illuminating the architecture of the greater Mount St. Helens magmatic systems from slab to surface	1	Ken Creager (2014): Collaborative Research: Illuminating the architecture of the greater Mount St. Helens magmatic systems from slab to surface. International Federation of Digital Seismograph Networks. Other/Seismic Network. https://doi.org/10.7914/SN/XD_2014
XG	Cascadia Array of Arrays	9	Ken Creager and John Vidale and Steve Malone (2009): Cascadia Array of Arrays. International Federation of Digital Seismograph Networks. Other/Seismic Network. https://doi.org/10.7914/SN/XG_2009
XH	Seismic Array Studies of Cascadia Deep Tremor (Cascadia Tremor)	2	Steve Malone (2004): Seismic Array Studies of Cascadia Deep Tremor. International Federation of Digital Seismograph Networks. Other/Seismic Network. https://doi.org/10.7914/SN/XH_2004

XN	Monitoring seismicity associated with a possible asperity on the Cascadia megathrust (COLZA/OSU)	13	Anne Trehu and Mark Williams (2010): Monitoring seismicity associated with a possible asperity on the Cascadia megathrust. International Federation of Digital Seismograph Networks. Other/Seismic Network. https://doi.org/10.7914/SN/XN_2010
XT	Western Idaho Shear Zone - Passive	28	Ray Russo (2011): Western Idaho Shear Zone - Passive. International Federation of Digital Seismograph Networks. Other/Seismic Network. https://doi.org/10.7914/SN/XT_2011
XU	Collaborative Research: Earthscope integrated investigations of Cascadia subduction zone tremor, structure and process (Cascadia Arrays for Earthscope/University of Washington)	52	Steve Malone and Ken Creager and Stephane Rondenay and Tim Melbourne and Geoffrey Abers (2006): Collaborative Research: Earthscope integrated investigations of Cascadia subduction zone tremor, structure and process. International Federation of Digital Seismograph Networks. Other/Seismic Network. https://doi.org/10.7914/SN/XU_2006
Y3	Wells, Nevada Aftershock Recording (RAMP NV)	10	Glenn Biasi (2008): Wells, Nevada Aftershock Recording. International Federation of Digital Seismograph Networks. Other/Seismic Network. https://doi.org/10.7914/SN/Y3_2008
YG	Collaborative Research: Imaging the Cascadia subduction zone - a ship-to-shore opportunity	39	Anne Trehu and Geoffrey Abers (2012): Collaborative Research: Imaging the Cascadia subduction zone - a ship-to-shore opportunity. International Federation of Digital Seismograph Networks. Other/Seismic Network. https://doi.org/10.7914/SN/YG_2012
YW	Resolving structural control of episodic tremor and slip along the length of Cascadia (Flexarray Along Cascadia Experiment for Segmentation/Berkeley)	23	Mike Brudzinski and Richard Allen (2007): Resolving structural control of episodic tremor and slip along the length of Cascadia. International Federation of Digital Seismograph Networks. Other/Seismic Network. https://doi.org/10.7914/SN/YW_2007
Z3	Detecting Structural changes During an Episodic Tremor and Slip Event: Proof of Concept (Structural change/Carnegie Institute of Washington and Department of Terrestial Magnetism)	5	Silver (2009): Detecting Structural changes During an ETS Event: Proof of Concept. International Federation of Digital Seismograph Networks. Other/Seismic Network. https://doi.org/10.7914/SN/Z3_2009

			John Näbälek and Jochen Braunmiller (2013):
Z5	Seismicity, Structure and Dynamics of the Gorda Deformation Zone	23	Seismicity, Structure and Dynamics of the Gorda Deformation Zone. International Federation of Digital Seismograph Networks. Other/Seismic Network. https://doi.org/10.7914/SN/Z5_2013
ZH	Monitoring seismicity associated with a possible asperity on the Cascadia megathrust (COLZA/OSU)	2	Anne Trehu and Mark Williams (2011): Monitoring seismicity associated with a possible asperity on the Cascadia megathrust. International Federation of Digital Seismograph Networks. Other/Seismic Network. https://doi.org/10.7914/SN/ZH_2011
ZK	Seismic signature of debris flume experiments	2	Kate Allstadt (2016): Seismic signature of debris flume experiments. International Federation of Digital Seismograph Networks. Other/Seismic Network. https://doi.org/10.7914/SN/ZK_2016
ZU	Repeating glacier quakes (clones) on Mount Rainier (Glacier Clones)	1	Steve Malone (2011): Repeating glacier quakes (clones) on Mount Rainier. International Federation of Digital Seismograph Networks. Other/Seismic Network. https://doi.org/10.7914/SN/ZU_2011
ZZ	Collaborative Research: Imaging the Cascadia subduction zone - a ship-to-shore opportunity	15	Anne Trehu and Geoffrey Abers (2012): Collaborative Research: Imaging the Cascadia subduction zone - a ship-to-shore opportunity. International Federation of Digital Seismograph Networks. Other/Seismic Network. https://doi.org/10.7914/SN/ZZ_2012

Table A.2: Results for cross correlation coefficient thresholds of 0.6 and 0.8.

CCC Threshold	Total events $M \geq 5$	Overall median stress drop (95% confidence limits)	NW No. events $M \geq 5$	NW median stress drop	SE No. events $M \geq 5$	SE median stress drop	Factor of difference
0.6	61	8 (6, 12)	30	6 (4, 11)	31	11 (6, 22)	1.7 (0.8, 3.5)
0.8	39	11 (7, 18)	20	8 (5, 14)	19	18 (8, 33)	2.1 (0.8, 4.7)

A.2 Results using a 0.8 cross correlation coefficient threshold

I rerun the phase coherence method, accepting only traces which have a cross correlation coefficient of 0.8 or higher for the 2-s window beginning on the P arrival. I find that the results are similar to those of the main study, where I use a cross correlation coefficient threshold of 0.6. These results are shown in Table A.2, Figure A.1 and Figure A.2.

A.3 Example phase coherence results

This section displays some example phase coherence results from my analysis. The phase coherence spectra are marked in blue with the blue shaded area defining the 95% confidence limits. The black solid lines are the estimated alignment uncertainty derived from the entire loop closure distribution, and the green lines are the estimated alignment uncertainty using only events within 4 km. Both have associated 95% confidence limits plotted as well. The dashed black lines represent the 0.5 coherence threshold for picking the falloff frequency, and the falloff frequency itself. The rest of the figures in this section will have this format.

Figures A.3, A.4, A.5, and A.6 are examples of results for a m_b 4.9 earthquake, which has the National Earthquake Information Center (NEIC) catalog identifier of us10007cvf. Figures A.7, A.8, and A.9 are phase coherence spectra examples for a M_W 5.6 event which has the NEIC catalog identifier usp000j99k, and should have a longer rupture diameter and thus a lower falloff frequency than the m_b 4.9 event.

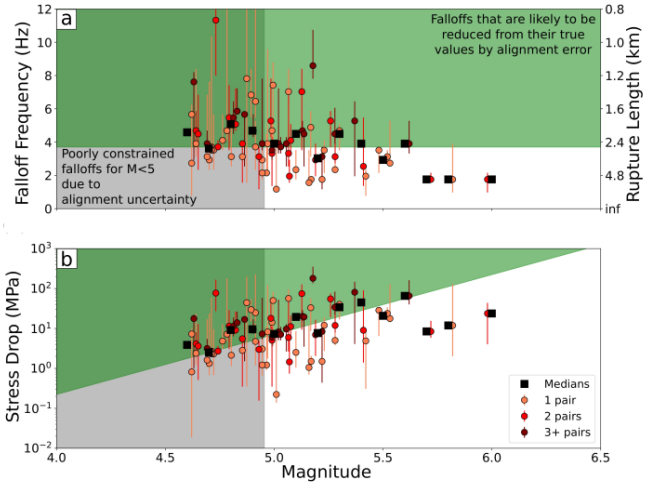

Figure A.1: (a): Falloff frequencies against magnitude for 75 events using a cross correlation coefficient of 0.8. (b): Stress drops plotted against magnitude for the same events using a cross correlation coefficient of 0.8. Note that magnitudes have been shifted by values less than 0.05 to differentiate between data points. Earthquakes with $M < 5.0$ which are unlikely to have the correct falloff frequency are highlighted by the gray shaded area on the plot. The 3.7 Hz limit on reliable falloff frequencies due to the alignment uncertainty is indicated by the green shaded area. Results are colored by the number of earthquake pairs available for each measurement. Lower bounds on falloff frequencies have been limited to 1 Hz due to significant low frequency noise. Medians for 0.1 magnitude bins are plotted as squares.

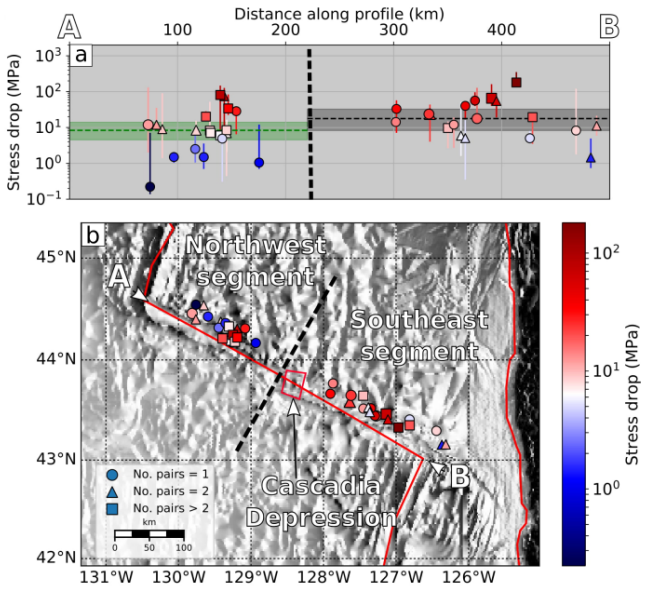

Figure A.2: (a): Stress drops calculated using a cross correlation coefficient of 0.8 for $M \geq 5.0$ earthquakes on the Blanco fault plotted along the fault from A to B. The thick black vertical dashed line in the centre of the plot indicates cutoff point I defined between the northeast and southwest segments (derived from the Cascadia Depression shown as the red square in (b)). Stress drops are colored by amplitude. Symbols indicate the number of earthquake pairs that were available for each measurement. The median stress drops for the northwest and southeast segments are shown by the dashed horizontal green and black lines, respectively. The shaded areas around these medians show the 95% confidence limits. (b): Stress drops for $M \geq 5.0$ earthquakes on the Blanco fault plotted in map view.

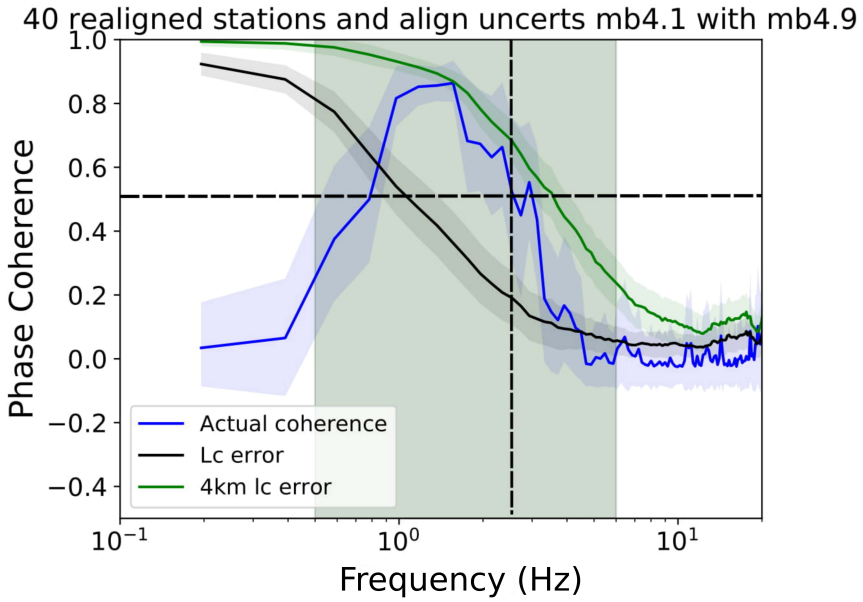

Figure A.3: The phase coherence spectrum for the m_b 4.9 event with a m_b 4.1 event, which has the NEIC catalog identifier us10002bbm.

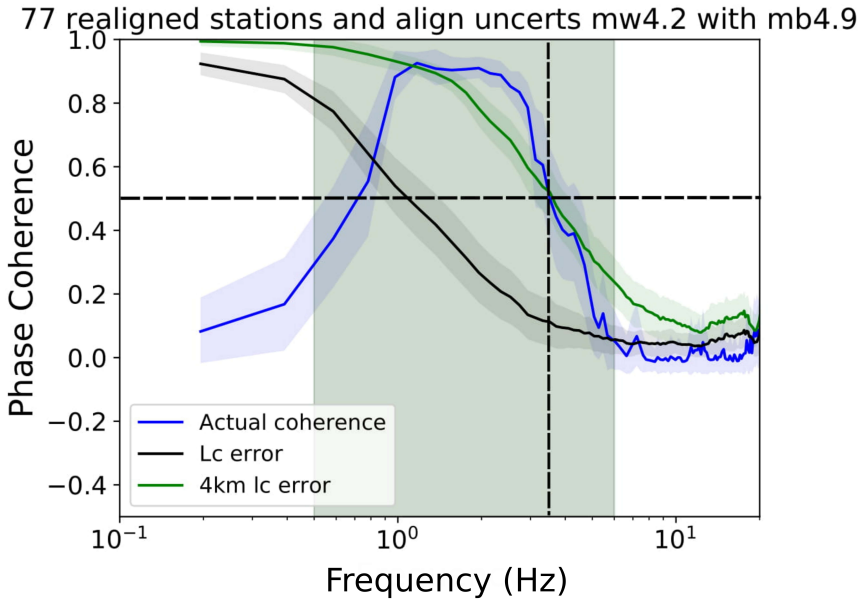

Figure A.4: The phase coherence spectrum for the m_b 4.9 event with a M_W 4.2 event, which has the NEIC catalog identifier us200025te.

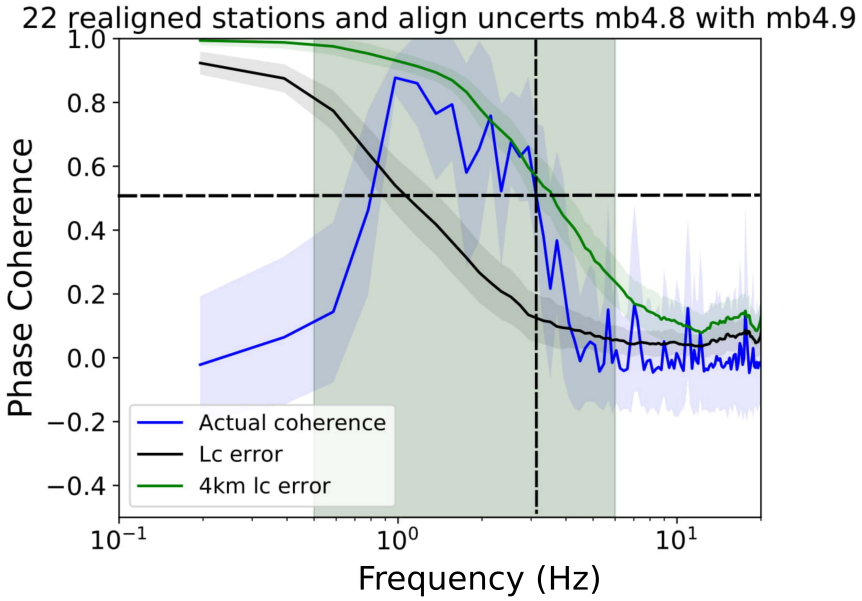

Figure A.5: The phase coherence spectrum for the m_b 4.9 event with a m_b 4.8 event, which has the NEIC catalog identifier usp000gugg.

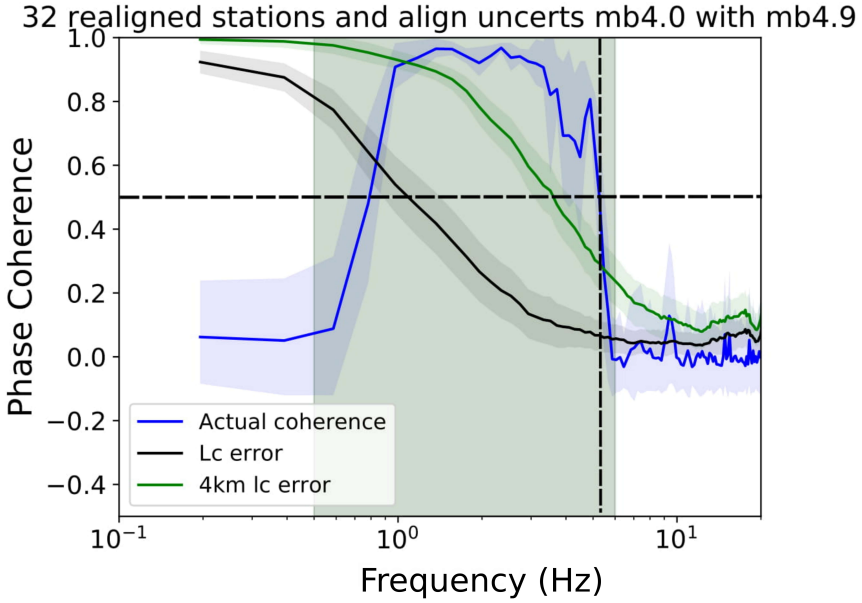

Figure A.6: The phase coherence spectrum for the m_b 4.9 event with a m_b 4.0 event, which has the NEIC catalog identifier usp000grbf.

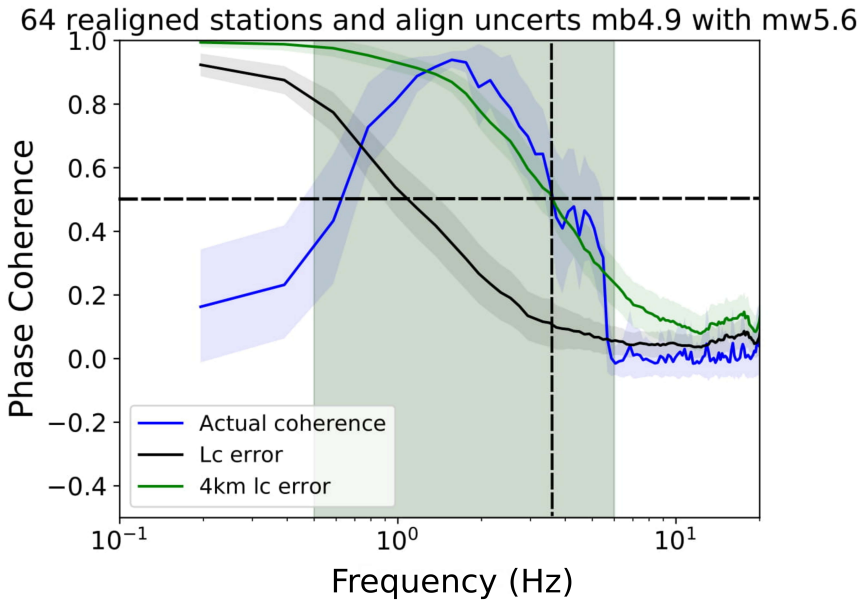

Figure A.7: The phase coherence spectrum for the M_W 5.6 event with a m_b 4.9 event, which has the NEIC catalog identifier us10007cvf.

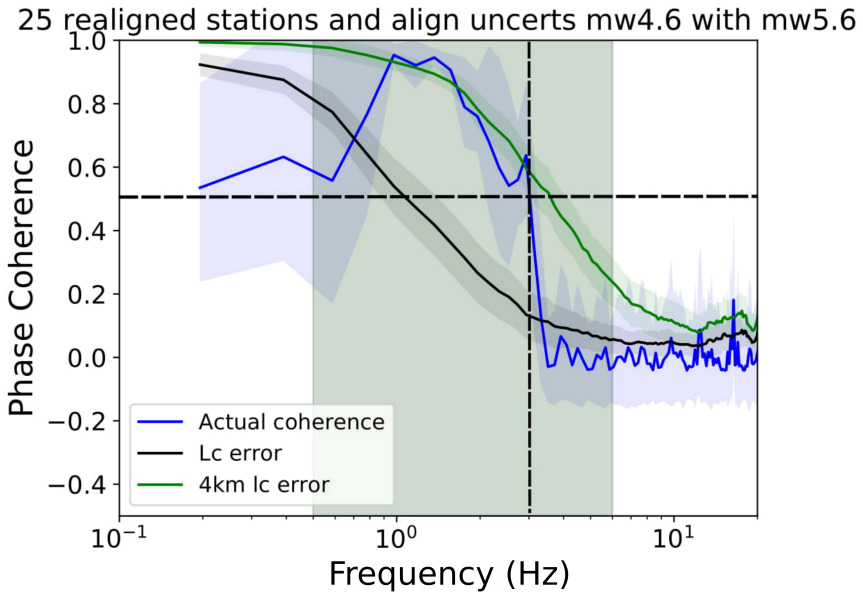

Figure A.8: The phase coherence spectrum for the M_W 5.6 event with a M_W 4.6 event, which has the NEIC catalog identifier usb000rtdy.

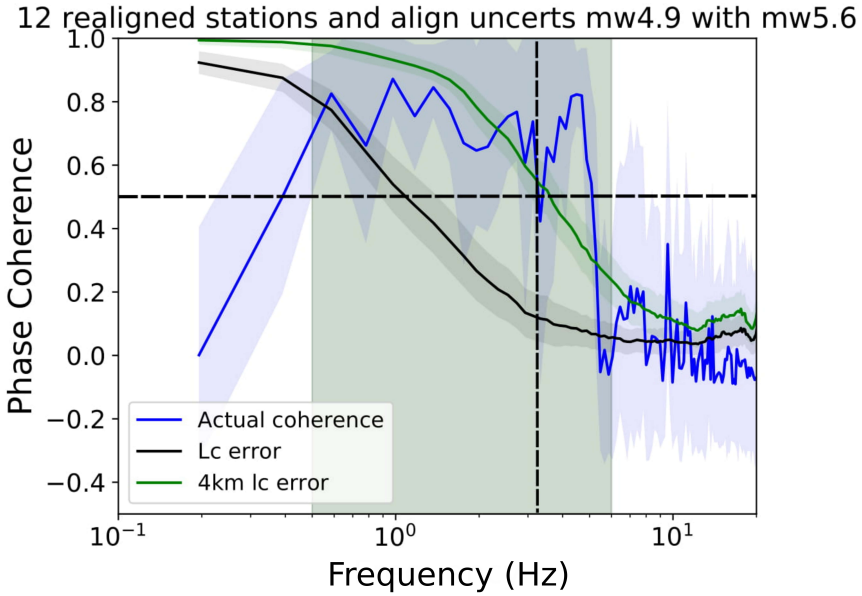

Figure A.9: The phase coherence spectrum for the M_W 5.6 event with a M_W 4.9 event, which has the NEIC catalog identifier usp000j20v.

A.4 Figures for loop closures and trace alignment uncertainties

This section contains histograms of the loop closures discussed in the incorrect trace alignment section, as well as histograms of the alignment uncertainties of traces derived from these loop closures by dividing loop closures by the square root of 3. Figures A.10 and A.11 are histograms of the loop closures and associated alignment errors, respectively, for the entire dataset being used to generate my final results. Figures A.12 and A.13 are histograms of the loop closures and associated alignment errors where I use only event loops where all three events within the loop are within 4 km of each other.

A.5 Azimuthal effect on falloff frequency

The azimuthal distribution of stations used in phase coherence calculation can change the resulting falloff frequency. To model this effect, I collaborated with my supervisor Jess Hawthorne.

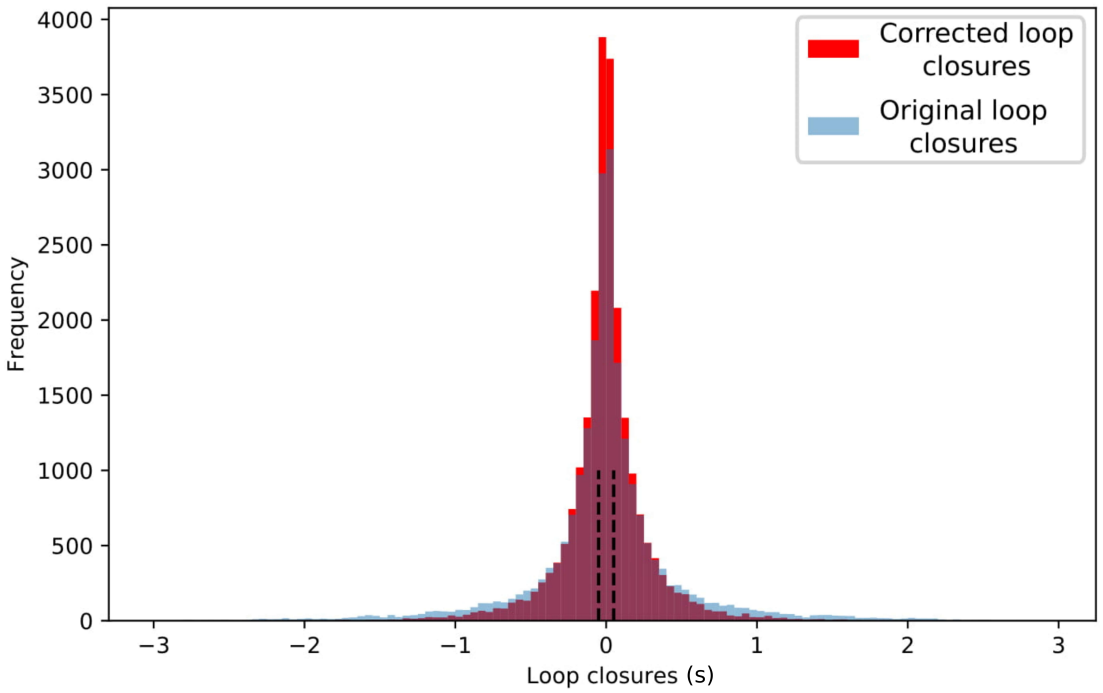

Figure A.10: Histogram of loop closures for the entire dataset. Black dashed lines indicate loop closures of ± 0.05. Loop closures were binned in increments of 0.05. The two colors refer to the original loop closures before I re-estimate alignment times using the event relocation, and after the correction from that process has been applied.

A heterogeneous slip distribution on a roughly circular fault patch was assumed. This heterogeneous slip distribution has a non-zero mean slip and tapers to zero at the edges. This earthquake model was used to generate apparent source time functions for each station around the patch depending on azimuth, convolve them with synthetic Green's functions, and compute the coherence between station cross spectra. Through this, I can evaluate the effect of station azimuthal distribution on the coherence falloff frequency. Figure A.14 shows the results of this analysis, with varying diameters for the smaller earthquake in the pair, and horizontal take-off angles for P waves.

I can infer from these results that for a random distribution of stations, I must include a factor F_{scal} of 1.1 in the rupture diameter calculation to account for the effect of azimuthal variation. I can also infer that the diameter of the smaller earthquake does not systematically affect the falloff frequency I measure, which supports the results I find later in this appendix, where I remove earthquake pairs with low magnitude unit

differences and see no change in my end result. However, I also consider the effect of my azimuthal distribution of stations on my falloff frequency results.

To do this, I obtained station distributions from four representative event pairs in my earthquake catalog, and Jess applied the same approach with heterogeneous slip distributions as in Figure A.14. Figure A.15 shows normalized falloff frequencies using station strikes and take-off angles from the 4 representative event pairs, two with good azimuthal distributions of stations and two with ok distributions. Earthquake diameters from 400 - 600 m at a depth of 10 km are simulated to evaluate any change in normalized falloff frequency with rupture diameter. The median normalized falloff frequency for all four events is around 1.2, and therefore I multiply my rupture diameters by a factor of 1.2 to account for the effect of azimuthal distribution of stations on the falloff frequency.

Finally I also compare my recorded stress drops to the proportion of station pairs for each stress drop that are within 45°, with the factor of 1.2 applied (Figure A.16). There is no clear variation in stress drop with proportion of station pairs that are within 35°, so I can assume the effect of azimuthal variation on the falloff frequency has been eliminated. Figure A.17 helps to illustrate why I find this factor of 1.2.

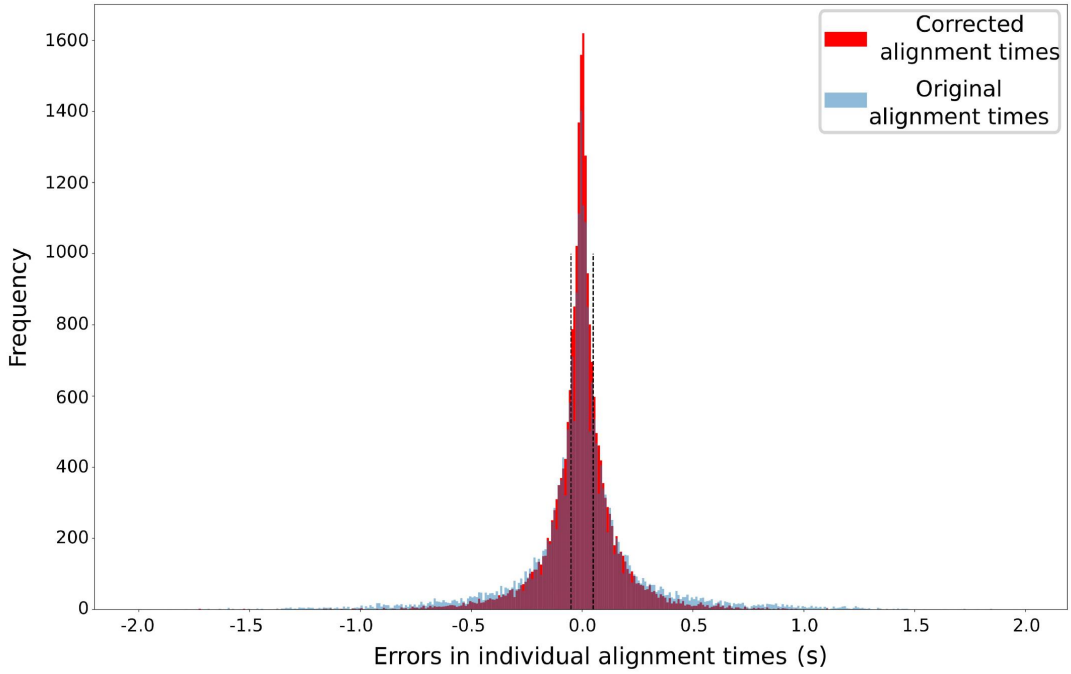

Figure A.11: Histogram of alignment uncertainties for each trace for the entire dataset. Alignment uncertainties were estimated by dividing loop closures by the square root of 3. Black dashed lines indicate alignment uncertainties of ± 0.05. Uncertainties were binned in increments of 0.01. The two colors refer to the original alignment uncertainties before I re-estimate alignment times using the event relocation, and after the correction from that process has been applied.

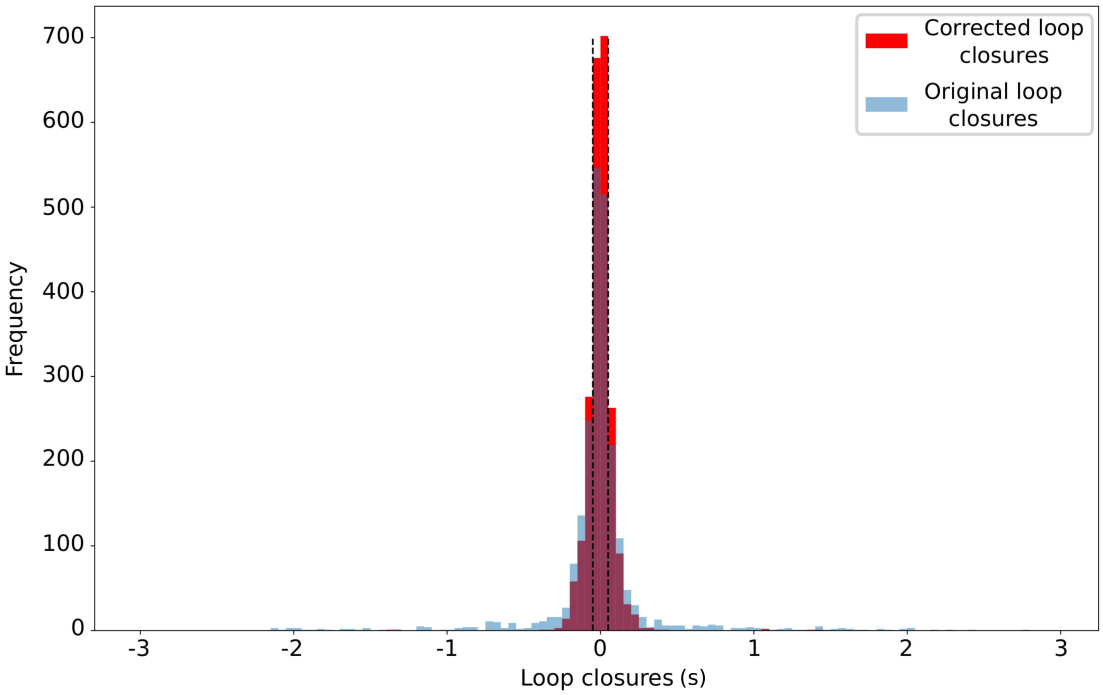

Figure A.12: Histogram of loop closures using only loops where all three events are within 4 km. Black dashed lines indicate loop closures of ±0.05. Loop closures were binned in increments of 0.05. The two colors refer to the original loop closures before I re-estimate alignment times using the event relocation, and after the correction from that process has been applied.

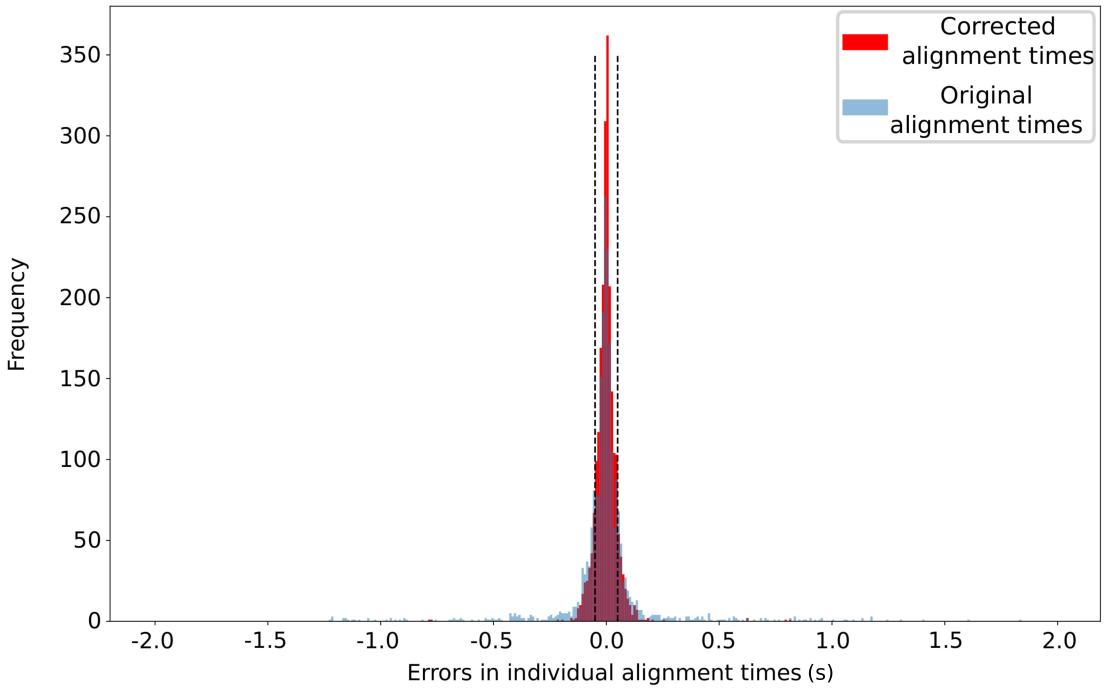

Figure A.13: Histogram of alignment uncertainties for each trace from loops where all three events are within 4 km. Alignment uncertainties were estimated by dividing loop closures by the square root of 3. Black dashed lines indicate alignment uncertainties of ±0.05. Uncertainties were binned in increments of 0.01. The two colors refer to the original alignment uncertainties before I re-estimate alignment times using the event relocation, and after the correction from that process has been applied. 80% of traces fall within 0.05 s of true alignment.

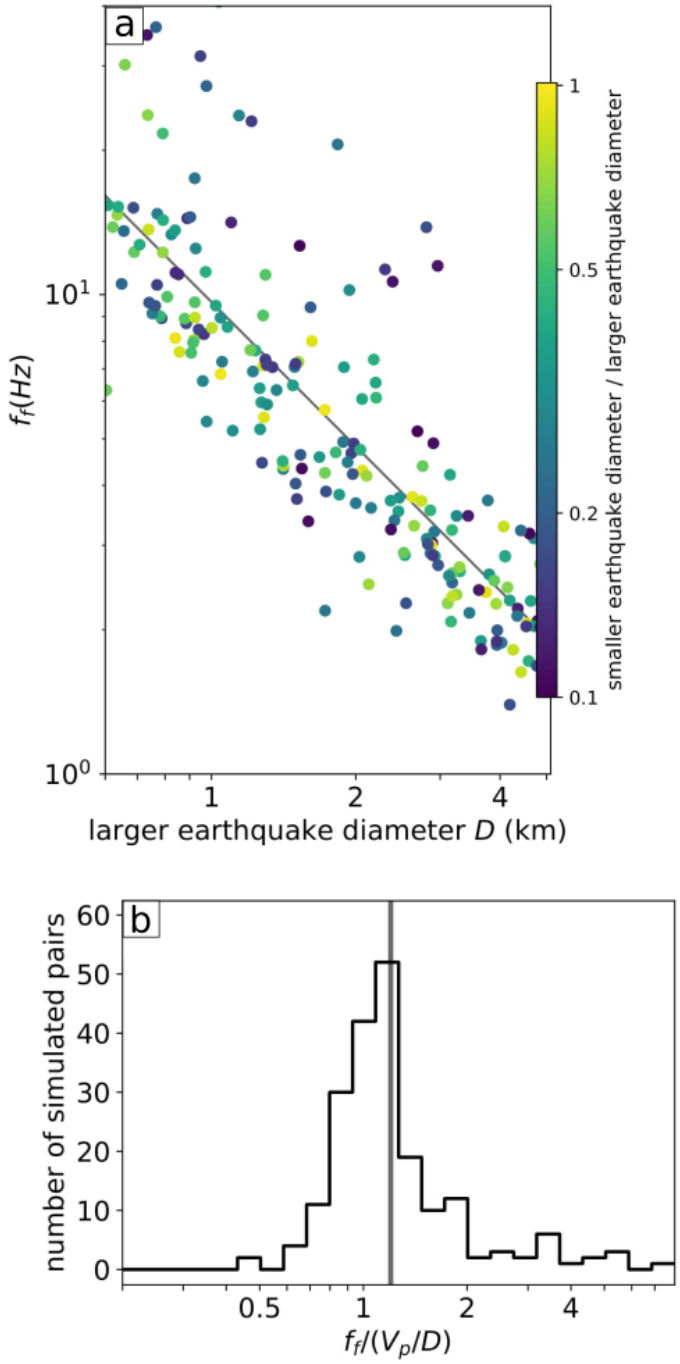

Figure A.14: (a): Derived falloff frequencies from the synthetic approach discussed in the text for different rupture diameters of the larger earthquake of the pair. Points are coloured by the diameter of the smaller earthquake in the pair. (b): Falloff frequencies normalized by the P wave velocity over the rupture diameter, to show what factor I should use for correcting the earthquake rupture diameters from the phase coherence method with random station distributions. The median value for the factor is 1.1.

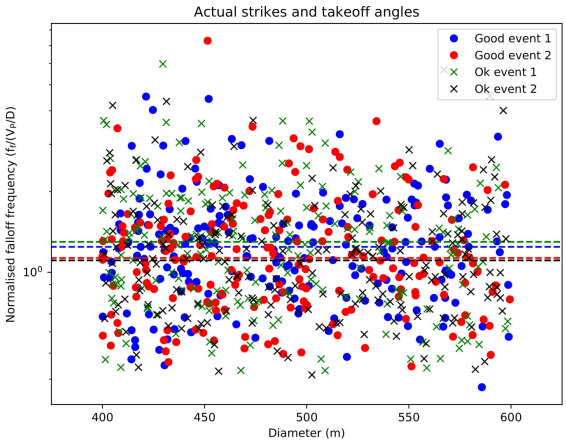

Figure A.15: Normalized falloff frequency versus earthquake diameter for stations with actual strikes and takeoff angles, using the iasp91 velocity model. Dashed lines indicate the median normalized falloff frequency for each of the four events. These medians cluster around a value of 1.2.

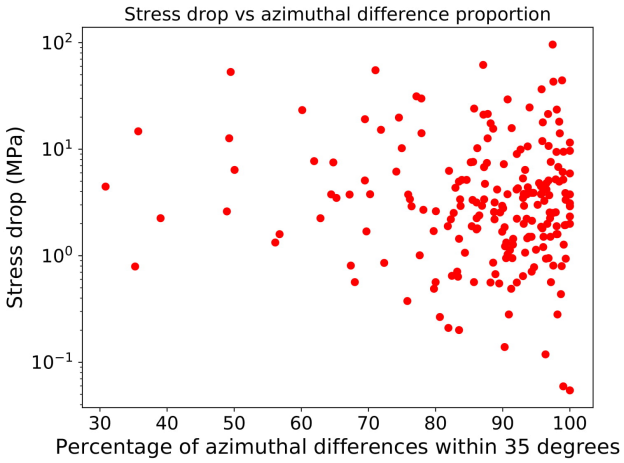

Figure A.16: Stress drop plotted against the proportion of station pairs for each earthquake pair that are within 45° azimuth.

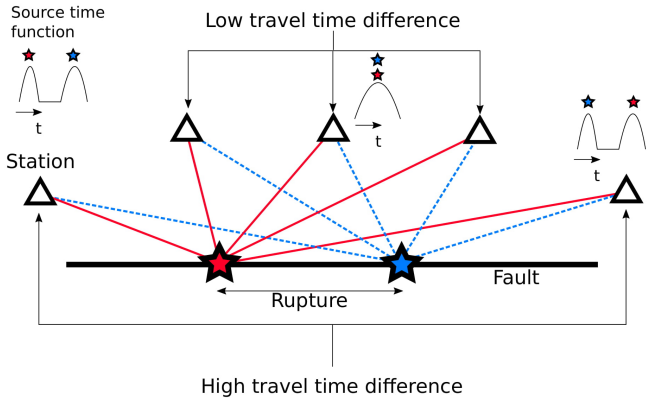

Figure A.17: Ray paths between rupture ends (stars) and stations (triangles) to illustrate the change in ray path length and thus travel time for different azimuths.

A.6 Depth phases

Figure A.18 demonstrates how the the arrival times of P and pP differ with earthquake-station distance and depth of the earthquake, as calculated using TauP (Crotwell et al., 1999) with the iasp91 earth model (Kennett and Engdahl, 1991).

A.7 Histogram of magnitude of events in each segment

The distributions of magnitudes of events on the northwest and southeast segments that I specified in my analysis of the Blanco fault are similar (Figure A.19).

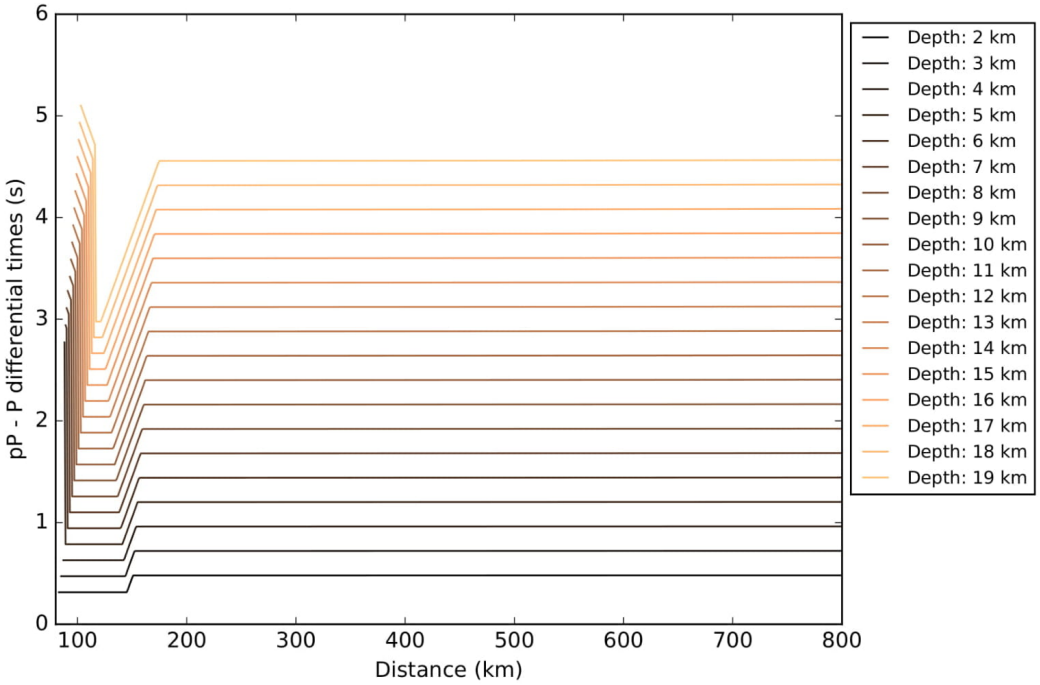

Figure A.18: Change in pP - P differential times with earthquake-station distance and depth of the earthquake.

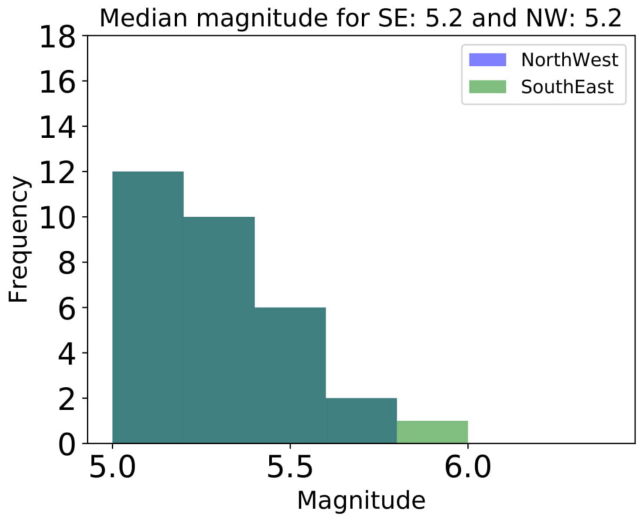

Figure A.19: Histogram of magnitude of events in each segment selected for looking at the spatial variation in stress drops along the Blanco fault.

A.8 Stress drops results

Table A.3 contains the results for my calculated stress drops for the Blanco fault.

Table A.3: Calculated stress drops for the Blanco fault. Negative uncertainties should be truncated at zero for cases where the uncertainty is greater than the value. Note that event magnitudes have been translated to moment magnitudes as discussed in the text, but the original magnitude and magnitude type is given in the event name. Lower and upper limits refer to the 2.5% and 97.5% confidence limits on the previous value in the same units. All event names begin with "us", excluded for space.

Event	Date	Lat.	Long.	Depth (km)	Mag.	No. of prs	f_f (Hz)	Low lim. f_f	High lim. f_f	Diam. D (km)	Low lim. D	High lim. D	$\Delta\sigma$ (MPa)	Low lim. $\Delta\sigma$	High lim. $\Delta\sigma$
10007cvf	2016-11-28T 04:34:42.500Z	43.41	-127.11	10.0	5.29	3	5.27	1.57	0.59	1.83	2.6	1.65	55.02	35.92	20.64
200063z1	2016-06-12T 18:47:04.130Z	43.53	-127.38	10.0	5.05	3	3.71	0.2	2.93	2.6	2.75	1.45	8.28	1.27	39.28
10005ir2	2016-05-20T 07:01:05.090Z	43.79	-128.46	10.0	5.0	1	3.12	0.79	0.4	3.09	4.12	2.74	4.22	2.45	1.81
20004wvh	2016-01-30T 03:42:23.980Z	43.44	-127.29	10.0	5.05	2	1.95	0.4	6.25	4.94	6.19	1.18	1.21	0.59	88.42
20002l01	2015-06-01T 10:46:27.260Z	44.54	-129.65	10.0	5.4	5	2.54	0.79	1.37	3.8	5.5	2.47	9.01	6.04	23.92
b000sz9m	2014-11-23T 11:01:25.120Z	43.82	-128.55	10.0	5.2	1	5.47	2.54	0.2	1.76	3.3	1.7	45.13	38.22	5.13
b000pzzj	2014-04-25T 21:18:30.240Z	43.41	-127.06	10.0	5.13	1	3.32	0.2	0.79	2.91	3.09	2.35	7.85	1.33	7.0
c000n8ii	2014-03-12T 00:31:44.470Z	44.31	-129.08	10.0	5.45	2	3.52	0.2	-1.75	2.74	2.91	5.47	28.53	4.6	-24.93
c000fe5b	2013-02-27T 22:25:43.920Z	43.22	-126.56	10.0	5.2	3	1.37	0.2	0.2	7.06	8.27	6.16	0.71	0.27	0.36
p000jtff	2012-10-03T 08:16:39.560Z	44.31	-129.19	10.0	5.13	3	5.86	2.35	1.57	1.65	2.75	1.3	43.13	33.85	44.69
p000jsb2	2012-09-14T 20:24:21.850Z	44.13	-129.07	10.0	5.13	2	2.93	0.2	1.18	3.29	3.53	2.35	5.39	1.03	9.45
p000jnpa	2012-07-06T 17:50:28.610Z	43.64	-127.45	10.0	5.05	3	3.91	1.57	0.2	2.47	4.12	2.35	9.66	7.59	1.56
p000jmz5	2012-06-19T 13:40:57.260Z	43.44	-127.27	10.0	5.53	2	3.12	0.59	0.98	3.09	3.81	2.35	26.5	12.37	33.63
p000jhpg	2012-04-11T 22:41:46.040Z	43.58	-127.64	8.0	6.0	2	1.76	0.79	0.2	5.49	9.93	4.93	23.75	19.74	9.06

p000jeyq	2012-02-15T 03:31:20.610Z	43.62	-127.52	11.0	5.8	2	2.93	0.98	1.96	3.29	4.95	1.97	55.11	38.9	200.76
p000j99k	2011-10-13T 04:14:00.510Z	43.46	-127.14	20.6	5.6	6	3.71	0.79	2.15	2.6	3.3	1.65	56.13	28.64	165.36
p000hvg9	2011-03-08T 01:26:58.190Z	44.32	-129.45	10.0	5.1	1	2.93	0.98	0.4	3.29	4.95	2.9	4.91	3.47	2.27
p000hvf2	2011-03-06T 22:23:15.580Z	44.29	-129.43	10.0	5.0	1	1.56	0.2	4.11	6.17	7.08	1.7	0.53	0.18	24.66
p000hvfl	2011-03-06T 21:35:47.420Z	44.37	-129.38	10.0	5.0	1	1.37	0.4	1.18	7.06	9.93	3.79	0.35	0.23	1.92
p000hu8d	2011-02-08T 22:02:01.870Z	43.54	-127.31	10.0	5.4	1	1.95	0.4	0.4	4.94	6.19	4.11	4.1	2.02	3.03
p000h9ep	2010-03-15T 12:37:49.980Z	44.21	-129.38	10.0	5.21	1	2.54	1.18	0.4	3.8	7.08	3.29	4.64	3.93	2.52
p000h99x	2010-03-13T 04:53:39.910Z	44.22	-129.35	10.0	5.0	6	3.91	0.4	3.32	2.47	2.75	1.33	8.24	2.26	44.05
p000h3r2	2009-11-04T 12:38:28.740Z	43.41	-126.81	10.0	5.3	2	2.54	0.4	0.2	3.8	4.5	3.52	6.38	2.54	1.63
p000gz2z	2009-07-10T 00:31:25.040Z	44.53	-129.93	10.0	5.3	1	3.71	0.4	0.59	2.6	2.91	2.24	19.92	5.71	11.1
p000gw6t	2009-04-16T 04:18:32.020Z	44.19	-129.27	10.0	5.0	2	3.32	0.4	0.4	2.91	3.3	2.6	5.06	1.6	2.03
p000gugg	2009-02-28T 22:24:40.460Z	43.33	-126.97	10.0	5.21	6	8.59	0.79	2.15	1.12	1.24	0.9	180.01	45.01	172.04
p000gnn5	2008-11-14T 01:48:37.110Z	43.5	-127.39	10.0	5.3	2	3.12	0.2	0.98	3.09	3.3	2.35	11.89	2.14	15.09
p000gcj7	2008-07-19T 01:00:22.940Z	44.33	-129.3	10.0	5.0	5	3.71	0.59	0.2	2.6	3.09	2.47	7.07	2.87	1.21
p000gcf5	2008-07-17T 22:51:55.320Z	44.37	-129.42	10.0	5.7	2	1.95	0.4	0.2	4.94	6.19	4.48	11.56	5.69	3.93
p000gcf1	2008-07-17T 22:36:18.780Z	44.37	-129.36	10.0	5.5	1	1.17	0.2	1.96	8.23	9.93	3.08	1.25	0.54	22.59
p000gbzb	2008-07-12T 15:46:02.310Z	43.29	-126.44	10.0	5.0	3	3.71	0.2	0.4	2.6	2.75	2.35	7.07	1.08	2.51
p000gays	2008-06-29T 19:33:40.930Z	44.25	-129.25	10.0	5.4	8	5.27	2.93	1.18	1.83	4.12	1.5	80.73	73.69	66.99

p000g9k6	2008-06-14T 06:47:09.030Z	44.23	-129.2	10.0	5.2	5	2.73	1.37	0.4	3.53	7.08	3.08	5.64	4.94	2.82
p000g8du	2008-06-02T 17:50:24.910Z	44.18	-129.22	10.0	5.2	3	3.12	1.96	0.59	3.09	8.27	2.6	8.42	7.98	5.73
p000g7pu	2008-05-24T 23:23:06.040Z	44.21	-129.39	10.0	5.1	7	4.69	0.4	0.4	2.06	2.25	1.9	20.12	4.67	5.53
p000g5ev	2008-05-04T 02:51:12.340Z	43.16	-126.37	10.0	5.1	4	2.54	0.79	0.2	3.8	5.5	3.52	3.2	2.14	0.82
p000g4r9	2008-04-24T 13:37:25.460Z	43.16	-126.32	10.0	5.05	4	4.1	0.79	0.98	2.35	2.91	1.9	11.18	5.28	10.1
p000g3ru	2008-04-12T 12:05:14.620Z	43.65	-127.62	10.0	5.5	3	3.12	0.2	0.4	3.09	3.3	2.74	23.73	4.27	10.19
p000g2xu	2008-04-02T 05:55:41.390Z	44.36	-129.35	10.0	5.2	1	2.93	0.59	0.59	3.29	4.12	2.74	6.94	3.41	5.1
p000fsxd	2007-11-19T 22:43:02.950Z	43.64	-127.47	10.0	5.0	3	3.12	0.4	1.76	3.09	3.53	1.97	4.22	1.41	11.92
p000fsx6	2007-11-19T 20:32:48.800Z	43.54	-127.41	10.0	5.8	1	1.56	0.59	0.4	6.17	9.93	4.93	8.36	6.35	8.09
p000fh84	2007-07-28T 00:20:38.240Z	44.54	-129.76	10.0	5.0	6	3.71	0.98	1.76	2.6	3.53	1.76	7.07	4.25	15.61
p000fh83	2007-07-28T 00:02:16.870Z	44.56	-129.7	10.0	5.05	2	1.37	0.2	3.72	7.06	8.27	1.9	0.41	0.16	20.87
p000fh7y	2007-07-27T 23:22:48.920Z	44.4	-129.76	10.0	5.3	2	3.71	0.98	0.79	2.6	3.53	2.15	19.92	11.99	15.52
p000fh5y	2007-07-27T 01:37:47.090Z	44.43	-129.59	10.0	5.2	4	1.76	0.2	0.2	5.49	6.19	4.93	1.5	0.46	0.57
p000f4w1	2007-02-14T 22:12:58.550Z	43.52	-127.45	10.0	5.2	2	3.52	1.37	0.59	2.74	4.5	2.35	11.99	9.27	7.11
p000f4pa	2007-02-11T 15:34:48.730Z	43.48	-127.36	10.0	5.0	1	3.91	2.54	0.59	2.47	7.08	2.15	8.24	7.89	4.33
p000e81b	2006-01-11T 10:02:32.560Z	43.51	-127.27	10.0	5.6	1	2.15	0.59	0.79	4.49	6.19	3.29	10.89	6.74	16.86
p000dwpg	2005-08-04T 18:36:55.630Z	43.19	-126.32	10.0	5.13	1	1.76	0.2	1.57	5.49	6.19	2.9	1.16	0.35	6.72
p000dq3w	2005-05-07T 04:30:31.250Z	44.46	-129.82	10.0	5.05	1	2.15	0.59	0.2	4.49	6.19	4.11	1.61	0.99	0.49

p000d170	2004-07-31T 14:44:23.010Z	43.35	-126.81	10.0	5.13	7	4.1	2.35	2.15	2.35	5.5	1.54	14.79	13.64	37.67
p000d0jk	2004-07-20T 19:20:01.560Z	43.66	-127.91	10.0	5.21	1	5.08	1.76	0.79	1.9	2.91	1.65	37.14	26.8	20.05
p000cg8w	2003-12-27T 15:23:15.610Z	43.52	-127.35	10.0	5.3	2	4.69	0.59	0.4	2.06	2.35	1.9	40.14	13.34	11.04
p000bs5j	2003-03-07T 22:11:28.260Z	43.53	-127.12	10.0	5.2	4	3.52	1.76	0.59	2.74	5.5	2.35	11.99	10.5	7.11
p000bp58	2003-01-25T 10:39:53.390Z	44.27	-129.26	10.0	5.21	1	3.91	2.54	1.76	2.47	7.08	1.7	16.91	16.19	34.76
p000bnn2	2003-01-16T 06:52:04.440Z	44.17	-128.93	10.0	5.2	2	1.56	0.2	2.74	6.17	7.08	2.24	1.05	0.35	20.91
p000bnms	2003-01-16T 05:03:29.390Z	44.15	-129.18	10.0	5.5	1	1.56	0.4	31.25	6.17	8.27	0.29	2.97	1.73	27479.79
p000bnmd	2003-01-16T 02:25:05.070Z	44.28	-129.35	10.0	5.7	2	1.17	0.4	1.18	8.23	12.42	4.11	2.5	1.77	17.6
p000bnm3	2003-01-16T 01:06:30.630Z	44.17	-129.26	10.0	5.45	1	1.76	0.98	0.59	5.49	12.42	4.11	3.57	3.26	4.94
p000bnkw	2003-01-16T 00:51:03.500Z	44.22	-129.19	10.0	5.29	5	4.69	1.57	0.59	2.06	3.09	1.83	38.64	27.25	16.53
p000b4bp	2002-05-15T 07:06:20.450Z	43.41	-127.08	10.0	5.4	2	1.76	0.2	5.28	5.49	6.19	1.37	2.99	0.91	188.75

Table A.4: Original results of study compared with results with only events with greater than 0.1 magnitude unit difference, greater than 0.2 magnitude unit difference, and greater than 0.5 magnitude unit difference.

Magnitude difference limit for event pairs	Total events	Overall median stress drop (95% confidence limits)	NW No. events $M \geq 5$	NW median stress drop	SE No. events $M \geq 5$	SE median stress drop	Factor of difference
No limit	61	8 (6, 12)	30	6 (4, 11)	31	11 (6, 22)	1.7 (0.8, 3.5)
Difference > 0.1	58	8 (6, 12)	28	6 (4, 11)	30	10 (6, 20)	1.6 (0.8, 3.4)
Difference > 0.2	55	8 (6, 12)	25	7 (5, 12)	30	10 (6, 20)	1.4 (0.7, 2.9)
Difference > 0.5	41	8 (5, 18)	21	7 (4, 16)	20	11 (4, 25)	1.6 (0.4, 4.1)

A.9 Results excluding earthquake pairs based on the difference in magnitudes

I test whether the source effect of the smaller event in an earthquake pair may contaminate the result. The synthetics in Figure A.14 demonstrate that the falloff frequency is not significantly affected by the ratio between the diameter of the larger earthquake and the smaller earthquake. However, if there any repeating earthquakes with similar slip distribution and directivity in the earthquake catalog, or if earthquakes of similar size have homogeneous slip distributions, then they will have high coherence out to to frequencies higher than the falloff frequency due to the similarity of their ruptures. I exclude earthquake pairs from results which have less than or equal to 0.1, 0.2, and 0.5 magnitude units between them. The results of this analysis are shown in Table A.4.

The overall results of this study do not significantly change when I exclude pairs with less than or equal to 0.1 or 0.2 magnitude units between them. There is also little difference for the 0.5 magnitude unit cutoff, although the uncertainty on the factor of difference does increase, but I think that the 0.5 magnitude unit difference is too harsh of a threshold because repeaters rarely have such large magnitude variation. This result agrees with my results for synthetic earthquake pairs, which are discussed earlier in this appendix.

Appendix B

Appendix for Chapter 3

B.1 Region of interest for aftershocks of El Mayor-Cucapah earthquake

In Table B.1 I define the region of interest which I used to identify aftershocks of the 2010 El Mayor-Cucapah earthquake.

Table B.1: Region I selected earthquakes from in the study of the aftershocks of the El Mayor-Cucapah earthquake.

Latitude (degrees)	Longitude (degrees)
31	-114
31	-116
33	-116
33	-114
31	-114

B.2 Networks

Here, I give details on the networks I used in this study (Table B.2).

Table B.2: Table of networks used in this study

Network Code	Full name	Number of stations used	Citation
AE	Arizona Broadband Seismic Network	1	Arizona Geological Survey (2009): Arizona Broadband Seismic Network. International Federation of Digital Seismograph Networks. Dataset/Seismic Network. https://doi.org/10.7914/SN/AE
AR	Northern Arizona Network	6	Northern Arizona University(NAU) (Arizona Earthquake Information Center)
AZ	ANZA Regional Network	16	Frank Vernon, UC San Diego (1982): ANZA Regional Network. International Federation of Digital Seismograph Networks. Dataset/Seismic Network. https://doi.org/10.7914/SN/AZ
BC	Red Sísmica del Noroeste de México (RESNOM)	14	Centro de Investigación Científica y de Educación Superior de Ensenada (CICESE), Ensenada (1980): Red Sísmica del Noroeste de México. International Federation of Digital Seismograph Networks. Dataset/Seismic Network. https://doi.org/10.7914/SN/BC
BK	Berkeley Digital Seismograph Network	22	Northern California Earthquake Data Center. (2014). Berkeley Digital Seismic Network (BDSN) Data set. Northern California Earthquake Data Center. https://doi.org/10.7932/bdsn
CE	California Strong Motion Instrumentation Program	4	California Division of Mines and Geology
LB	Leo Brady Network	1	Lee, J.W., 2001. A new seismic data system for determining nuclear test yields at the Nevada Test Site (No. SAND2001-3373). Sandia National Labs., Albuquerque, NM (U.S.); Sandia National Labs., Livermore, CA (U.S.).
LI	Laser Interferometer Gravitational-Wave Experiment (LIGO)	1	California Institute of Technology (Caltech) (2000): Laser Interferometer Gravitational-Wave Experiment (LIGO). International Federation of Digital Seismograph Networks. Other/Seismic Network. https://doi.org/10.7914/SN/LI

NC	USGS Northern California Regional Network	29	USGS Menlo Park (1967): USGS Northern California Network. International Federation of Digital Seismograph Networks. Other/Seismic Network. https://doi.org/10.7914/SN/NC
NN	Nevada Seismic Network	18	University of Nevada, Reno (1971): Nevada Seismic Network. International Federation of Digital Seismograph Networks. Dataset/Seismic Network. https://doi.org/10.7914/SN/NN
NP	United States National Strong-Motion Network	30	U.S. Geological Survey (1931): United States National Strong-Motion Network. International Federation of Digital Seismograph Networks. Dataset/Seismic Network. https://doi.org/10.7914/SN/NP
PB	Plate Boundary Observatory Borehole Seismic Network	14	UNAVCO
PG	Central Coast Seismic Network	11	Pacific Gas and Electric Company
SB	University of California: Santa Barbara Engineering Seismology Network	1	University of California: Santa Barbara
SN	Southern Great Basin Network	9	University of Nevada, Reno (1995): Southern Great Basin Network. International Federation of Digital Seismograph Networks. Dataset/Seismic Network. https://doi.org/10.7914/SN/SN
TA	USArray Transportable Array (NSF EarthScope Project)	6	IRIS Transportable Array (2003): USArray Transportable Array. International Federation of Digital Seismograph Networks. Other/Seismic Network. https://doi.org/10.7914/SN/TA
US	United States National Seismic Network	2	Albuquerque Seismological Laboratory (ASL)/USGS (1990): United States National Seismic Network. International Federation of Digital Seismograph Networks. Dataset/Seismic Network. https://doi.org/10.7914/SN/US
WR	California Division of Water Resources	5	n/a
ZY	Portable Southern California Seismic Networks (Caltech)	10	California Institute of Technology

Table B.3: Velocity models from *Wei et al.* (2011).

Depth range (km)	P wave velocity (km/s)	S wave velocity (km/s)
0.0 - 5.5	5.50	3.18
5.5 - 16.0	6.30	3.64
16.0 - 32.0	6.70	3.87

B.3 Velocity models from *Wei et al.* (2011)

In my analysis of the stress drops, I use the velocity models from *Wei et al.* (2011) to pick an appropriate P wave and S wave velocity for each earthquake. These models are shown in Table B.3.

B.4 Histograms of alignment uncertainties

Here, I plot histograms of the loop closures and alignment uncertainties estimated from the alignment times of both the P- and S wave for the El Mayor-Cucapah aftershocks. The loop closures and alignment uncertainties are calculated as described in the main text. The loop closure and alignment error histograms for the P wave (Figures B.1 - B.2) and S wave (Figures B.3 - B.4) are similar.

B.5 Correcting for the azimuthal range of stations

I plot the results from the synthetic code used in Sec. 3.4.4, but for the S wave. The representative distribution of stations for the S wave is narrower than the P wave (Figure 3.7), and mostly includes stations within a -20 - 30° azimuthal range despite the 120° azimuthal range that I require, and the requirement that a 10° azimuthal bin cannot have more than 2 stations within it. I find a factor F_{scal} of 2.32 for the representative distribution of stations for the S wave using an S wave velocity of 3.56 km/s and a rupture velocity that is 90% of the S wave velocity. The factor is higher than the 1.39 factor I found for the P wave as described in the main text, because of the more narrow distribution of stations for the S wave.

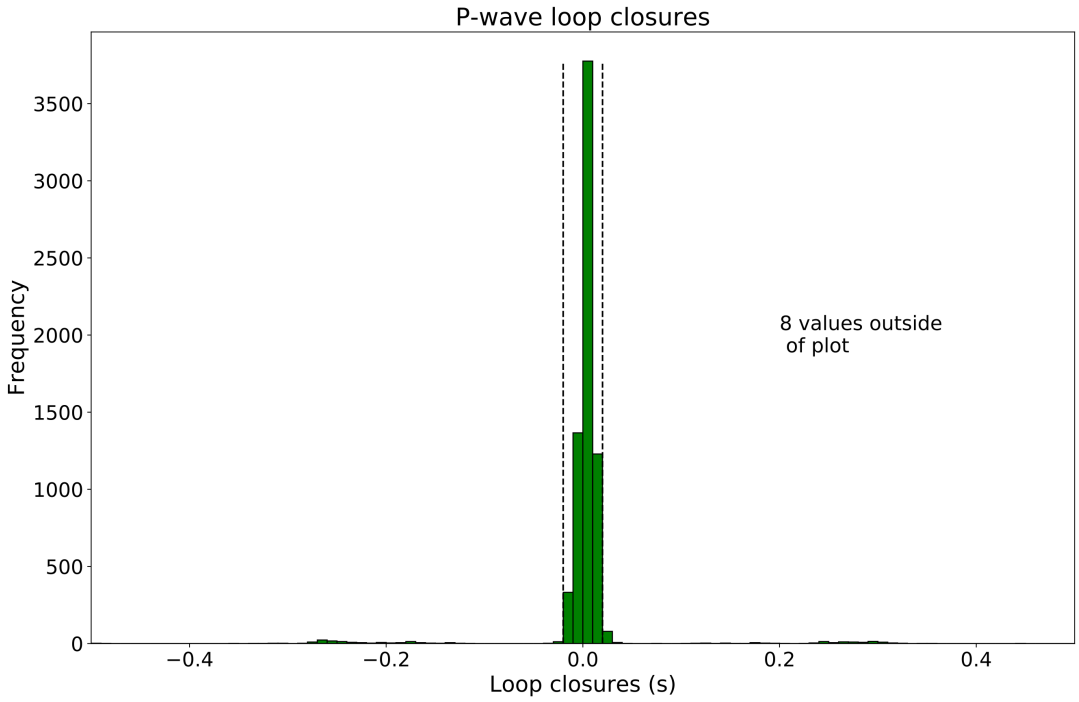

Figure B.1: Histogram of loop closures for the results of the P wave analysis on the aftershocks of the El Mayor-Cucapah earthquake. The dashed black lines indicate a 0.02 s limit. Some values have been excluded from the plot.

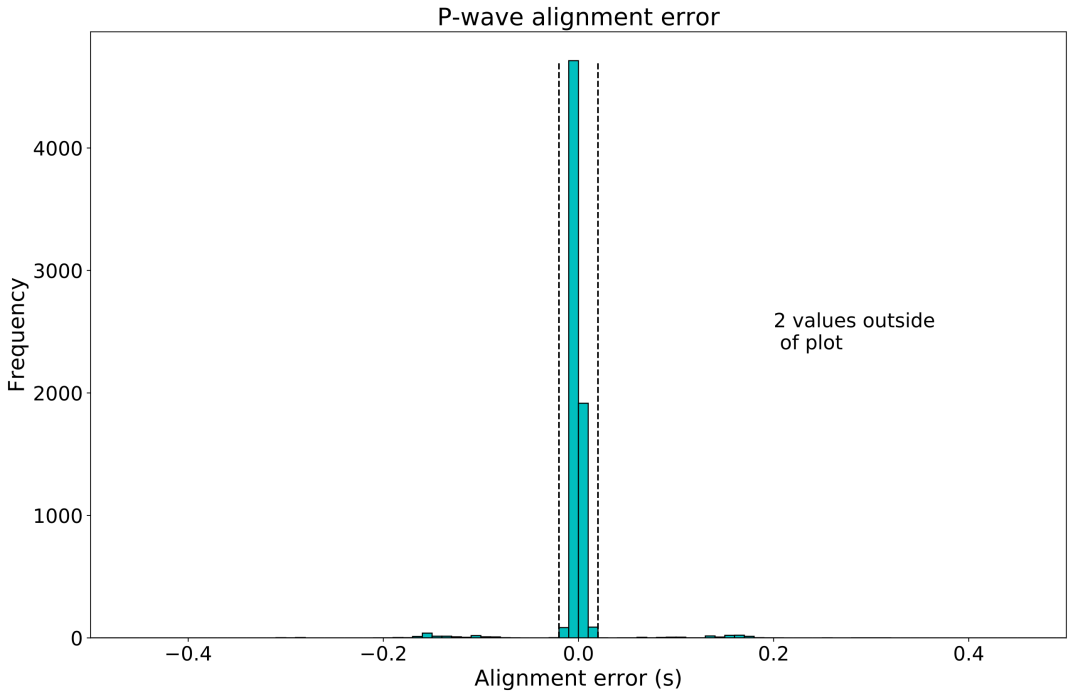

Figure B.2: Histogram of alignment errors for the results of the P wave analysis on the aftershocks of the El Mayor-Cucapah earthquake. The dashed black lines indicate a 0.02 s limit. Some values have been excluded from the plot.

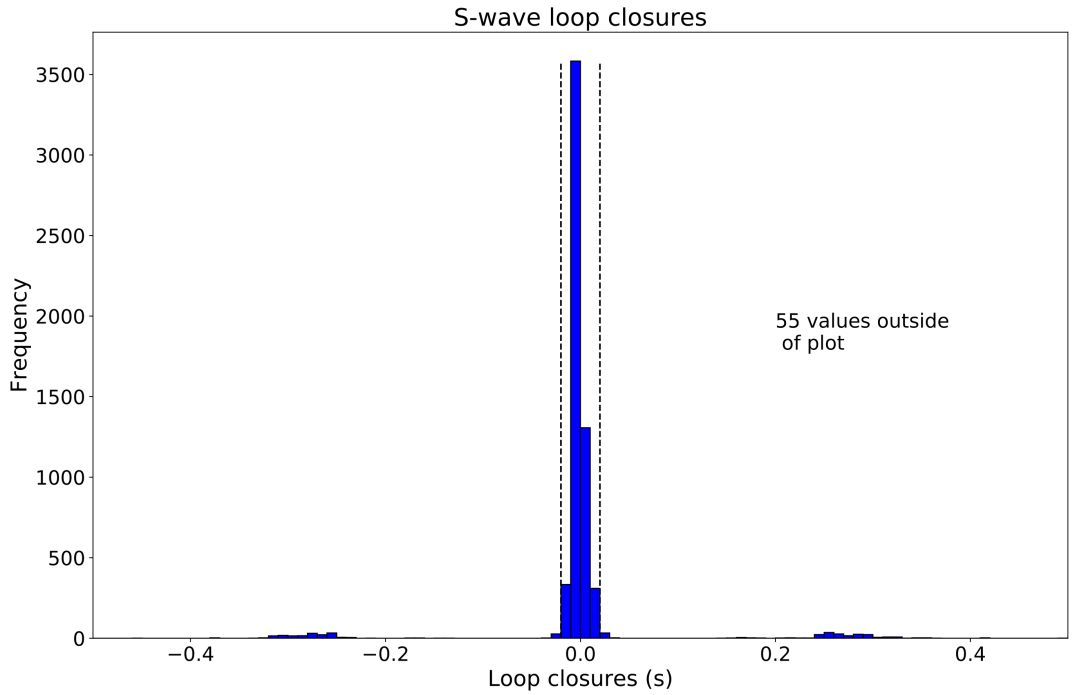

Figure B.3: Histogram of loop closures for the results of the S wave analysis on the aftershocks of the El Mayor-Cucapah earthquake. The dashed black lines indicate a 0.02 s limit. Some values have been excluded from the plot.

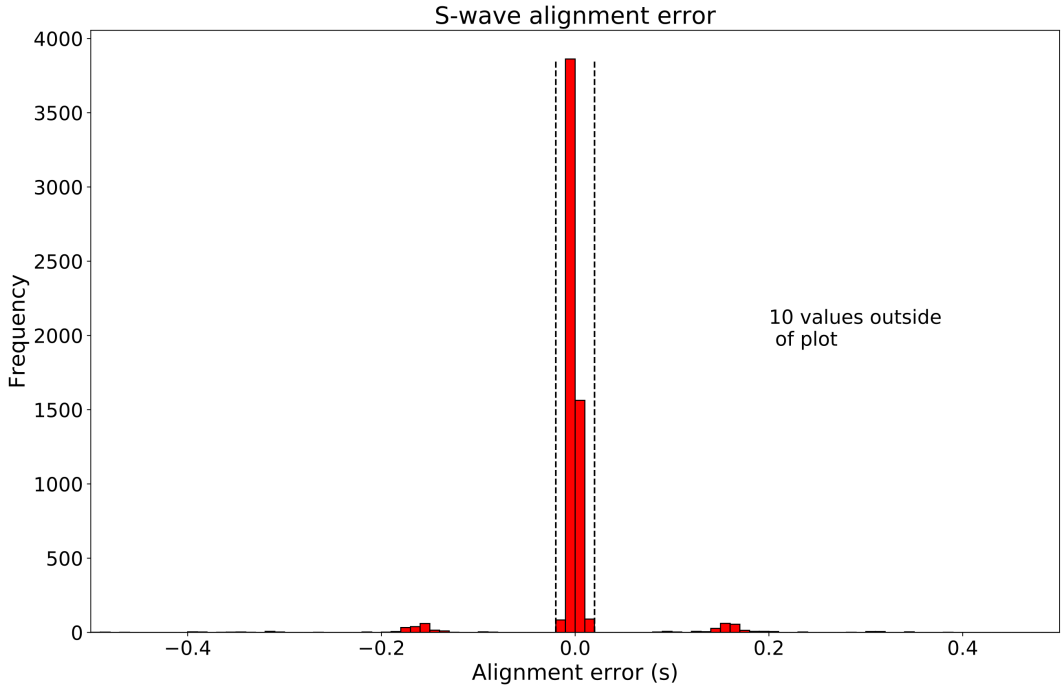

Figure B.4: Histogram of alignment errors for the results of the S wave analysis on the aftershocks of the El Mayor-Cucapah earthquake. The dashed black lines indicate a 0.02 s limit. Some values have been excluded from the plot.

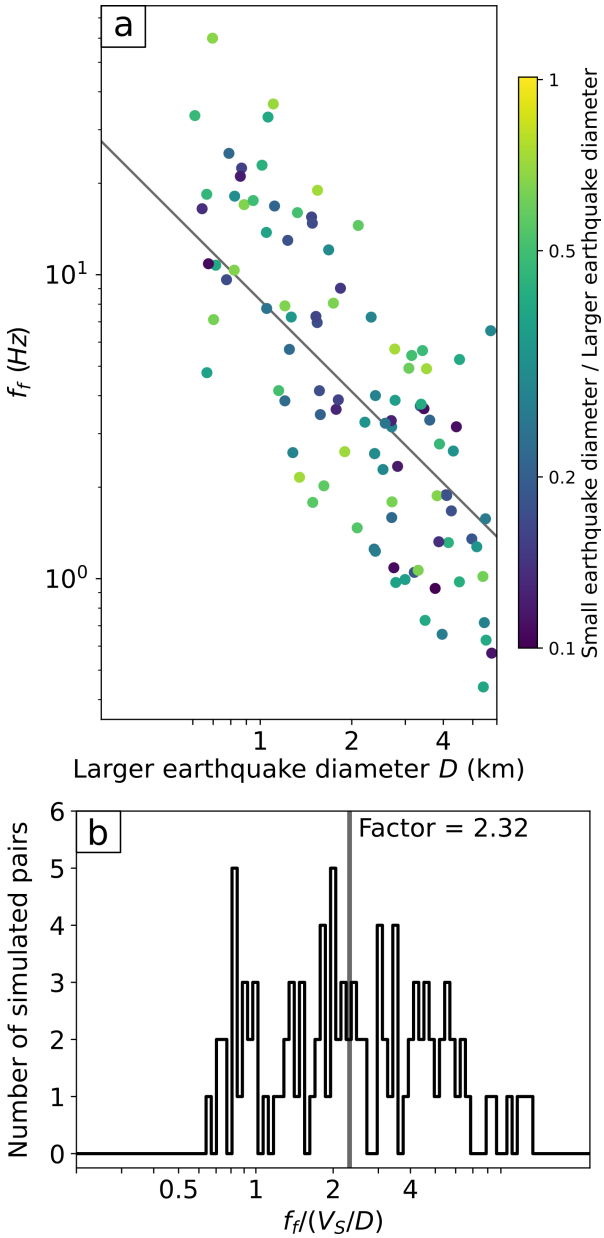

Figure B.5: The effect of the representative station distribution on synthetic falloff frequencies of varying earthquake radii for the S wave. The representative station distribution is picked as described in the text. (a): Synthetic falloff frequencies for different earthquake diameters. Points are coloured by the ratio of the smaller earthquake diameter used in the pair with the larger earthquake diameter used in the pair. The grey line is the log-log fit through the synthetic falloff frequencies with diameter. (b): Histogram of the factor F_{scal} required to obtain the true rupture length from the apparent falloff frequency of each synthetic earthquake. The grey line indicates the median factor of the histogram, which is 2.32 for the S wave.

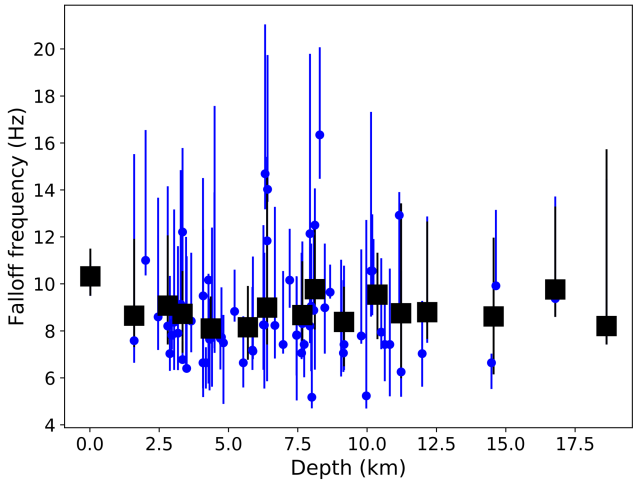

Figure B.6: Falloff frequencies for aftershocks of the 2010 El Mayor-Cucapah earthquake plotted against the depths of earthquakes (blue dots). The black squares are the median falloff frequencies in bins of 1 km depth calculated using the same approach as in the main text. The error bars on each falloff frequency and median falloff frequency are the 95% confidence limits.

B.6 Change in falloff frequency with depth

Here I plot the falloff frequencies from the P wave against the depths of earthquakes. If the depth phases reduce the coherence as suggested in Sec. 3.4.5, then the phase coherence should be reduced for shallow earthquakes. The falloff frequencies for these shallow earthquake should therefore be systematically lower than the falloff frequencies of deeper earthquakes. I observe a constant falloff frequency with depth (Figure B.6) which suggests that the presence of depth phases in the analysis time window do not affect the phase coherence.

B.7 Results from S waves

I performed the analysis in Chapter 3 on both the P wave and the S wave. Although I focus on the P wave within the main chapter, I looked for the same variations in stress drops with earthquake properties in the results of the S wave. Here I recreate the figures in the main text using the results from the S wave (Figures B.7 - B.9). I also compute the median stress drops for each segment of the model of *Wei et al.* (2011). I calculate a median stress drop of 9.2 MPa (95% confidence limits of 6.8 and 25.4 MPa) for the

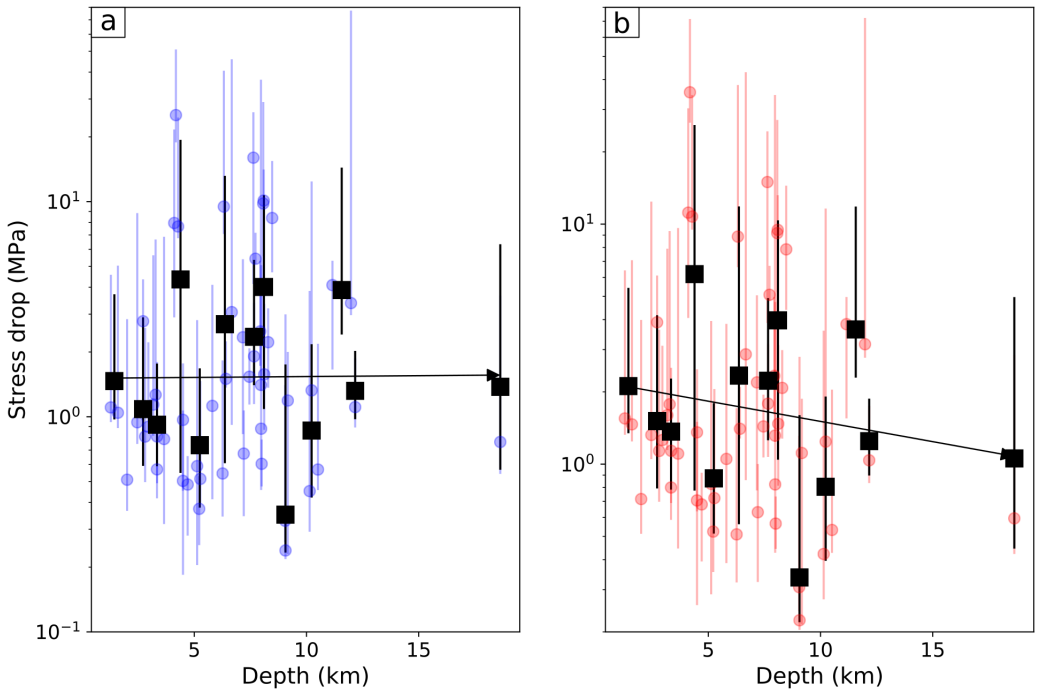

Figure B.7: Stress drops versus depth where the S wave velocity used for each earthquake is (a): constant and (b): increases with depth following the velocity model used by *Wei et al.* (2011). These stress drops were obtained by analysing the S wave. The fitted black arrows show the constant stress drop with increasing depth for (a), and decreasing stress drop with increasing depth for (b).

single earthquake on Segment 1 on Figure B.8. There are no events on Segment 2. I calculate a median stress drop of 1.6 MPa (1.0, 2.8) for the 8 earthquakes on Segment 3. Finally, I calculate a median stress drop of 1.8 MPa (1.3, 3.3) for the 29 earthquakes on Segment 4.

B.8 Changing length of moving average windows for stress drop against time

I experimented with the number of values to include in the moving average window for the calculation of the median stress drops for comparing the average stress drop with time. I tried using 4 (Figure B.10) and 6 (Figure B.11) as the number of values to be included in the moving average window. I observed no significant difference in the trend of increasing stress drops with time.

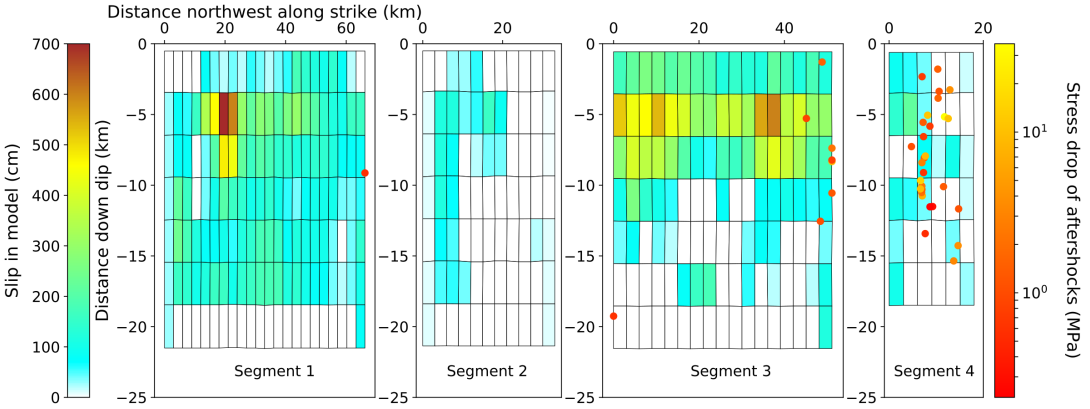

Figure B.8: Stress drops of aftershocks (coloured dots) projected onto the slip model (coloured rectangles) of *Wei et al.* (2011). These stress drops were obtained by analysing the S wave. The stress drop of each aftershock is indicated by the colour bar on the right of the figure. The slip of the slip model is indicated by the colours of the slip segments and the colour bar on the left of the figure. Segment 1 is the most southeastern segment of the slip model shown in Figure 3.3a, and the number of the segment increases as you move northwest on the slip model. Only stress drops of earthquakes inside of the region of the slip model are allowed which is defined as latitudes south of 32.73° and longitudes east of -115.8°.

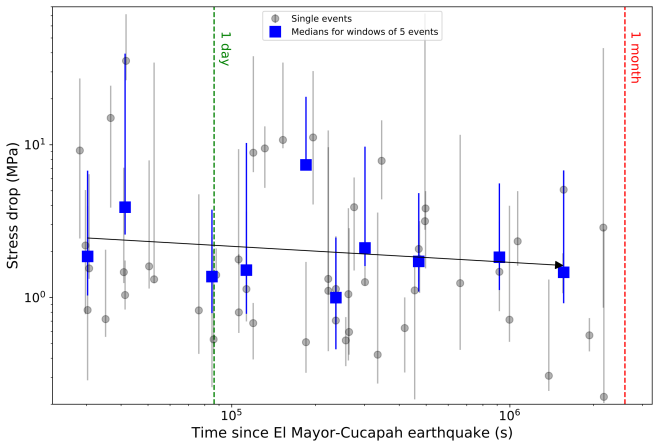

Figure B.9: Stress drops of the aftershocks of the El Mayor-Cucapah earthquake plotted against the time since the earthquake. These stress drops were obtained by analysing the S wave. Medians of windows including six values are plotted as black squares. These medians were calculated following the approach described in the text. The 95% confidence limits on these medians are shown by the error bars, and are calculated as described in the text.

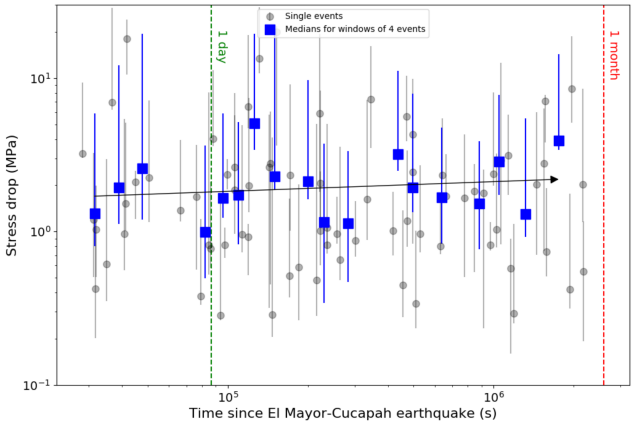

Figure B.10: Stress drops of the aftershocks of the El Mayor-Cucapah earthquake plotted against the time since the earthquake. These stress drops were obtained by analysing the P wave. Medians of windows including four values are plotted as black squares. These medians were calculated following the approach described in the text. The 95% confidence limits on these medians are shown by the error bars, and are calculated as described in the text.

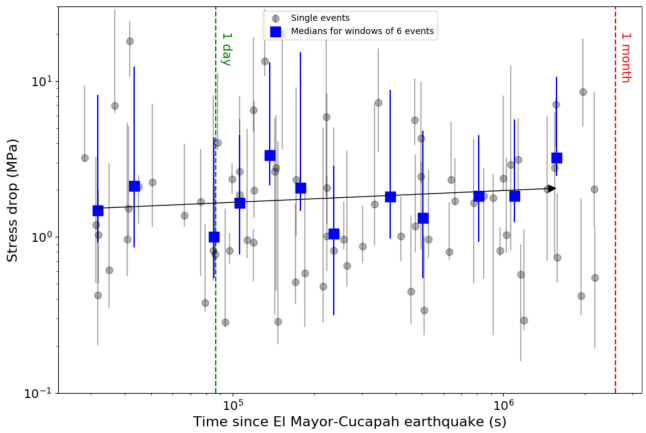

Figure B.11: Stress drops of the aftershocks of the El Mayor-Cucapah earthquake plotted against the time since the earthquake. These stress drops were obtained by analysing the P wave. Medians for single day windows are plotted as red triangles, and medians of windows including six values are plotted as black squares. These medians were calculated following the approach described in the text. The 95% confidence limits on these medians are shown by the error bars, and are calculated as described in the text.

Appendix C

Appendix for Chapter 4

C.1 Details of the earthquake catalog

Table C.1: The exact coordinates for the area I analyzed in the NCSN catalog.

Latitude (deg)	Longitude (deg)
36.19	-120.85
36.25	-120.76
35.73	-120.19
35.67	-120.28

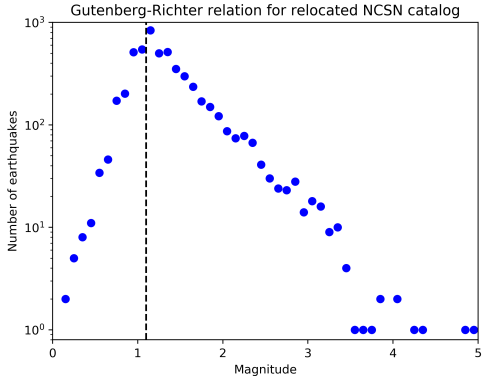

Figure C.1: The number of earthquakes in a 0.1-width magnitude bin against the midpoint of said magnitude bins. The dashed black line indicates a magnitude of 1.1.

C.2 Testing for bias

C.2.1 Using wider distance and moment bins

I test whether the choice of bins for the moment ratios and distance between sequences could be affecting the slopes I calculate. I increase the width of the moment ratio bins to 1 log unit and change the distance bins to 0 - 250 m, 250 - 500 m, and 500 - 1000 m. Using these wider distance bins makes the variation in slope with distance bin less obvious, but the lowest distance bin of 0 - 250 m still has a higher slope (Figure C.2).

C.2.2 Calculating the mode rather than the median

I check whether using a mode rather than a median average affects the slopes in my analysis. To obtain modes, I take the pairs of sequences that appear in a bin, look at the histogram of the recurrence intervals or ratios of these sequences (bins computed using the Freedman Diaconis Estimator (*Freedman and Diaconis*, 1981)), and pick the mode as the central value of the recurrence interval bin with the most values. I find no change in the results using modes rather than medians (Figure C.3).

C.2.3 Excluding 2-earthquake sequences with recurrence intervals of less than 1 month

I exclude 2-earthquake sequences which have recurrence intervals of less than a month from the moment and recurrence interval ratios to check for any effect of aftershocks on the slopes. I find no change in the pattern of slopes for different distance bins, although the slope of the 0 - 100 m distance bin is reduced (Figure C.4).

I also check further for any effect of earthquake triggering on my result. I exclude 2-earthquakes sequences which have recurrence intervals of less than a month, but also exclude 2-earthquake sequences if the second earthquake in the sequence is within a

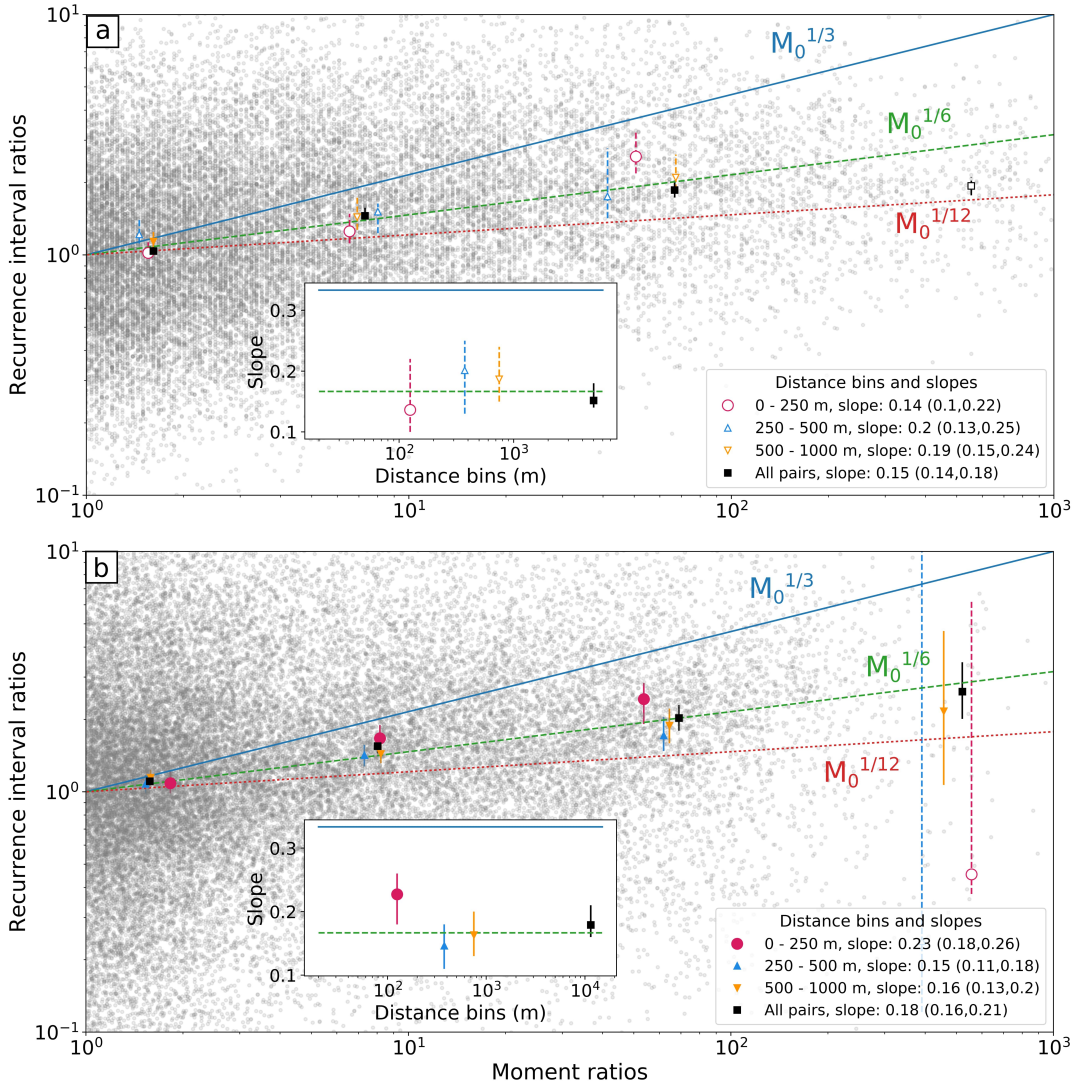

Figure C.2: The moment and recurrence interval ratios with wider distance bins and twice the spacing between moment bins for pairs of sequences in (a): the catalog of *Lengliné and Marsan* (2009) and (b): the relocated NCSN catalog (*Waldhauser and Schaff*, 2008, *Waldhauser*, 2009).

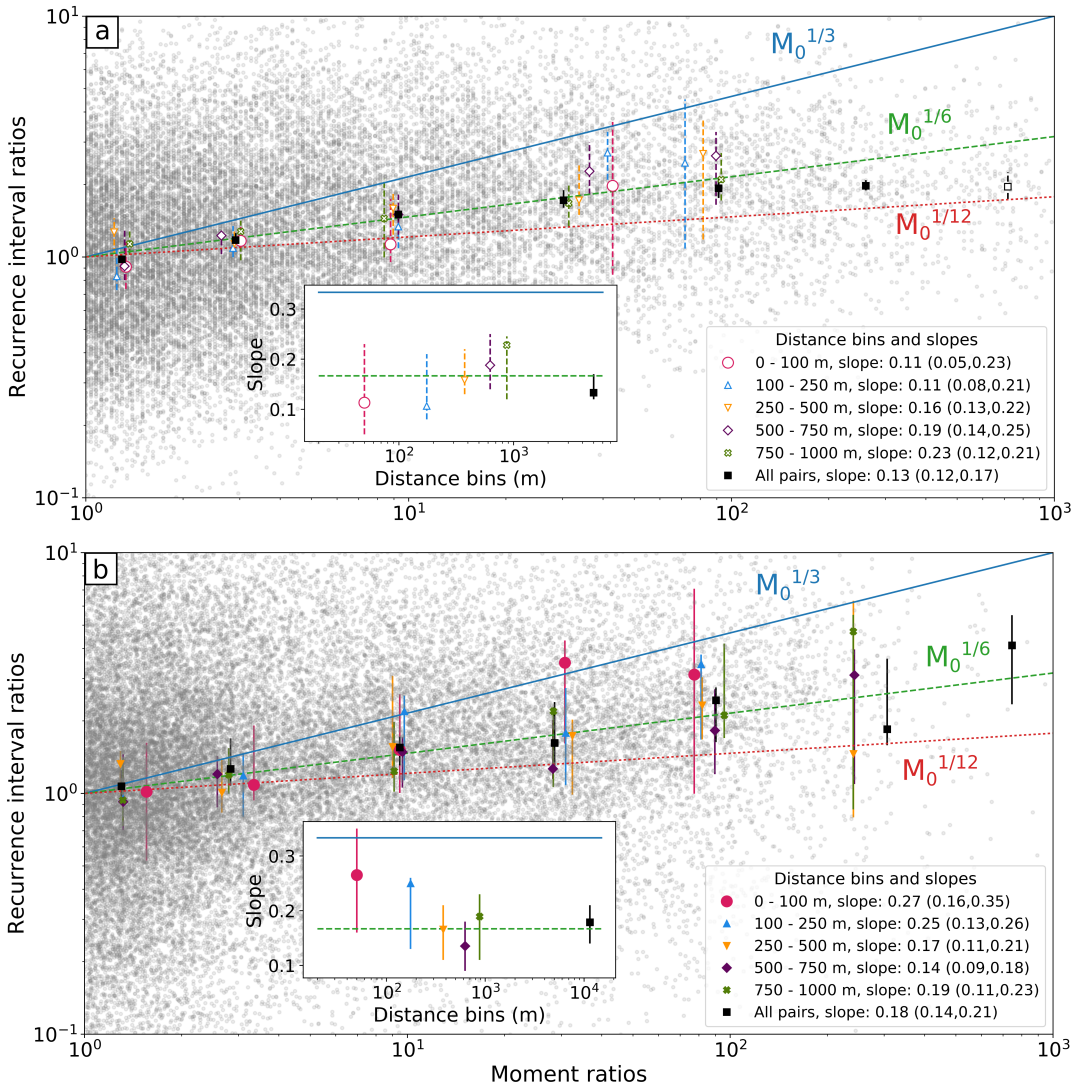

Figure C.3: The moment and recurrence interval ratios with averages calculated as modes for pairs of sequences in (a): the catalog of *Lengliné and Marsan* (2009) and (b): the relocated NCSN catalog (*Waldhauser and Schaff*, 2008, *Waldhauser*, 2009).

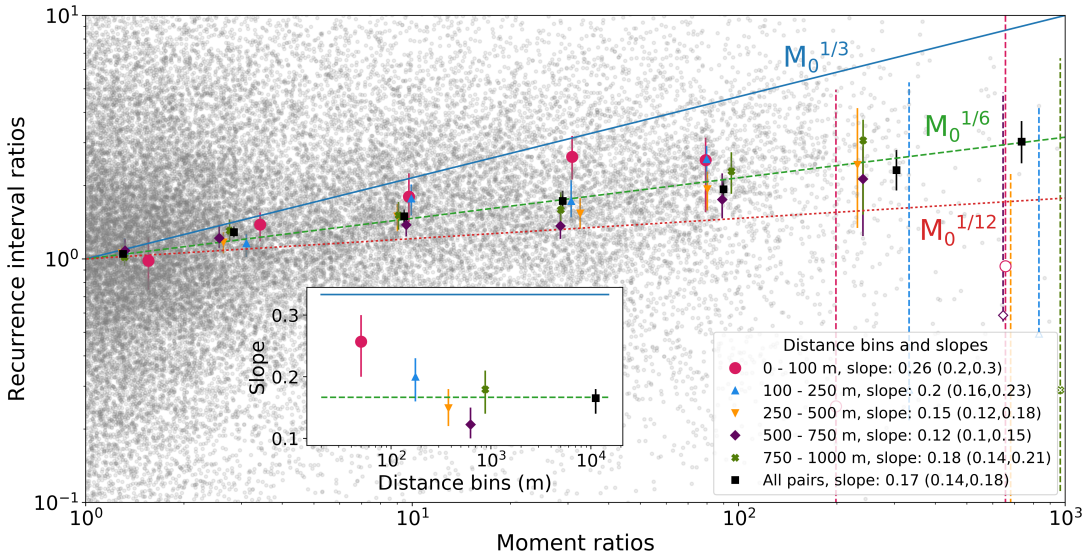

Figure C.4: The moment and recurrence interval ratios with 2-earthquake sequences eliminated if they have recurrence intervals of less than 1 month.

month and 250 m of any earthquake before it (Figure C.5). I observe no significant change in the pattern of scaling exponents for different distance bins, but some of the moment ratio bins have far fewer results within them, resulting in a highly uncertain estimated scaling exponent.

C.2.4 Excluding 6 months before Parkfield

In my analysis, I excluded earthquakes from repeating earthquake sequences if they occur a day before the 2004 M_W 6.0 Parkfield earthquake. I did this to avoid the perturbation of repeating earthquakes as noted by *Lengliné and Marsan* (2009). As a further precaution, here I exclude earthquakes from 6 months before the Parkfield earthquake, and recalculate the ratios and slopes (Figure C.6). This precaution tests whether there is preseismic activity before the Parkfield earthquake that may affect the slopes. I observe no major difference in the slopes of recurrence interval ratios versus moment ratios with earthquakes from 6 months before the M_W 6.0 earthquake excluded.

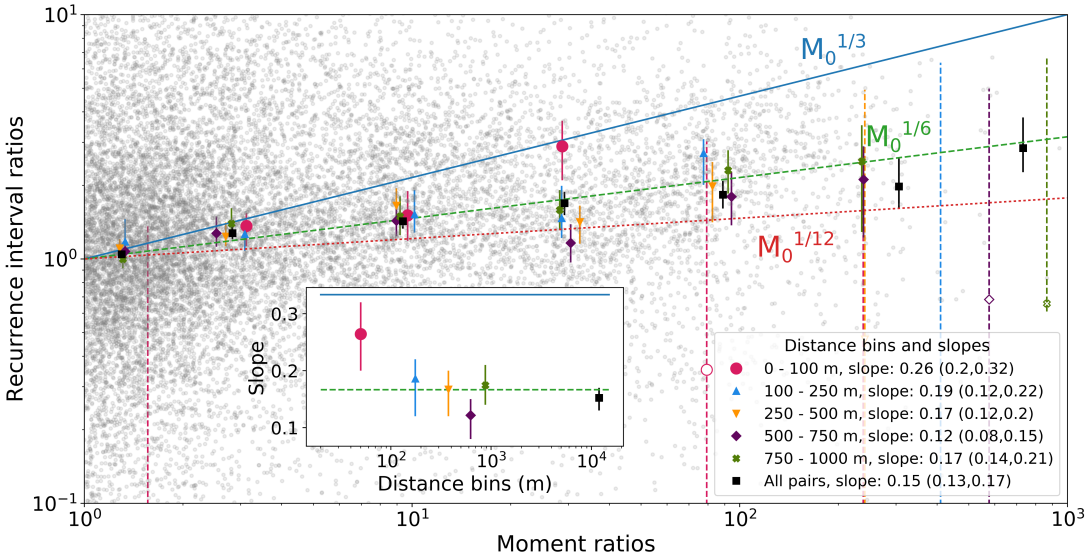

Figure C.5: The moment and recurrence interval ratios with 2-earthquake sequences eliminated if they have recurrence intervals of less than 1 month and if the second earthquake in the sequence is within a month and 250 m of any earthquake before it.

C.2.5 Avoiding bias in recurrence intervals due to the end of the catalog

It is possible that I could be biasing the ratios to lower recurrence intervals due to the end of the catalog. For example, as I cut the catalog off at the 2004 M_W 6 Parkfield earthquake, a repeating earthquake which occurs in 2002 and then repeats in 2003 will be included in the ratios calculations. However, if the repeating earthquake occurs in 2002 and then repeats in 2005, it will not be included in the calculations. This may bias the average recurrence interval ratios lower than the true average in the catalog.

To address this, I exclude 2-earthquake sequences where the first earthquake happens after 31st December 2000, as a 3-year recurrence interval is probably close to the maximum I expect for these repeating earthquakes. I find that this makes no difference to the overall results of this study (Figure C.7), although does reduce the slope of the 0 - 100 m distance bin slightly.

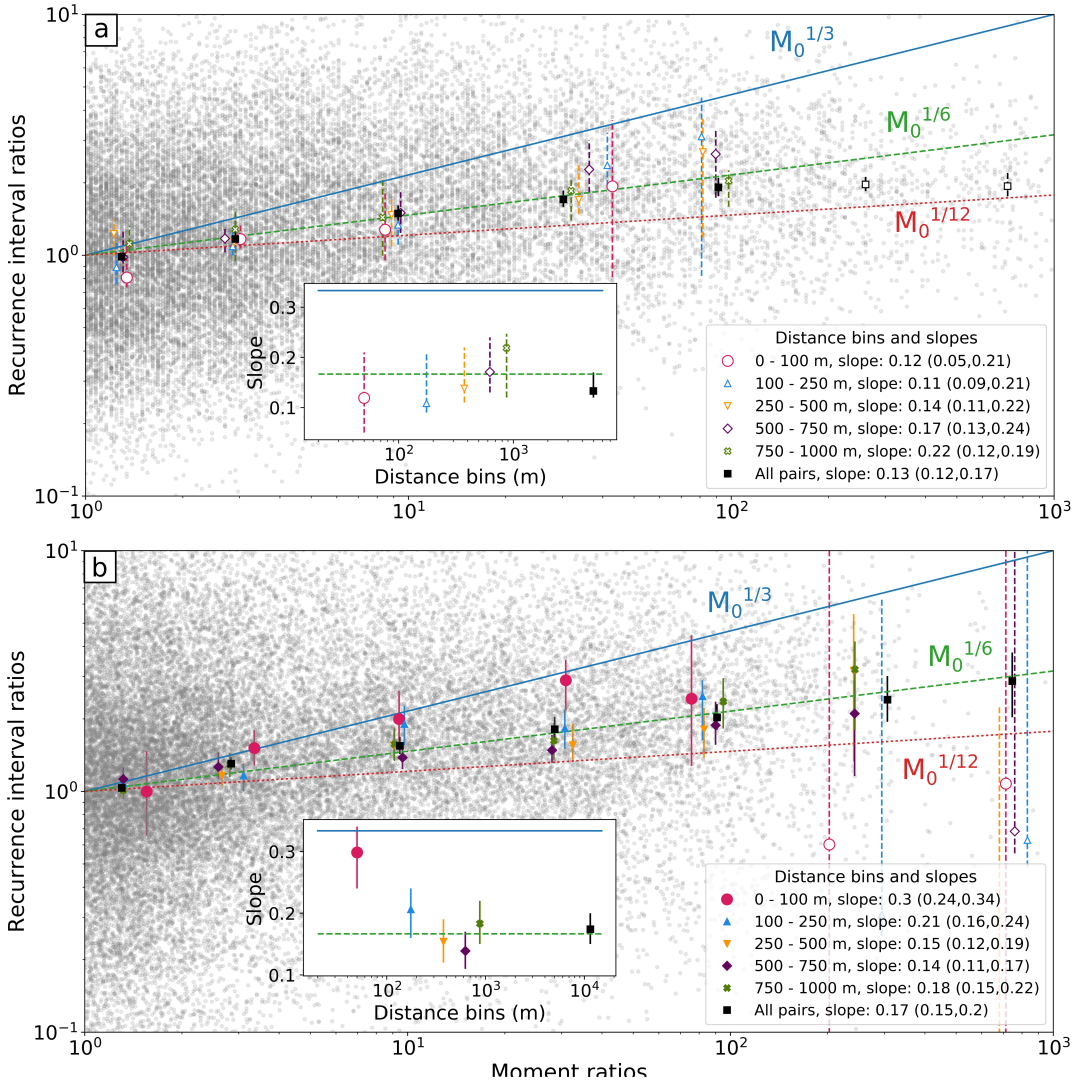

Figure C.6: The moment and recurrence interval ratios with earthquakes from 6 months before the 2004 M_W 6 Parkfield earthquake excluded for pairs of sequences in (a): the catalog of *Lengliné and Marsan* (2009) and (b): the relocated NCSN catalog (*Waldhauser and Schaff*, 2008, *Waldhauser*, 2009).

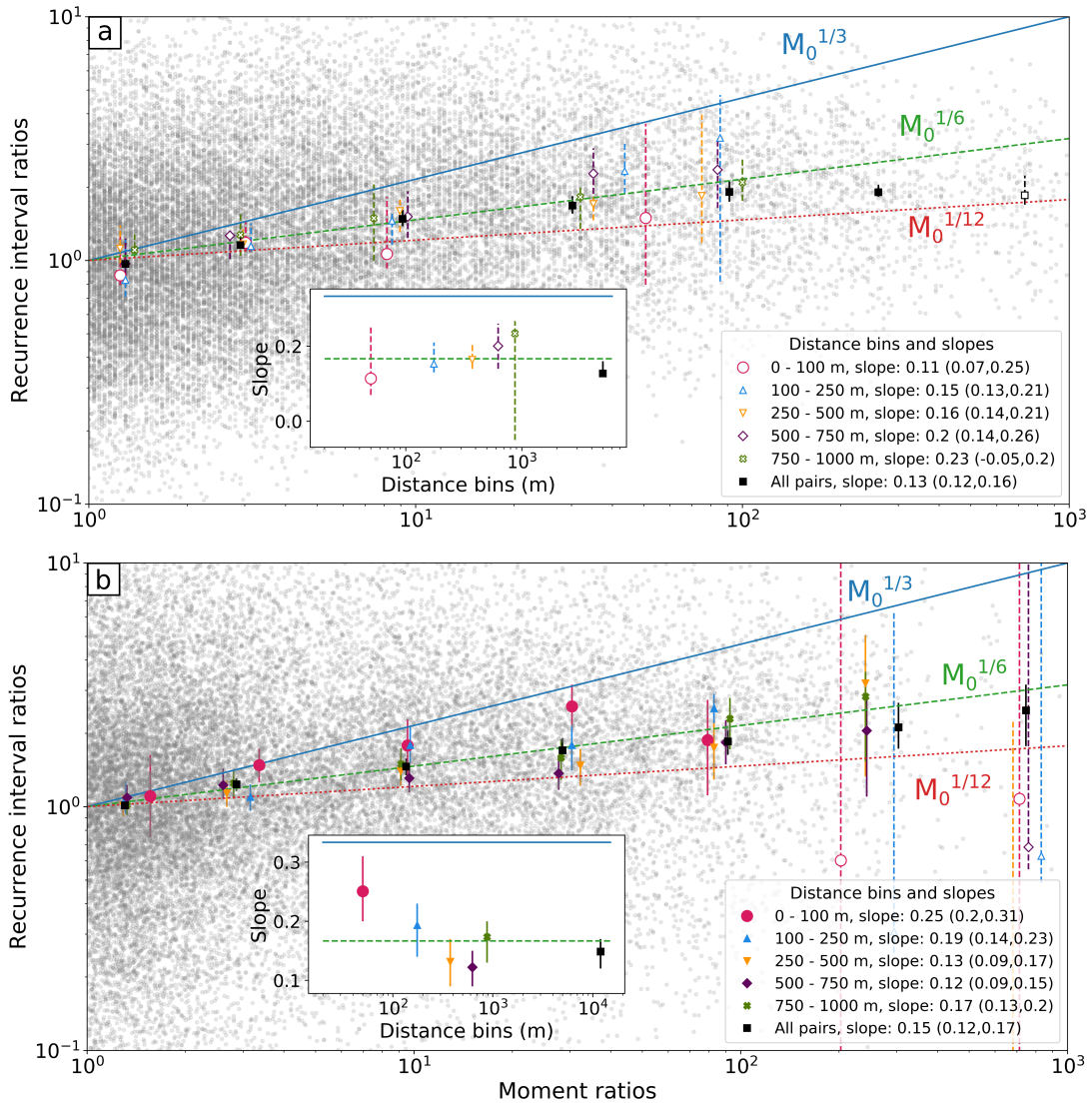

Figure C.7: The moment and recurrence interval ratios excluding 2-earthquake sequences that occur too close to the end of the catalog and may bias median recurrence intervals lower for pairs of sequences in (a): the catalog of *Lengliné and Marsan* (2009) and (b): the relocated NCSN catalog (*Waldhauser and Schaff*, 2008, *Waldhauser*, 2009).

C.2.6 Using probability distributions of earthquake locations

I attempt to account for the uncertainty in the earthquake locations of the NCSN catalog by readjusting the average locations of the 2-earthquake sequences within the location uncertainty. I create normal distributions of location shifts for both horizontal locations and depths using the uncertainties of 34 m and 80 m, respectively. For each pair of 2-earthquake sequences, I shift the sequence locations by picking randomly from the normal distributions of horizontal and depth location shifts, and then recalculate the distance between them. I repeat this 1000 times to approximate a probability distribution of the distance between the pair of 2-event sequences. I perform this approach for every pair of 2-event sequences.

I can use these probability distributions to get a rough idea of how the location uncertainty on the earthquakes may change the distance bin that pairs of 2-earthquake sequences will be included in, and whether this is affecting the slopes I calculate. I take 10 examples for each pair and place them in different distance bins according to the results of their probability distribution. I then recompute the average ratios and slopes of different distance bins (Figure C.8). I find that this does not change the pattern of slopes with distance bins.

C.2.7 Calculating earthquake radius using a stress drop of 3 MPa

I test if the stress drop I use is appropriate for my analysis. I change the stress drop I use in the calculation of earthquake radii to 3 MPa, to reflect the global average stress drop (e.g., *Allmann and Shearer*, 2009) rather than the 10 MPa average stress drop of Parkfield (e.g., *Imanishi et al.*, 2004, *Allmann and Shearer*, 2007, *Abercrombie*, 2014). I then form the 2-earthquake sequences and calculate averages of moment and recurrence interval ratios (Figure C.9). I observe little difference to the results using the lower 3 MPa stress drop, although the slope of the 0 - 100 m distance bin is reduced.

I also use an even lower stress drop of 1 MPa to see if this affects my results. I find

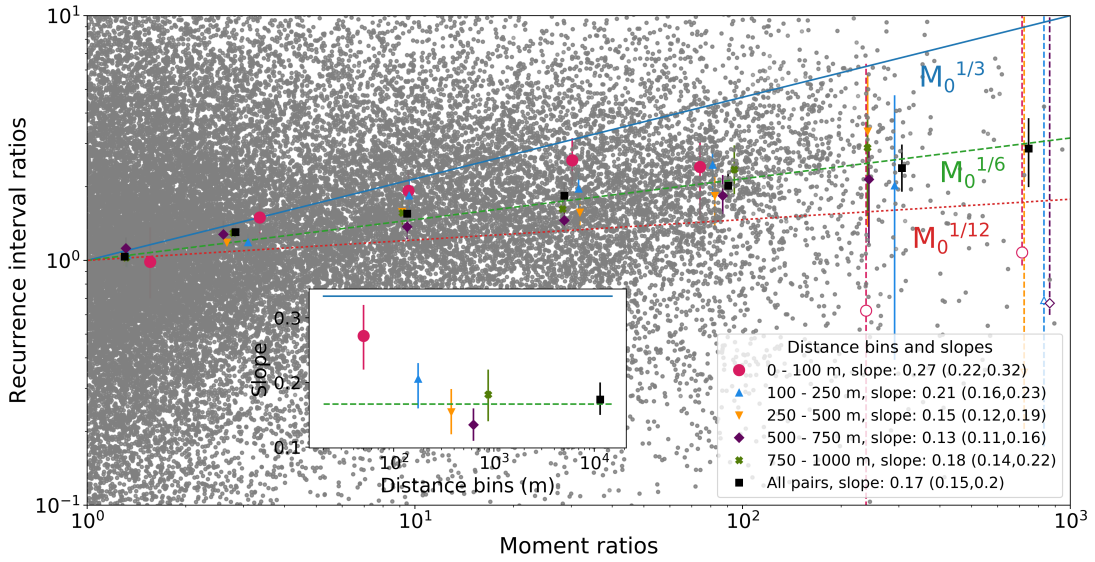

Figure C.8: The moment and recurrence interval ratios with the uncertainty in earthquake locations of the NCSN catalog accounted for using probability distributions.

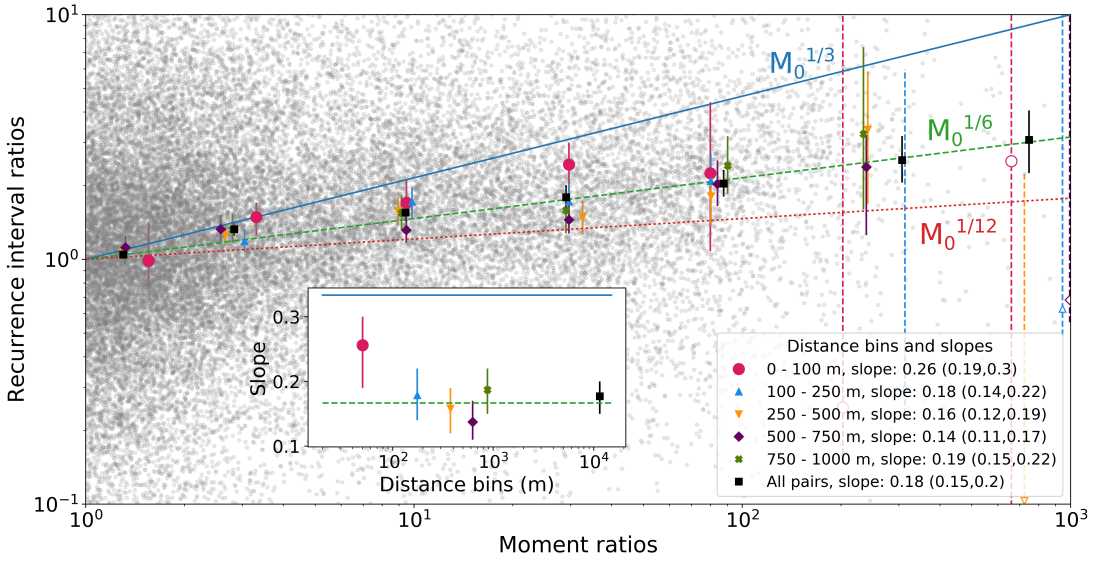

Figure C.9: The moment and recurrence interval ratios from the NCSN catalog with rupture radius calculated using a stress drop of 3 MPa.

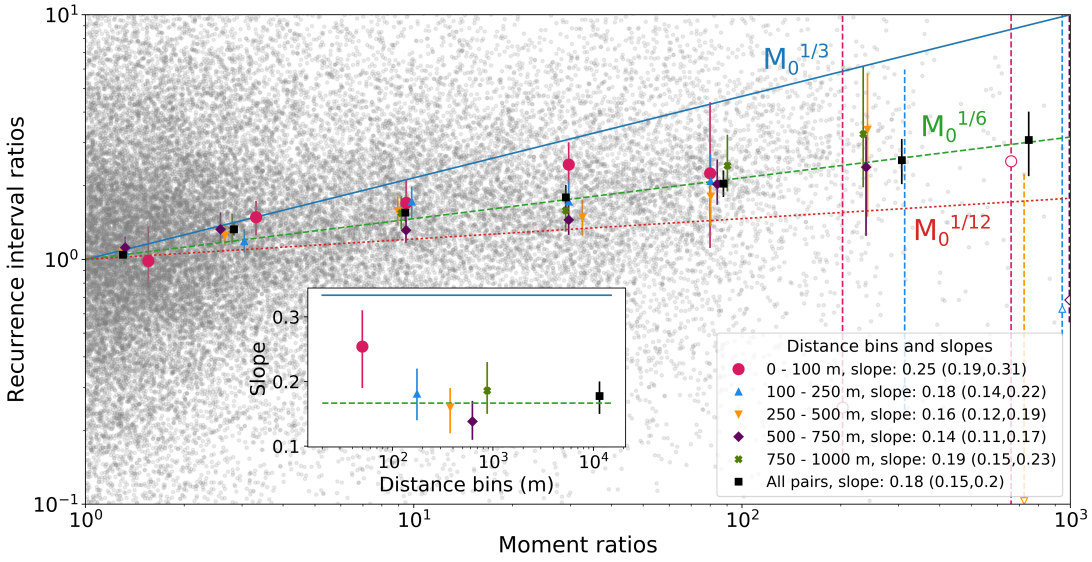

Figure C.10: The moment and recurrence interval ratios from the NCSN catalog with rupture radius calculated using a stress drop of 1 MPa.

no significant change in the variation of scaling exponents for different distance bins which I observe in the main text.

C.2.8 Computing ratios between multiple-event sequences for the relocated NCSN catalog

I examine whether ratios of multiple-earthquake sequence recurrence intervals and moments for the relocated northern California catalog follow the same relation as the ratios of 2-earthquake sequences. I form multiple-earthquake sequences from the 2-event sequences formed in the main text by joining the 2-event sequences through time, for example if earthquake 1 matches with earthquake 2, and earthquake 2 matches with 3, I form a sequence with earthquakes 1, 2, and 3. I find that multiple-earthquake sequences produce the same pattern of slopes as 2-earthquake sequences (Figure C.11).

I also compute the coefficient of variation (COV) for these sequences, which is the standard deviation of the recurrence intervals of a sequence divided by the mean. I redo the analysis for both the NCSN and the catalog of *Lengliné and Marsan* (2009) using sequences with COVs of less than 0.5. I exclude sequences with only two events.

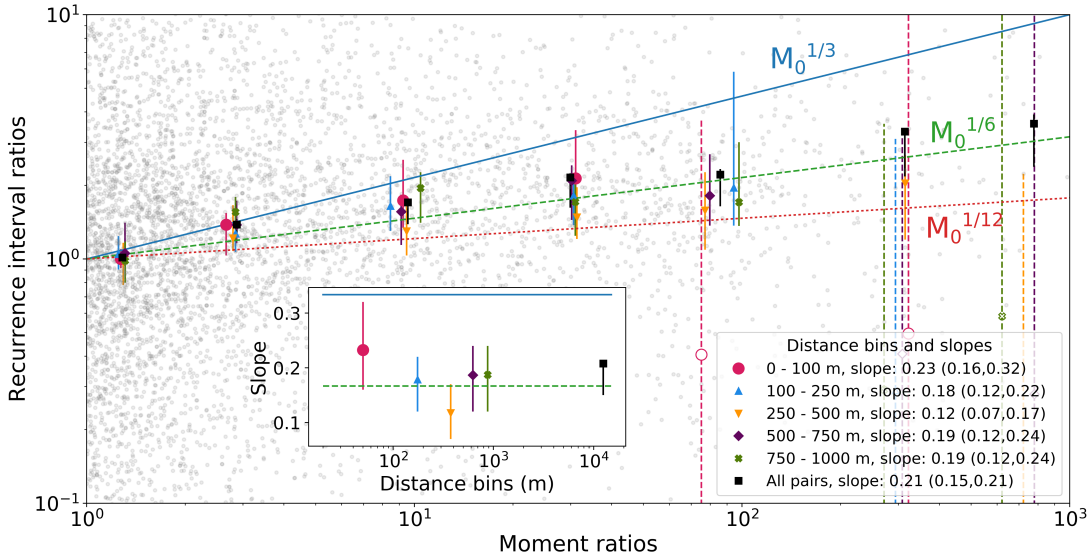

Figure C.11: The moment and recurrence interval ratios for multiple-event sequences in the NCSN catalog. These multiple-event sequences were formed by tracing 2-earthquake sequences through time.

After restricting the earthquake sequences using the COV, I examine the scaling of recurrence interval ratios with moment ratios (Figure C.12). Unfortunately, the COV filtering severely reduces the number of sequences, and the slope estimates become unstable. I cannot conclude whether filtering by the COV makes a difference to the slopes.

C.2.9 Using a magnitude constant of 1.2 to obtain moments

I test whether my assumptions on the relationship between magnitude and moment in the Parkfield region could affect the slopes for moments and distance bins. I adjust the moment calculation from $M_0 = 10^{1.6M+9.05}\ Nm$ (*Wyss et al.*, 2004) to $M_0 = 10^{1.2M+10.65}\ Nm$, whilst still using the old moment scaling to calculate the rupture radius to avoid any effect on the identification of 2-earthquake sequences. I also reduce the spacing between moment bins to check I do not miss any variation. This change in moment calculation should multiply the slope by a factor of 1.6/1.2, or $\frac{4}{3}$. Therefore if the slope has a similar pattern with distance bins to the results of the main text, the 0 - 100 m distance bin should have a slope close to 0.39, the 100 - 250 m distance bin

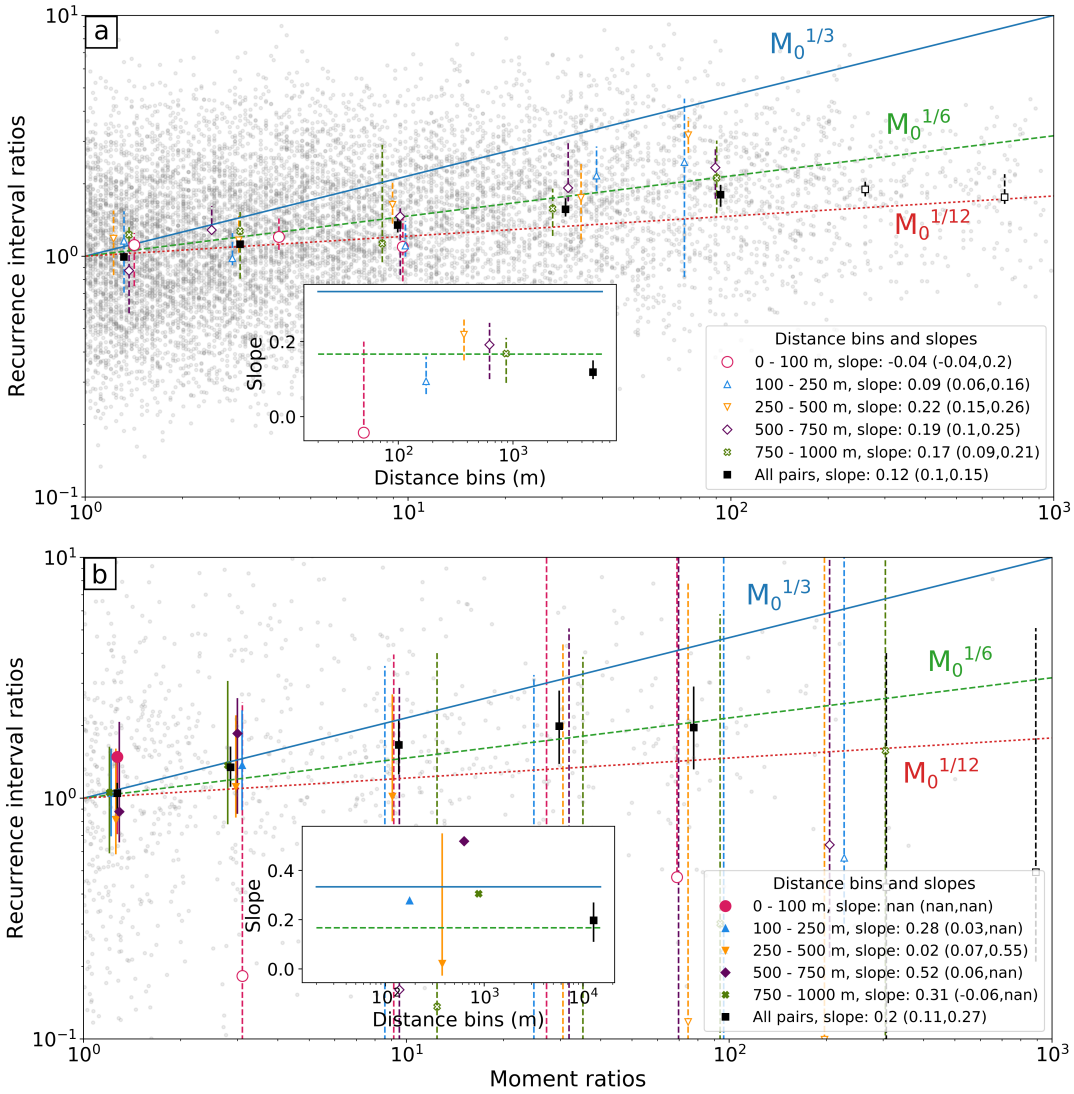

Figure C.12: The moment and recurrence interval ratios for multiple-event sequences in both catalogs, filtered to remove those which have coefficients of variation higher than 0.5 for pairs of sequences in (a): the catalog of *Lengliné and Marsan* (2009) and (b): the relocated NCSN catalog (*Waldhauser and Schaff*, 2008, *Waldhauser*, 2009).

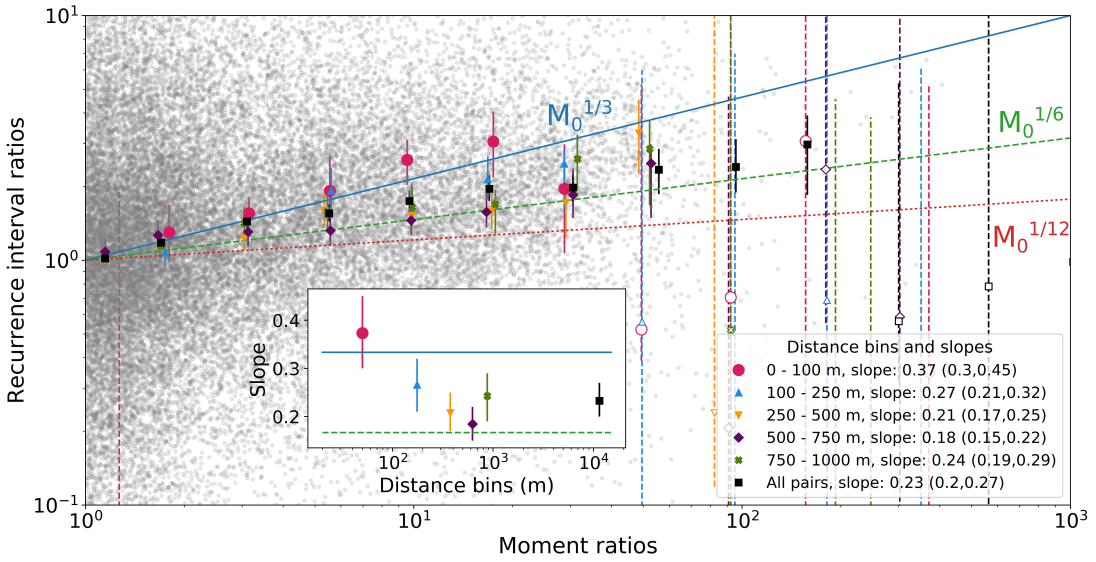

Figure C.13: The moment and recurrence interval ratios using a different magnitude scaling relation of $M_0 = 10^{1.2M+10.65}\ Nm$ as opposed to $M_0 = 10^{1.6M+9.05}\ Nm$. The old moment equation is still used to calculate the rupture radius to avoid any effect on the identification of 2-earthquake sequences.

should have a slope close to 0.27, and the rest of the bins should have a slope close to 0.21. The slopes of the distance bins are close to these values (Figure C.13), which suggests that change in moment calculation does not affect the results.

C.2.10 Calculating slopes using an L1-norm minimum

I check whether my choice of method for slope calculation could be affecting the slopes. I change the calculation of slopes from an L2-norm minimisation to an L1-norm minimisation (Figure C.14). I observe no change in the pattern of slopes with this new approach.

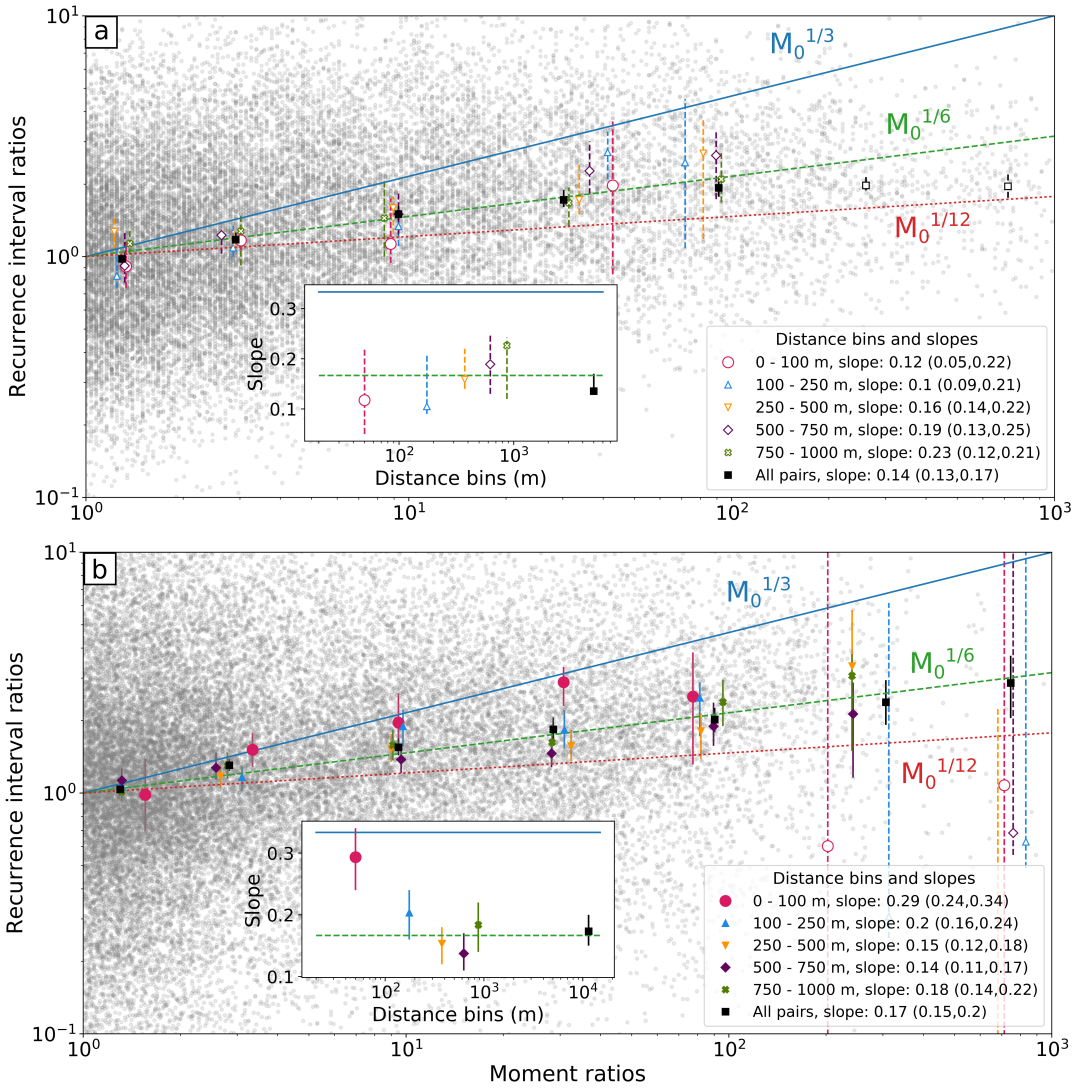

Figure C.14: The moment and recurrence interval ratios with slopes calculated by minimising an L1-norm rather than an L2-norm for pairs of sequences in (a): the catalog of *Lengliné and Marsan* (2009) and (b): the relocated NCSN catalog (*Waldhauser and Schaff*, 2008, *Waldhauser*, 2009).

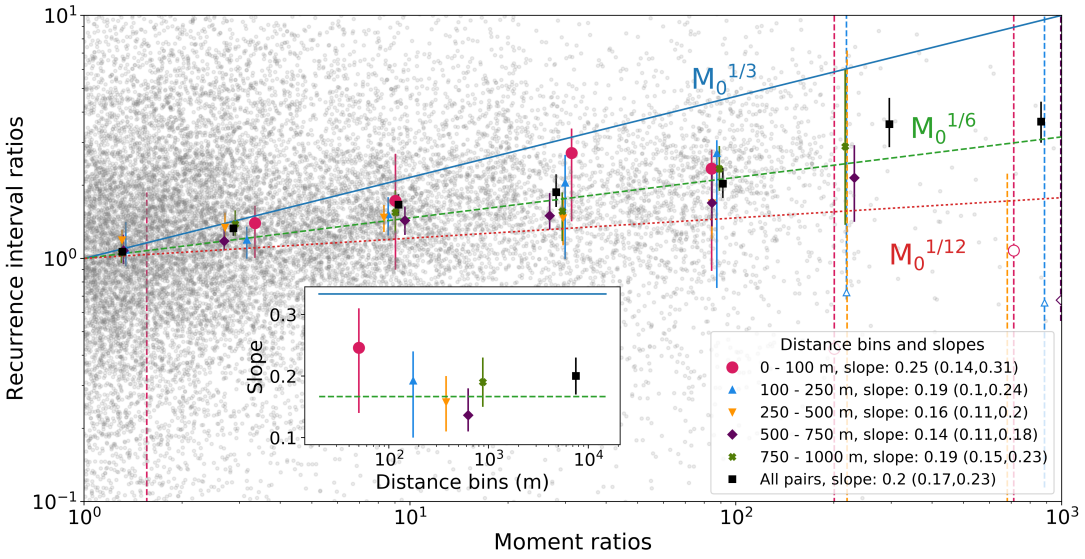

Figure C.15: The moment and recurrence interval ratios for the NCSN catalog using earthquakes from around the SAFOD seismic stations.

Table C.2: The exact coordinates for the SAFOD area analyzed.

Latitude (deg)	Longitude (deg)
36.	-120.63
36.04	-120.54
35.88	-120.36
35.84	-120.45

C.2.11 Using only earthquakes near the SAFOD seismic stations

I select a smaller sub-area of the catalog around the San Andreas Fault Observatory at Depth (SAFOD) seismic stations, as these earthquakes should have more accurate locations, and perform the analysis on this subset of earthquakes (Figure C.15). I find little difference to the results using the entire catalog, although the slope of the 0 - 100 m distance bin is reduced and the uncertainties are larger. The exact coordinates of this region are given in Table C.2.

C.2.12 Using different magnitude unit thresholds

I change the 0.3 magnitude unit threshold that I use in the main text to see whether it affects that variation in scaling exponents that I observe for different distance bins. I use 0.2 (Figure C.16) and 0.5 (Figure C.17) magnitude unit thresholds. I observe no

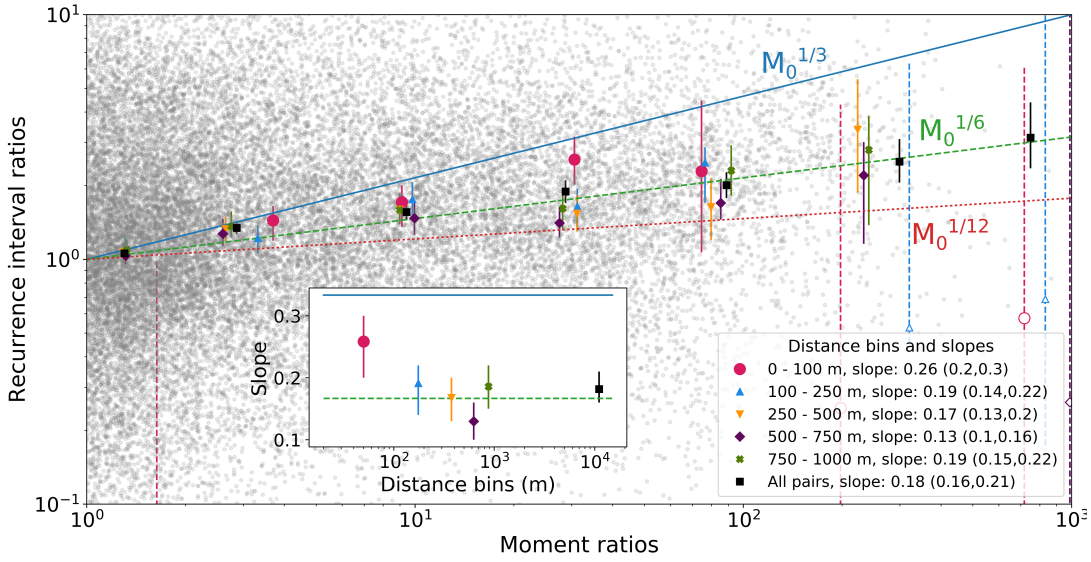

Figure C.16: The moment and recurrence interval ratios for the NCSN catalog using a 0.2 magnitude unit threshold to define 2-earthquake sequences.

significant change in the variation of scaling exponents, although the exponent for the 0 - 100 m distance bin is slightly reduced.

C.2.13 Different definitions of the distance between sequences

I test whether our results change if I define the distances between sequences differently. In the main text, I define inter-sequence distance as the distance between the first events in each 2-earthquake sequence. Here I compute the inter-sequence distance as the distance between the second events in each sequences (Figure C.18), and as the distance between the average locations of each sequence (Figure C.19). I redo my analysis with these different methods of computing inter-sequence distances to see if it affects my observed variation in recurrence interval-moment scaling exponents for different distance bins. I find that the variation of scaling exponent with distance bin is similar to the result I observed in the main text, although the exponent of the 0 - 100 m distance bin is slightly reduced.

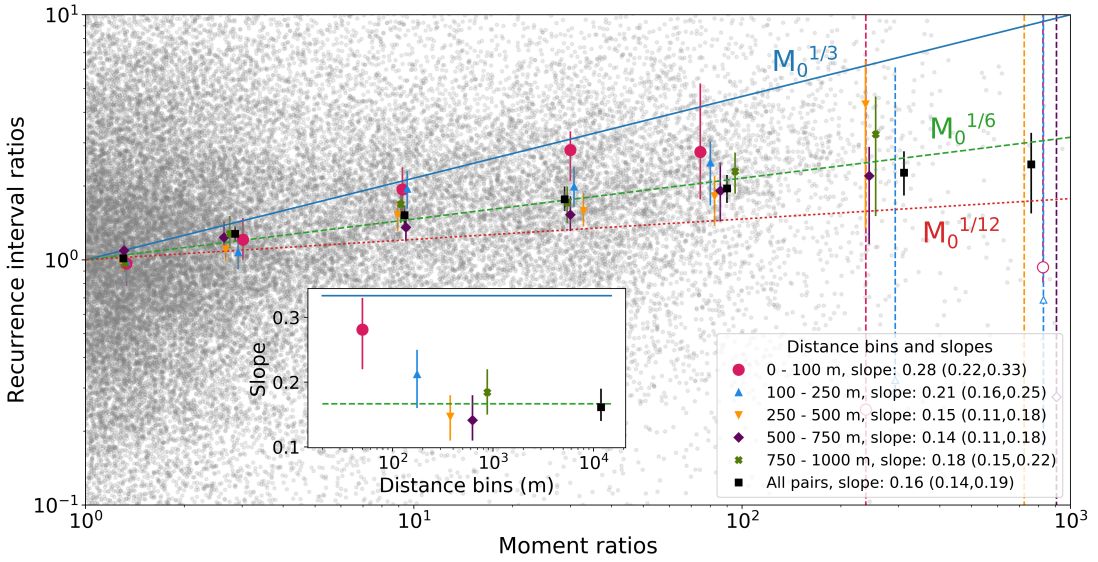

Figure C.17: The moment and recurrence interval ratios for the NCSN catalog using a 0.5 magnitude unit threshold to define 2-earthquake sequences.

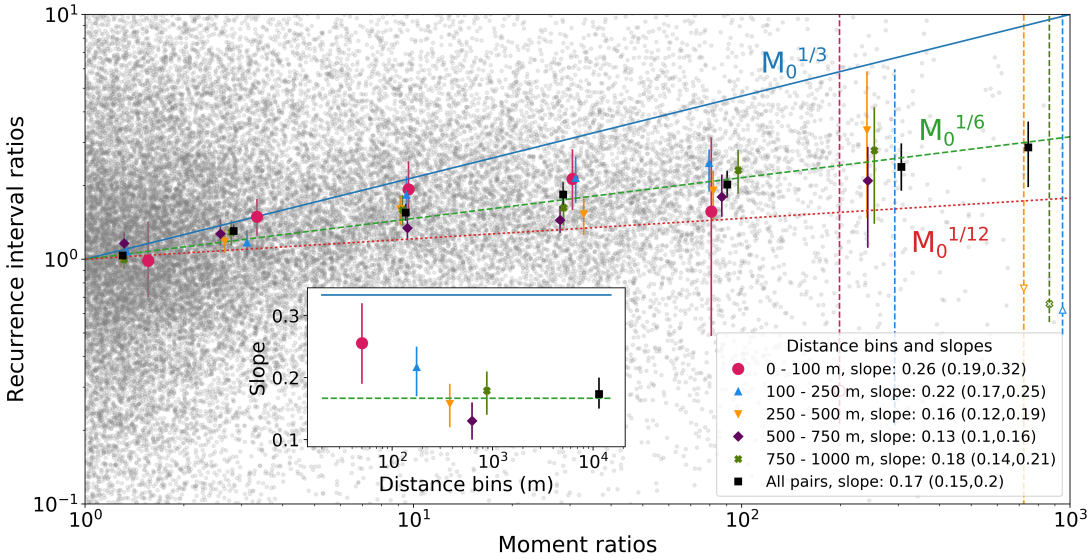

Figure C.18: The moment and recurrence interval ratios where the inter-sequence distance has been computed between the locations of the second events in each 2-earthquake sequence.

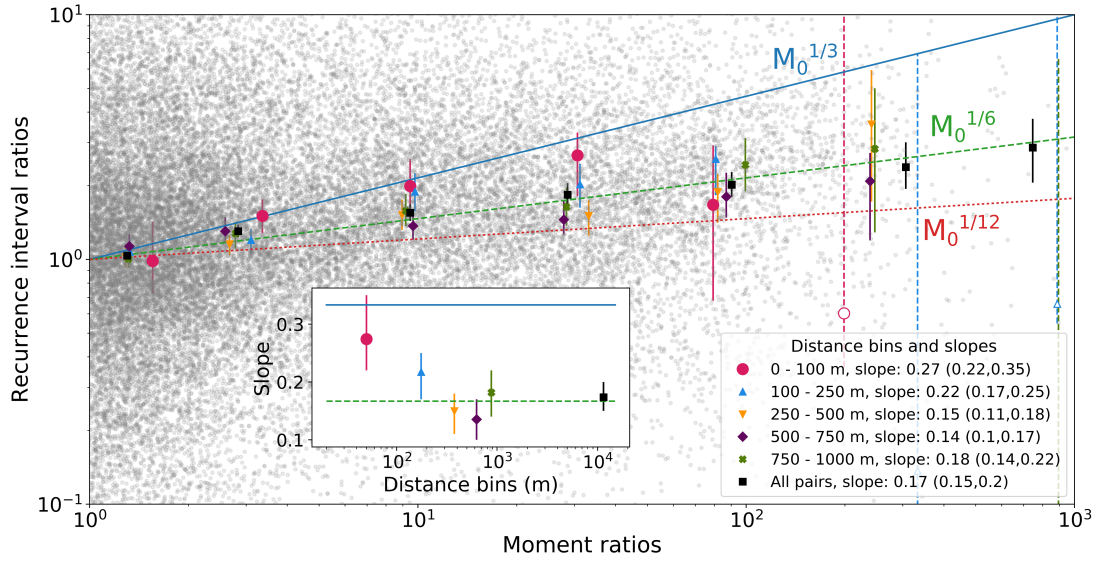

Figure C.19: The moment and recurrence interval ratios where the inter-sequence distance has been computed between the median locations of each 2-earthquake sequence.

C.3 Sequence catalog information

C.3.1 Histograms of relative locations between earthquake sequences

I test whether location uncertainties in the NCSN catalog could be affecting a single distance bin more than the others. I plot the relative locations between 2-earthquake sequences for the NCSN catalog for each distance bin for all sequences used including multiple instances of the same sequences (Figure C.20) and for unique sequences only (Figure C.21). I plot the relative locations as a percentage of the acceptable distance (first earthquake rupture radius) plus the location uncertainty from the NCSN catalog (combination of horizontal and depth uncertainty). I observe that the distribution of percentage distances is similar across all distance bins for both all and unique earthquakes, which suggests that location uncertainties are not significantly affecting any particular distance bin. Specifically for the 0 - 100 m distance bin, the distribution of distances between earthquakes in sequences is concentrated at lower percentages. This indicates that earthquakes are indeed clustered on this fault, as a higher number of earthquakes used in the sequences are very close to each other, rather than at the higher end of the distribution.

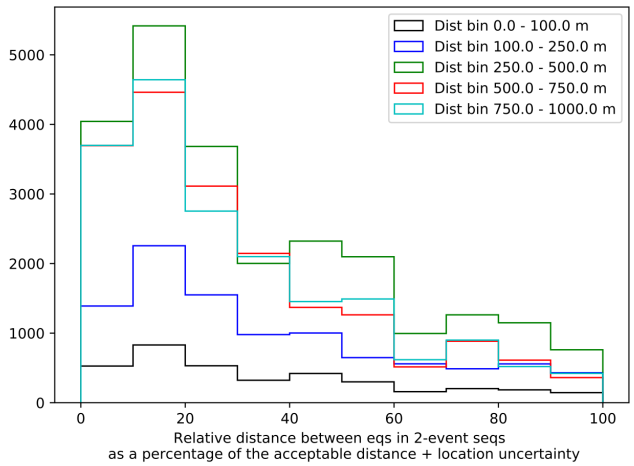

Figure C.20: Histogram of the distance between earthquakes in the 2-earthquake sequences which were used to calculate moment and recurrence intervals in the main text. All 2-earthquake sequences used are included here, which includes repeats of the same sequences. The distance is plotted as a percentage of the acceptable distance (rupture radius) plus the location uncertainty of the NCSN catalog. The color indicates the distance bin.

C.4 Using synthetic catalogs to validate the simple approach to identify repeaters

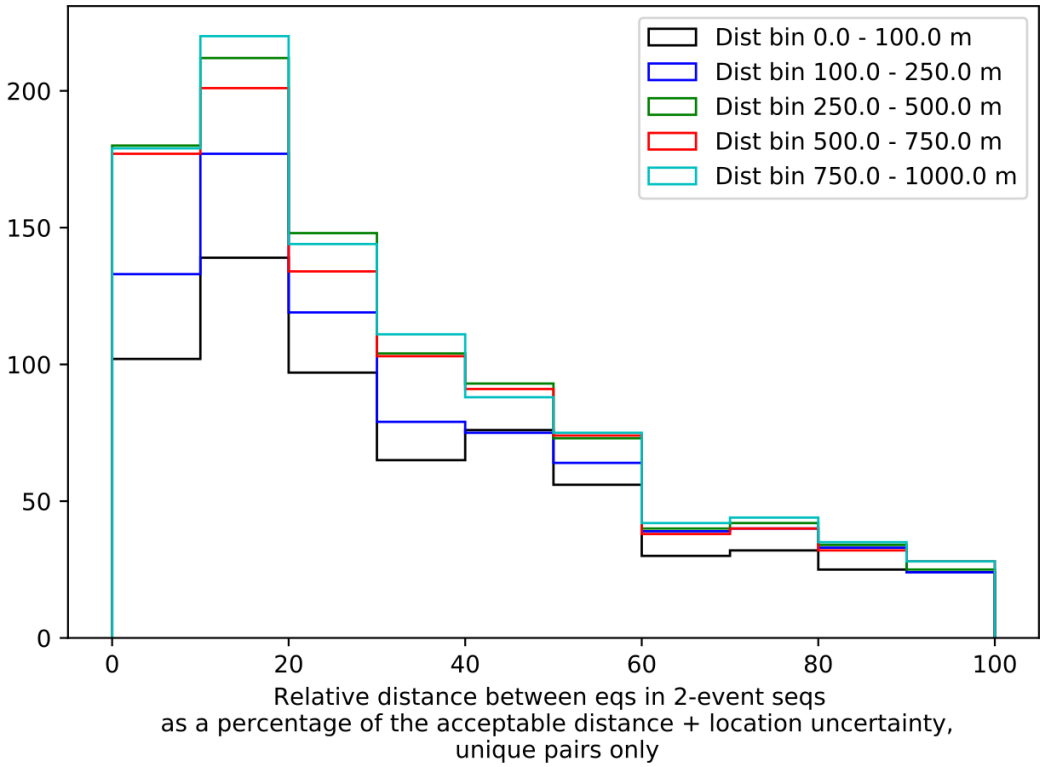

Figure C.21: Histogram of the distance between earthquakes in the 2-earthquake sequences which were used to calculate moment and recurrence intervals in the main text. Only unique sequences are included here, so there are no repeats in the histograms, but some sequences appear in multiple distance bins. The distance is plotted as a percentage of the acceptable distance (rupture radius) plus the location uncertainty of the NCSN catalog. The color indicates the distance bin.

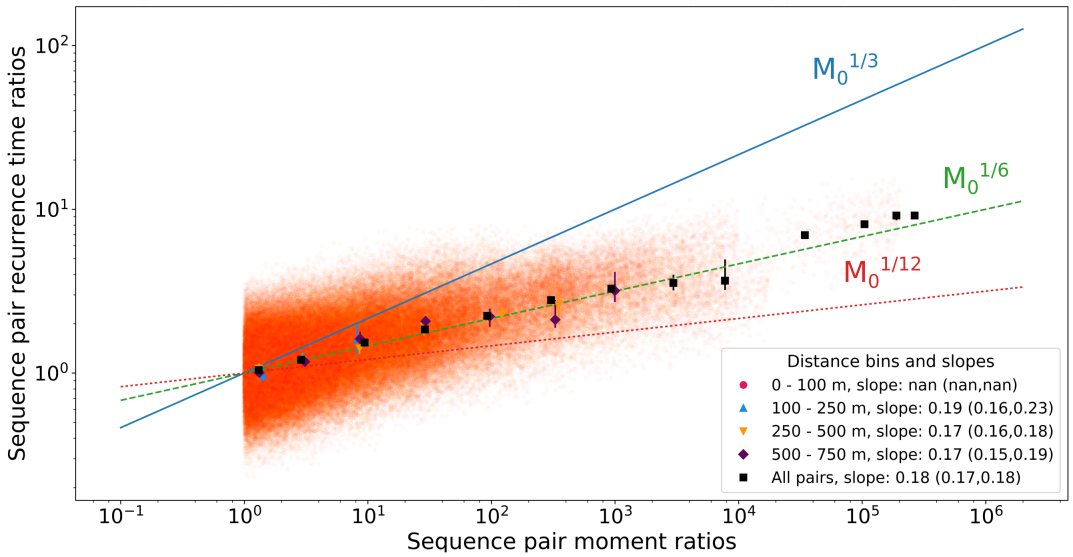

Figure C.22: The moment and recurrence interval ratios for a synthetic catalog where recurrence intervals of earthquakes scale with moment as $M_0^{0.17}$.

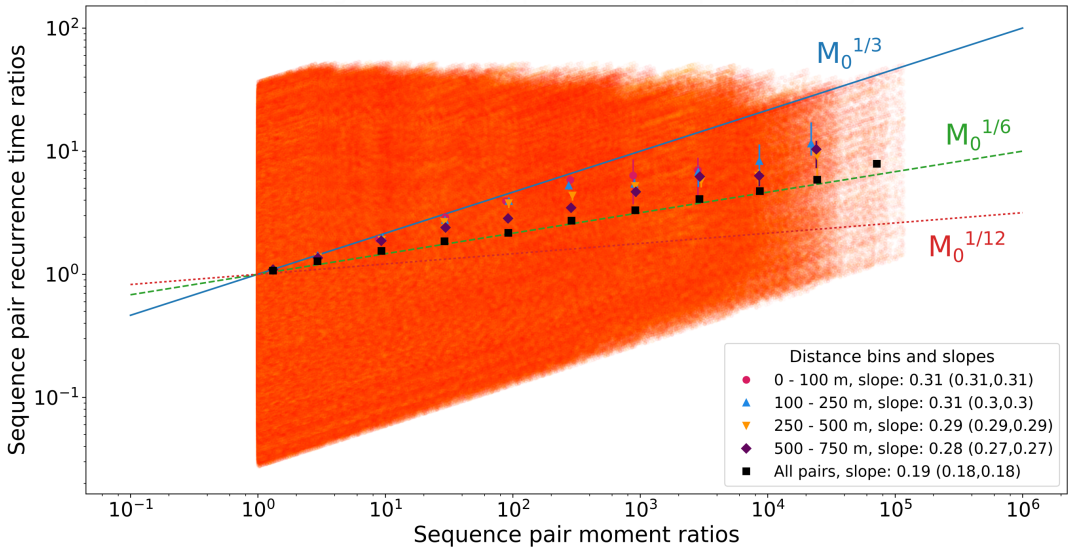

Figure C.23: The moment and recurrence interval ratios for a synthetic catalog with multiple fault strands. One each fault, the recurrence intervals scale as $M_0^{\frac{1}{3}}$. The streaks in this catalog are the recurrence interval-moment ratios along individual faults, similar to the concept shown in Figure 4.1.

References

Abercrombie, R., and P. Leary (1993), Source parameters of small earthquakes recorded at 2.5 km depth, Cajon Pass, southern California: implications for earthquake scaling, *Geophysical Research Letters*, *20*(14), 1511–1514.

Abercrombie, R. E. (1995), Earthquake source scaling relationships from- 1 to 5 ML using seismograms recorded at 2.5-km depth, *Journal of Geophysical Research: Solid Earth*, *100*(B12), 24,015–24,036.

Abercrombie, R. E. (2014), Stress drops of repeating earthquakes on the San Andreas fault at Parkfield, *Geophysical Research Letters*, *41*(24), 8784–8791.

Abercrombie, R. E. (2015), Investigating uncertainties in empirical Green's function analysis of earthquake source parameters, *Journal of Geophysical Research: Solid Earth*, *120*(6), 4263–4277.

Abercrombie, R. E., and G. Ekström (2001), Earthquake slip on oceanic transform faults, *Nature*, *410*(6824), 74–77.

Abercrombie, R. E., and G. Ekström (2003), A reassessment of the rupture characteristics of oceanic transform earthquakes, *Journal of Geophysical Research: Solid Earth*, *108*(B5).

Abercrombie, R. E., and J. Mori (1996), Occurrence patterns of foreshocks to large earthquakes in the western United States, *Nature*, *381*(6580), 303.

Abercrombie, R. E., S. Bannister, J. Ristau, and D. Doser (2017), Variability of earth-

quake stress drop in a subduction setting, the Hikurangi Margin, New Zealand, *Geophysical Journal International*, *208*(1), 306–320.

Aki, K. (1967), Scaling law of seismic spectrum, *Journal of Geophysical Research*, *72*(4), 1217–1231.

Algermissen, S. T. (1972), *A study of earthquake losses in the San Francisco Bay Area: Data and analysis*, US Department of Commerce, National Oceanic & Atmospheric Administration.

Allen, C. R., L. Zhuoli, Q. Hong, W. Xueze, Z. Huawei, and H. Weishi (1991), Field study of a highly active fault zone: The Xianshuihe fault of southwestern China, *Geological Society of America Bulletin*, *103*(9), 1178–1199.

Allmann, B. P., and P. M. Shearer (2007), Spatial and temporal stress drop variations in small earthquakes near Parkfield, California, *Journal of Geophysical Research: Solid Earth*, *112*(B4).

Allmann, B. P., and P. M. Shearer (2009), Global variations of stress drop for moderate to large earthquakes, *Journal of Geophysical Research: Solid Earth*, *114*(B1).

Amante, C., and B. Eakins (2009), ETOPO1 1 Arc-Minute Global Relief Model: Procedures, Data Sources and Analysis., *NOAA Technical Memorandum NESDIS NGDC-24.*, *n/a*(National Geophysical Data Center, NOAA.).

Amato, A., P. Montone, and M. Cesaro (1995), State of stress in Southern Italy from borehole breakout and focal mechanism data, *Geophysical Research Letters*, *22*(23), 3119–3122.

Anderson, E. M. (1951), *The dynamics of faulting*, 2nd ed ed., Edinburgh: Oliver & Boyd.

Anderson, J. G., and S. E. Hough (1984), A model for the shape of the Fourier amplitude spectrum of acceleration at high frequencies, *Bulletin of the Seismological Society of America*, *74*(5), 1969–1993.

Andrews, D. (1986), Objective determination of source parameters and similarity of earthquakes of different size, *Earthquake Source Mechanics*, *37*, 259–267.

Andrews, D., and M. Barall (2011), Specifying initial stress for dynamic heterogeneous earthquake source models, *Bulletin of the Seismological Society of America*, *101*(5), 2408–2417.

Anooshehpoor, A., and J. N. Brune (2001), Quasi-static slip-rate shielding by locked and creeping zones as an explanation for small repeating earthquakes at Parkfield, *Bulletin of the Seismological Society of America*, *91*(2), 401–403.

Aytun, A. (1982), Creep measurements in the Ismetpaşa region of the North Anatolian Fault Zone, in *Multidisciplinary approach to earthquake prediction*, pp. 279–292, Springer.

Azzaro, R., M. Mattia, and G. Puglisi (2001), Fault creep and kinematics of the eastern segment of the Pernicana Fault (Mt. Etna, Italy) derived from geodetic observations and their tectonic significance, *Tectonophysics*, *333*(3-4), 401–415.

Badawy, A. (2001), Status of the crustal stress in Egypt as inferred from earthquake focal mechanisms and borehole breakouts, *Tectonophysics*, *343*(1-2), 49–61.

Baisch, S., and G. H. Bokelmann (2001), Seismic waveform attributes before and after the Loma Prieta earthquake: Scattering change near the earthquake and temporal recovery, *Journal of Geophysical Research: Solid Earth*, *106*(B8), 16,323–16,337.

Bakun, W., B. Aagaard, B. Dost, W. Ellsworth, J. Hardebeck, R. Harris, C. Ji, M. Johnston, J. Langbein, J. Lienkaemper, and others (2005), Implications for prediction and hazard assessment from the 2004 Parkfield earthquake, *Nature*, *437*(7061), 969.

Bakun, W. H., and A. G. Lindh (1985), The Parkfield, California, earthquake prediction experiment, *Science*, *229*(4714), 619–624.

Baltay, A., S. Ide, G. Prieto, and G. Beroza (2011), Variability in earthquake stress drop and apparent stress, *Geophysical Research Letters*, *38*(6).

Barka, A. (1992), The north Anatolian fault zone, in *Annales tectonicae*, vol. 6, pp. 164–195.

Barton, C. A., and M. D. Zoback (1994), Stress perturbations associated with active faults penetrated by boreholes: Possible evidence for near-complete stress drop and a new technique for stress magnitude measurement, *Journal of Geophysical Research: Solid Earth*, *99*(B5), 9373–9390.

Báth, M., and S. J. Duda (1964), Earthquake volume, fault plane area, seismic energy, strain, deformation and related quantities, *Annals of Geophysics*, *17*(3), 353–368.

Beeler, N., D. Lockner, and S. Hickman (2001), A simple stick-slip and creep-slip model for repeating earthquakes and its implication for microearthquakes at Parkfield, *Bulletin of the Seismological Society of America*, *91*(6), 1797–1804.

Behn, M. D., J. Lin, and M. T. Zuber (2002), Evidence for weak oceanic transform faults, *Geophysical Research Letters*, *29*(24), 60–1.

Bell, A. F. (2018), Predictability of Landslide Timing From Quasi-Periodic Precursory Earthquakes, *Geophysical Research Letters*, *45*(4), 1860–1869.

Bergen, K., and J. Shaw (2010), Displacement profiles and displacement-length scaling relationships of thrust faults constrained by seismic-reflection data, *Bulletin of the Geological Society of America*, *122*(7-8), 1209–1219.

Beroza, G. C., and T. H. Jordan (1990), Searching for slow and silent earthquakes using free oscillations, *Journal of Geophysical Research: Solid Earth*, *95*(B3), 2485–2510.

Beyreuther, M., R. Barsch, L. Krischer, T. Megies, Y. Behr, and J. Wassermann (2010), ObsPy: A Python Toolbox for Seismology, *Seismological Research Letters*, *81*(3), 530–533.

Bilham, R. (1989), Surface slip subsequent to the 24 November 1987 Superstition Hills, California, earthquake monitored by digital creepmeters, *Bulletin of the Seismological Society of America*, *79*(2), 424–450.

Bindi, D., F. Cotton, D. Spallarossa, M. Picozzi, and E. Rivalta (2018), Temporal variability of ground shaking and stress drop in Central Italy: A hint for fault healing?, *Bulletin of the Seismological Society of America*, *108*(4), 1853–1863.

Bird, P. (2003), An updated digital model of plate boundaries, *Geochemistry, Geophysics, Geosystems*, *4*(3).

Bird, P., Y. Y. Kagan, and D. D. Jackson (2002), *Plate tectonics and earthquake potential of spreading ridges and oceanic transform faults*, American Geophysical Union, Washington D. C.

Boettcher, M. S., and T. Jordan (2004), Earthquake scaling relations for mid-ocean ridge transform faults, *Journal of Geophysical Research: Solid Earth*, *109*(B12).

Boettcher, M. S., and J. J. McGuire (2009), Scaling relations for seismic cycles on mid-ocean ridge transform faults, *Geophysical Research Letters*, *36*(21).

Boettcher, M. S., G. Hirth, and B. Evans (2007), Olivine friction at the base of oceanic seismogenic zones, *Journal of Geophysical Research: Solid Earth*, *112*(B1).

Bormann, P., K. Klinge, and S. Wendt (2002), Data analysis and seismogram interpretation, *IASPEI New Manual of Seismological Observatory Practice (NMSOP)*, *1*(Chap. 11), 100.

Bosl, W., and A. Nur (2002), Aftershocks and pore fluid diffusion following the 1992 Landers earthquake, *Journal of Geophysical Research: Solid Earth*, *107*(B12), ESE–17.

Bouchon, M., M.-P. Bouin, H. Karabulut, M. N. Toksöz, M. Dietrich, and A. J. Rosakis (2001), How fast is rupture during an earthquake? New insights from the 1999 Turkey earthquakes, *Geophysical Research Letters*, *28*(14), 2723–2726.

Bouchon, M., H. Karabulut, M. Aktar, S. Özalaybey, J. Schmittbuhl, and M.-P. Bouin (2011), Extended nucleation of the 1999 Mw 7.6 Izmit earthquake, *Science*, *331*(6019), 877–880.

Brace, W., and D. Kohlstedt (1980), Limits on lithospheric stress imposed by laboratory experiments, *Journal of Geophysical Research: Solid Earth*, *85*(B11), 6248–6252.

Brace, W., J. D. Byerlee, and others (1966), Recent experimental studies of brittle fracture of rocks, in *The 8th US Symposium on Rock Mechanics (USRMS)*, American Rock Mechanics Association.

Braunmiller, J., and J. Nábělek (2008), Segmentation of the Blanco Transform Fault Zone from earthquake analysis: Complex tectonics of an oceanic transform fault, *Journal of Geophysical Research: Solid Earth*, *113*(B7).

Brodsky, E. E. (2019), The importance of studying small earthquakes, *Science*, *364*(6442), 736–737.

Brodsky, E. E., J. J. Gilchrist, A. Sagy, and C. Collettini (2011), Faults smooth gradually as a function of slip, *Earth and Planetary Science Letters*, *302*(1-2), 185–193.

Brune, J. N. (1968), Seismic moment, seismicity, and rate of slip along major fault zones, *Journal of Geophysical Research*, *73*(2), 777–784.

Brune, J. N. (1970), Tectonic stress and the spectra of seismic shear waves from earthquakes, *Journal of Geophysical Research*, *75*(26), 4997–5009.

Brune, J. N. (1976), The physics of earthquake strong motion, in *Developments in Geotechnical Engineering*, vol. 15, pp. 141–177, Elsevier.

Brune, J. N., and W. Thatcher (2002), Strength and energetics of active fault zones, in *International Geophysics*, vol. 81, pp. 569–cp1, Elsevier.

Brune, J. N., J. Fletcher, F. Vernon, L. Haar, T. Hanks, and J. Berger (1986), Low stress-drop earthquakes in the light of new data from the Anza, California telemetered digital array, *Earthquake Source Mechanics*, *37*, 237–245.

Bucknam, R., G. Plafker, and R. Sharp (1978), Fault movement (afterslip) following the Guatemala earthquake of February 4, 1976, *Geology*, *6*(3), 170–173.

Bürgmann, R., D. Schmidt, R. Nadeau, M. d'Alessio, E. Fielding, D. Manaker, T. McEvilly, and M. Murray (2000), Earthquake potential along the northern Hayward fault, California, *Science*, *289*(5482), 1178–1182.

Byerlee, J. (1978), Friction of rocks, in *Rock friction and earthquake prediction*, pp. 615–626, Springer.

Byrnes, J. S., D. R. Toomey, E. E. Hooft, J. Nábělek, and J. Braunmiller (2017), Mantle dynamics beneath the discrete and diffuse plate boundaries of the Juan de Fuca plate: Results from Cascadia Initiative body wave tomography, *Geochemistry, Geophysics, Geosystems*, *18*(8), 2906 – 2929.

Candela, T., F. Renard, J. Schmittbuhl, M. Bouchon, and E. E. Brodsky (2011), Fault slip distribution and fault roughness, *Geophysical Journal International*, *187*(2), 959–968.

Carafa, M. M., G. Valensise, and P. Bird (2017), Assessing the seismic coupling of shallow continental faults and its impact on seismic hazard estimates: a case-study from Italy, *Geophysical Journal International*, *209*(1), 32–47.

Carvell, J., T. Blenkinsop, G. Clarke, and M. Tonelli (2014), Scaling, kinematics and evolution of a polymodal fault system: Hail Creek Mine, NE Australia, *Tectonophysics*, *632*(C), 138–150.

Castro, R., J. Anderson, and S. Singh (1990), Site response, attenuation and source spectra of S waves along the Guerrero, Mexico, subduction zone, *Bulletin of the Seismological Society of America*, *80*(6A), 1481–1503.

Castro, R. R., J. G. Acosta, V. M. Wong, A. Perez-Vertti, A. Mendoza, and L. Inzunza (2011), Location of aftershocks of the 4 April 2010 M w 7.2 El Mayor–Cucapah earthquake of Baja California, Mexico, *Bulletin of the Seismological Society of America*, *101*(6), 3072–3080.

Cattania, C., and P. Segall (2019), Crack models of repeating earthquakes predict

observed moment-recurrence scaling, *Journal of Geophysical Research: Solid Earth*, *124*(1), 476–503.

Cattania, C., S. Hainzl, L. Wang, B. Enescu, and F. Roth (2015), Aftershock triggering by postseismic stresses: A study based on Coulomb rate-and-state models, *Journal of Geophysical Research: Solid Earth*, *120*(4), 2388–2407.

Causse, M., L. Dalguer, and P. M. Mai (2013), Variability of dynamic source parameters inferred from kinematic models of past earthquakes, *Geophysical Journal International*, *196*(3), 1754–1769.

Chang, C., J. B. Lee, and T.-S. Kang (2010), Interaction between regional stress state and faults: Complementary analysis of borehole in situ stress and earthquake focal mechanism in southeastern Korea, *Tectonophysics*, *485*(1-4), 164–177.

Chen, C., and A. A. Holland (2016), PhasePApy: A robust pure Python package for automatic identification of seismic phases, *Seismological Research Letters*, *87*(6), 1384–1396.

Chen, K. H., R. M. Nadeau, and R.-J. Rau (2007), Towards a universal rule on the recurrence interval scaling of repeating earthquakes?, *Geophysical Research Letters*, *34*(16).

Chen, K. H., R. M. Nadeau, and R.-J. Rau (2008), Characteristic repeating earthquakes in an arc-continent collision boundary zone: The Chihshang fault of eastern Taiwan, *Earth and Planetary Science Letters*, *276*(3-4), 262–272.

Chen, K. H., R. Bürgmann, R. M. Nadeau, T. Chen, and N. Lapusta (2010), Postseismic variations in seismic moment and recurrence interval of repeating earthquakes, *Earth and Planetary Science Letters*, *299*(1-2), 118–125.

Chen, T., and N. Lapusta (2009), Scaling of small repeating earthquakes explained by interaction of seismic and aseismic slip in a rate and state fault model, *Journal of Geophysical Research: Solid Earth*, *114*(B1).

Chen, T., and N. Lapusta (2019), On behaviour and scaling of small repeating earthquakes in rate and state fault models, *Geophysical Journal International*, *218*(3), 2001–2018.

Chen, X., and J. J. McGuire (2016), Measuring earthquake source parameters in the Mendocino triple junction region using a dense OBS array: Implications for fault strength variations, *Earth and Planetary Science Letters*, *453*, 276–287.

Chen, X., and P. Shearer (2011), Comprehensive analysis of earthquake source spectra and swarms in the Salton Trough, California, *Journal of Geophysical Research: Solid Earth*, *116*(B9).

Chen, X., and P. M. Shearer (2013), California foreshock sequences suggest aseismic triggering process, *Geophysical Research Letters*, *40*(11), 2602–2607.

Chinnery, M. A. (1969), Earthquake magnitude and source parameters, *Bulletin of the Seismological Society of America*, *59*(5), 1969–1982.

Chlieh, M., J.-P. Avouac, V. Hjorleifsdottir, T.-R. A. Song, C. Ji, K. Sieh, A. Sladen, H. Hebert, L. Prawirodirdjo, Y. Bock, and others (2007), Coseismic slip and afterslip of the great M w 9.15 Sumatra–Andaman earthquake of 2004, *Bulletin of the Seismological Society of America*, *97*(1A), S152–S173.

Christophersen, A., N. Litchfield, K. Berryman, R. Thomas, R. Basili, L. Wallace, W. Ries, G. P. Hayes, K. M. Haller, T. Yoshioka, and others (2015), Development of the Global Earthquake Model's neotectonic fault database, *Natural Hazards*, *79*(1), 111–135.

Clark, R., and S. Cox (1996), A modern regression approach to determining fault displacement-length scaling relationships, *Journal of Structural Geology*, *18*(2-3), 147–152.

Cocco, M., and A. Rovelli (1989), Evidence for the variation of stress drop between normal and thrust faulting earthquakes in Italy, *Journal of Geophysical Research: Solid Earth*, *94*(B7), 9399–9416.

Cocco, M., and E. Tinti (2008), Scale dependence in the dynamics of earthquake propagation: Evidence from seismological and geological observations, *Earth and Planetary Science Letters*, *273*(1-2), 123–131.

Cocco, M., E. Tinti, and A. Cirella (2016), On the scale dependence of earthquake stress drop, *Journal of Seismology*, *20*(4), 1151–1170.

Cotton, F., and M. Campillo (1995), Frequency domain inversion of strong motions: application to the 1992 Landers earthquake, *Journal of Geophysical Research: Solid Earth*, *100*(B3), 3961–3975.

Cotton, F., R. Archuleta, and M. Causse (2013), What is sigma of the stress drop?, *Seismological Research Letters*, *84*(1), 42–48.

Cowie, P. A., and C. H. Scholz (1992), Displacement-length scaling relationship for faults: data synthesis and discussion, *Journal of Structural Geology*, *14*(10), 1149–1156.

Cowie, P. A., C. H. Scholz, M. Edwards, and A. Malinverno (1993), Fault strain and seismic coupling on mid-ocean ridges, *Journal of Geophysical Research: Solid Earth*, *98*(B10), 17,911–17,920.

Crotwell, H. P., T. J. Owens, and J. Ritsema (1999), The TauP Toolkit: Flexible seismic travel-time and ray-path utilities, *Seismological Research Letters*, *70*, 154–160.

Dauteuil, O. (1995), Fault pattern from Seabeam processing: the western part of the Blanco Fracture Zone (NE Pacific), *Marine Geophysical Researches*, *17*(1), 17–35.

Dawers, N. H., M. H. Anders, and C. H. Scholz (1993), Growth of normal faults: Displacement-length scaling, *Geology*, *21*(12), 1107–1110.

DeCharon, A. V. (1989), *Structure and tectonics of Cascadia segment, central Blanco Transform Fault Zone*, Oreg. State Univ., Corvallis.

Delaney, J. R., H. P. Johnson, and J. L. Karsten (1981), The Juan de Fuca ridge—hot spot—propagating rift system: new tectonic, geochemical, and magnetic data, *Journal of Geophysical Research: Solid Earth*, *86*(B12), 11,747–11,750.

Dickinson-Lovell, H., M.-H. Huang, A. M. Freed, E. Fielding, R. Bürgmann, and C. Andronicos (2017), Inferred rheological structure and mantle conditions from postseismic deformation following the 2010 M w 7.2 El Mayor-Cucapah Earthquake, *Geophysical Journal International*, *213*(3), 1720–1730.

Dieterich, J. H. (1978), Time-dependent friction and the mechanics of stick-slip, in *Rock Friction and Earthquake Prediction*, pp. 790–806, Springer.

Dieterich, J. H., and B. D. Kilgore (1994), Direct observation of frictional contacts: New insights for state-dependent properties, *Pure and Applied Geophysics*, *143*(1-3), 283–302.

Dodge, D. A., G. C. Beroza, and W. Ellsworth (1996), Detailed observations of California foreshock sequences: Implications for the earthquake initiation process, *Journal of Geophysical Research: Solid Earth*, *101*(B10), 22,371–22,392.

Dominguez, L. A., T. Taira, and M. A. Santoyo (2016), Spatiotemporal variations of characteristic repeating earthquake sequences along the Middle America Trench in Mexico, *Journal of Geophysical Research: Solid Earth*, *121*(12), 8855–8870.

Donnellan, A., and G. A. Lyzenga (1998), GPS observations of fault afterslip and upper crustal deformation following the Northridge earthquake, *Journal of Geophysical Research: Solid Earth*, *103*(B9), 21,285–21,297.

Dreger, D., R. M. Nadeau, and A. Chung (2007), Repeating earthquake finite source models: Strong asperities revealed on the San Andreas Fault, *Geophysical Research Letters*, *34*(23).

Dziak, R. P., C. G. Fox, and R. W. Embley (1991), Relationship between the seismicity and geologic structure of the Blanco Transform Fault Zone, *Marine Geophysical Researches*, *13*(3), 203–208.

Dziak, R. P., C. G. Fox, R. W. Embley, J. L. Nábělek, J. Braunmiller, and R. A. Koski (2000), Recent tectonics of the Blanco Ridge, eastern Blanco transform fault zone, *Marine Geophysical Researches*, *21*(5), 423–450.

Dziewonski, A. M., and D. L. Anderson (1981), Preliminary reference Earth model, *Physics of the Earth and Planetary Interiors*, *25*(4), 297–356.

Ellsworth, W., A. Lindh, W. Prescott, and D. Herd (1981), The 1906 San Francisco earthquake and the seismic cycle, *Earthquake prediction: An international review*, *4*, 126–140.

Embley, R. W., and D. S. Wilson (1992), Morphology of the Blanco Transform Fault Zone-NE Pacific: implications for its tectonic evolution, *Marine Geophysical Researches*, *14*(1), 25–45.

Engeln, J. F., D. A. Wiens, and S. Stein (1986), Mechanisms and depths of Atlantic transform earthquakes, *Journal of Geophysical Research: Solid Earth*, *91*(B1), 548–577.

Escudero, C. R., and D. I. Doser (2012), Relative Source–Time Function Studies and Stress Drop of Earthquakes in Southeastern Alaska–Northwestern Canada, *Bulletin of the Seismological Society of America*, *102*(4), 1820–1828.

Eshelby, J. D. (1957), The determination of the elastic field of an ellipsoidal inclusion, and related problems, in *Proceedings of the Royal Society of London A: Mathematical, Physical and Engineering Sciences*, vol. 241, pp. 376–396, The Royal Society.

Famin, V., H. Raimbourg, S. Garcia, N. Bellahsen, Y. Hamada, A.-M. Boullier, O. Fabbri, L. Michon, T. Uchide, T. Ricci, and others (2014), Stress rotations and the long-term weakness of the Median Tectonic Line and the Rokko-Awaji Segment, *Tectonics*, *33*(10), 1900–1919.

Fan, W., and P. M. Shearer (2015), Detailed rupture imaging of the 25 April 2015 Nepal earthquake using teleseismic P waves, *Geophysical Research Letters*, *42*(14), 5744–5752.

Felzer, K. R., R. E. Abercrombie, and G. Ekström (2004), A common origin for aftershocks, foreshocks, and multiplets, *Bulletin of the Seismological Society of America*, *94*(1), 88–98.

Fletcher, J. M., O. J. Teran, T. K. Rockwell, M. E. Oskin, K. W. Hudnut, K. J. Mueller, R. M. Spelz, S. O. Akciz, E. Masana, G. Faneros, and others (2014), Assembly of a large earthquake from a complex fault system: Surface rupture kinematics of the 4 April 2010 El Mayor–Cucapah (Mexico) Mw 7.2 earthquake, *Geosphere*, *10*(4), 797–827.

Fossen, H., and J. Hesthammer (1997), Geometric analysis and scaling relations of deformation bands in porous sandstone, *Journal of Structural Geology*, *19*(12), 1479–1493.

Fossen, H., R. A. Schultz, Z. K. Shipton, and K. Mair (2007), Deformation bands in sandstone: a review, *Journal of the Geological Society*, *164*(4), 755–769.

Francis, T. (1981), Serpentinization faults and their role in the tectonics of slow spreading ridges, *Journal of Geophysical Research: Solid Earth*, *86*(B12), 11,616–11,622.

Freedman, D., and P. Diaconis (1981), On the histogram as a density estimator: L 2 theory, *Zeitschrift für Wahrscheinlichkeitstheorie und verwandte Gebiete*, *57*(4), 453–476.

Gaetani, G. A., S. E. DeLong, and D. A. Wark (1995), Petrogenesis of basalts from the Blanco Trough, northeast Pacific: Inferences for off-axis melt generation, *Journal of Geophysical Research: Solid Earth*, *100*(B3), 4197–4214.

Galehouse, J. S., and J. J. Lienkaemper (2003), Inferences drawn from two decades of alinement array measurements of creep on faults in the San Francisco Bay region, *Bulletin of the Seismological Society of America*, *93*(6), 2415–2433.

Gardonio, B., D. Marsan, A. Socquet, M. Bouchon, J. Jara, Q. Sun, N. Cotte, and M. Campillo (2018), Revisiting slow slip events occurrence in Boso Peninsula, Japan, combining GPS data and repeating earthquakes analysis, *Journal of Geophysical Research: Solid Earth*, *123*(2), 1502–1515.

Géli, L., J.-M. Piau, R. Dziak, V. Maury, D. Fitzenz, Q. Coutellier, and P. Henry

(2014), Seismic precursors linked to super-critical fluids at oceanic transform faults, *Nature Geoscience*, *7*(10), 757–761.

Gibowicz, S. (1998), Partial stress drop and frictional overshoot mechanism of seismic events induced by mining, in *Seismicity Caused by Mines, Fluid Injections, Reservoirs, and Oil Extraction*, pp. 5–20, Springer.

Gillespie, P., J. J. T. Walsh, and J. Watterson (1992), Limitations of dimension and displacement data from single faults and the consequences for data analysis and interpretation, *Journal of Structural Geology*, *14*(10), 1157–1172.

Goebel, T., E. Hauksson, P. Shearer, and J. Ampuero (2015), Stress-drop heterogeneity within tectonically complex regions: a case study of San Gorgonio Pass, southern California, *Geophysical Journal International*, *202*(1), 514–528.

Goebel, T., E. Hauksson, A. Plesch, and J. Shaw (2017), Detecting Significant Stress Drop Variations in Large Micro-Earthquake Datasets: A Comparison Between a Convergent Step-Over in the San Andreas Fault and the Ventura Thrust Fault System, Southern California, *Pure and Applied Geophysics*, *174*(6), 2311–2330.

Goertz-Allmann, B. P., A. Goertz, and S. Wiemer (2011), Stress drop variations of induced earthquakes at the Basel geothermal site, *Geophysical Research Letters*, *38*(9), L09,308.

Gomberg, J., and P. Johnson (2005), Seismology: Dynamic triggering of earthquakes, *Nature*, *437*(7060), 830.

Gonzalez-Ortega, A., Y. Fialko, D. Sandwell, F. A. Nava-Pichardo, J. Fletcher, J. Gonzalez-Garcia, B. Lipovsky, M. Floyd, and G. Funning (2014), El Mayor-Cucapah (Mw 7.2) earthquake: Early near-field postseismic deformation from InSAR and GPS observations, *Journal of Geophysical Research: Solid Earth*, *119*(2), 1482–1497.

Goodfellow, S., and R. Young (2014), A laboratory acoustic emission experiment under in situ conditions, *Geophysical Research Letters*, *41*(10), 3422–3430.

Grandin, R., M. Vallée, C. Satriano, R. Lacassin, Y. Klinger, M. Simoes, and L. Bollinger (2015), Rupture process of the Mw= 7.9 2015 Gorkha earthquake (Nepal): Insights into Himalayan megathrust segmentation, *Geophysical Research Letters*, *42*(20), 8373–8382.

Gutenberg, B., and C. F. Richter (1944), Frequency of earthquakes in California, *Bulletin of the Seismological Society of America*, *34*(4), 185–188.

Hanks, T. C. (1977), Earthquake stress drops, ambient tectonic stresses and stresses that drive plate motions, in *Stress in the Earth*, pp. 441–458, Springer.

Hanks, T. C., and D. A. Johnson (1976), Geophysical assessment of peak accelerations, *Bulletin of the Seismological Society of America*, *66*(3), 959–968.

Hanks, T. C., and H. Kanamori (1979), A moment magnitude scale, *Journal of Geophysical Research: Solid Earth*, *84*(B5), 2348–2350.

Hanks, T. C., and R. K. McGuire (1981), The character of high-frequency strong ground motion, *Bulletin of the Seismological Society of America*, *71*(6), 2071–2095.

Hansen, G. C., and E. Condon (1989), *Denial of disaster*, Cameron and Company San Francisco.

Hardebeck, J. L., and A. Aron (2009), Earthquake Stress Drops and Inferred Fault Strength on the Hayward Fault, East San Francisco Bay, California, *Bulletin of the Seismological Society of America*, *99*(3), 1801–1814.

Hardebeck, J. L., and E. Hauksson (1997), Static stress drop in the 1994 Northridge, California, aftershock sequence, *Bulletin of the Seismological Society of America*, *87*(6), 1495–1501.

Hardebeck, J. L., and J. P. Loveless (2018), Creeping subduction zones are weaker than locked subduction zones, *Nature Geoscience*, *11*(1), 60.

Hardebeck, J. L., J. J. Nazareth, and E. Hauksson (1998), The static stress change triggering model: Constraints from two southern California aftershock sequences, *Journal of Geophysical Research: Solid Earth*, *103*(B10), 24,427–24,437.

Harrington, R. M., and E. E. Brodsky (2009), Source duration scales with magnitude differently for earthquakes on the San Andreas Fault and on secondary faults in Parkfield, California, *Bulletin of the Seismological Society of America*, *99*(4), 2323 – 2334.

Hasegawa, A., K. Yoshida, and T. Okada (2011), Nearly complete stress drop in the 2011 M w 9.0 off the Pacific coast of Tohoku Earthquake, *Earth, planets and space*, *63*(7), 35.

Hatakeyama, N., N. Uchida, T. Matsuzawa, and W. Nakamura (2017), Emergence and disappearance of interplate repeating earthquakes following the 2011 M9. 0 Tohoku-oki earthquake: Slip behavior transition between seismic and aseismic depending on the loading rate, *Journal of Geophysical Research: Solid Earth*, *122*(7), 5160–5180.

Hauksson, E. (2015), Average stress drops of Southern California earthquakes in the context of crustal geophysics: implications for fault zone healing, *Pure and Applied Geophysics*, *172*(5), 1359–1370.

Hauksson, E., J. Stock, K. Hutton, W. Yang, J. A. Vidal-Villegas, and H. Kanamori (2011), The 2010 M w 7.2 El Mayor-Cucapah Earthquake Sequence, Baja California, Mexico and Southernmost California, USA: Active Seismotectonics along the Mexican Pacific Margin, *Pure and Applied Geophysics*, *168*(8-9), 1255–1277.

Hauksson, E., W. Yang, and P. M. Shearer (2012), Waveform relocated earthquake catalog for southern California (1981 to June 2011), *Bulletin of the Seismological Society of America*, *102*(5), 2239–2244.

Hawthorne, J., and J.-P. Ampuero (2017), A phase coherence approach to identifying co-located earthquakes and tremor, *Geophysical Journal International*, *209*(2), 623–642.

Hawthorne, J., M. Simons, and J.-P. Ampuero (2016), Estimates of aseismic slip associated with small earthquakes near San Juan Bautista, CA, *Journal of Geophysical Research: Solid Earth*, *121*(11), 8254–8275.

Hawthorne, J. C., A. M. Thomas, and J.-P. Ampuero (2018), The rupture extent of low frequency earthquakes near Parkfield, CA, *Geophysical Journal International*, *216*(1), 621–639.

He, C., Z. Wang, and W. Yao (2007), Frictional sliding of gabbro gouge under hydrothermal conditions, *Tectonophysics*, *445*(3-4), 353–362.

Hearn, E., S. McClusky, S. Ergintav, and R. Reilinger (2009), Izmit earthquake postseismic deformation and dynamics of the North Anatolian Fault Zone, *Journal of Geophysical Research: Solid Earth*, *114*(B8).

Heidbach, O., M. Rajabi, K. Reiter, M. Ziegler, W. S. M. team, and others (2016), World stress map database release 2016, *GFZ Data Services*, *10*.

Helmstetter, A., and B. E. Shaw (2009), Afterslip and aftershocks in the rate-and-state friction law, *Journal of Geophysical Research: Solid Earth*, *114*(B1).

Helmstetter, A., and D. Sornette (2003a), Foreshocks explained by cascades of triggered seismicity, *Journal of Geophysical Research: Solid Earth*, *108*(B10).

Helmstetter, A., and D. Sornette (2003b), Predictability in the epidemic-type aftershock sequence model of interacting triggered seismicity, *Journal of Geophysical Research: Solid Earth*, *108*(B10).

Herman, M. W., K. P. Furlong, G. P. Hayes, and H. M. Benz (2016), Foreshock triggering of the 1 April 2014 Mw 8.2 Iquique, Chile, earthquake, *Earth and Planetary Science Letters*, *447*, 119–129.

Hines, T. T., and E. A. Hetland (2016), Rheologic constraints on the upper mantle from 5 years of postseismic deformation following the El Mayor-Cucapah earthquake, *Journal of Geophysical Research: Solid Earth*, *121*(9), 6809–6827.

Hough, S., and D. Dreger (1995), Source parameters of the 23 April 1992 M 6.1 Joshua Tree, California, earthquake and its aftershocks: Empirical Green's function analysis of GEOS and TERRAscope data, *Bulletin of the Seismological Society of America*, *85*(6), 1576–1590.

Hough, S., and L. Seeber (1991), Seismological constraints on source properties of the mb= 4.0, 1985 Ardsley, New York, earthquake: a characteristic rupture?, *Journal of Geophysical Research: Solid Earth*, *96*(B11), 18,183–18,195.

Hough, S. E., and A. Elliot (2004), Revisiting the 23 February 1892 Laguna Salada Earthquake, *Bulletin of the Seismological Society of America*, *94*(4), 1571–1578.

Houston, H. (2001), Influence of depth, focal mechanism, and tectonic setting on the shape and duration of earthquake source time functions, *Journal of Geophysical Research: Solid Earth*, *106*(B6), 11,137–11,150.

Hsu, Y.-J., M. Simons, J.-P. Avouac, J. Galetzka, K. Sieh, M. Chlieh, D. Natawidjaja, L. Prawirodirdjo, and Y. Bock (2006), Frictional afterslip following the 2005 Nias-Simeulue earthquake, Sumatra, *Science*, *312*(5782), 1921–1926.

Huang, H., W. Xu, L. Meng, R. Bürgmann, and J. C. Baez (2017a), Early aftershocks and afterslip surrounding the 2015 Mw 8.4 Illapel rupture, *Earth and Planetary Science Letters*, *457*, 282–291.

Huang, M.-H., E. J. Fielding, H. Dickinson, J. Sun, J. A. Gonzalez-Ortega, A. M. Freed, and R. Bürgmann (2017b), Fault geometry inversion and slip distribution of the 2010 Mw 7.2 El Mayor-Cucapah earthquake from geodetic data, *Journal of Geophysical Research: Solid Earth*, *122*(1), 607–621.

Hussain, E., T. J. Wright, R. J. Walters, D. Bekaert, A. Hooper, and G. A. Houseman (2016), Geodetic observations of postseismic creep in the decade after the 1999 Izmit earthquake, Turkey: Implications for a shallow slip deficit, *Journal of Geophysical Research: Solid Earth*, *121*(4), 2980–3001.

Igarashi, T., T. Matsuzawa, and A. Hasegawa (2003), Repeating earthquakes and interplate aseismic slip in the northeastern Japan subduction zone, *Journal of Geophysical Research: Solid Earth*, *108*(B5).

Ihmlé, P. F., and T. H. Jordan (1994), Teleseismic search for slow precursors to large earthquakes, *Science*, *266*(5190), 1547–1551.

Ihmlé, P. F., P. Harabaglia, and T. H. Jordan (1993), Teleseismic detection of a slow precursor to the great 1989 Macquarie Ridge earthquake, *Science*, *261*(5118), 177–183.

Imanishi, K., and T. Uchide (2017), Non-self-similar source property for microforeshocks of the 2014 Mw 6.2 Northern Nagano, central Japan, earthquake, *Geophysical Research Letters*, *44*(11), 5401–5410.

Imanishi, K., W. L. Ellsworth, and S. G. Prejean (2004), Earthquake source parameters determined by the SAFOD Pilot Hole seismic array, *Geophysical Research Letters*, *31*(12).

Ingleby, T., and T. Wright (2017), Omori-like decay of postseismic velocities following continental earthquakes, *Geophysical Research Letters*, *44*(7), 3119–3130.

Isacks, B., J. Oliver, and L. R. Sykes (1968), Seismology and the new global tectonics, *Journal of Geophysical Research*, *73*(18), 5855–5899.

Jansen, G., C. Ruhl, and S. Miller (2019), Fluid pressure triggered foreshock sequence of the 2008 Mogul earthquake sequence: Insights from stress inversion and numerical modeling, *Journal of Geophysical Research: Solid Earth*.

Jin, A., C. A. Moya, and M. Ando (2000), Simultaneous Determination of Site Responses and Source Parameters of Small Earthquakes along the Atotsugawa Fault Zone, Central Japan, *Bulletin of the Seismological Society of America*, *90*(6), 1430–1445.

Johnson, L. R., and R. M. Nadeau (2002), Asperity model of an earthquake: Static problem, *Bulletin of the Seismological Society of America*, *92*(2), 672–686.

Jones, L. E., and D. V. Helmberger (1996), Seismicity and stress-drop in the Eastern Transverse Ranges, southern California, *Geophysical Research Letters*, *23*(3), 233–236.

Jones, L. E., and D. V. Helmberger (1998), Earthquake source parameters and fault

kinematics in the eastern California shear zone, *Bulletin of the Seismological Society of America*, *88*(6), 1337–1352.

Jones, L. M., and P. Molnar (1979), Some characteristics of foreshocks and their possible relationship to earthquake prediction and premonitory slip on faults, *Journal of Geophysical Research: Solid Earth*, *84*(B7), 3596–3608.

Juteau, T., D. Bideau, O. Dauteuil, G. Manac'h, D. Naidoo, P. Nehlig, H. Ondreas, M. Tivey, K. Whipple, and J. Delaney (1995), A submersible study in the Western Blanco Fracture Zone, NE Pacific: Structure and evolution during the last 1.6 Ma, *Marine Geophysical Researches*, *17*(5), 399–430.

Kanamori, H. (1977), *Seismic and Aseismic Slip Along Subduction Zones and their Tectonic Implications, in Island Arcs, Deep Sea Trenches and Back-Arc Basins*, American Geophysical Union, Washington, D. C.

Kanamori, H., and D. L. Anderson (1975), Theoretical basis of some empirical relations in seismology, *Bulletin of the Seismological Society of America*, *65*(5), 1073–1095.

Kanamori, H., and G. S. Stewart (1976), Mode of the strain release along the Gibbs fracture zone, Mid-Atlantic Ridge, *Physics of the Earth and Planetary Interiors*, *11*(4), 312–332.

Kanamori, H., J. Mori, E. Hauksson, T. H. Heaton, L. K. Hutton, and L. M. Jones (1993), Determination of earthquake energy release and ML using TERRAscope, *Bulletin of the Seismological Society of America*, *83*(2), 330–346.

Kane, D. L., P. M. Shearer, B. P. Goertz-Allmann, and F. L. Vernon (2013), Rupture directivity of small earthquakes at Parkfield, *Journal of Geophysical Research: Solid Earth*, *118*(1), 212–221.

Kaneko, Y., and P. Shearer (2014), Seismic source spectra and estimated stress drop derived from cohesive-zone models of circular subshear rupture, *Geophysical Journal International*, *197*(2), 1002–1015.

Kaneko, Y., and P. Shearer (2015), Variability of seismic source spectra, estimated stress drop, and radiated energy, derived from cohesive-zone models of symmetrical and asymmetrical circular and elliptical ruptures, *Journal of Geophysical Research: Solid Earth*, *120*(2), 1053–1079.

Karner, S. L., and C. Marone (2000), Effects of loading rate and normal stress on stress drop and stick-slip recurrence interval, *Geophysical Monograph-American Geophysical Union*, *120*, 187–198.

Kastens, K., K. Macdonald, K. Becker, and K. Crane (1979), The Tamayo transform fault in the mouth of the Gulf of California, *Marine Geophysical Researches*, *4*(2), 129–151.

Kato, A., and S. Nakagawa (2014), Multiple slow-slip events during a foreshock sequence of the 2014 Iquique, Chile Mw 8.1 earthquake, *Geophysical Research Letters*, *41*(15), 5420–5427.

Kato, A., K. Obara, T. Igarashi, H. Tsuruoka, S. Nakagawa, and N. Hirata (2012), Propagation of slow slip leading up to the 2011 Mw 9.0 Tohoku-Oki earthquake, *Science*, *335*(6069), 705–708.

Kawasaki, I., Y. Asai, and Y. Tamura (2001), Space–time distribution of interplate moment release including slow earthquakes and the seismo-geodetic coupling in the Sanriku-oki region along the Japan trench, *Tectonophysics*, *330*(3-4), 267–283.

Kennett, B., and E. Engdahl (1991), Traveltimes for global earthquake location and phase identification, *Geophysical Journal International*, *105*(2), 429–465.

Kilb, D., J. Gomberg, and P. Bodin (2000), Triggering of earthquake aftershocks by dynamic stresses, *Nature*, *408*(6812), 570.

Kilb, D., J. Gomberg, and P. Bodin (2002), Aftershock triggering by complete Coulomb stress changes, *Journal of Geophysical Research: Solid Earth*, *107*(B4), ESE–2.

Kim, A., and D. S. Dreger (2008), Rupture process of the 2004 Parkfield earthquake

from near-fault seismic waveform and geodetic records, *Journal of Geophysical Research: Solid Earth*, *113*(B7).

Kim, A., D. S. Dreger, T. Taira, and R. M. Nadeau (2016), Changes in repeating earthquake slip behavior following the 2004 Parkfield main shock from waveform empirical Green's functions finite-source inversion, *Journal of Geophysical Research: Solid Earth*, *121*(3), 1910–1926.

Kim, Y.-S., and D. J. Sanderson (2005), The relationship between displacement and length of faults: a review, *Earth-Science Reviews*, *68*(3-4), 317–334.

King, C.-Y., and L. Knopoff (1968), Stress drop in earthquakes, *Bulletin of the Seismological Society of America*, *58*(1), 249–257.

Kinoshita, S., and M. Ohike (2002), Scaling Relations of Earthquakes That Occurred in the Upper Part of the Philippine Sea Plate beneath the Kanto Region, Japan, Estimated by Means of Borehole Recordings, *Bulletin of the Seismological Society of America*, *92*(2), 611–624.

Kolyukhin, D., and A. Torabi (2012), Statistical analysis of the relationships between faults attributes, *Journal of Geophysical Research: Solid Earth*, *117*(5).

Kroll, K. A., E. S. Cochran, K. B. Richards-Dinger, and D. F. Sumy (2013), Aftershocks of the 2010 Mw 7.2 El Mayor-Cucapah earthquake reveal complex faulting in the Yuha Desert, California, *Journal of Geophysical Research: Solid Earth*, *118*(12), 6146–6164.

Kuna, V. M., J. L. Nábělek, and J. Braunmiller (2019), Mode of slip and crust–mantle interaction at oceanic transform faults, *Nature Geoscience*, *12*(2), 138 – 142.

Kwiatek, G., F. Bulut, M. Bohnhoff, and G. Dresen (2014), High-resolution analysis of seismicity induced at Berlín geothermal field, El Salvador, *Geothermics*, *52*, 98–111.

Lay, T., L. Ye, C. J. Ammon, A. Dunham, and K. D. Koper (2016), The 2 March 2016 Wharton basin Mw 7.8 earthquake: High stress drop north-south strike-slip rupture

in the diffuse oceanic deformation zone between the Indian and Australian plates, *Geophysical Research Letters*, *43*(15), 7937–7945.

Lay, T., L. Ye, Y. Bai, K. F. Cheung, and H. Kanamori (2018), The 2018 MW 7.9 Gulf of Alaska earthquake: Multiple fault rupture in the Pacific plate, *Geophysical Research Letters*, *45*(18), 9542–9551.

Lengliné, O., and D. Marsan (2009), Inferring the coseismic and postseismic stress changes caused by the 2004 Mw= 6 Parkfield earthquake from variations of recurrence times of microearthquakes, *Journal of Geophysical Research: Solid Earth*, *114*(B10).

Lengliné, O., B. Enescu, Z. Peng, and K. Shiomi (2012), Decay and expansion of the early aftershock activity following the 2011, Mw9. 0 Tohoku earthquake, *Geophysical Research Letters*, *39*(18).

Lengliné, O., L. Lamourette, L. Vivin, N. Cuenot, and J. Schmittbuhl (2014), Fluid-induced earthquakes with variable stress drop, *Journal of Geophysical Research: Solid Earth*, *119*(12), 8900–8913.

Letort, J., J. Guilbert, F. Cotton, I. Bondár, Y. Cano, and J. Vergoz (2015), A new, improved and fully automatic method for teleseismic depth estimation of moderate earthquakes (4.5< M< 5.5): application to the Guerrero subduction zone (Mexico), *Geophysical Journal International*, *201*(3), 1834–1848.

Lin, Y.-Y., and N. Lapusta (2018), Microseismicity simulated on asperity-like fault patches: On scaling of seismic moment with duration and seismological estimates of stress drops, *Geophysical Research Letters*, *45*(16), 8145–8155.

Lin, Y.-Y., K.-F. Ma, and V. Oye (2012), Observation and scaling of microearthquakes from the Taiwan Chelungpu-fault borehole seismometers, *Geophysical Journal International*, *190*(1), 665–676.

Lin, Y.-Y., K.-F. Ma, H. Kanamori, T.-R. A. Song, N. Lapusta, and V. C. Tsai (2016), Evidence for non-self-similarity of microearthquakes recorded at a Taiwan borehole seismometer array, *Geophysical Journal International*, *206*(2), 757–773.

Ljunggren, C., Y. Chang, T. Janson, and R. Christiansson (2003), An overview of rock stress measurement methods, *International Journal of Rock Mechanics and Mining Sciences*, *40*(7-8), 975–989.

Lohman, R. B., and J. J. McGuire (2007), Earthquake swarms driven by aseismic creep in the Salton Trough, California, *Journal of Geophysical Research: Solid Earth*, *112*(B4).

Loveless, J. P., and B. J. Meade (2016), Two decades of spatiotemporal variations in subduction zone coupling offshore Japan, *Earth and Planetary Science Letters*, *436*, 19–30.

Madariaga, R. (1976), Dynamics of an expanding circular fault, *Bulletin of the Seismological Society of America*, *66*(3), 639–666.

Mai, P. M., and G. C. Beroza (2000), Source scaling properties from finite-fault-rupture models, *Bulletin of the Seismological Society of America*, *90*(3), 604–615.

Mai, P. M., and K. Thingbaijam (2014), SRCMOD: An online database of finite-fault rupture models, *Seismological Research Letters*, *85*(6), 1348–1357.

Malagnini, L., F. P. Lucente, P. De Gori, A. Akinci, and I. Munafo (2012), Control of pore fluid pressure diffusion on fault failure mode: Insights from the 2009 L'Aquila seismic sequence, *Journal of Geophysical Research: Solid Earth*, *117*(B5).

Mann, P., M. R. Hempton, D. C. Bradley, and K. Burke (1983), Development of pull-apart basins, *The Journal of Geology*, *91*(5), 529–554.

Marone, C. (1998), The effect of loading rate on static friction and the rate of fault healing during the earthquake cycle, *Nature*, *391*(6662), 69.

Marone, C., J. E. Vidale, and W. L. Ellsworth (1995), Fault healing inferred from time dependent variations in source properties of repeating earthquakes, *Geophysical Research Letters*, *22*(22), 3095–3098.

Marone, C. J., C. Scholtz, and R. Bilham (1991), On the mechanics of earthquake afterslip, *Journal of Geophysical Research: Solid Earth*, *96*(B5), 8441–8452.

Marrett, R., and R. W. Allmendinger (1991), Estimates of strain due to brittle faulting: sampling of fault populations, *Journal of Structural Geology*, *13*(6), 735–738.

Marsan, D., and O. Lengline (2008), Extending earthquakes' reach through cascading, *Science*, *319*(5866), 1076–1079.

Martínez-Garzón, P., M. Bohnhoff, Y. Ben-Zion, and G. Dresen (2015), Scaling of maximum observed magnitudes with geometrical and stress properties of strike-slip faults, *Geophysical Research Letters*, *42*(23), 10–230.

Materna, K., T. Taira, and R. Bürgmann (2018), Aseismic Transform Fault Slip at the Mendocino Triple Junction From Characteristically Repeating Earthquakes, *Geophysical Research Letters*, *45*(2), 699–707.

Matsuzawa, T., T. Igarashi, and A. Hasegawa (2002), Characteristic small-earthquake sequence off Sanriku, northeastern Honshu, Japan, *Geophysical Research Letters*, *29*(11), 38–1.

Mayeda, K., and W. R. Walter (1996), Moment, energy, stress drop, and source spectra of western United States earthquakes from regional coda envelopes, *Journal of Geophysical Research: Solid Earth*, *101*(B5), 11,195–11,208.

McGarr, A. (1984), Scaling of ground motion parameters, state of stress, and focal depth, *Journal of Geophysical Research: Solid Earth*, *89*(B8), 6969–6979.

McGarr, A., and N. Gay (1978), State of stress in the Earth's crust, *Annual Review of Earth and Planetary Sciences*, *6*(1), 405–436.

McGarr, A., M. Zoback, and T. Hanks (1982), Implications of an elastic analysis of in situ stress measurements near the San Andreas fault, *Journal of Geophysical Research: Solid Earth*, *87*(B9), 7797–7806.

McGuire, J. J. (2008), Seismic cycles and earthquake predictability on East Pacific Rise transform faults, *Bulletin of the Seismological Society of America*, *98*(3), 1067–1084.

McGuire, J. J., and T. H. Jordan (2000), Further evidence for the compound nature of slow earthquakes: The Prince Edward Island earthquake of April 28, 1997, *Journal of Geophysical Research: Solid Earth*, *105*(B4), 7819–7827.

McGuire, J. J., P. F. Ihmle, and T. H. Jordan (1996), Time-domain observations of a slow precursor to the 1994 Romanche transform earthquake, *Science*, *274*(5284), 82–85.

McGuire, J. J., M. S. Boettcher, and T. H. Jordan (2005), Foreshock sequences and short-term earthquake predictability on East Pacific Rise transform faults, *Nature*, *434*(7032), 457–461.

McGuire, J. J., J. A. Collins, P. Gouédard, E. Roland, D. Lizarralde, M. S. Boettcher, M. D. Behn, and R. D. van der Hilst (2012), Variations in earthquake rupture properties along the Gofar transform fault, East Pacific Rise, *Nature Geoscience*, *5*(5), 336–341.

McLaskey, G. C., B. D. Kilgore, D. A. Lockner, and N. M. Beeler (2014), Laboratory generated M-6 earthquakes, *Pure and Applied Geophysics*, *171*(10), 2601–2615.

Mendoza, C., and S. Hartzell (2013), Finite-fault source inversion using teleseismic P waves: Simple parameterization and rapid analysis, *Bulletin of the Seismological Society of America*, *103*(2A), 834–844.

Meng, L., H. Huang, R. Bürgmann, J. P. Ampuero, and A. Strader (2015), Dual megathrust slip behaviors of the 2014 Iquique earthquake sequence, *Earth and Planetary Science Letters*, *411*, 177–187.

Meng, X., and Z. Peng (2014), Seismicity rate changes in the Salton Sea Geothermal Field and the San Jacinto Fault Zone after the 2010 M w 7.2 El Mayor-Cucapah earthquake, *Geophysical Journal International*, *197*(3), 1750–1762.

Miller, S. A., C. Collettini, L. Chiaraluce, M. Cocco, M. Barchi, and B. J. Kaus (2004), Aftershocks driven by a high-pressure CO 2 source at depth, *Nature*, *427*(6976), 724.

Miyazaki, S.-i., P. Segall, J. Fukuda, and T. Kato (2004), Space time distribution of afterslip following the 2003 Tokachi-oki earthquake: Implications for variations in fault zone frictional properties, *Geophysical Research Letters*, *31*(6).

Moody, J. B. (1976), Serpentinization: a review, *Lithos*, *9*(2), 125–138.

Mori, J. (1996), Rupture directivity and slip distribution of the M 4.3 foreshock to the 1992 Joshua Tree earthquake, Southern California, *Bulletin of the Seismological Society of America*, *86*(3), 805–810.

Mori, J., R. E. Abercrombie, and H. Kanamori (2003), Stress drops and radiated energies of aftershocks of the 1994 Northridge, California, earthquake, *Journal of Geophysical Research: Solid Earth*, *108*(B11).

Morita, Y., and H. Hamaguchi (1984), Automatic Detection of Onset Time of Seismic Waves and its Confidence Interval Using the Autoregressive Model Fitting, *Zisin (Journal of the Seismological Society of Japan. 2nd ser.)*, *37*, 281–293.

Moyer, P. A., M. S. Boettcher, J. J. McGuire, and J. A. Collins (2018), Spatial and Temporal Variations in Earthquake Stress Drop on Gofar Transform Fault, East Pacific Rise: Implications for Fault Strength, *Journal of Geophysical Research: Solid Earth*, *123*(9), 7722 – 7740.

Nadeau, R. M., and L. R. Johnson (1998), Seismological studies at Parkfield VI: Moment release rates and estimates of source parameters for small repeating earthquakes, *Bulletin of the Seismological Society of America*, *88*(3), 790–814.

Nadeau, R. M., and T. V. McEvilly (1999), Fault slip rates at depth from recurrence intervals of repeating microearthquakes, *Science*, *285*(5428), 718–721.

Nadeau, R. M., W. Foxall, and T. McEvilly (1995), Clustering and periodic recurrence of microearthquakes on the San Andreas fault at Parkfield, California, *Science*, *267*(5197), 503–507.

Nadeau, R. M., A. Michelini, R. A. Uhrhammer, D. Dolenc, and T. V. McEvilly (2004),

Detailed kinematics, structure and recurrence of micro-seismicity in the SAFOD target region, *Geophysical Research Letters*, *31*(12).

Niemeijer, A., and C. Spiers (2006), Velocity dependence of strength and healing behaviour in simulated phyllosilicate-bearing fault gouge, *Tectonophysics*, *427*(1-4), 231–253.

Okal, E. A., and A. R. Langenhorst (2000), Seismic properties of the Eltanin transform system, South Pacific, *Physics of the Earth and Planetary Interiors*, *119*(3-4), 185–208.

Okal, E. A., and L. M. Stewart (1982), Slow earthquakes along oceanic fracture zones: evidence for asthenospheric flow away from hotspots?, *Earth and Planetary Science Letters*, *57*(1), 75–87.

Okuda, T., and S. Ide (2018), Streak and hierarchical structures of the Tohoku–Hokkaido subduction zone plate boundary, *Earth, Planets and Space*, *70*(1), 132.

Omori, F. (1894), On the after-shocks of earthquakes, *Journal of the College of Science, Imperial University of Tokyo*, *7*, 111–200.

Oth, A. (2013), On the characteristics of earthquake stress release variations in Japan, *Earth and Planetary Science Letters*, *377*, 132–141.

Pacheco, J. F., L. R. Sykes, and C. H. Scholz (1993), Nature of seismic coupling along simple plate boundaries of the subduction type, *Journal of Geophysical Research: Solid Earth*, *98*(B8), 14,133–14,159.

Park, J., C. R. Lindberg, and F. L. Vernon (1987), Multitaper spectral analysis of high-frequency seismograms, *Journal of Geophysical Research: Solid Earth*, *92*(B12), 12,675–12,684.

Passelègue, F. X., A. Schubnel, S. Nielsen, H. S. Bhat, D. Deldicque, and R. Madariaga (2016), Dynamic rupture processes inferred from laboratory microearthquakes, *Journal of Geophysical Research: Solid Earth*, *121*(6), 4343–4365.

Peng, Z., and Y. Ben-Zion (2005), Spatiotemporal variations of crustal anisotropy from similar events in aftershocks of the 1999 M 7.4 Izmit and M 7.1 Düzce, Turkey, earthquake sequences, *Geophysical Journal International*, *160*(3), 1027–1043.

Peng, Z., and J. Gomberg (2010), An integrated perspective of the continuum between earthquakes and slow-slip phenomena, *Nature Geoscience*, *3*(9), 599–607.

Peng, Z., and P. Zhao (2009), Migration of early aftershocks following the 2004 Parkfield earthquake, *Nature Geoscience*, *2*(12), 877.

Pérez-Campos, X., J. McGuire, and G. Beroza (2003), Resolution of the slow earthquake/high apparent stress paradox for oceanic transform fault earthquakes, *Journal of Geophysical Research: Solid Earth*, *108*(B9).

Perfettini, H., and J.-P. Avouac (2007), Modeling afterslip and aftershocks following the 1992 Landers earthquake, *Journal of Geophysical Research: Solid Earth*, *112*(B7).

Perfettini, H., W. Frank, D. Marsan, and M. Bouchon (2018), A model of aftershock migration driven by afterslip, *Geophysical Research Letters*, *45*(5), 2283–2293.

Pinkston, J., and S. Kirby (1982), Experimental deformation of dunite under conditions appropriate to the lithosphere, *Eos Trans. AGU*, *63*, 1094.

Pollitz, F. F., R. Bürgmann, and W. Thatcher (2012), Illumination of rheological mantle heterogeneity by the M7. 2 2010 El Mayor-Cucapah earthquake, *Geochemistry, Geophysics, Geosystems*, *13*(6).

Porritt, R. W., R. M. Allen, D. C. Boyarko, and M. R. Brudzinski (2011), Investigation of Cascadia segmentation with ambient noise tomography, *Earth and Planetary Science Letters*, *309*(1-2), 67–76.

Poupinet, G., W. Ellsworth, and J. Frechet (1984), Monitoring velocity variations in the crust using earthquake doublets: An application to the Calaveras Fault, California, *Journal of Geophysical Research: Solid Earth*, *89*(B7), 5719–5731.

Poupinet, G., A. Ratdomopurbo, and O. Coutant (1996), On the use of earthquake multiplets to study fractures and the temporal evolution of an active volcano, *Annals of Geophysics*, *39*(2).

Prieto, G. A., P. M. Shearer, F. L. Vernon, and D. Kilb (2004), Earthquake source scaling and self-similarity estimation from stacking P and S spectra, *Journal of Geophysical Research: Solid Earth*, *109*(B8).

Prioul, R., F. Cornet, C. Dorbath, L. Dorbath, M. Ogena, and E. Ramos (2000), An induced seismicity experiment across a creeping segment of the Philippine fault, *Journal of Geophysical Research: Solid Earth*, *105*(B6), 13,595–13,612.

Purvance, M. D., and J. G. Anderson (2003), A comprehensive study of the observed spectral decay in strong-motion accelerations recorded in Guerrero, Mexico, *Bulletin of the Seismological Society of America*, *93*(2), 600–611.

Quin, H. (1990), Dynamic stress drop and rupture dynamics of the October 15, 1979 Imperial Valley, California, earthquake, *Tectonophysics*, *175*(1-3), 93–117.

Rajmeny, P., U. Singh, and B. Sinha (2002), Predicting rock failure around boreholes and drives adjacent to stopes in Indian mines in high stress regions, *International Journal of Rock Mechanics and Mining Sciences*, *39*(2), 151–164.

Reasenberg, P. A. (1999), Foreshock occurrence before large earthquakes, *Journal of Geophysical Research: Solid Earth*, *104*(B3), 4755–4768.

Reinen, L. A., J. D. Weeks, and T. E. Tullis (1991), The frictional behavior of serpentinite: Implications for aseismic creep on shallow crustal faults, *Geophysical Research Letters*, *18*(10), 1921–1924.

Reinen, L. A., J. D. Weeks, and T. E. Tullis (1994), The frictional behavior of lizardite and antigorite serpentinites: Experiments, constitutive models, and implications for natural faults, *Pure and Applied Geophysics*, *143*(1-3), 317–358.

Rietbrock, A., I. Ryder, G. Hayes, C. Haberland, D. Comte, S. Roecker, and H. Lyon-Caen (2012), Aftershock seismicity of the 2010 Maule Mw= 8.8, Chile, earthquake:

Correlation between co-seismic slip models and aftershock distribution?, *Geophysical Research Letters*, *39*(8).

Robinson, D., C. Brough, and S. Das (2006), The Mw 7.8, 2001 Kunlunshan earthquake: Extreme rupture speed variability and effect of fault geometry, *Journal of Geophysical Research: Solid Earth*, *111*(B8).

Rodríguez-Pérez, Q., L. Ottemöller, and R. R. Castro (2012), Stochastic finite-fault ground-motion simulation and source characterization of the 4 April 2010 Mw 7.2 El Mayor-Cucapah Earthquake, *Seismological Research Letters*, *83*(2), 235–249.

Roland, E., D. Lizarralde, J. J. McGuire, and J. A. Collins (2012), Seismic velocity constraints on the material properties that control earthquake behavior at the Quebrada-Discovery-Gofar transform faults, East Pacific Rise, *Journal of Geophysical Research: Solid Earth*, *117*(B11).

Rollins, C., S. Barbot, and J.-P. Avouac (2015), Postseismic Deformation Following the 2010$$ M= 7.2$$ El Mayor-Cucapah Earthquake: Observations, Kinematic Inversions, and Dynamic Models, *Pure and Applied Geophysics*, *172*(5), 1305–1358.

Ross, Z. E., Y. Ben-Zion, M. C. White, and F. L. Vernon (2016), Analysis of earthquake body wave spectra for potency and magnitude values: Implications for magnitude scaling relations, *Geophysical Supplements to the Monthly Notices of the Royal Astronomical Society*, *207*(2), 1158–1164.

Ross, Z. E., C. Rollins, E. S. Cochran, E. Hauksson, J.-P. Avouac, and Y. Ben-Zion (2017), Aftershocks driven by afterslip and fluid pressure sweeping through a fault-fracture mesh, *Geophysical Research Letters*, *44*(16), 8260–8267.

Ruhl, C., R. Abercrombie, and K. Smith (2017), Spatiotemporal variation of stress drop during the 2008 Mogul, Nevada, earthquake swarm, *Journal of Geophysical Research: Solid Earth*, *122*(10), 8163–8180.

Rymer, M. J., J. A. Treiman, K. J. Kendrick, J. J. Lienkaemper, R. J. Weldon, R. Bilham, M. Wei, E. J. Fielding, J. L. Hernandez, B. P. Olson, and others (2011), Trig-

gered surface slips in southern California associated with the 2010 El Mayor-Cucapah, Baja California, Mexico, earthquake, *Tech. rep.*, US Geological Survey.

Sagy, A., E. E. Brodsky, and G. J. Axen (2007), Evolution of fault-surface roughness with slip, *Geology*, *35*(3), 283–286.

Sammis, C. G., and J. R. Rice (2001), Repeating earthquakes as low-stress-drop events at a border between locked and creeping fault patches, *Bulletin of the Seismological Society of America*, *91*(3), 532–537.

Savage, J., and M. Wood (1971), The relation between apparent stress and stress drop, *Bulletin of the Seismological Society of America*, *61*(5), 1381–1388.

Schaff, D. P., and P. G. Richards (2004), Repeating seismic events in China, *Science*, *303*(5661), 1176–1178.

Schaff, D. P., G. C. Beroza, and B. E. Shaw (1998), Postseismic response of repeating aftershocks, *Geophysical Research Letters*, *25*(24), 4549–4552.

Schlische, R. W., S. S. Young, R. V. Ackermann, and A. Gupta (1996), Geometry and scaling relations of a population of very small rift-related normal faults, *Geology*, *24*(8), 683–686.

Schmidt, D., R. Bürgmann, R. Nadeau, and M. d'Alessio (2005), Distribution of aseismic slip rate on the Hayward fault inferred from seismic and geodetic data, *Journal of Geophysical Research: Solid Earth*, *110*(B8).

Schmittbuhl, J., H. Karabulut, O. Lengliné, and M. Bouchon (2016), Long-lasting seismic repeaters in the Central Basin of the Main Marmara Fault, *Geophysical Research Letters*, *43*(18), 9527–9534.

Schoenball, M., and W. L. Ellsworth (2017), Waveform-relocated earthquake catalog for Oklahoma and southern Kansas illuminates the regional fault network, *Seismological Research Letters*, *88*(5), 1252–1258.

Scholz, C., N. Dawers, J.-Z. Yu, M. Anders, and P. Cowie (1993), Fault growth and fault scaling laws: preliminary results, *Journal of Geophysical Research: Solid Earth*, *98*(B12), 21,951–21,961.

Scholz, C. H. (2002), *The mechanics of earthquakes and faulting*, Cambridge University Press.

Scholz, C. H., and J. Campos (2012), The seismic coupling of subduction zones revisited, *Journal of Geophysical Research: Solid Earth*, *117*(B5).

Scholz, C. H., C. Aviles, and S. G. Wesnousky (1986), Scaling differences between large interplate and intraplate earthquakes, *Bulletin of the Seismological Society of America*, *76*(1), 65–70.

Schultz, R., C. Klimczak, H. Fossen, J. Olson, U. Exner, D. Reeves, and R. Soliva (2013), Statistical tests of scaling relationships for geologic structures, *Journal of Structural Geology*, *48*, 85–94.

Schultz, R. A., R. Soliva, H. Fossen, C. H. Okubo, and D. M. Reeves (2008), Dependence of displacement–length scaling relations for fractures and deformation bands on the volumetric changes across them, *Journal of Structural Geology*, *30*(11), 1405–1411.

Segall, P., and D. D. Pollard (1983), Nucleation and growth of strike slip faults in granite, *Journal of Geophysical Research: Solid Earth*, *88*(B1), 555–568.

Seif, S., J. D. Zechar, A. Mignan, S. Nandan, and S. Wiemer (2018), Foreshocks and Their Potential Deviation from General Seismicity, *Bulletin of the Seismological Society of America*, *109*(1), 1–18.

Sellers, E. J., M. O. Kataka, and L. M. Linzer (2003), Source parameters of acoustic emission events and scaling with mining-induced seismicity, *Journal of Geophysical Research: Solid Earth*, *108*(B9).

Şengör, A., O. Tüysüz, C. Imren, M. Sakınç, H. Eyidoğan, N. Görür, X. Le Pichon, and C. Rangin (2005), The North Anatolian fault: A new look, *Annual Review of Earth and Planetary Sciences*, *33*, 37–112.

Sharma, M., and H. Wason (1994), Occurrence of low stress drop earthquakes in the Garhwal Himalaya region, *Physics of the Earth and Planetary Interiors*, *85*(3-4), 265–272.

Shearer, P. M. (2009), *Introduction to Seismology*, 2 ed., Cambridge University Press.

Shearer, P. M., G. A. Prieto, and E. Hauksson (2006), Comprehensive analysis of earthquake source spectra in southern California, *Journal of Geophysical Research: Solid Earth*, *111*(B6).

Shearer, P. M., R. E. Abercrombie, D. T. Trugman, and W. Wang (2019), Comparing EGF Methods for Estimating Corner Frequency and Stress Drop From P Wave Spectra, *Journal of Geophysical Research: Solid Earth*.

Sibson, R. H. (1974), Frictional constraints on thrust, wrench and normal faults, *Nature*, *249*(5457), 542.

Sibson, R. H. (1982), Fault zone models, heat flow, and the depth distribution of earthquakes in the continental crust of the United States, *Bulletin of the Seismological Society of America*, *72*(1), 151–163.

Sibson, R. H. (1984), Roughness at the base of the seismogenic zone: contributing factors, *Journal of Geophysical Research: Solid Earth*, *89*(B7), 5791–5799.

Smith, K. D., J. N. Brune, and K. F. Priestley (1991), The seismic spectrum, radiated energy, and the Savage and Wood inequality for complex earthquakes, *Tectonophysics*, *188*(3-4), 303–320.

Smith, S. W., and M. Wyss (1968), Displacement on the San Andreas fault subsequent to the 1966 Parkfield earthquake, *Bulletin of the Seismological Society of America*, *58*(6), 1955–1973.

Snoke, J., A. Linde, and I. Sacks (1983), Apparent stress: an estimate of the stress drop, *Bulletin of the Seismological Society of America*, *73*(2), 339–348.

Somerville, P. G., N. F. Smith, R. W. Graves, and N. A. Abrahamson (1997), Modification of empirical strong ground motion attenuation relations to include the amplitude and duration effects of rupture directivity, *Seismological Research Letters*, *68*(1), 199–222.

Stacey, J., and others (1998), In situ stresses in mining areas in South Africa, *Journal of the Southern African Institute of Mining and Metallurgy*, *98*(7), 365–368.

Staszek, M., B. Orlecka-Sikora, K. Leptokaropoulos, G. Kwiatek, and P. Martínez-Garzón (2017), Temporal static stress drop variations due to injection activity at The Geysers geothermal field, California, *Geophysical Research Letters*, *44*(14), 2017GL073,929.

Stein, R. S., A. A. Barka, and J. H. Dieterich (1997), Progressive failure on the North Anatolian fault since 1939 by earthquake stress triggering, *Geophysical Journal International*, *128*(3), 594–604.

Stein, S., and M. Wysession (2013), *An introduction to seismology, earthquakes, and earth structure*, Blackwell Pub, Maiden, MA.

Stirling, M. W., N. Litchfield, P. Villamor, R. Van Dissen, A. Nicol, J. Pettinga, P. Barnes, R. Langridge, T. Little, D. Barrell, and others (2017), The Mw 7.8 2016 Kaikōura earthquake: Surface fault rupture and seismic hazard context, *Bulletin of the New Zealand Society for Earthquake Engineering*, *50*, 73–84.

Sumy, D. F., C. J. Neighbors, E. S. Cochran, and K. M. Keranen (2017), Low stress drops observed for aftershocks of the 2011 Mw 5.7 Prague, Oklahoma, earthquake, *Journal of Geophysical Research: Solid Earth*, *122*(5), 3813–3834.

Taira, T., R. Bürgmann, R. M. Nadeau, and D. S. Dreger (2014), Variability of fault slip behavior along the San Andreas Fault in the San Juan Bautista Region, *Journal of Geophysical Research: Solid Earth*, *119*(12), 8827–8844.

Tan, Y., and D. Helmberger (2010), Rupture directivity characteristics of the 2003 Big Bear sequence, *Bulletin of the Seismological Society of America*, *100*(3), 1089–1106.

Taylor, G., S. Rost, and G. Houseman (2016), Crustal imaging across the North Anatolian Fault Zone from the autocorrelation of ambient seismic noise, *Geophysical Research Letters*, *43*(6), 2502–2509.

Templeton, D. C., R. M. Nadeau, and R. Bürgmann (2008), Behavior of repeating earthquake sequences in central California and the implications for subsurface fault creep, *Bulletin of the Seismological Society of America*, *98*(1), 52–65.

Thomson, D. J. (1982), Spectrum estimation and harmonic analysis, *Proceedings of the IEEE*, *70*(9), 1055–1096.

Toké, N. A., J. R. Arrowsmith, M. J. Rymer, A. Landgraf, D. E. Haddad, M. Busch, J. Coyan, and A. Hannah (2011), Late Holocene slip rate of the San Andreas fault and its accommodation by creep and moderate-magnitude earthquakes at Parkfield, California, *Geology*, *39*(3), 243–246.

Torabi, A., and S. S. Berg (2011), Scaling of fault attributes: A review, *Marine and Petroleum Geology*, *28*(8), 1444–1460.

Trnkoczy, A. (1999), Topic Understanding and parameter setting of STA/LTA trigger algorithm, *New manual of seismological observatory practice*, *2*.

Trugman, D. T., and P. M. Shearer (2018), Strong Correlation between Stress Drop and Peak Ground Acceleration for Recent M 1–4 Earthquakes in the San Francisco Bay Area, *Bulletin of the Seismological Society of America*, *108*(2), 929–945.

Tse, S. T., and J. R. Rice (1986), Crustal earthquake instability in relation to the depth variation of frictional slip properties, *Journal of Geophysical Research: Solid Earth*, *91*(B9), 9452–9472.

Turner, R. C., R. M. Nadeau, and R. Bürgmann (2013), Aseismic slip and fault interaction from repeating earthquakes in the Loma Prieta aftershock zone, *Geophysical Research Letters*, *40*(6), 1079–1083.

Uchida, N., and R. Bürgmann (2019), Repeating earthquakes, *Annual Review of Earth and Planetary Sciences*, *47*.

Uchida, N., and T. Matsuzawa (2011), Coupling coefficient, hierarchical structure, and earthquake cycle for the source area of the 2011 off the Pacific coast of Tohoku earthquake inferred from small repeating earthquake data, *Earth, Planets and Space*, *63*(7), 30.

Uchida, N., T. Matsuzawa, A. Hasegawa, and T. Igarashi (2003), Interplate quasi-static slip off Sanriku, NE Japan, estimated from repeating earthquakes, *Geophysical Research Letters*, *30*(15).

Uchida, N., Y. Asano, and A. Hasegawa (2016), Acceleration of regional plate subduction beneath Kanto, Japan, after the 2011 Tohoku-oki earthquake, *Geophysical Research Letters*, *43*(17), 9002–9008.

Uchide, T., H. Yao, and P. M. Shearer (2013), Spatio-temporal distribution of fault slip and high-frequency radiation of the 2010 El Mayor-Cucapah, Mexico earthquake, *Journal of Geophysical Research: Solid Earth*, *118*(4), 1546–1555.

Uchide, T., P. M. Shearer, and K. Imanishi (2014), Stress drop variations among small earthquakes before the 2011 Tohoku-oki, Japan, earthquake and implications for the main shock, *Journal of Geophysical Research: Solid Earth*, *119*(9), 7164 – 7174.

Urano, S., Y. Hiramatsu, T. Yamada, and others (2015), Relationship between co-seismic slip and static stress drop of similar aftershocks of the 2007 Noto Hanto earthquake, *Earth, Planets and Space*, *67*(1), 101.

Utsu, T. (1961), A statistical study on the occurrence of aftershocks, *The Geophysical Magazine*, *30*, 521–605.

Valoroso, L., L. Chiaraluce, R. Di Stefano, and G. Monachesi (2017), Mixed-mode slip behavior of the Altotiberina low-angle normal fault system (Northern Apennines, Italy) through high-resolution earthquake locations and repeating events, *Journal of Geophysical Research: Solid Earth*, *122*(12), 10–220.

Velasco, A. A., C. J. Ammon, and T. Lay (1994), Empirical green function deconvolution of broadband surface waves: Rupture directivity of the 1992 Landers, California

(Mw= 7.3), earthquake, *Bulletin of the Seismological Society of America*, *84*(3), 735–750.

Velasco, A. A., S. Hernandez, T. Parsons, and K. Pankow (2008), Global ubiquity of dynamic earthquake triggering, *Nature Geoscience*, *1*(6), 375.

Waldhauser, F. (2009), Near-real-time double-difference event location using long-term seismic archives, with application to Northern California, *Bulletin of the Seismological Society of America*, *99*(5), 2736–2748.

Waldhauser, F., and D. P. Schaff (2008), Large-scale relocation of two decades of northern California seismicity using cross-correlation and double-difference methods, *Journal of Geophysical Research: Solid Earth*, *113*(B8).

Waldhauser, F., W. Ellsworth, D. P. Schaff, and A. Cole (2004), Streaks, multiplets, and holes: High-resolution spatio-temporal behavior of Parkfield seismicity, *Geophysical Research Letters*, *31*(18).

Walsh, J. J., and J. Watterson (1988), Analysis of the relationship between displacements and dimensions of faults, *Journal of Structural Geology*, *10*(3), 239–247.

Watterson, J. (1986), Fault dimensions, displacements and growth, *Pure and Applied Geophysics*, *124*(1-2), 365–373.

Wei, S., E. Fielding, S. Leprince, A. Sladen, J.-P. Avouac, D. Helmberger, E. Hauksson, R. Chu, M. Simons, K. Hudnut, and others (2011), Superficial simplicity of the 2010 El Mayor–Cucapah earthquake of Baja California in Mexico, *Nature Geoscience*, *4*(9), 615.

Wei, S., D. Helmberger, S. Owen, R. W. Graves, K. W. Hudnut, and E. J. Fielding (2013), Complementary slip distributions of the largest earthquakes in the 2012 Brawley swarm, Imperial Valley, California, *Geophysical Research Letters*, *40*(5), 847–852.

Wells, D. L., and K. J. Coppersmith (1994), New empirical relationships among magni-

tude, rupture length, rupture width, rupture area, and surface displacement, *Bulletin of the Seismological Society of America*, *84*(4), 974–1002.

Werner, K., E. Graven, T. Berkman, and M. Parker (1991), Direction of maximum horizontal compression in western Oregon determined by borehole breakouts, *Tectonics*, *10*(5), 948–958.

Wesson, R. L. (1987), Modelling aftershock migration and afterslip of the San Juan Bautista, California, earthquake of October 3, 1972, *Tectonophysics*, *144*(1-3), 215–229.

Wetzler, N., T. Lay, E. E. Brodsky, and H. Kanamori (2018), Systematic deficiency of aftershocks in areas of high coseismic slip for large subduction zone earthquakes, *Science Advances*, *4*(2).

Wiens, D. A., and S. Stein (1983), Age dependence of oceanic intraplate seismicity and implications for lithospheric evolution, *Journal of Geophysical Research: Solid Earth*, *88*(B8), 6455–6468.

Williams, J. R., J. C. Hawthorne, S. Rost, and T. J. Wright (2019), Stress Drops on the Blanco Oceanic Transform Fault from Interstation Phase Coherence, *Bulletin of the Seismological Society of America*.

Willoughby, E. C., and R. D. Hyndman (2005), Earthquake rate, slip rate, and the effective seismic thickness for oceanic transform faults of the Juan de Fuca plate system, *Geophysical Journal International*, *160*(3), 855–868.

Wilson, D. S. (1993), Confidence intervals for motion and deformation of the Juan de Fuca plate, *Journal of Geophysical Research: Solid Earth*, *98*(B9), 16,053–16,071.

Withers, M., R. Aster, C. Young, J. Beiriger, M. Harris, S. Moore, and J. Trujillo (1998), A comparison of select trigger algorithms for automated global seismic phase and event detection, *Bulletin of the Seismological Society of America*, *88*(1), 95–106.

Wolfson-Schwehr, M., M. S. Boettcher, J. J. McGuire, and J. A. Collins (2014), The

relationship between seismicity and fault structure on the Discovery transform fault, East Pacific Rise, *Geochemistry, Geophysics, Geosystems*, *15*(9), 3698–3712.

Wright, T. J., J. R. Elliott, H. Wang, and I. Ryder (2013), Earthquake cycle deformation and the Moho: Implications for the rheology of continental lithosphere, *Tectonophysics*, *609*, 504–523.

Wu, C., J. Gomberg, E. Ben-Naim, and P. Johnson (2014), Triggering of repeating earthquakes in central California, *Geophysical Research Letters*, *41*(5), 1499–1505.

Wu, J., D. Yao, X. Meng, Z. Peng, J. Su, and F. Long (2017), Spatial-temporal evolutions of early aftershocks following the 2013 Mw 6.6 Lushan earthquake in Sichuan, China, *Journal of Geophysical Research: Solid Earth*, *122*(4), 2873–2889.

Wu, Q., and M. Chapman (2017), Stress-drop estimates and source scaling of the 2011 Mineral, Virginia, mainshock and aftershocks, *Bulletin of the Seismological Society of America*, *107*(6), 2703–2720.

Wyss, M., C. G. Sammis, R. M. Nadeau, and S. Wiemer (2004), Fractal dimension and b-value on creeping and locked patches of the San Andreas fault near Parkfield, California, *Bulletin of the Seismological Society of America*, *94*(2), 410–421.

Xia, K., A. J. Rosakis, and H. Kanamori (2004), Laboratory earthquakes: The sub-Rayleigh-to-supershear rupture transition, *Science*, *303*(5665), 1859–1861.

Xu, S., A. Nieto-Samaniego, G. Murillo-Muñetón, S. Alaniz-Álvarez, J. Grajales-Nishimura, and L. Velasquillo-Martinez (2016), Effects of Physical Processes and Sampling Resolution on Fault Displacement Versus Length Scaling: The Case of the Cantarell Complex Oilfield, Gulf of Mexico, *Pure and Applied Geophysics*, *173*(4), 1125–1142.

Xu, W., S. Wu, K. Materna, R. Nadeau, M. Floyd, G. Funning, E. Chaussard, C. W. Johnson, J. R. Murray, X. Ding, and others (2018), Interseismic ground deformation and fault slip rates in the greater San Francisco Bay Area from two decades of space geodetic data, *Journal of Geophysical Research: Solid Earth*, *123*(9), 8095–8109.

Yabe, S., and S. Ide (2018), Why Do Aftershocks Occur Within the Rupture Area of a Large Earthquake?, *Geophysical Research Letters*, *45*(10), 4780–4787.

Yamada, T., P. G. Okubo, and C. J. Wolfe (2010), Kīholo Bay, Hawai ‘i, earthquake sequence of 2006: Relationship of the main shock slip with locations and source parameters of aftershocks, *Journal of Geophysical Research: Solid Earth*, *115*(B8).

Yamada, T., Y. Saito, Y. Tanioka, and J. Kawahara (2017), Spatial pattern in stress drops of moderate-sized earthquakes on the Pacific Plate off the south-east of Hokkaido, Japan: implications for the heterogeneity of frictional properties, *Progress in Earth and Planetary Science*, *4*(1), 38.

Yamashita, Y., H. Shimizu, and K. Goto (2012), Small repeating earthquake activity, interplate quasi-static slip, and interplate coupling in the Hyuga-nada, southwestern Japan subduction zone, *Geophysical Research Letters*, *39*(8).

Ye, L., T. Lay, K. D. Koper, R. Smalley Jr, L. Rivera, M. G. Bevis, A. F. Zakrajsek, and F. N. Teferle (2014), Complementary slip distributions of the August 4, 2003 Mw 7.6 and November 17, 2013 Mw 7.8 South Scotia Ridge earthquakes, *Earth and Planetary Science Letters*, *401*, 215–226.

Ye, L., T. Lay, H. Kanamori, and L. Rivera (2016), Rupture characteristics of major and great (Mw¿= 7.0) megathrust earthquakes from 1990 to 2015: 1. Source parameter scaling relationships, *Journal of Geophysical Research: Solid Earth*, *121*(2), 826–844.

Yoon, C. E., N. Yoshimitsu, W. L. Ellsworth, and G. C. Beroza (2019), Foreshocks and Mainshock Nucleation of the 1999 M w 7.1 Hector Mine, California, Earthquake, *Journal of Geophysical Research: Solid Earth*, *124*(2), 1569–1582.

Yoshida, K., T. Saito, Y. Urata, Y. Asano, and A. Hasegawa (2017), Temporal Changes in Stress Drop, Frictional Strength, and Earthquake Size Distribution in the 2011 Yamagata-Fukushima, NE Japan, Earthquake Swarm, Caused by Fluid Migration, *Journal of Geophysical Research: Solid Earth*, p. 2017JB014334.

Yu, W.-c. (2013), Shallow-focus repeating earthquakes in the

Tonga–Kermadec–Vanuatu subduction zones, *Bulletin of the Seismological Society of America*, *103*(1), 463–486.

Zhang, H., J. Chen, and Z. Ge (2012), Multi-fault rupture and successive triggering during the 2012 Mw 8.6 Sumatra offshore earthquake, *Geophysical Research Letters*, *39*(22).

Zhang, J., P. G. Richards, and D. P. Schaff (2008), Wide-scale detection of earthquake waveform doublets and further evidence for inner core super-rotation, *Geophysical Journal International*, *174*(3), 993–1006.

Zheng, Z., J. Kemeny, and N. G. Cook (1989), Analysis of borehole breakouts, *Journal of Geophysical Research: Solid Earth*, *94*(B6), 7171–7182.

Zhu, S., and M. Miao (2015), How did the 2013 Lushan earthquake (Ms= 7.0) trigger its aftershocks? Insights from static Coulomb stress change calculations, *Pure and Applied Geophysics*, *172*(10), 2481–2494.

Zoback, M. D., and G. C. Beroza (1993), Evidence for near-frictionless faulting in the 1989 (M 6.9) Loma Prieta, California, earthquake and its aftershocks, *Geology*, *21*(2), 181–185.

Zoback, M. D., M. L. Zoback, V. S. Mount, J. Suppe, J. P. Eaton, J. H. Healy, D. Oppenheimer, P. Reasenberg, L. Jones, C. B. Raleigh, and others (1987), New evidence on the state of stress of the San Andreas fault system, *Science*, *238*(4830), 1105–1111.

Zoback, M. L. (1992a), First-and second-order patterns of stress in the lithosphere: The World Stress Map Project, *Journal of Geophysical Research: Solid Earth*, *97*(B8), 11,703–11,728.

Zoback, M. L. (1992b), Stress field constraints on intraplate seismicity in eastern North America, *Journal of Geophysical Research: Solid Earth*, *97*(B8), 11,761–11,782.